SUBMARINE LANDSLIDE FLOWS SIMULATION THROUGH CENTRIFUGE MODELLING

by

Chang Shin GUE

A dissertation submitted for the degree of
Doctor of Philosophy
at the University of Cambridge

Churchill College January 2012

“Do not go where the path may lead, go instead where there is no path and leave a trail”

- Ralph Waldo Emerson

“If I have seen further than others, it is by standing upon the shoulders of giants”

- Isaac Newton

“Continuous effort – not strength or intelligence – is the key to unlocking our potential”

- Winston Churchill

ABSTRACT

SUBMARINE LANDSLIDE FLOWS SIMULATION THROUGH CENTRIFUGE MODELLING

Chang Shin GUE

Landslides occur both onshore and offshore. However, little attention has been given to offshore landslides (submarine landslides). Submarine landslides have significant impacts and consequences on offshore and coastal facilities. The unique characteristics of submarine landslides include large mass movements and long travel distances at very gentle slopes. This thesis is concerned with developing centrifuge scaling laws for submarine landslide flows through the study of modelling submarine landslide flows in a mini-drum centrifuge. A series of tests are conducted at different gravity fields in order to understand the scaling laws involved in the simulation of submarine landslide flows. The model slope is instrumented with miniature sensors for measurements of pore pressures at different locations beneath the landslide flow. A series of digital cameras are used to capture the landslide flow in flight. Numerical studies are also carried out in order to compare the results obtained with the data from the centrifuge tests. The Depth Averaged Material Point Method (DAMPM) is used in the numerical simulations to deal with large deformation (such as the long runout of submarine landslide flows). Parametric studies are performed to investigate the validity of the developed centrifuge scaling laws under the initial and boundary conditions given in the centrifuge tests. Both the results from the centrifuge tests and numerical simulations appear to follow the proposed centrifuge scaling laws, which differ from the conventional centrifuge scaling laws. The results provide a better understanding of the centrifuge scaling laws that need to be adopted for centrifuge experiments involving submarine landslide flows, as well as giving an insight into the flow mechanism involved in submarine landslide flows.

ACKNOWLEDGEMENTS

I am deeply grateful to my supervisor, Prof. Kenichi Soga, for his interest, help and encouragement throughout this study. His advice and constructive criticism during the preparation of this dissertation are very much appreciated. In addition, I am particularly indebted for his time spent and patience.

Sincere thanks are extended to Prof. Malcolm Bolton for his encouragement, enthusiasm, many invaluable discussions, comments and guidance, which inspired me tremendously throughout this study.

Thanks must also go to Dr. Stuart Haigh for his advice and expertise with the mini-drum centrifuge and the creative ideas for developing the centrifuge model. I am also grateful to Dr. N.I. Thusyanthan and Dr. Dongfang Liang for their practical advice on the research topic as well as carrying out the experiments.

I am grateful to Keita Abe for his kind assistance and advice in using and implementing the DAMPM code for the numerical simulations involved in this study.

I would like to thank all the technicians at Schofield Centre for helping me on countless occasions; my laboratory work would not have been able to progress without their expertise.

Special thanks to Dr. Suzanne Lacasse of the Norwegian Geotechnical Institute (NGI) for her endless support; first by providing the financial support through NGI and, later, the fellowship at NGI. Similarly, special thanks to Dr. Farrokh Nadim of the International Centre for Geohazards (ICG). This study and the once-in-a-lifetime experience at Cambridge would not have been possible without the financial support from NGI, ICG and the Cambridge Commonwealth Trust.

I would also like to thank my fellow students in the Geotechnical Research Group for their assistance, friendship and great memories in Cambridge: Alec, Andrew, Andy, Christopher, Chris, Fiona, Hisham, Kaushal, Khalid, Kok Hun, Leonard, Leo, Matthew, Mohammed, Panos, Piau, Senthil, Sidney, Shun, Te and Zheming.

I would like to extend my gratitude to my colleagues at NGI during the final writing-up stage of the dissertation, in particular Tom Lunne and Karl Henrik Mokkelbost for their patience and encouragement. Thanks also to Dr. Jörgen Johansson, Dr. Vaughan Meyer and Tore Kvalstad of NGI for their kind assistance and discussions.

I wish to express my heartiest appreciation to my parents in Malaysia, who have supported me from afar. Finally, but by no means least, I would like to thank my wife Tricia, for her unconditional support and encouragement throughout the preparation of this dissertation, and for taking care of our son, Isaac. This dissertation is dedicated to them.

DECLARATION

I hereby declare that, except where specific reference is made to the work of others, the contents of this dissertation are original and have not been submitted in whole or in part for consideration for any other degree or qualification at this, or any other University. This dissertation is the result of my own work and includes nothing which is the outcome of work done in collaboration except where specifically indicated in the text. This dissertation is presented within the limits of 65,000 words and 150 figures.

Chang Shin GUE

January 2012

TABLE OF CONTENTS

ABSTRACT i
ACKNOWLEDGMENTS ii
DECLARATION iii
TABLE OF CONTENTS iv
LIST OF FIGURES viii
LIST OF TABLES xiv
NOTATIONS xvi

CHAPTER I INTRODUCTION

1.1 Background 1
1.2 State of the Art - Limitations 2
1.3 Objectives and Purpose of 4
1.4 Significance of Study 5
1.5 Report Structure 5

CHAPTER II LITERATURE REVIEW – SUBMARINE LANSLIDES

2.1 Introduction 7
2.2 Submarine Landslides 7
2.3 Classification and Characteristics 8
2.4 Documentation and Recognition 12
2.5 Causes of Failure 18
2.5.1 Rapid sedimentation 18
2.5.2 Retrogressive failure 19
2.5.3 Earthquake and tectonic activity 22
2.5.4 Gas hydrate 23
2.5.5 Wave loading 24
2.5.6 Other possible causes 25
2.6 Mechanics of Submarine Landslides 26
2.6.1 Limit equilibrium 26
2.6.2 Possible boundary conditions 29
2.6.3 Flow behaviour 30

2.6.4 Governing equations and analytical solutions through mass and momentum conservations 39
2.6.5 A numerical model that incorporates various rheologies 47
2.6.6 Runout efficiency 49
2.7 Major Research Efforts 52
2.8 Experimental Works by Other Researchers 54
2.8.1 Past experimental works in 1 g environment 55
2.8.2 Overview of other submarine slope experimental works in 1 g 72
2.8.3 Past experimental works in centrifuge 74
2.9 Constraints of Past Experimental Works in Submarine Slopes 78
2.10 Summary 79

CHAPTER III CENTRIFUGE MODELLING

3.1 Introduction 80
3.2 Principles of Centrifuge Modelling 80
3.3 Centrifuge Scaling Laws 82
3.3.1 General scaling laws 82
3.3.2 Development of Scaling laws for soil flow through analytical solutions 84
3.3.3 Discussion of the proposed scaling laws for soil flow 87
3.4 Restrictions and Limitations of Centrifuge Modelling 89
3.4.1 Variations of stress and gravity field with depth 89
3.4.2 Radial gravity field 90
3.4.3 Coriolis effects 91
3.4.4 Particle size effects 92
3.4.5 Natural earth acceleration field (1 g effects) 92
3.5 Mini-Drum Centrifuge 93
3.6 Summary 96

CHAPTER IV CENTRIFUGE MODELLING OF SUBMARINE LANDSLIDE FLOWS

4.1 Introduction 97
4.2 Design of the Centrifuge Model 97
4.2.1 Geometry of the Model 97
4.2.2 Compartments for Slope and Cameras 100
4.2.3 Instrumentation 104
4.3 Choice of Slurry for the Experiments 109

4.4 Experimental Procedures 110
4.4.1 Before the experiment 110
4.4.2 During the experiment 112
4.4.3 After the experiment 114
4.5 Initial Encountered Challenges 114
4.5.1 Challenges encountered and comments 115
4.5.2 Brief description of some trial tests 116
4.6 Results and Interpretations 118
4.6.1 Series 1: Experiments at various g levels and flow rates 118
4.6.2 Series 2: Experiments at 30 g only with various flow rates 129
4.6.3 Series 3: Experiments at various g levels with a large flow rate 140
4.6.4 Series 4: Experiments at various g levels with a large flow rate in the dry condition 148
4.7 Repeatability of the Centrifuge Experiments 160
4.8 Summary 162

CHAPTER V NUMERICAL SIMULATIONS AND PARAMETRIC STUDIES

5.1 Introduction 165
5.2 Depth Average Material Point Method (DAMPM) 165
5.2.1 Governing equations 167
5.3 Model Details 172
5.4 Simulations of Experiments at Various g Levels with Scaled Flow Velocity and Height 174
5.5 Sensitivity of the Model 185
5.5.1 Background mesh 185
5.5.2 Number of particles 186
5.5.3 Time step 188
5.5.4 Side wall friction 189
5.5.5 Basal friction and pore pressure ratio (λ) 194
5.6 Summary 196

CHAPTER VI DISCUSSION AND COMPARISONS OF RESULT

6.1 Introduction 198
6.2 Comparisons of Results with the Developed Scaling Laws 198
6.3 Comparisons of Centrifuge Experiments with Numerical Simulations (All series) 202

6.3.1 Flow velocity and flow height 202
6.3.2 Relationship of flow height, flow velocity and change in pore pressure 210
6.4 Summary 217

CHAPTER VII CONCLUSIONS AND RECOMMENDATIONS FOR FUTURE WORK

7.1 Introduction 219
7.2 Summary and Conclusions 219
7.3 Recommendation for Future Research Work 222

REFERENCES AND BIBLIOGRAPHY

APPENDIX 1 – Summary of the characteristics of selected submarine landslides
APPENDIX 2 – Weight balancing in the mini-drum centrifuge
APPENDIX 3 – Calculation of bending moments against Perspex window
APPENDIX 4 – Checklist for operating the mini-drum centrifuge

LIST OF FIGURES

Chapter II

Figure 2.1: Offshore geohazards (modified after NGI, 2005) 8
Figure 2.2: Various types of submarine landslides – a continuum of slides and flows (reproduced after Prior, 1984 9
Figure 2.3: Relationship of slope inclination and the maximum runout length 10
Figure 2.4: Relationship of volume and the maximum runout length 11
Figure 2.5: Relationship of volume and the ratio of (L_{max}/H_{max}) 11
Figure 2.6: Failure at Trondheim Harbour, Norway in 1888 (after Andresen and Bjerrum, 1967) 14
Figure 2.7: Failure at Helsinki Harbour, Finland in 1936 (after Andresen and Bjerrum, 1967) 14
Figure 2.8: Storegga slide, Norway 8200 years ago (after Bryn et al., 2005) 15
Figure 2.9: Interpreted morphology of slide through bathymetry and seismic profiles (after Kvalstad et al., 2005) 20
Figure 2.10: Retrogressive slide model (after Kvalstad et al., 2005) 22
Figure 2.11: The failure (a) and post-failure (b) mechanics along an infinite slope (after Locat and Lee, 2000) 28
Figure 2.12: The mechanistic illustration of conditions leading to: (a) failure in soils (b) onset of liquefaction (after Locat and Lee) 29
Figure 2.13: Possible boundary conditions for submarine landslides (after Locat and Lee, 2000) 30
Figure 2.14: Stress-strain rate relationships (Modified after Hance, 2003) 31
Figure 2.15: Submarine, uniform Bingham flow (after Huang and Garcia, 1999) 32
Figure 2.16: Bilinear rheological model (after Hance, 2003) 37
Figure 2.17: Schematic cut-away view of an unsteady flow down a curvilinear slope (after Iverson and Denlinger, 2001) 41
Figure 2.18: Energy conversion for debris flows (modified after Iverson, 1997) 50
Figure 2.19: Schematic cross-section defining H and L, after Iverson (1997) 51
Figure 2.20: Sequence of research leading to the mitigation of offshore geohazards 54
Figure 2.21: Illustration of the experimental facility (after Mohrig et al., 1998, 1999) 59
Figure 2.22: Fronts of laboratory debris flows (after Mohrig et al., 1998) 63
Figure 2.23: Schematic profiles of the fronts of observed debris flows (after Mohrig et al., 1998) 63
Figure 2.24: Front velocity ‘vs’ distance downslope (modified after Mohrig et al., 1999) 64

Figure 2.25: Illustration of the experimental setup (modified after Ilstad et al. 2004a, b) 66
Figure 2.26: Fronts of laboratory subaqueous debris flows (after Ilstad et al. 2004a, b) 69
Figure 2.27: Materials from the base of the debris flow are eroded and incorporated into basal layer (after Ilstad et al. 2004b) 69
Figure 2.28: Pressure measurements at the base of a clay rich flow (modified after Ilstad et al. 2004b) 70
Figure 2.29: Schematic overview of the three main pressure patterns (after Ilstad et al. 2004a) 71
Figure 2.30: Trendlines of the front velocity along the channel for various slurry compositions (after Ilstad et al. 2004b) 71

Chapter III

Figure 3.1: Different soil behaviour at different stress level 81
Figure 3.2: Basic principle of scaling law 84
Figure 3.3: Conceptual flow profile in prototype and model 88
Figure 3.4: Stress variation with depth in a centrifuge model and its corresponding prototype (after Taylor, 1995) 90
Figure 3.5: Error due to radial gravity field (after Madabhushi, 2006) 91
Figure 3.6: Elevation of the mini-drum centrifuge with axis horizontal (after Barker, 1998) 94
Figure 3.7: Cross-section of the mini-drum centrifuge with axis vertical (after Barker, 1998) 94
Figure 3.8: Internal dimensions of the mini-drum centrifuge (after Barker, 1998) 95
Figure 3.9: Water supply and channel drainage of the mini-drum centrifuge (after Barker, 1998) 95

Chapter IV

Figure 4.1: Geometry of the slope 98
Figure 4.2: Geometry of the circular slope in the ring channel 98
Figure 4.3: Overview of the centrifuge model 99
Figure 4.4: Details of Perspex windows 102
Figure 4.5: Perspex windows 102
Figure 4.6: Slope and camera compartments 103
Figure 4.7: Slope and camera compartments sealed at the bottom 103
Figure 4.8: Experimental setup in the mini-drum centrifuge 104

Figure 4.9: Instrumentation layout in the model 105
Figure 4.10: The digital camera used in the experiments 107
Figure 4.11: Array of LED lights mounted around the centre shaft 108
Figure 4.12: LED push lights mounted on the centrifuge model 108
Figure 4.13: Segregation of materials 110
Figure 4.14: Illustration of the experiment 112
Figure 4.15: Various funnel opening sizes 113
Figure 4.16: Flow rate accuracy from various funnel opening sizes 113
Figure 4.17: View of debris flow sequence from camera 5 at 10 g (slope not Submerged – picture interval at 0.033s) 117
Figure 4.18: The change in pore pressure for various g levels at various locations along the slope 119
Figure 4.19: Side view of submarine landslide flows for various g levels from Camera 1 (0 m from opening of head tank) 121
Figure 4.20: Side view of submarine landslide flows for various g levels from Camera 2 (0.17 m from opening of head tank) 121
Figure 4.21: Side view of submarine landslide flows for various g levels from Camera 3 (0.36 m from opening of head tank) 122
Figure 4.22: Side view of submarine landslide flows for various g levels from Camera 4 (0.57 m from opening of head tank) 122
Figure 4.23: Plan view of submarine landslide flows from Camera 5 (picture Interval at 0.033s) 123
Figure 4.24: Combined picture frames from plan view for flow at 30 g 124
Figure 4.25: Combined picture frames from plan view for flow at 40 g 124
Figure 4.26: Combined picture frames from plan view for flow at 50 g 125
Figure 4.27: Combined picture frames from plan view for flow at 60 g 125
Figure 4.28: Flow distance against time for flows at various g levels 126
Figure 4.29: Prototype flow distance against prototype flow time based in the proposed scaling laws 128
Figure 4.30: Relationship of flow velocity and g level 129
Figure 4.31: The change in pore pressure for experiments at 30 g at various locations along the slope 131
Figure 4.32: Relationship of pore pressure and input flow rate for Series 2 132
Figure 4.33: Side view of submarine landslide flows for various flow rates at 30 g from Camera 1 (0 m from opening of head tank) 132
Figure 4.34: Side view of submarine landslide flows for various flow rates at 30 g from Camera 2 (0.17 m from opening of head tank) 133
Figure 4.35: Side view of submarine landslide flows for various flow rates at 30 g from Camera 3 (0.36 m from opening of head tank) 133
Figure 4.36: Side view of submarine landslide flows for various flow rates at 30 g from Camera 4 (0.57 m from opening of head tank) 134
Figure 4.37: Flow distance against time for flows at various flow rates 135
Figure 4.38: Relationship of flow velocity and flow rate at 30 g 136

Figure 4.39: Relationship of prototype flow velocity and prototype flow rate for Series 1 and 2 137
Figure 4.40: Relationship of measured and back-calculated flow height and input flow rate for Series 2 139
Figure 4.41: Relationship of prototype and back-calculated flow height and input flow rate for Series 1 and 2 139
Figure 4.42: The change in pore pressure for various g levels with the large flow rate at various locations along the slope 141
Figure 4.43: Relationship of pore pressure and the prototype input flow rate for Series 3 141
Figure 4.44: Flow distance against time for Series 3 142
Figure 4.45: Relationship of flow velocity and g levels for Series 3 144
Figure 4.46: Relationship of prototype flow velocity and prototype flow rate for Series 3 145
Figure 4.47: Relationship of prototype flow height and prototype flow rate for Series 3 145
Figure 4.48: Relationship of prototype flow velocity and prototype flow rate for Series 1,2 & 3 146
Figure 4.49: Relationship of prototype back-calculated flow height and prototype flow rate for Series 1,2 & 3 147
Figure 4.50: Relationship of measured change in pore pressure and prototype flow rate for Series 1,2 & 3 147
Figure 4.51: The change in pore pressure for various g levels with the large flow rate at various locations along the slope in the dry condition 149
Figure 4.52: Side view of the dry landslide flows for various g levels from Camera 1 (0 m from opening of head thank) 150
Figure 4.53: Side view of the dry landslide flows for various g levels from Camera 2 (0.17 m from opening of head thank) 150
Figure 4.54: Side view of the dry landslide flows for various g levels from Camera 3 (0.36 m from opening of head thank) 151
Figure 4.55: Plan view of the dry landslide flows from Camera 5 at 30 g (picture interval at 0.033 s) 153
Figure 4.56: Plan view of the dry landslide flows from Camera 5 at 40 g (picture interval at 0.033 s) 153
Figure 4.57: Plan view of the dry landslide flows from Camera 5 at 50 g (picture interval at 0.033 s) 154
Figure 4.58: Plan view of the dry landslide flows from Camera 5 at 60 g (picture interval at 0.033 s) 154
Figure 4.59: Flow distance against time at various g levels with a large flow rate in the dry condition 156
Figure 4.60: Relationship of flow velocity and g levels for various g levels with a large flow rate in the dry condition 157
Figure 4.61: Relationship of prototype flow velocity and prototype flow rate for Series 3 & 4 159

Figure 4.62: Relationship of prototype back-calculated flow height and prototype flow rate for Series 3 & 4 159
Figure 4.63: Relationship of averaged measured change in pore pressure and prototype flow rate for Series 3 & 4 160
Figure 4.64: The change in pore pressure for three experiments at 30g with flow rate of $3.5*10^{-4}$ m^3/s at various locations along the slope 161
Figure 4.65: Flow distance against time for the two experiments at 30g with flow rate of $3.5*10^{-4}$ m^3/s 162

Chapter V

Figure 5.1: Hungr's depth-averaged concept (modified after Hungr, 1995) 166
Figure 5.2: Illustration of DAMPM (after Abe, 2008) 167
Figure 5.3: Condition of a unit of a mass in submerged case 171
Figure 5.4: Schematic of numerical simulation 172
Figure 5.5: Flow developments at 30 g 176
Figure 5.6: Flow developments at 40 g 177
Figure 5.7: Flow developments at 50 g 178
Figure 5.8: Flow developments at 60 g 179
Figure 5.9: Averaged flow velocity against time for various g levels 180
Figure 5.10: Averaged flow height against time for various g levels 180
Figure 5.11: Flow height development against slope distance at various time interval 181
Figure 5.12: Flow distance against time for various g levels 183
Figure 5.13: Prototype flow distance for various g levels 184
Figure 5.14: Effects of background mesh on the averaged flow velocity 185
Figure 5.15: Effects of background mesh on the averaged flow height 186
Figure 5.16: Effects of number of particles on the averaged flow velocity 187
Figure 5.17: Effects of number of particles on the averaged flow height 187
Figure 5.18: Effects of time step on the averaged flow velocity 189
Figure 5.19: Effects of time step on the averaged flow height 189
Figure 5.20: Effects of various side wall frictions on the averaged flow velocity 190
Figure 5.21: Effects of various side wall frictions on the averaged flow height 190
Figure 5.22: Velocity profile at various side wall frictions 191
Figure 5.23: Effects of various side wall frictions on the flow developments 192
Figure 5.24: Effects of various λ on the flow velocity at basal friction = 0° 194
Figure 5.25: Effects of various λ on the flow velocity at basal friction = 12.5^o 194
Figure 5.26: Effects of various λ on the flow height at basal friction = 0° 195
Figure 5.27: Effects of various λ on the flow height at basal friction = 12.5^o 195

Chapter VI

Figure 6.1: Averaged flow height against averaged flow velocity from centrifuge experiments and numerical simulations 201
Figure 6.2: Comparisons of averaged prototype flow height between centrifuge experiments and numerical simulations 201
Figure 6.3: Comparisons of averaged prototype flow velocity between centrifuge experiments and numerical simulations 202
Figure 6.4: Comparisons of averaged prototype flow height between centrifuge experiments and numerical simulations (Series 3) 203
Figure 6.5: Comparisons of averaged prototype flow velocity between centrifuge experiments and numerical simulations (Series 3) 204
Figure 6.6: Contours of λ values on the averaged prototype flow height (Series 3) 205
Figure 6.7: Contours of λ values on the averaged prototype flow velocity (Series 3) 206
Figure 6.8: Contours of λ values on the averaged prototype flow height (Series 4) 207
Figure 6.9: Contours of λ values on the averaged prototype flow velocity (Series 4) 207
Figure 6.10: Comparisons of averaged prototype flow height between centrifuge experiments and numerical simulations (All series) 208
Figure 6.11: Comparisons of averaged prototype flow velocity between centrifuge experiments and numerical simulations (All series) 209
Figure 6.12: Comparison of the measured change in pore pressure and the back-calculated change in pore pressure 211
Figure 6.13: Designed and back-calculated water depths along the slope 213
Figure 6.14: Uplifting of foam slope 214
Figure 6.15: Evidence of uplifting of foam slope in the centrifuge experiment 214
Figure 6.16: Relationship of error in measured change in pore pressure and prototype flow velocity 216

LIST OF TABLES

Chapter II

Table 2.1: Summary of flow velocity, distance and thickness of various Submarine landslides 16
Table 2.2: Summary of submarine slope experimental works in 1 g environment 56
Table 2.3: Slurry compositions in percentage of weight of total mass (after Ilstad et al., 2004a, b) 68
Table 2.4: Summary of submarine slope experimental works in centrifuges 77
Table 2.5: Summary of various submarine slope experimental works 78

Chapter III

Table 3.1: Summary of basic centrifuge modelling scaling laws (after Barker, 1998) 83

Chapter IV

Table 4.1: Initial encountered challenges while developing the model 115
Table 4.2: Experimental details of flow rates and flow heights 118
Table 4.3: Summary of the measured flow velocities for various g levels 127
Table 4.4: Summary of the measured and back-calculated flow heights for various g levels 128
Table 4.5: Experimental details of flow rates for experiments at 30 g 130
Table 4.6: Summary of the measured flow velocities for various flow rates at 30 g 136
Table 4.7: Summary of the measured and back calculated flow heights for Various flow rates at 30 g 138
Table 4.8: Experimental details of flow rates and funnel opening diameter for the series of experiments at the large flow rate 140
Table 4.9: Summary of the measured flow velocities for various g levels with the large flow rate 143
Table 4.10: Summary of the measured back-calculated flow heights for various g levels with the large flow rate 143
Table 4.11: Experimental details of flow rates and funnel opening diameter for experiments in the dry condition 148

Table 4.12: Summary of the measured flow velocities at various g levels with the large flow rate in the dry condition 156
Table 4.13: Summary of the measured back-calculated flow heights for various g levels with the large flow rate in the dry condition 157

Chapter V

Table 5.1: Basic parameters for the numerical simulations 174
Table 5.2: Initial details for the numerical simulations for experiments in various g levels with scaled flow velocity and height 175
Table 5.3: Summary of results from numerical simulations 184

Chapter VI

Table 6.1: Summary of results from centrifuge experiments and numerical simulations 200

NOTATIONS

A	area
a	inertia acceleration
a_c	coriolis acceleration
B	breadth
c	empirical constant
c'	effective cohesion
d_{10}, d_{50}	particle size
e	void ratio
G_s	specific gravity
g	gravitational acceleration
H	height or vertical elevation
H_{max}	maximum slope height
h	flow height
h_s	height of shear layer
h_p	height of plug layer
$\bar{h}$	average flow height
$\bar{h}_{BC}$	average back calculated flow height
$\bar{h}_{PBC}$	average prototype back calculated flow height
$\bar{h}_p$	average prototype flow height
i	hydraulic Gradient
K	hydraulic conductivity
k	hydraulic permeability
$k_{act/pass}$	lateral stress coefficient
L	horizontal length or flow distance
L_{max}	maximum runout distance
M	mass
N	Normal force
N	N times gravity
n	flow index number

p_{bed}	excess pore fluid pressure at base
p_w	pore water pressure
p_{we}	excess pore water pressure
p_{ws}	static pore water pressure
Q	flow rate
Q_{Pul}	prototype flow rate per unit length
Q_{ul}	flow rate per unit length
R	dimensionless net resistance coefficient
R_e	effective centrifuge radius
R_t	centrifuge radius from the centre of rotation to the top of model
r	centrifuge radius
r_u	pore pressure ratio
r_x	radius of local bed curvature in the *x* direction
S	shear resistance of flow
S_{tr}	strength ratio
$s_{u,ref}$	shear strength at the reference strain rate
s	stagnation point
T	pressure tensor
T_f	stress of the fluid phase
T_s	stress of the solid phase
$\overline{T}_{ijkl}$	local stiffness
t	time
u	pore water pressure
Vol	volume
V_p	flow velocity in the plug flow region
v	flow velocity
$\overline{v}$	average flow velocity
$\overline{v}_p$	average prototype flow velocity
v_s	flow velocity in the shear region or the solid phase
v_t	flow velocity in the top of the flow layer
W	vertical component of body force of slice
WC	water content

w	width
x,y,z	x, y and z direction
Y	normalised vertical coordinate with flow height
z	depth
α_1, α_2	shape factor
β	rate parameter
β_1	shape factor
$\Delta\sigma$	total incremental stress
ΔU	change in pore pressure
γ	unit weight
$\dot{\gamma}$	rates of shear strain
$\dot{\gamma}_0$	rheological constant
$\dot{\gamma}_{ref}$	reference strain rate
δL	displacement
ε	strain
η	rate parameter
λ	pore pressure ratio
μ	viscosity
υ_f	fluid volume fraction
ρ	mixture density
ρ_ω	density of water
σ	total normal stress
σ'	effective total normal stress
σ_{xz}, σ_{yz}	basal frictional stresses
$\overline{\sigma}_{zz}$	depth average total normal stress
$\overline{\sigma'}_{zz}$	depth average effective normal stress
τ	shear strength
τ_{ya}	apparent yield strength
τ_b	bed shear stress
τ_y	yield strength
ϕ'	effective friction angle

ϕ_{bed}	bed friction angle
ϕ_{int}	mixture internal friction angle
θ	slope angle
ω	angular velocity
ψ	$\tau_b/\tau_{ya}\ sgn\ (V_p)$
ζ	slope of the existing bed
Θ	parameter constant

CHAPTER I

1.0 INTRODUCTION

1.1 Background

Landslides occur both onshore and offshore. However, rather little attention has been given to offshore landslides (submarine landslides). They occur below water level, and our knowledge of their development is quite limited. These submarine landslides are rather mysterious, as they frequently occur in slopes that should be stable beyond any doubt according to conventional stability analyses (Andresen and Bjerrum, 1967). However, substantial progress has been made in the understanding of the geological process and physical mechanisms operating at different stages of a submarine landslide event (Vanneste et al., 2011).

Both onshore landslides (subaerial landslides) and submarine landslides have many similarities in terms of landslide mechanics (Hampton et al., 1996; Locat and Lee, 2000). Nevertheless, they also have some significant and remarkable differences. In particular, the unique characteristics of submarine landslides are the huge volume of mass movements and large travel distances at very gentle slopes.

These submarine landslides are known to have significant impacts and consequences on offshore and coastal facilities such as oil and gas production wells, platforms, pipelines, seafloor communication cables, as well as marine habitats. Furthermore, submarine landslides may also trigger tsunamis as a result of their own displacements, leading to considerable damage to properties and loss of lives. Therefore, a further understanding of submarine landslides is essential in order to mitigate these occurrences.

This study is a pilot study of simulations of submarine landslide flows through centrifuge modelling, which aims to give an insight in the centrifuge

scaling laws as well as the flow mechanism involved in submarine landslide flows. This study also explores the usage of a geotechnical centrifuge to model submarine landslide flows. The experimental works are carried out using the mini-drum centrifuge at the Schofield Centre of the Engineering Department, University of Cambridge.

1.2 State of the Art - Limitations

Considering the increasing interest in offshore developments and potential hazards to mankind, research has been active particularly in the COSTA-Canada project (Locat and Lee, 2000) 2000–2004, and the development of the Ormen Lange gas field in Norway (Kvalstad et al., 2005), which is considered the world's largest subsea pipeline project. Most interestingly, the Ormen Lange gas field is located near to an ancient submarine landslide, which leads to a number of researches principally carried out by the Norwegian Geotechnical Institute (NGI) and the International Centre for Geohazards (ICG).

According to the available literature, the main factors that initiate submarine landslides include rapid deposition, extremely high pore water pressure, earthquakes and gas hydrate dissociation (Schwarz, 1982; Hampton et al., 1996; Locat and Lee, 2000; Kvalstad et al., 2005). The state-of-the-art paper by Kvalstad et al. (2005) has proposed a retrogressive slide model, which demonstrates that large-scale submarine slide processes are possible even at a low slope gradient.

A number of laboratory experimental works have been carried out to investigate the mechanisms of long runout submarine landslides and submarine debris flows (Mohrig, et al., 1998; Mohrig, et al., 1999; Mohrig and Marr, 2003; Ilstad et al., 2004a; Ilstad et al., 2004b; Ilstad et al., 2004c; Ilstad, 2005). Interestingly, all the above findings suggest that hydroplaning is the main reason for the mobility of long runout submarine landslides at very

gentle slopes. However, it is important to note that all these experimental works were performed in a 1 g test environment. Actual submarine slides are very large while the scaled model in a 1 g test environment is relatively small, hence the stresses in such conditions are also small. It is, therefore, questionable whether the findings in the above studies are representative of actual submarine landslides, as the stress-strain behaviour of soils is stress-level dependent. Therefore, the behaviour of a small-scale model may not represent the behaviour of its prototype if the stress-strain behaviour is not properly modelled.

With centrifuge modelling, soil stresses related to self-weight are able to be correctly reproduced and observations from small scale-models can be related to the full-scale prototype situation using appropriate scaling laws. Through the available literature, laboratory experimental works on submarine landslides simulation using centrifuge modelling are rather limited. Coulter and Phillips (2003) and Coulter (2005) carried out experimental works using centrifuge modelling, specifically focused on seismic initiation of submarine landslides. Zhou et al. (2002) investigated the critical gradient for slopes under water at various g-levels. More recently, Boylan et al. (2010) developed a centrifuge model capable of modelling submarine slides using a drum centrifuge. They focused on the initiation of submarine slides, in which they have developed a slide triggering device for use in the drum centrifuge.

Centrifuge modelling on the mobility of long runout submarine landslide flows, which is considered as one of the key areas with great importance for subsea development projects, is yet to be conducted. Clearly, there is a pushing need to conduct research work in this area. It is also important to note that there are no centrifuge scaling laws for submarine landslide flows available prior to this study. Thus, this study aims to explore the centrifuge scaling laws for submarine landslide flows in order to fill in the gap of knowledge in this particular field.

1.3 Objectives and Purpose of Research

The key to understanding the phenomena of submarine landslide flows is obviously to model the problem and be able to correctly relate to the actual situation. There is no doubt that the knowledge and further understanding of submarine landslide flows is vital, that it will enable further innovative and economical engineering works on both nearshore and offshore developments.

Simulations of submarine landslide flows with a very gentle slope using the mini-drum centrifuge are conducted in this research. A series of tests are conducted in different gravity fields in order to understand the scaling laws involved in the simulation of submarine landslide flows in centrifuge modelling. The slope is instrumented with miniature sensors in order to measure pore pressures and soil stresses at different locations beneath the landslide flow. A series of digital cameras are used to capture the landslide flow in flight.

In addition to centrifuge modelling, numerical studies are also carried out to compare the results obtained through centrifuge modelling. Hence, parametric studies through numerical studies are also performed to investigate the validity of the developed centrifuge scaling laws for given initial conditions applied by the centrifuge tests conducted in this study.

The specific objectives of the research are as follows:

- To investigate and deduce the centrifuge scaling laws for submarine landslide flows.
- To develop a centrifuge model package capable of modelling submarine landslide flows and to examine the validity of the deduced centrifuge scaling laws.
- To compare the results of centrifuge tests with numerical simulations.
- To further explore any errors associated with the deduced centrifuge scaling laws with numerical simulations.

1.4 Significance of Study

During the 1990s petroleum exploration and field development activities expanded to continental deepwater slopes and into water depths greater than 1000 m. Since then, offshore geohazards have been crucial to the developments of the oil and gas industry, in which submarine landslides have been the central scientific topic in offshore geohazards (NGI, 2005 and Vanneste et al., 2011).

The consequences of submarine landslides are immense as they do not only affect offshore facilities and generate tsunamis. Retrogressive slides as a result of submarine landslides, may progress back onshore and hence present potential hazards to mankind and infrastructure, both offshore and near coastal. These consequences will result in a severe loss of lives and damage to properties.

Although a number of pieces of literature on submarine landslides exist, the knowledge in this particular field is still indeed lacking. Therefore, the knowledge and further understanding of submarine landslide flows through simulations using centrifuge modelling is essential in order to understand the phenomena, and thus mitigate these occurrences which enables further innovative and economical engineering works for both near coastal and offshore developments.

1.5 Report Structure

Chapter 2 presents the phenomena of submarine landslides, which include the characteristics and the significant consequences of submarine landslides. This chapter also summarises documented submarine landslides from the available literature. The mechanics of submarine landslide flows with the governing equations and analytical solutions are discussed. In addition,

this chapter presents experimental works (at both 1 g and centrifuge scales) that have been carried out by researchers around the world.

Chapter 3 contains the background knowledge of centrifuge testing and briefly presents the mini-drum centrifuge at the Schofield Centre of the Engineering Department, University of Cambridge. This chapter also proposes and discusses the centrifuge scaling laws for submarine landslide flows through analytical solutions.

Chapter 4 presents the design of the centrifuge model package for modelling of submarine landslide flows and the experimental procedures, as well as some of the initial challenges encountered at the early stages of the experiments. This chapter also presents the results and interpretations of the experiments, which include experiments at different g levels with various scaled flow rates as well as experiments in dry conditions (not submerged in water). This facilitates an understanding of the influence of surrounding fluid towards the development of submarine landslide flows.

Chapter 5 presents the results and interpretations of the numerical simulations, which include parametric studies using the Depth Average Material Point Method (DAMPM). The sensitivity of the DAMPM model is also discussed.

Chapter 6 discusses the comparisons of the developed centrifuge scaling laws and the results from the centrifuge experiments. This chapter also compares the numerical simulations with the centrifuge experiments in order to investigate the two methods more thoroughly.

Chapter 7 gives the research summaries and conclusions, as well as the recommendations for future research.

CHAPTER II

2.0 Literature Review – Submarine Landslides

2.1 Introduction

The term "submarine landslide" essentially refers to landslides under water, which is known for their extensive mass movements. This chapter introduces some of the unique features and characteristics of submarine landslides, as well as a brief history of their documentation and recognition. Further in this chapter, the causes of failure, the mechanics (governing equations & analytical solutions) of submarine landslides, as well as the importance and significance of submarine landslides, are discussed. Experimental works by other researchers, both in 1 g and centrifuge modelling, are also included in this chapter, which gives the general picture of the major research efforts into submarine landslides.

2.2 Submarine Landslides

Submarine landslides are considered to be potential offshore geohazards. Figure 2.1 shows the typical offshore geohazards in which submarine landslides are considered as the most serious offshore threats on both local and regional scales; the figure is modified after the Norwegian Geotechnical Institute (NGI), 2005.

Submarine landslides have been the central scientific topic in offshore geohazards in recent years. This focus has increased significantly over the last decade, as more offshore and nearshore structures will be constructed in the future. It is therefore essential to consider the risks associated with submarine landslides.

It is important to note that submarine landslides generally consist of two parts: sliding and debris flow. The key characteristics of submarine landslides, which are distinct from subaerial landslides, are their long runout distances and volumes, which fail at a very gentle slope inclination.

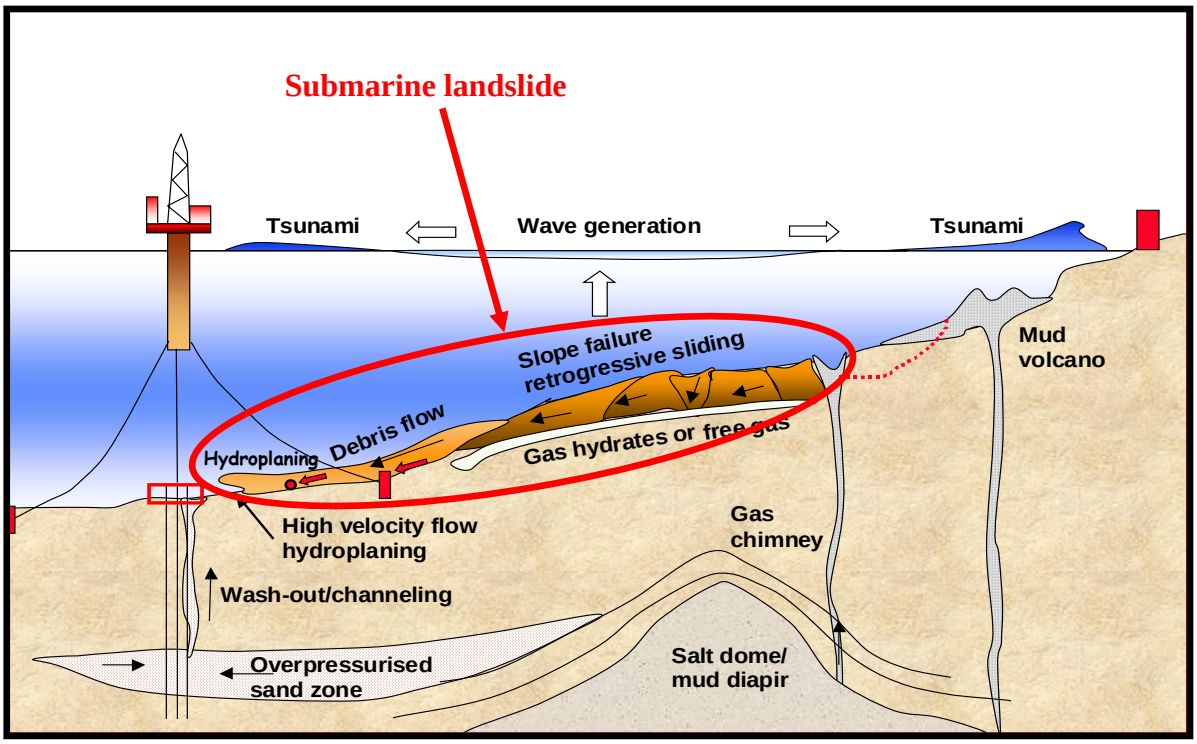

Figure 2.1: Offshore geohazards (modified after NGI, 2005)

2.3 Classification and Characteristics

Classification of submarine landslides is particularly complex as the landslide movements are not directly observed. Many authors have commented and proposed different types of submarine landslides and their characteristics. For example, Schwarz (1982) and Prior (1984) suggested a classification scheme in which the concept of slides to flows is a continuum process. Locat and Lee (2000) classified slides and flows as different types of submarine landslides. Mulder and Cochonat (1996) used the term “slides” and “slump”; in addition, they also include "creep" and "cyclic mobility" in their classification of offshore mass movements. In marine geological literature, authors overuse the term “slump”, which is applied to extensively different

types of offshore mass movement. Above all, many classifications create confusion and misapplication. Figure 2.2 shows an example of the proposed scheme of various types of submarine landslides reproduced after Prior (1984), indicating a wide range of submarine landslides.

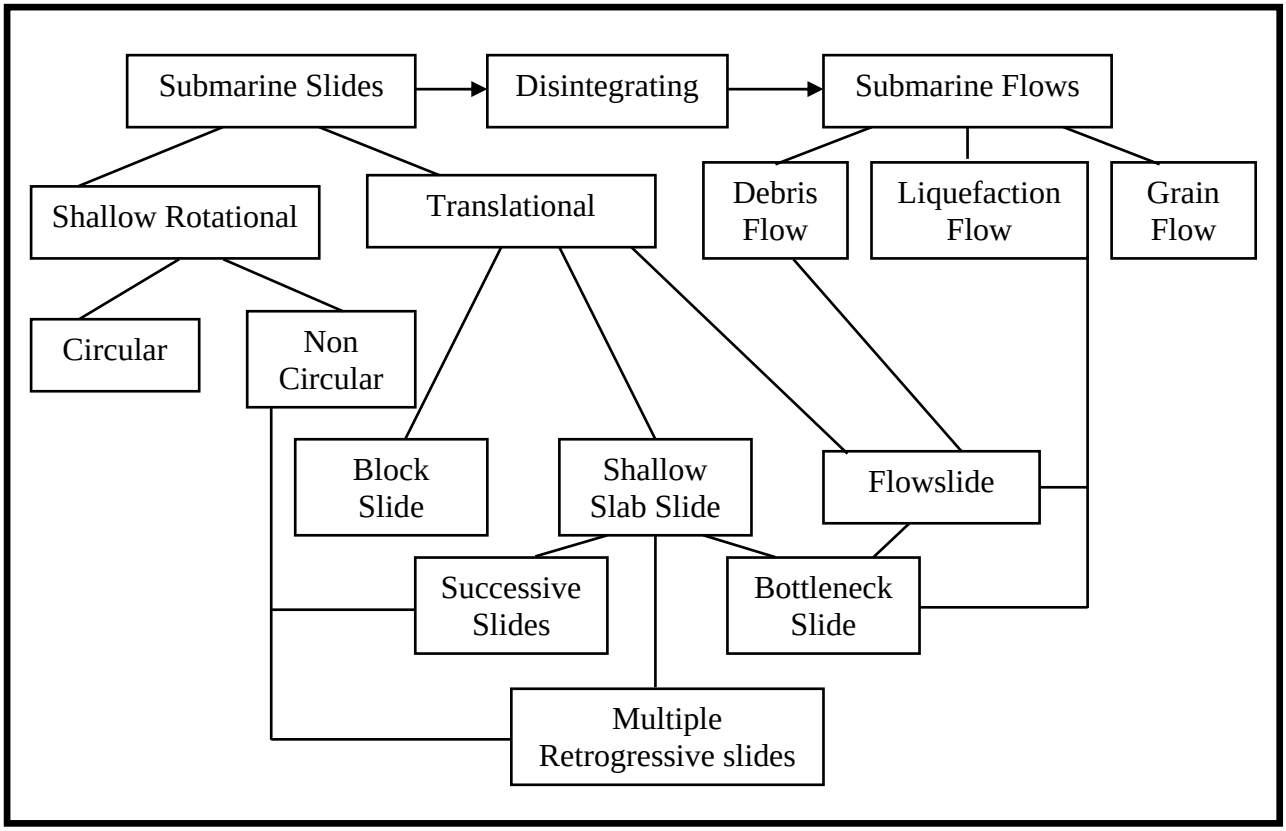

Figure 2.2: Various types of submarine landslides – a continuum of slides and flows (reproduced after Prior, 1984)

The unique features of submarine landslides, which are distinct from normal subaerial landslides, can be summarised as follows:

- Enormous size involving large volumes of mass movements
- Long runout distance
- Failure can occur on very low slope inclination

Appendix 1 summarises the characteristics of submarine landslides from the available literature. It is found that the slope inclination of a submarine landslide may be as low as 1° or less while the runout distance may be more than hundreds of kilometres. Hence, the volume of failure may be

more than a trillion cubic metres. The characteristics tabulated in Appendix 1 include maximum runout distance (L_{max}), maximum height (H_{max}), volume, slope inclination and the ratio of (L_{max}/H_{max}).

Figure 2.3 shows the relationship of slope inclination and the maximum runout length. The data in this graph is obtained from Appendix 1. It can be seen that the slope inclinations for submarine landslides are generally small (< 10°). Figures 2.4 and 2.5 show the relationship of the submarine landslide volume with the maximum runout length and the ratio of (L_{max}/H_{max}) respectively. It can be seen that there are no specific trends for the relationships of runout, and the ratios of L_{max}/H_{max} with the submarine landslides volume as the data are quite scattered.

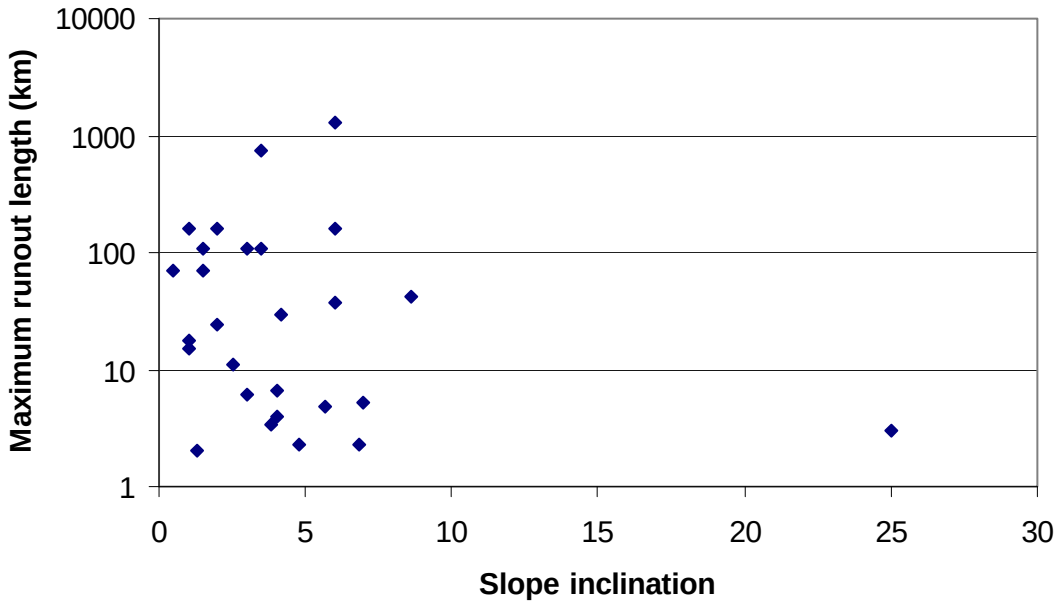

Figure 2.3: Relationship of slope inclination and the maximum runout length

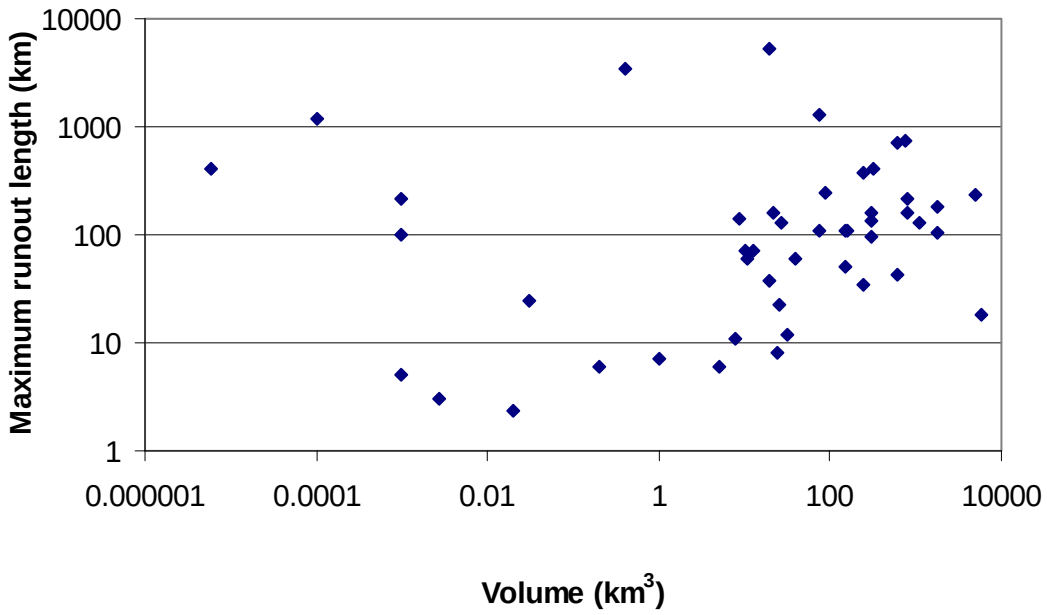

Figure 2.4: Relationship of volume and the maximum runout length

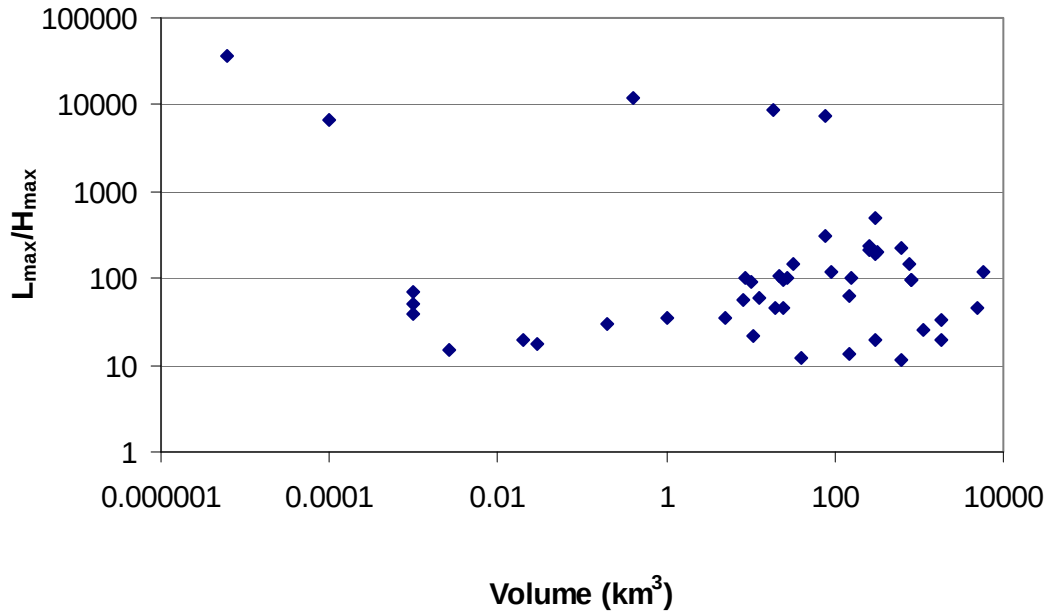

Figure 2.5: Relationship of volume and the ratio of (L_{max}/H_{max})

2.4 Documentation and Recognition

Most recorded submarine landslides occurred in prehistoric times. The phrase "submarine landslide" has not been commonly used until recently, after improved techniques in seismic profiling that have allowed observation of certain characteristics such as deposits, shapes and geometries. Usually, a potential submarine landslide problem is initially revealed by the geomorphology and topography of the sea floor, suggesting that the sea floor or slope has been modified in a catastrophic manner (Locat and Lee, 2000).

One of the earliest pieces of literature on submarine landslides is documented by Terzaghi (1956). Terzaghi recognised submarine landslides as spontaneous mass movements of short duration involving large quantities of material on both steep and gentle slopes. Moore (1961), who studied the shear strength of the sediment and deposits of submarine landslides, found that the rate of sedimentation required to produce unstable slope occurs only in areas of relatively rapid accumulation. Andresen and Bjerrum (1967) compiled some case studies on submarine slope failures such as the flow slide in Trondheim Harbour, Norway in 1888 (Figure 2.6) and Helsinski Harbour, Finland in 1936 (Figure 2.7). They found that it is useful to distinguish between flow slides and liquefaction slides, where the former shows typical retrogressive development that fails in shear, while the latter propagates with great speed in all direction. Morgenstern (1967) looked into submarine slope failures which initiate turbidity currents and found that the mixing of soil with overlaying water is an important factor in the development of a turbidity current, and controls its density. Henkel (1970) investigated the role of waves in causing submarine landslides, and found that there is limited evidence to suggest that the pressure differences on the sea floor associated with waves may be important in the development of submarine landslides. Lewis (1971) studied the failure of submarine slopes at inclinations of 1° – 4°. It was found that normal submarine slopes can occur at a slope angle of 1°, while the data that Lewis gathered supported the theory that soft sediments could be deformed by gravitational forces on gentle slopes on the open continental shelf

or continental slope. Coleman and Prior (1978) reported submarine landslides in the Mississippi River Delta with the aid of seismic profiling and surveys, which concluded that the submarine landslide is a complex problem that may occur as a result of a combination of rapid sedimentation that generates high pore water pressure, wave-induced stresses and methane gas pressures .

In 1982 Edgers and Karlsrud investigated soil flows generated by submarine slides through a collection of case studies, including field data such as runout distance and volume of submarine landslides. The data in Figures 2.3 to 2.5 are mostly from this study. They found that the maximum possible extent of a submarine landslide may be estimated from the relative runout distances observed in previous slides, but it requires an estimate of the volume of the potential slide masses. Furthermore, the thickness of the slide masses at a site can only be roughly estimated from the volume of available slide materials and some reasonable estimate of their distribution along the slide runout. Prior (1984) revealed the methods of submarine landslides identification, such as echo sounding, side-scan sonar and subbottom seismic profiles. It can be seen that active studies on submarine landslides began with the improvements of seismic profiling and advancements of bathymetric surveys.

Developments within the oil and gas industry in the 1990s have given more momentum for research in submarine landslides. Hampton et al. (1996) and Locat and Lee (2000) have given state-of-the-art reviews on submarine landslides. Both describe an in-depth assessment on submarine landslides and their challenges. These will be discussed in the following sections.

In connection with petroleum exploration, one of the most famous submarine landslides, is the Storegga slide (Figure 2.8), in which the failure occurred about 8,200 years ago. The enormous slide mass involved 3,000 km^3 of material volume and affected an area of 90,000 km^2. The average slope inclination was in the order of 0.6-0.7^o (Kvalstad et al., 2005).

Figure 2.6: Failure at Trondheim Harbour, Norway in 1888 (after Andresen and Bjerrum, 1967)

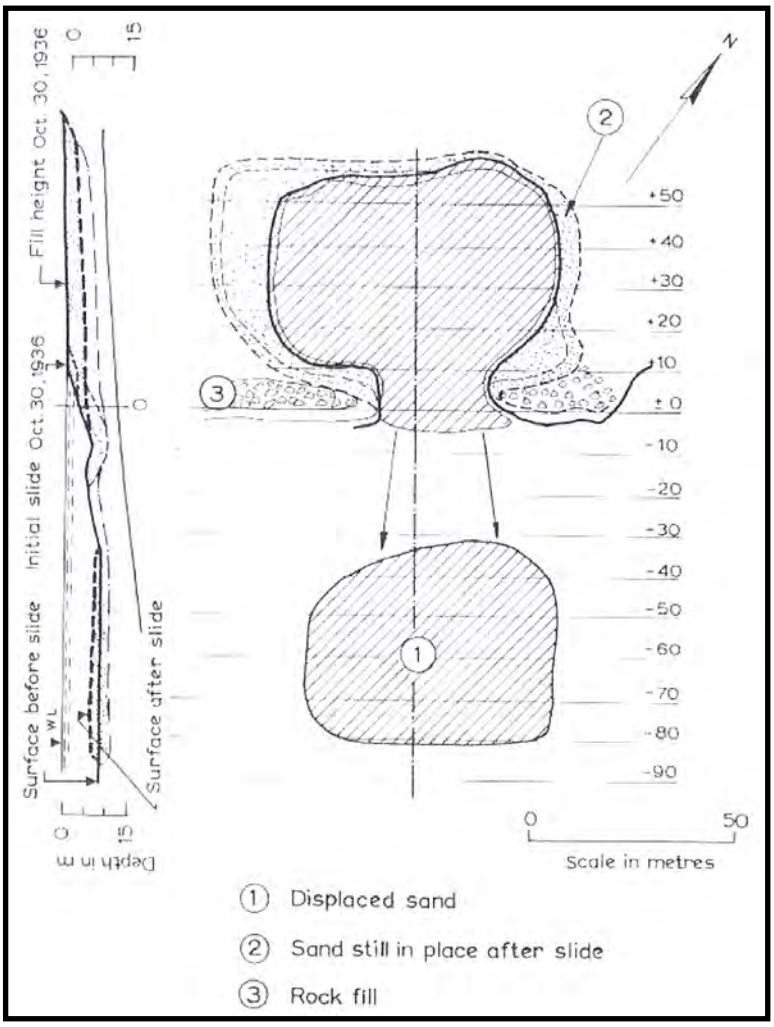

Figure 2.7: Failure at Helsinki Harbour, Finland in 1936 (after Andresen and Bjerrum, 1967)

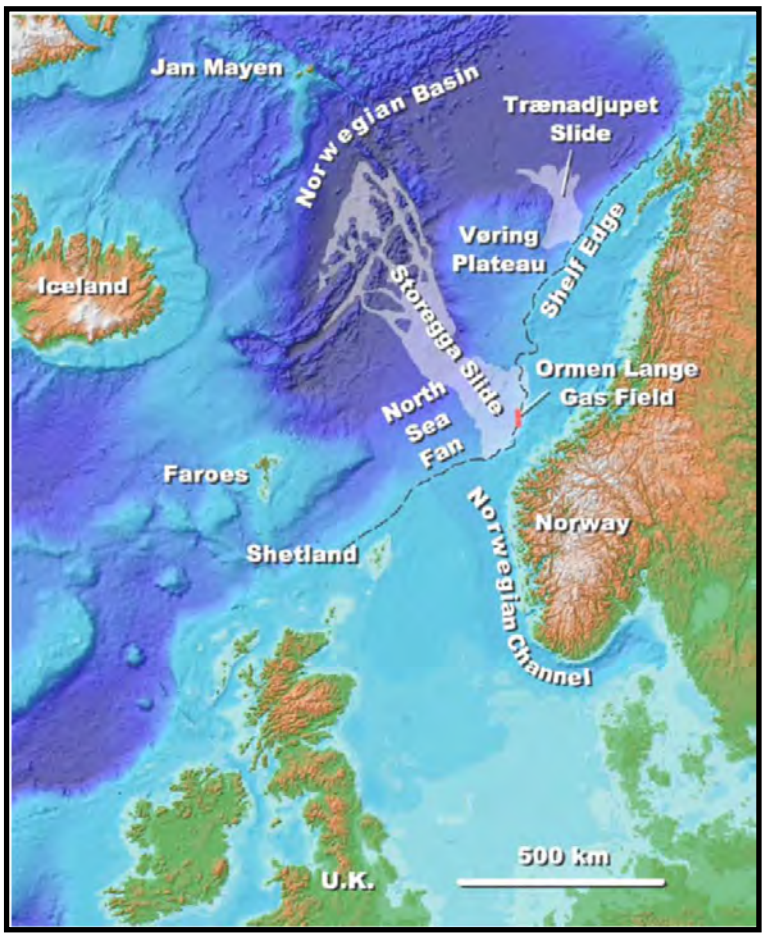

Figure 2.8: Storegga slide, Norway 8200 years ago (after Bryn et al., 2005)

Though most of the submarine landslides occurred in prehistoric times, there are some which occurred more recently. These include the failure at Helsinki Harbour in 1936 and the 1994 submarine landslide at Skagway, Alaska. A massive submarine landslide at Skagway, Alaska on 3 November 1994 destroyed 275 m of dock during a reconstruction project. Bathymetric surveys before and after the failure showed that the ground had been scoured to depths of up to 21 m immediately downslope from the dock and the volume of the failure was estimated at around 760,000 m^3 (Cornforth, 2004).

It is important to note that there is very limited information regarding the flow velocity of the documented submarine landslides as they occurred under water. Table 2.1 summaries the available information on the velocities of submarine landslides. The information in Table 2.1 includes data from field and laboratory experiments. Some of the field data are collected by various

authors through literature. It can be seen that the flow distances from the field data are several magnitudes larger than the flow distances produced in the laboratory experiments.

Table 2.1: Summary of flow velocity, distance and thickness of various submarine landslides

Reference	Flow Velocity (m/s)	Flow Distance (m)	Flow Thickness (m)	Notes
De Blasio et al. (2004)	20 - 50	10000 - 200000	5 - 50	Finneidfjord, Norway field data.
De Blasio et al. (2005)	60	400000++	50	Numerical simulation of Storegga slide based on the generated tsunami wave.
Edgers and Karlsrud (1982)	0.8 – 7.7	1200 – 750000++	-	Data collected from various literatures. Flow velocity estimated based on time sequence of submarine cable breaks.
Marr et al. (2001)	0.65	7.2	0.01 – 0.07	Data from 1 g test
Norem et al. (1990)	23.5	2000	15 - 20	Calculated velocity
Ilstad (2005)	0.74 - 1.04	9	0.03 0.06	Data from 1 g test
Schwarz (1982)	4 - 28	-	-	Data collected from various literatures.
Terzaghi (1956)	5.8 – 28	1000	12	Flow velocity estimated based on time sequence of submarine cable breaks at Folla fjord.

Appendix 1 tabulates some submarine landslides which are summarised from literature available to date. It should be noted that not all the information on each submarine landslide is presented, as it is only based on the best available information from the literature. A more comprehensive list of submarine landslides can be found in Schwarz (1982), which tabulated the occurrences of submarine landslides through the available information at the time of the publication.

The consequences of submarine landslides are no doubt immense. Submarine landslides impose a serious threat to offshore industries, in which they have a direct impact on offshore structures such as oil and gas rigs (platforms). A submarine landslide may not only affect any structures immediately above it; it may also affect adjacent or nearby structures, since submarine landslides are massive and have long runout distances. The results of failure towards oil and gas rigs are unimaginable, an occurrence which would cost lives and cause damage to properties. Subsea pipelines and utilities are also considered to be directly affected by submarine landslides. The effects from submarine landslides are not only limited to offshore structures and subsea pipelines; near shore or coastal structures and facilities are also affected.

Submarine landslides may also generate tsunamis by their own displacements. A study carried out by Silva (2003) stated that the displacements due to submarine landslides may induce tsunami. Synolakis et al. (2002) showed evidence on the generation of the 1998 Papua New Guinea tsunami by submarine landslides which killed over 2100 people, based on fundamental geological and geotechnical information. It is, therefore, recognised that tsunamis could be generated by large submarine landslides; hence, they pose significant threats to mankind.

Since submarine landslides are increasingly recognised and documented, research on the causes and the mechanics of failure are no doubt actively ongoing at present.

2.5 Causes of Failure

A great deal of notable literature on submarine landslides has specified some of the most probable causes of failure. Although many proposed the possibility of different causes of failure, all are in close agreement regarding the most common and probable causes of failure, such as rapid sedimentation, retrogressive failure, earthquake and tectonic activity, gas hydrate dissociation and wave loading. These causes of failure are discussed in this sub-section.

2.5.1 Rapid sedimentation

High excess pore water pressures are commonly associated with submarine landslides. Numerous authors have referred to rapid sedimentation as being one of the most probable causes for submarine landslides. These include, but are not limited to, Moore (1961), Schwarz (1982), Prior (1984), Hampton et al. (1996), Locat and Lee (2000), and Kvalstad et al. (2005).

Rapid sedimentation may cause the development of excess pore water pressures when the length of the drainage path increases faster than the time required for consolidation within the buried sediment and does not allow the normal increase in shear strength with the depth of burial. Terzaghi (1956) mentioned that, for fine-grained soil, rapidly deposited sediment may accumulate so fast that the process of consolidation through dissipation of excess pore water pressures may not keep pace with it. Sediments rich in coarse silt and very fine sand frequently have low shear strengths and often accumulate with loose, open metastable packing. Deposits of this type are called underconsolidated soil and are normally found in the marine environment (Moore, 1961).

Schwarz (1982) made a rigorous compilation of submarine landslides and found that 29.3% of submarine landslides are due to rapid sedimentation, which is the highest cause of other submarine landslides. He sorted rapid sedimentation into four sub categories:

- Long-term high sedimentation rate which favours sliding. As a releasing mechanism, this process is generally combined with an additional triggering effect.
- Short-term heavy sediment supply can be considered as self-sufficient to generate slope failures at suitable places, such as off-river mouths.
- Overloading of insufficiently consolidated slope by periodical accumulation off-river mouths and progradation of marine foreset beds.
- Oversteepening of a depositional slope, which is possibly increased by tectonic movements.

According to Schwarz (1982), the sedimentation rates found in failure areas generally range from 0.1mm to 1mm/year on continental slopes. Moore (1961), based on various literature, found a tremendous variation in the rate of sedimentation, which could be as low as 0.5mm in 1000 years and as high as 300mm a year.

2.5.2 Retrogressive failure

As cited in Hampton et al. (1996), retrogressive failure is defined as sliding that occurs serially as numerous adjacent failures that progress upslope. Other authors who quote that retrogressive failure is one of the causes of submarine landslides include Andresen and Bjerrum (1967), Coleman and Prior (1978), Hampton et al. (1996), and Kvalstad et al. (2005).

It could be asked how a retrogressive failure is discovered, since submarine landslides occur under water. The retrogressive failure can be deduced from slide scar and debris formation through bathymetry and seismic profiles. Figure 2.9 shows an example of deducing retrogressive failure of the Storegga slide through bathymetry and seismic profiles; the figure is adopted

from Kvalstad et al. (2005). The black lines are the interpreted morphology of the slide.

The retrogressive failure has significant impact on structures near shore, as a retrogressive failure may fail and progress upslope. This phenomenon is most commonly referred to the Trondheim Harbour slide in 1888 (Andresen and Bjerrum, 1967). The slide retrogressed across the shoreline, sinking sections of coastal land, harbour facilities and railways. It is therefore important to understand how retrogressive failures take place in order to mitigate failures near shore.

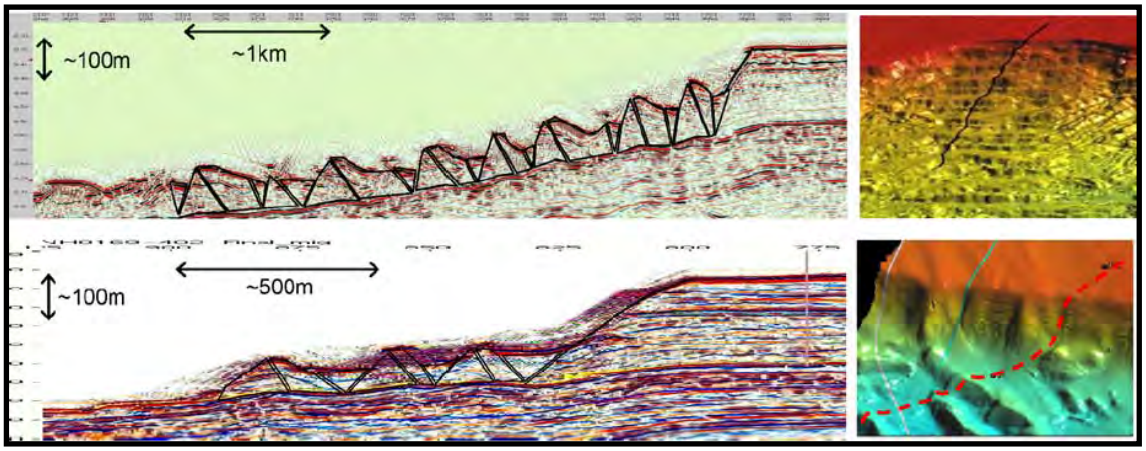

Figure 2.9: Interpreted morphology of slide through bathymetry and seismic profiles (after Kvalstad et al., 2005)

Kvalstad et al. (2005) proposed a model for evaluation of retrogressive failure. This can be described as follows:

- An initial slide is developed in the lower and possibly steeper part of a slope, and the mobility of the slide material is sufficient to more or less completely unload the earth pressure against the initially developed headwall (Figure. 2.10a).
- The unloading of the headwall causes undrained lateral expansion of the soil, while strain concentrations develop in the toe area of the headwall.

- The large shear strain in the strain concentration zones causes strain softening, primarily in the marine clay base layer, and progressive failure develops along this layer.
- The safety factor decreases below unity and the failing soil mass (Figure. 2.10b) starts to accelerate downslope. A triangular front wedge is formed, being pushed along the slide base by a gradually distorted rhomb and triangular wedge creating a graben behind the front wedge, thus forming a new headwall (Figure. 2.10c).
- The released potential energy is partly consumed as friction along the base and circumference of the slide mass, and partly in remoulding of the slide material along the slide base and internally in the distorted slide mass.
- Excess potential energy is transformed to kinetic energy accelerating the slide mass further downslope.
- The reduction in strength gives sufficient mobility to unload the next headwall. The process then repeats itself (Figure. 2.10d) until soil strength and layering or geometry change sufficiently to reduce mobility and decelerate the sliding process.
- If the mobility is too low, the slide mass will block further retrogression along the base layer and the process will, if possible, continue along shallower marine clay layers, creating steps in the slide base (Figure. 2.10e).

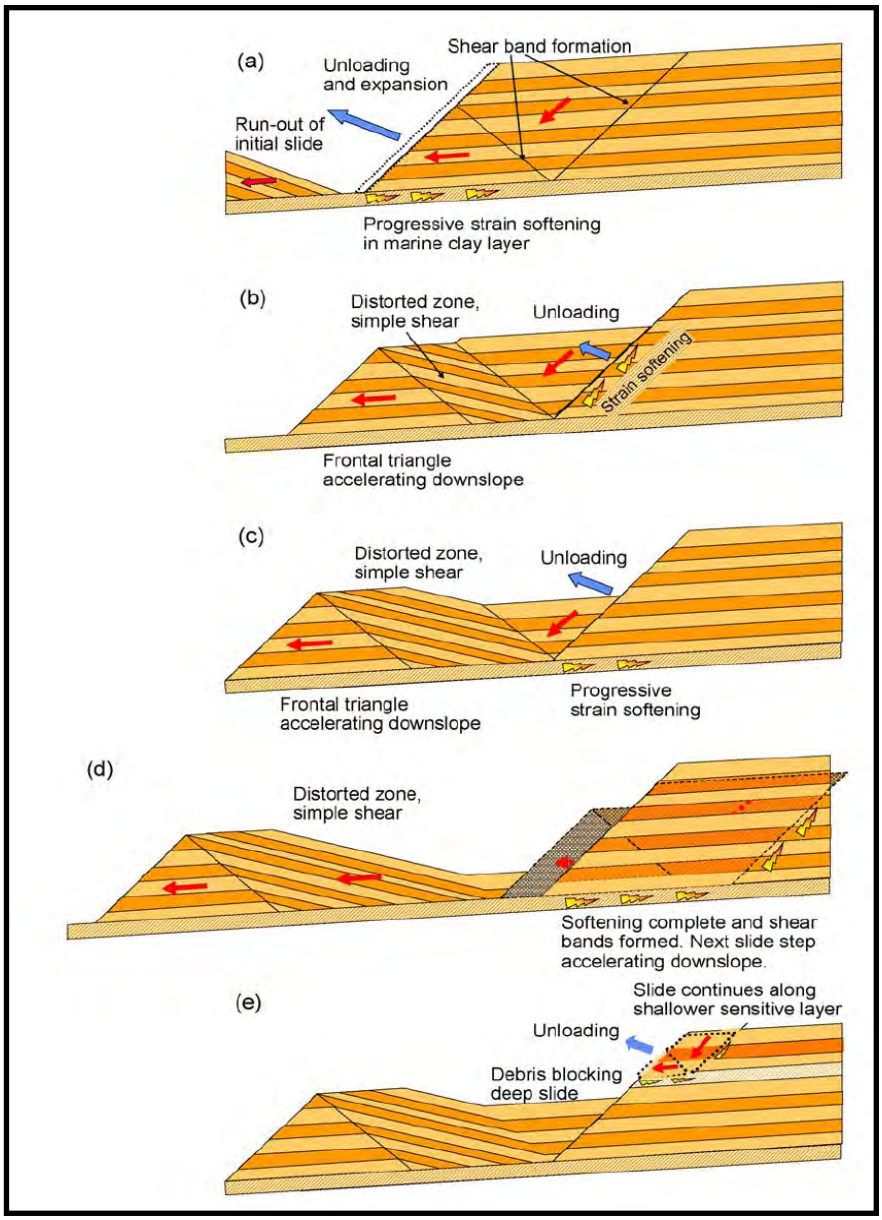

Figure 2.10: Retrogressive slide model (after Kvalstad et al., 2005)

2.5.3 Earthquake and tectonic activity

Earthquakes and tectonic activities are generally thought to be one of the most effective triggering mechanisms for submarine landslides. Many researchers recognise that earthquake and tectonic activities pose a significant threat to submarine slopes, such as Prior (1984), Hampton et al. (1996), Locat and Lee (2000), Biscontin et al. (2004), Kvalstad et al. (2005), and Coulter (2005).

Coulter (2005) states that the main effect of earthquakes is the creation of horizontal waves which travel through the bedrock and soil deposits. In the case of a submarine slope, these waves will cause significant shear stress, both dynamic and cyclic, and may also cause the loss of soil resistance. Cyclic loading of clay continues with the accumulation of plastic strains and shear-induced excess pore water pressure with increasing number of cycles (Biscontin et al., 2004). As mentioned in Kvalstad et al. (2005), earthquake-induced shear strains generating excess pore pressure leads to the reduction of effective stress and hence initiates failure.

Besides earthquakes-induced shear strains, tectonic activities will also trigger submarine landslides. As mentioned in Prior (1984), in areas of active crustal tectonism, bottom slope angles can be increased by upwarping and faulting. The increase of slope angles causes instability to submarine slopes and hence initiates failure.

The most notable submarine landslide associated with an earthquake is the Grand Banks slide in Canada. Mulder and Cochonat (1996) mention that the Grand Banks slide can be attributed to cyclic liquefaction that arose from earthquake exposure. There are other notable earthquake-induced landslides including the Humboldt slide off of Northern California, USA, in the Saguenay Fjord in Quebec, Canada, the slide off of Vancouver Island, British Columbia, Canada in 1946, and the slide cause by the 1964 Alaska Earthquake (Coulter, 2005).

2.5.4 Gas hydrate

Gas hydrate dissociation contributing to submarine landslides is currently gaining more and more attention. The potential of gas hydrates being associated with submarine landslides is mentioned in Hampton et al. (1996), Locat and Lee (2000), and Paull et al. (2000).

Gas hydrates are ice-like substances consisting of natural gas and water, which are stable under certain pressure and temperature conditions that are common in the seafloor. When temperatures increase or pressures decrease, the stability field changes and some of the hydrates may disassociate and release bubble-phase natural gas (Locat and Lee, 2000). A drop in sea level also reduces the pressure existing on the seafloor, causing gas hydrates to disassociate.

According to Paull et al. (2000), the formation and dissociation of gas hydrates in the sea floor appears to have a direct influence upon the mechanical properties of marine sediments. When gas hydrates become unstable, they disassociate into water plus gas. The dissociation of gas hydrates leads to excess pore pressure and reduces slope stability.

The connection between submarine slope failures and gas hydrates can be linked to the coincidence of slide scars and known gas hydrate distribution. According to Paull et al. (2000), bottom simulating reflectors (BSR) are the most commonly available remote detection indicators for the presence of gas hydrates that occur in sediments around the slide scar. One of the huge submarine landslides known to be associated with gas hydrates is the Cape Fear slide of the United States Atlantic margin. Paull et al. (2000) pointed out that the level of BSR rises at the edges of the slide scar but disappears near its centre, where gas hydrates apparently escaped. This suggests that the base of gas hydrate stability is associated with a zone of weakness and failure within the sediments.

2.5.5 Wave loading

A number of authors have recognised that wave loading could be an initiation of submarine landslides. These include Henkel (1970), Schwarz (1982), Prior (1984), Hampton et al. (1996), Locat and Lee (2000) and Coulter (2005). Wave action causes a bottom pressure that is a function of the wave height, wave length and water depth. This wave induced bottom pressure acts

as a driving force and exerts stress in the bottom sediments, which can be felt horizontally, vertically and, most importantly in the shear direction (Coulter, 2005).

Henkel (1970) cited that one of the effects of ocean waves is to produce pressure changes within the water, in which the differential loading of the water will impose stresses on underlying soil. If the stresses exceed the strength of the soil, significant displacements may occur. It is also considered that there is an energy transfer between the wave and the moving soil, and the work done against the shearing strength of the soil provides damping to the oscillatory motion imposed by the wave.

Although many recognise that wave loading can be the cause of submarine landslides, limited evidence has been presented in the literature that points to the fact that a particular submarine landslide is due to wave loading. Wave loading is a complex dynamics problem where satisfactory evidence and investigation depends on the acquisition of data on the actual bottom pressures found on the seabed. More information such as shear strength distribution with depth and the solution of the energy transfer problem between waves and the submarine sediments are needed to assess the influence of wave loading towards submarine landslides.

2.5.6 Other possible causes

As seen from a number of pieces of literature, there are several other possible causes of submarine landslides. Tidal changes, as quoted in Prior (1984), Hampton et al. (1996), and Coulter (2005), are a possible causes for submarine landslides. The concept is similar to rapid drawdown for the case of instability of dams or river banks.

Schwarz (1982) cited an increase in sensitivity of soils due to the leaching of marine sediments by influx of fresh water into marine sediments, resulting in the weakening of sediment strength.

Erosion causes an undercutting of slope deposits as well as oversteepening of slopes, which may cause submarine landslides (Schwarz, 1982). This has also been recognised in Hampton et al. (1996) and Locat and Lee (2000).

Chemical decomposition of organic and inorganic sedimentary components, which lead to changes in physical and chemical properties, may reduce shear strength and so contribute to failure (Schwarz, 1982).

Man-made slope failures can be initiated particularly during constructions of harbours and dams. Such an increased use of aqueous environments will cause submarine landslides if proper protection works are not implemented. Such failures in the past include the Helsinki harbour failure in 1936, where failure occurred after the additional load from filling the basin with sand (Andresen and Bjerrum, 1967), and failure at Skagway, Alaska in 1994 due to the additional fill that had been placed upslope for the dock renovation project at Skagway (Cornforth and Lowell, 1996).

2.6 Mechanics of Submarine Landslides

It is essential to understand the basic mechanics of submarine landslides, as such information is particularly important for assessing offshore geohazards in areas considered for offshore construction, as well as for in-depth research into the governing factors of submarine landslides. In addition, understanding the physics and mechanics of submarine landslides enables laboratory experiments to be quantified.

2.6.1 Limit equilibrium

Generally, initiation of a landslide is widely accepted when the driving shear stress exceeds the shear strength of the slope-forming material. This phenomenon is also true for submarine landslides. Figure 2.11a shows the

forces acting on a slice in a submarine infinite slope adopted from Locat and Lee (2000). Parameters can be defined as follows:

S	=	shear resistance of sediment
N	=	normal force
W	=	vertical component of body force of slice
z	=	depth of sediment
h	=	height of slice
θ	=	slope angle

The failure criterion can be described with the Mohr-Coulomb failure criterion:

$$\tau = (\sigma - u)\tan\phi' + c' \qquad (2.1)$$

where,

τ	=	shear strength
σ	=	normal stress acting to the failure surface
u	=	pore water pressure
ϕ'	=	friction angle
c'	=	effective cohesion

The term (σ-u) is the effective normal stress, generally summarised as σ'. It should be noted that the Mohr-Coulomb failure criterion indicates a linear relationship between shear strength, τ and effective stress, σ'. This means that, when effective stress is reduced by the increase of pore water pressure, shear strength will be reduced.

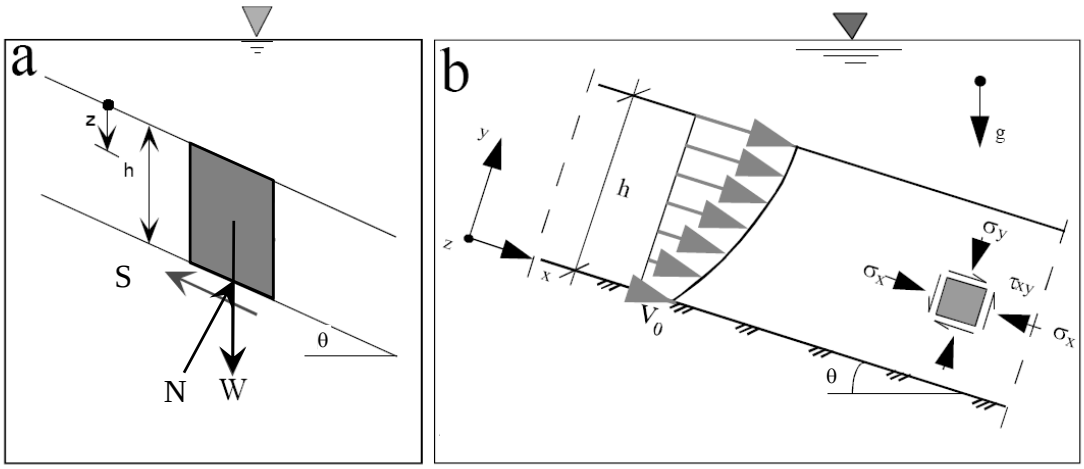

Figure 2.11: The failure (a) and post-failure (b) mechanics along an infinite slope (after Locat and Lee, 2000)

Locat and Lee (2000) showed that, following an initial failure (Figure 2.11a), some submarine landslides mobilise into flows, whereas others remain as limited deformation slides and slumps. Figure 2.11b shows the general model of submarine landslide failure. Although the diagram shown in the figure is limited in its ability to describe the full flow, nevertheless it may be able to predict the final shape of the failure deposits. More detail regarding the flow behaviour is given in the later part of this chapter. Furthermore, they mentioned that, although the mechanisms for mobilisation into flows are not well understood, the initial density state of the sediment is the likely controlling factor. Figure 2.12a shows the mechanistic condition leading to failure of soils. The annotation A is the dilative failure, B is the contractive failure, and C is the generation of pore pressure due to cyclic loading, while D is the cyclic loading failure. As cited, if the sediment is less dense than an appropriate steady state condition (contractive behaviour), the sediment appears to be more likely to flow than one that is denser than the steady state (dilative behaviour) as shown in Figure 2.12b.

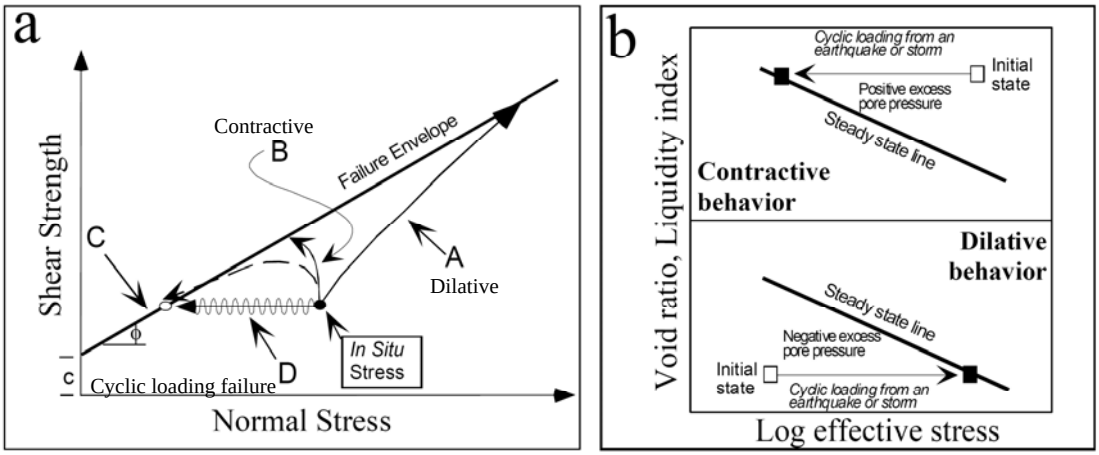

Figure 2.12: The mechanistic illustration of conditions leading to: (a) failure in soils (b) onset of liquefaction (after Locat and Lee, 2000)

It should be noted that the majority of the submarine landslides occurred at a very low slope inclination. For a fully submerged soil at low slope inclination, the soil will not fail if solely quantified by the Mohr-Coulomb failure criterion. From the Mohr-Coulomb failure criterion, the only way for a failure to take place is to have a very high pore water pressure. It can also be interpreted that a failure is affected by other possible boundary conditions.

2.6.2 Possible boundary conditions

As cited in Locat and Lee (2000), the possible boundary conditions during a submarine landslide event are illustrated in Figure 2.13. It can be seen that the flowing material is divided into two components; the dense flow and suspension flow. The dense flow is generally associated with debris flow, while the suspension flow is generated by the drag forces acting on the upper surface of the dense flow.

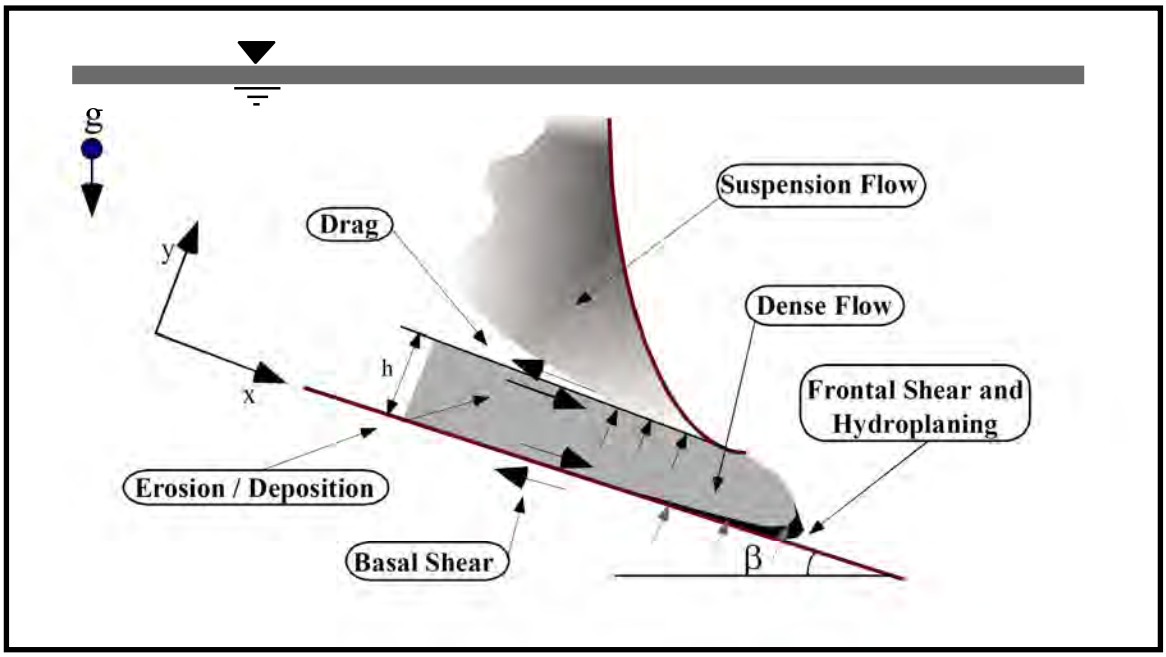

Figure 2.13: Possible boundary conditions for submarine landslides (after Locat and Lee, 2000)

Research, such as Mohrig et al. (1998), De Blasio et al. (2004), and Ilstad (2005), consider hydroplaning as the phenomena that increases the mobility of submarine landslides, which makes the long runout distances are made possible. Hydroplaning reduces the shearing resistance at the base of the flowing mass as shown in Figure 2.13. It is known that this process will tend to lift the frontal portion of the dense flow, thus reducing the shearing resistance at the interface with the underlying immobile layer.

It is assumed that, once a dense flow is generated (i.e. in the event that the velocity of the flowing material is fast enough), it remains under undrained conditions. In such a scenario, considering the high rate of movement, the phenomenon is commonly described by means of fluid mechanics rather than soil mechanics (Locat and Lee, 2000). However, soil may still show geotechnical behaviour.

2.6.3 Flow behaviour

As mentioned previously, dense flow is best described by fluid mechanics. It is therefore important to study the rheology, which is the

deformation and flow of matter under the influence of an applied stress. Locat and Lee (2000) quoted that the flow behaviour can be represented by three types of rheology, namely Bingham, Herschel-Bulkley and bilinear rheologies.

These rheological models treat a moving slide mass as a flowing, fluid-like material; thus, the soil described in a rheological model is typically referred to as fluid. The typical quantities used to define the properties of materials are yield stress (strength), τ_y, and dynamic viscosity, μ. These quantities are defined by measurements of shear stress, τ, and rates of shear strain, $\dot{\gamma}$ or dv/dy, using a viscometer. The yield stress, τ_y, is the shear stress required to cause motion of the fluid. The motion of a fluid stops when the shear stress falls below the yield stress. The dynamic viscosity, μ, is the slope of the shear stress-strain rate curve, which itself depends on the type of sediment and the rate of shear (Hance, 2003).

Figure 2.14 shows the classical types of fluid behaviour. It should be noted that Newtonian and Bingham fluids have a viscosity that remains constant with the shear strain rate. The viscosity of shear thickening fluids increases with rate of shear strain, while Herschel-Bulkley fluids have a viscosity that decreases with increasing rate of shear strain. It is also important to note that Newtonian fluids have no yield strength, τ_y while the other fluids have yield strength.

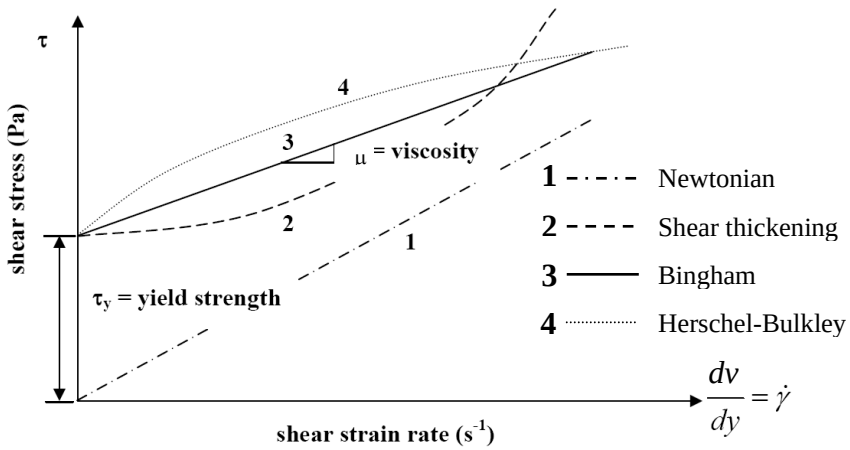

Figure 2.14: Stress-strain rate relationships (Modified after Hance, 2003)

2.6.3.1 Bingham rheology

Bingham rheology, also known as linear visco-plastic fluid, is a material that behaves as a rigid body at low stresses but flows as a viscous fluid at high stress. Figure 2.15 shows the submarine uniform Bingham flow. The Bingham rheology is the most common rheological model applied to submarine flowslides. Several authors have presented models for submarine landslides based on Bingham fluid assumptions, such as Edgers and Karlsrud (1982), Norem et al. (1990), Huang and Garcia (1997), and Huang and Garcia (1999).

As cited in Huang and Garcia (1997), the relationship between shear stress and shear strain rate for a Bingham fluid can be expressed as:

$$\mu \frac{\partial v}{\partial y} = \begin{cases} 0 & if\,|\tau| < \tau_y \\ \tau - \tau_y \operatorname{sgn}\left(\frac{\partial v}{\partial y}\right) & if\,|\tau| \geq \tau_y \end{cases} \qquad (2.2)$$

or

$$\tau = \tau_y + \mu\dot{\gamma} \qquad (2.3)$$

where τ is the shear stress, τ_y is the yield stress and μ is the dynamic viscosity. The sgn ($\partial v/\partial y$) notation is the standard form for obtaining the correct sign in the Bingham rheology.

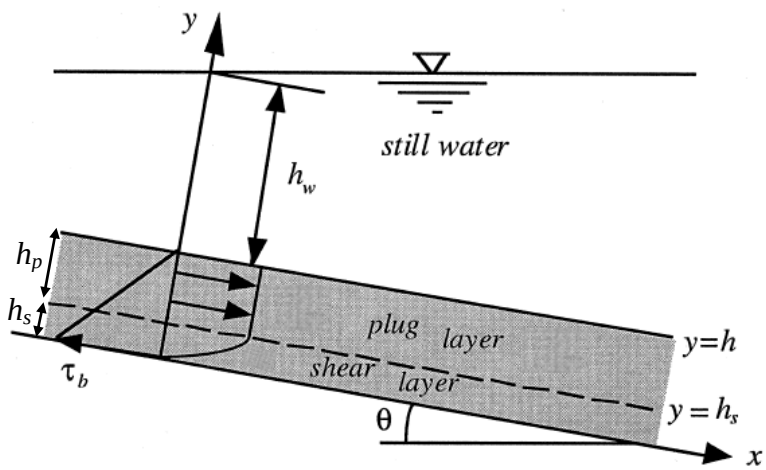

Figure 2.15: Submarine, uniform Bingham flow (after Huang and Garcia, 1999)

As shown in Figure 2.15, it is assumed that the shear stress is linearly increasing with depth, as shown by the following equation:

$$\tau = \rho g\left(h_s + h_p - y\right)\sin\theta \qquad (2.4)$$

where y is the distance above the bed and $h = h_s$ (height of shear layer) + h_p (height of plug layer).

For $0 \leq y \leq h_s$, inserting equation (2.4) into (2.2) and integrating with the no slip boundary condition $v = 0$ at the bed and $v = V_p$ at the yield surface, results in a parabolic distribution of the velocity in the shear flow region given by:

$$v = \frac{\rho g \sin\theta}{2\mu}\left(2h_s y - y^2\right) \qquad (2.5)$$

and the velocity at the plug flow regions is given by:

$$V_p = \frac{\rho g h_s^2 \sin\theta}{2\eta} \qquad (2.6)$$

then, the averaged velocity over the entire flow depth is given by:

$$v = V_p\left(1 - \frac{h_s}{3h}\right) \qquad (2.7)$$

Hence, the bed shear stress is given by:

$$\tau_b = \tau_y \operatorname{sgn}\left(V_p\right) + 2\mu\frac{V_P}{h_s} \qquad (2.8)$$

The basic feature for a submarine uniform Bingham flow is that the velocity has uniform and parabolic distributions in the plug layer and shear

layer (viscous flow) respectively. The parabolic distribution in the shear layer is based on the assumption of the shear stress, which varies linearly from zero to τ_b on the basal surface. The plug layer has a constant downslope velocity and there is no velocity gradient within the plug layer. In the shear layer (viscous flow), however, the downslope velocity decreases from the velocity of the plug layer to zero at the base of the flow.

Although it is assumed that the shear stress varies linearly on the basal surface, it is also known that this may overestimate the true yield stress significantly due to shear thinning at low shear rates (Huang and Garcia, 1998). Shear thinning is a phenomenon where viscosity decreases with shearing rate.

2.6.3.2 Herschel-Bulkley rheology

Herschel-Bulkley rheology is also known as nonlinear visco-plastic fluid, which allows shear thinning. Similar to Bingham rheology, the Herschel-Bulkley model consists of a distinct shear layer and a plug layer. The shear stress at the interface of these two layers is the yield stress. The material can deform only if the applied stress exceeds the yield strength (Imran et al., 2001).

As cited in Huang and Garcia (1998), the relationship between shear stress and shear strain rate for a Herschel-Bulkley fluid in laminar flows can be expressed as:

$$\mu\left|\frac{\partial v}{\partial y}\right|^{n}\operatorname{sgn}\left(\frac{\partial v}{\partial y}\right)=\begin{cases}0 & if\,|\tau|<\tau_y\\ \tau-\tau_y\operatorname{sgn}\left(\frac{\partial v}{\partial y}\right) & if\,|\tau|\geq\tau_y\end{cases} \tag{2.9}$$

or

$$\tau=\tau_y+\eta\dot{\gamma}^{n} \tag{2.10}$$

where n is the flow index and n = 1 corresponds to the Bingham rheology.

Similar to the derivation for Bingham rheology, assuming shear stress varies linearly with depth, for $0 \leq y \leq h_s$, and integrating with the no slip boundary condition $v = 0$ at the bed and $v = V_p$ at the yield surface, this results in a depth averaged velocity:

$$v = V_p\left(1 - \frac{n}{2n+1}\frac{h_s}{h}\right) \qquad (2.11)$$

where V_p is the plug flow velocity, given by:

$$V_p = \frac{n}{n+1}\left(\frac{\rho g h_s^{n+1}\sin\theta}{\mu}\right)^{1/n} \qquad (2.12)$$

Hence, the bed shear stress is given by:

$$\tau_b = \left(\tau_y + \mu\left|\frac{n+1}{n}\frac{V_p}{h_s}\right|^n\right)\mathrm{sgn}\left(V_p\right) \qquad (2.13)$$

It is important to note that the fluid is qualified as pseudo plastic for n < 1, as a dilatant fluid for n > 1, and as Bingham fluid for n = 1. Therefore, the Bingham rheology is a limiting case of Herschel-Bulkley rheology with a linear stress-strain relationship (Locat and Lee, 2000). In addition, the Herschel-Bulkley rheology has been found to be more appropriate for depicting the nonlinear visco-plastic behaviour of debris flows (Huang and Garcia, 1998; Imran et al., 2001). Coussot and Piau (1994) cited that the Herschel-Bulkley rheology fits well with their experimental data but not with Bingham rheology.

2.6.3.3 Bilinear rheology

The bilinear rheology is based on a slightly different philosophy as compared to the Bingham and Herschel-Bulkley rheologies. The bilinear

rheology does not consider a separate plug and viscous layer. The formulation uses apparent yield strength to distinguish between behaviour at low and high shear stress, which allows a smooth transition between viscous and plastic behaviour of the flow (Imran et al., 2001).

Figure 2.16 shows the relationship between shear stress and shear strain rate. It can be seen that the bilinear model is a hybrid of a Bingham and Newtonian fluid at sufficiently low strain rates; the fluid behaves as a Newtonian fluid with viscosity, μ_1, and no yield strength, τ_y. While at sufficiently high strain rates, the fluid behaves as a Bingham fluid with lower viscosity, μ_2 (Hance, 2003).

As cited in Locat and Lee (2000) and Hance (2003), the general bilinear rheology can be written as:

$$\tau = \tau_y + \mu_2 \dot{\gamma} + \left(\frac{c}{\dot{\gamma} + \dot{\gamma}_0} \right) \qquad (2.14)$$

where, τ_y is the apparent yield strength, $\dot{\gamma}_0$ is a rheological constant with units of the inverse of time and c is an empirical constant that has a negative value and units of pressure divided by time.

According to Imran et al. (2001), unlike the Bingham and Herschel-Bulkley rheologies, a closed form solution for a function describing the velocity profile for the case of a steady developed debris flow cannot be obtained with the bilinear rheological model. However, as proposed in Imran et al. (2001), the relationship of the depth averaged flow velocity is given by:

$$v = \alpha_1 V_p \qquad (2.15)$$

where α_1 is the shape factor and V_p is the top surface flow velocity.

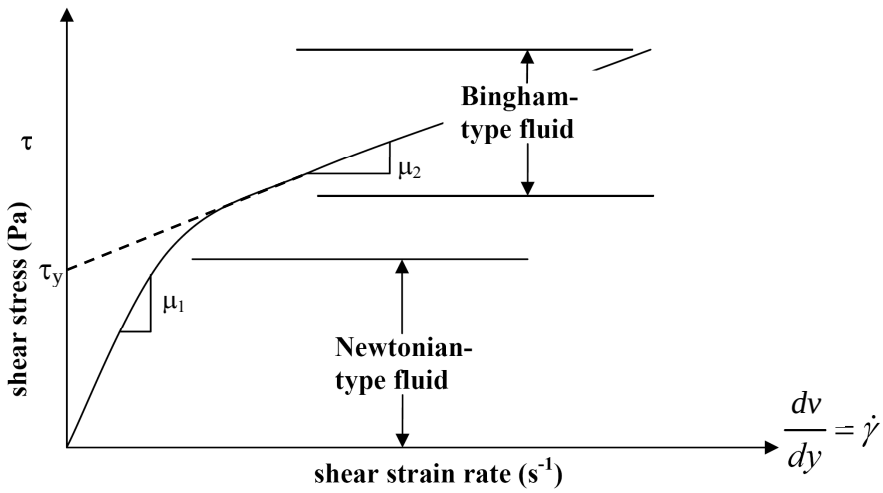

Figure 2.16: Bilinear rheological model (after Hance, 2003)

2.6.3.4 Power Law and Logarithmic Law

Boukpeti et al. (2011) proposed two models to describe the velocity distribution in the slide for the case of a steady uniform flow material obeying the Herschel-Bulkley model: (i) the Power Law and (ii) the Logarithmic Law.

The equilibrium of shear stresses in the debris layer, which is assumed to obey the Power Law, is expressed as:

$$\tau_b(1-Y) = s_{u,ref}\left(\frac{\dot{\gamma}}{\dot{\gamma}_{ref}}\right)^{\beta} \qquad (2.16)$$

where τ_b is the shear stress at the base, Y is the vertical coordinate normalised with the flow height, $s_{u,ref}$ is the shear strength at the reference strain rate $\dot{\gamma}_{ref}$ and β is the rate parameter. From the equation (2.16), the strain rate distribution is obtained as:

$$\frac{du}{dy} = \dot{\gamma}_b(1-Y)^{1/\beta} \qquad (2.17)$$

where $\dot{\gamma}_b$ is the strain rate at the bed, $\dot{\gamma}_b = \dot{\gamma}_{ref}\, S_{tr}^{-1/\beta}$ and $S_{tr} = s_{u,ref} / \tau_b$ which is called the strength ratio. By integrating equation (2.17) with the boundary condition $v(0) = 0$ (no slip), this yields the velocity profile:

$$v = v_t\left[1-(1-Y)^{(1+\beta)/\beta}\right] \tag{2.18}$$

where u_t denotes the velocity at the top of the flow layer:

$$v_t = \left(\frac{\beta}{1+\beta}\right) h\,\dot{\gamma}_{ref}\, S_{tr}^{-1/\beta} \tag{2.19}$$

Following the same derivation procedure as for the Power Law, the strain rate and velocity profiles for Logarithmic Law can be expressed as:

$$\frac{dv}{dy} = \dot{\gamma}_b\, 10^{-(1/\eta S_{tr})Y} \tag{2.20}$$

and

$$v = v_t\, \frac{\left(1-10^{-(1/\eta S_{tr})Y}\right)}{\left(1-10^{-(1/\eta S_{tr})}\right)} \tag{2.21}$$

with

$$u_t = \frac{\lambda S_{tr}}{\ln(10)} h\,\dot{\gamma}_{ref}\left(10^{(1/\eta)[(1-S_{tr})/S_{tr}]} - 10^{-(1/\eta)}\right) \tag{2.22}$$

where η is the rate parameter.

Boukpeti et al. (2011) pointed out that, for the Power Law, it can be seen that when the parameter β increases, the thickness of the layer where significant shearing occurs increases. The increased rate dependence of shear strength leads to a diffusion of the shearing, thus reducing the maximum strain rate. Similarly for the Logarithmic Law, an increase in η results in an increase in the thickness of the layer where significant shearing occurs, reducing the

maximum strain rate. The authors concluded that the Power Law stands out for its simplicity in which the velocity profile is governed by the parameter β.

2.6.4 Governing equations and analytical solutions through mass and momentum conservations

As mentioned earlier in this chapter, many investigators have modelled flow events by specifying rheological rules that govern flow behaviour. However, in general, specified rheologies are neither well-constrained nor sufficient to explain flow dynamics; this is because steady, uniform, rheometric flows of grain-fluid mixtures do not occur in nature (Iverson and Denlinger, 2001).

Savage and Hutter (1989) developed a mathematical model which describes the motion and the spreading of a finite mass of fluid-like granular material along a rough plane bed. The model was based on the balance laws of mass and momentum and depth averaging. The balance of mass and momentum can be defined as:

$$\nabla \cdot v = 0 \tag{2.23}$$

$$\rho \frac{dv}{dt} = -\nabla \cdot T + \rho g \tag{2.24}$$

where,

v = flow velocity

ρ = mixture density

t = time

g = gravitational acceleration

T = pressure tensor

The Coulomb friction model for characterising continuum-scale stresses in slowly deforming granular material was used in the model by Savage and Hutter (1989). The main limitation of this model is that the

interparticle interactions are not accounted for, in which the intergranular pore fluid pressures influence the Coulomb friction in deforming granular masses. It is important to note that the pressure tensor term T in equation 2.24, which is the total stress of the mixture and does not separate the mixture into the effective stress and the pore fluid pressure. It is well known that the effective stress principle can describe the effects of pore fluid pressures; this leads to the model which incorporated the effective stress principle to account for the influence of pore fluid pressured, developed by Iverson and Denlinger (2001).

Iverson and Denlinger (2001) developed a model to describe a spectrum of flows in order to clarify the physical basis of similarities and differences among events. This model generalises depth-averaged mass and momentum balance equations. The equations describe the behaviour of finite masses of variably fluidised grain-fluid mixtures that move unsteadily across three-dimensional terrain, from initiation to deposition.

It is important to note that mass and momentum conservation equations provide the fundamental tools for analysis of debris-flow continuum mechanics. As quoted in Iverson and Denlinger (2001), the simplified mass and momentum conservation equations can be written as follows (assuming that the density change of the soil is negligible):

$$\nabla \cdot v_s = 0 \tag{2.25}$$

$$\rho\left(\partial v_s / \partial t + v_s \cdot \nabla v_s\right) = -\nabla \cdot \left(T_s + T_f\right) + \rho g \tag{2.26}$$

where,

v_s = flow velocity of solid phase

ρ = mixture density

t = time

g = gravitational acceleration

T_s = stress of the solid phase

T_f = stress of the fluid phase

It should be noted that depth averaging is used to further simplify the equations of motion in order to eliminate explicit dependence on the coordinate normal to bed. Figure 2.17 shows the schematic cut-away view of an unsteady flow down a curvilinear slope. This illustrates the local coordinate system and dependent variables $h(x,y,t), \bar{v}_x(x,y,t), \bar{v}_y(x,y,t)$ that describe depth-averaged flow.

As cited in Iverson and Denlinger (2001), the depth averaged theory uses the kinematic boundary conditions where mass neither enters nor leaves at the free surface or base of the flow as:

$$\frac{\partial h}{\partial t} + v_x \frac{\partial h}{\partial x} + v_y \frac{\partial h}{\partial y} - v_z = 0 \qquad z = h(x,y,t) \quad (2.27)$$

$$v_z = 0 \qquad z = 0 \quad (2.28)$$

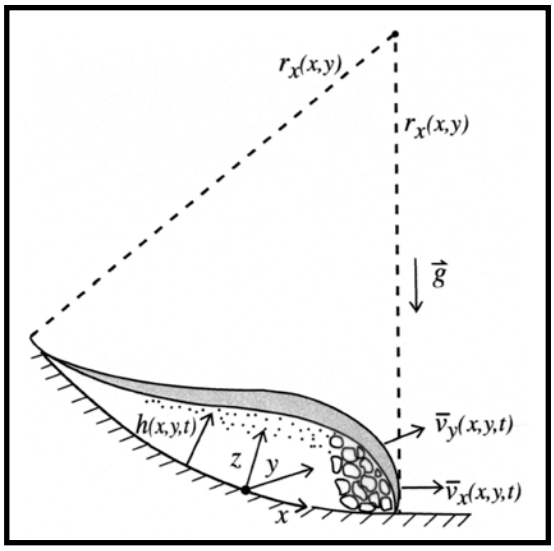

Figure 2.17: Schematic cut-away view of an unsteady flow down a curvilinear slope (after Iverson and Denlinger, 2001)

Depth averaging also implies that the total normal stress (the sum of solid and fluid normal stresses) in the *z* direction balances the *z* component of the mixture weight, which gives the following equation:

$$T_{s(zz)} + T_{f(zz)} = (h - z)\rho g_z \quad (2.29)$$

Quantities with subscript *s* refer to the solid phase, subscript *f* refers to the fluid phase, while those with no subscript refer to the solid-fluid mixture phase. g_z is the gravity contribution in the z-direction.

Equation (2.29) leads to expressions for the total normal stress at the bed, while the depth averaged total normal stress in the *z* direction gives the following equations:

$$T_{s(zz)}\big|_{z=0} + T_{f(zz)}\big|_{z=0} = \rho g_z h \qquad (2.30)$$

$$\overline{T}_{s(zz)} + \overline{T}_{f(zz)} = \frac{1}{h}\int_0^h \rho g_z (h-z)dz = \frac{1}{2}\rho g_z h \qquad (2.31)$$

Similarly, the depth averaged velocities components can be written as:

$$\overline{v}_x = \frac{1}{h}\int_{z=0}^{z=h} v_x dz \qquad \overline{v}_y = \frac{1}{h}\int_{z=0}^{z=h} v_y dz \qquad \overline{v}_z = \frac{1}{h}\int_{z=0}^{z=h} v_z dz \quad (2.32)$$

While the depth averaged stress components (denoted generically by subscript *ij*) can be defined as:

$$\overline{T}_{ij} = \frac{1}{h}\int_{z=0}^{z=h} T_{ij} dz \qquad (2.33)$$

Combining the mass and momentum conservations as well as the depth averaged components yield the following equations:

$$\frac{\partial h}{\partial t} + \frac{\partial\left(h\overline{v}_x\right)}{\partial x} + \frac{\partial\left(h\overline{v}_y\right)}{\partial y} = 0 \qquad (2.34)$$

$$\rho\left[\frac{\partial h\overline{v}_x}{\partial t} + \frac{\partial\left(h\overline{v}_x^2\right)}{\partial x} + \frac{\partial\left(h\overline{v}_x\overline{v}_y\right)}{\partial y}\right] = -\int_0^h\left[\frac{\partial T_{s(xx)}}{\partial x} + \frac{\partial T_{f(xx)}}{\partial x} + \frac{\partial T_{s(yx)}}{\partial y} + \frac{\partial T_{f(yx)}}{\partial y} + \frac{\partial T_{s(zx)}}{\partial z} + \frac{\partial T_{f(zx)}}{\partial z} - \rho g_x\right]dz$$

(2.35)

Iverson and Denlinger (2001), assumed that the pore fluid pressure varies linearly from a maximum of p_{bed} at the base of the flow to zero at the flow surface, yielding:

$$\overline{T}_{f(zz)} = \frac{1}{h}\int_0^h T_{f(zz)}dz = \frac{1}{2}T_{f(zz)}\Big|_{z=0} = \frac{1}{2}p_{bed} \qquad (2.36)$$

Due to the assumption of linear variation of fluid pressure, the fluid pressure can also be expressed as a fraction λ of the total basal normal stress, in which,

$$p_{bed} = \lambda \rho g_z h \qquad @ \qquad \lambda = \frac{p_{bed}}{\rho g_z h} \qquad (2.37)$$

It should be noted that when $\lambda = 1$, this represents a case of zero basal effective stress or complete liquefaction.

In addition to the fluid pressure, the viscous resistance comes from the viscosity of the fluid phase, μ, which is multiplied by a fluid volume fraction, υ_f, because only this fraction of mixture produces viscous stresses (Iverson and Denlinger, 2001). By integration of the velocity derivatives in equation (2.35), in which adapting the Navier-Stokes equations for flow of incompressible Newtonian fluids into the fluid stress terms in equation (2.35), and by depth averaging yields the viscous stress term:

$$-3\upsilon_f \mu \frac{\overline{v}_x}{h} \qquad (2.38)$$

Based on Iverson and Denlinger (2001), by combining the equations above, which include solid and fluid stresses, and by using depth average theory, the final form of the depth averaged x direction momentum equation can be written as:

$$\rho\left[\frac{\partial(h\bar{v}_x)}{\partial t}+\frac{\partial(h\bar{v}^2_x)}{\partial x}+\frac{\partial(h\bar{v}_x\bar{v}_y)}{\partial y}\right]$$
$$=-\mathrm{sgn}\left(\bar{v}_x\right)\left(\rho g_z h-p_{bed}\right)\left(1+\frac{\bar{v}^2_x}{r_x g_z}\right)\tan\phi_{bed}-3\upsilon_f\mu\frac{\bar{v}_x}{h}$$
$$-hk_{act/pass}\frac{\partial}{\partial x}\left(\rho g_z h-p_{bed}\right)-h\frac{\partial p_{bed}}{\partial x}+\upsilon_f\mu h\frac{\partial^2\bar{v}_x}{\partial x^2}$$
$$-\mathrm{sgn}\left(\frac{\partial\bar{v}_x}{\partial y}\right)hk_{act/pass}\frac{\partial}{\partial y}\left(\rho g_z h-p_{bed}\right)\sin\phi_{\mathrm{int}}$$
$$+\upsilon_f\mu h\frac{\partial^2\bar{v}_x}{\partial y^2}$$
$$+\rho g_x h \qquad (2.39)$$

where,

r_x	= radius of local bed curvature in the *x* direction
ϕ_{bed}	= bed friction angle
υ_f	= fluid volume fraction
μ	= mixture viscosity
$k_{act/pass}$	= lateral stress coefficient
ϕ_{int}	= mixture internal friction angle
sgn	= sign function (+1 for positive number and -1 for negative number)

The terms on the right-hand side of equation (2.39) are grouped by line according to type of stress: the first line represents basal shear stresses from the soil skeleton and fluid, the second line represents longitudinal normal stress, the third and fourth lines represent transverse shear stresses, while the fifth line represents the driving stress due to the gravitational body force in the x-direction.

It is important to note that the governing equation proposed by Iverson and Denlinger (2001) was for describing typical flowing of grain-fluid mixtures on land. This does not account for the case of grain-fluid mixture flows under fully-submerged conditions as in submarine landslide flows.

To account for this, the buoyancy effect has to be considered for fully submerged conditions. This can be done by deducting the density of the surrounding fluid (i.e. water), ρ_w from the mixture mass density, ρ, in which the density term becomes $(\rho - \rho_w)$. Note that the viscosity of the fluid medium may also affect the flow; however the fluid medium in this study is water therefore, the governing equation for the fully submerged condition can then be written as:

$$
\begin{aligned}
&(\rho - \rho_w)\left[\frac{\partial(h\bar{v}_x)}{\partial t} + \frac{\partial(h\bar{v}^2_x)}{\partial x} + \frac{\partial(h\bar{v}_x\bar{v}_y)}{\partial y}\right] \\
&= -\operatorname{sgn}(\bar{v}_x)\left((\rho - \rho_w)g_z h - p_{bed}\right)\left(1 + \frac{\bar{v}^2_x}{r_x g_z}\right)\tan\phi_{bed} - 3\upsilon_f \mu \frac{\bar{v}_x}{h} \\
&- hk_{act/pass}\frac{\partial}{\partial x}\left((\rho - \rho_w)g_z h - p_{bed}\right) - h\frac{\partial p_{bed}}{\partial x} + \upsilon_f \mu h \frac{\partial^2 \bar{v}_x}{\partial x^2} \\
&- \operatorname{sgn}\left(\frac{\partial \bar{v}_x}{\partial y}\right) hk_{act/pass}\frac{\partial}{\partial y}\left((\rho - \rho_w)g_z h - p_{bed}\right)\sin\phi_{\text{int}} \\
&+ \upsilon_f \mu h \frac{\partial^2 \bar{v}_x}{\partial y^2} \\
&+ (\rho - \rho_w)g_x h
\end{aligned}
\tag{2.40}
$$

For specific cases, analytical solutions can be obtained to predict phenomena in the field as well as aiding comparisons with numerical solutions. An example of the analytical solution for an unsteady motion of a mass of uniform height descending down a slope, as proposed by Iverson and Denlinger (2001), is shown in equation (2.41). It should be noted that this equation is modified after the original equation in Iverson and Denlinger (2001) to incorporate the submerged conditions. This simplified linear equation describing translational motion is reduced from the governing equation (2.40), with the assumption of a flow with uniform thickness moving downslope with no velocity gradients in the *x* and *y* directions.

$$(\rho-\rho_w)\frac{d(h\bar{v}_x)}{dt}=-((\rho-\rho_w)g_z h-p_{bed})\tan\phi_{bed} \\ -3\upsilon_f\mu\frac{\bar{v}_x}{h}+(\rho-\rho_w)g_x h \tag{2.41}$$

With algebraic manipulation including the substitution of $g_x = g_z \tan\theta$, where θ is the slope angle, this gives the following equations:

$$\frac{d\bar{v}_x}{dt}+3\frac{\upsilon_f\mu}{(\rho-\rho_w)h^2}\bar{v}_x = g_z\Theta \tag{2.42}$$

where,

$$\Theta = \tan\theta-(1-\lambda)\tan\phi_{bed} \tag{2.43}$$

It should be noted that the parameter Θ is constant if the pore pressure ratio λ (ratio of the excess pore pressure and the effective stress), slope angle θ, and friction angle ϕ_{bed} are constant, or if changes in their values cancel one another. For constant Θ the solution of (2.42), subjected to the initial condition of $\bar{v}_x = \bar{v}_0$ at $t = 0$, yields the following equation:

$$\bar{v}_x = \frac{(\rho-\rho_w)g_z h^2}{3\upsilon_f\mu}\Theta\left[1-\exp\left(-t\Big/\frac{(\rho-\rho_w)h^2}{3\upsilon_f\mu}\right)\right] \\ +\bar{v}_0\exp\left(-t\Big/\frac{(\rho-\rho_w)h^2}{3\upsilon_f\mu}\right) \tag{2.44}$$

Equation (2.44) enables the prediction of flow velocities with given material parameters and the gravitational levels. Most importantly, this facilitates the developments of centrifuge scaling laws, which will be described in more detail in Chapter III.

Based on equation (2.44), the dimensionless groups for deducing variation in importance of mechanisms for the submarine landslide flows can be deduced as:

$$\bar{v}_x \frac{3\upsilon_f \mu}{(\rho - \rho_w) g_z h^2} \tag{2.45}$$

$$t \frac{3\upsilon_f \mu}{(\rho - \rho_w) h^2} \tag{2.46}$$

2.6.5 A numerical model that incorporates various rheologies

A 1-D depth average numerical model that incorporates the Bingham, Herschel-Bulkley, and bilinear rheologies to simulate dynamics of an unsteady subaqueous debris flow called "BING" was proposed by Imran et al. (2001). The formulation of this model is based on the laminar flow of a constant-volume high-density debris mass evolving in the down slope direction. Incorporation of different rheological formulations within the framework of a single numerical model provides the opportunity to select a rheology that is most appropriate for any specific case. The numerical model code is written in the visual basic programming language and has a graphical user interface. The code starts from an initial debris mass and is allowed to collapse and propagate on a given topography. By assuming that shear stress increases linearly with depth, the velocity profile within the debris mass can be derived from a rheological model. The depth average technique is then used to solve the governing equations.

The governing equations for the momentum conservation (based on equations 2.23 and 2.24) used in the BING code for the Herschel-Bulkley and the bilinear rheology, as mentioned by Imran et al. (2001), are defined as follows:

For the Herschel-Bulkley rheology,

$$\frac{dv}{dt} = \frac{1}{h}\frac{\partial}{\partial x}\left(\bar{v}^2 h + \frac{\alpha_1 - \alpha_2}{1-\alpha_1} V_p^2 h - \frac{1-\alpha_2}{1-\alpha_1} V_p \bar{v} h\right)$$
$$- \Delta\rho g \frac{\partial h}{\partial x} - \frac{\tau_y \operatorname{sgn}(V_p)}{\rho h}$$
$$- \frac{\beta_1 \tau_y}{\rho h}\left|\frac{V_p}{\gamma_r h_s}\right|^n \operatorname{sgn}(V_p) \qquad (2.47)$$

and for the bilinear rheology,

$$\frac{dv}{dt} = \left(1 - \frac{\alpha_2}{\alpha_1^2}\right)\frac{1}{h}\frac{\partial}{\partial x}\left(v^2 h\right) - \Delta\rho g \frac{\partial h}{\partial x} + \Delta\rho g \zeta - \frac{\tau_{ya} \operatorname{sgn}(V_p)}{\rho h}\Psi \qquad (2.48)$$

where,

$\bar{v}$	= depth averaged mean velocity
V_p	= plug layer velocity (velocity at the top flow surface)
h	= debris flow thickness ($h = h_S + h_P$)
h_S	= shear layer thickness
h_P	= plug layer thickness
α_1	= shape factor
α_2	= shape factor
τ_y	= yield stress
τ_b	= bed shear stress
τ_{ya}	= apparent yield strength
ρ	= density of debris material
γ_r	= reference strain rate
β_1	= shape factor
ζ	= slope of the existing bed
Ψ	= $\tau_b/\tau_{ya}\ sgn\ (V_p)$

This numerical model is able to evaluate the dynamics and the final deposit shape of debris flows of different sizes, sources and rheologies. However, there are certain limitations to it. One limitation is that the hydrodynamic pressure and tensile strength of debris materials in the theoretical treatment of debris flow hydrodynamics are not included.

2.6.6 Runout efficiency

The runout efficiency, commonly known as the net efficiency, defines as the ratio of the horizontal distance of flow from source to deposit, L and the vertical elevation of flow above deposit, H. (L/H) has always been the research focal point for subaerial debris flow and submarine landslides. Iverson (1997) quoted that the energetics and runout efficiency of debris flow differ dramatically from those of a homogenous solid or fluid. Logically, one can consider that a mixture of solid grains and fluid (less dense than the solid) which loses energy as it moves downslope due to viscous shearing as well as energy dissipation caused by grain contact friction and collisions. It can also be comprehended that viscous fluid increases energy dissipation and reduces runout. In addition, plastic deformation of soil also contributes to the dissipation mechanism.

It is interesting to note that water-saturated debris flows show that the presence of viscous fluid (i.e. water) increases runout even though the fluid dissipates energy. Interactions of viscous fluid with dissipative solid grains of widely varying sizes produce this behaviour and merit an emphasis in efforts to understand debris flow motion. Debris flow motion involves a cascade of energy that begins with incipient slope movement and ends with deposition (Iverson, 1997). As a debris flow moves downslope, its energy degrades and undergoes the conversions shown in Figure 2.18. The one-way arrows indicate conversions that are irreversible, whereas the two-way arrow indicates a conversion that involves significant transfer of energy.

Figure 2.18 describes the conversion of gravitational potential energy to the work done during the flow translation. As cited in Iverson (1997), the

more efficiently this conversion occurs, the less vigorously energy degrades to irrecoverable forms such as heat, and the further the flows run out before stopping.

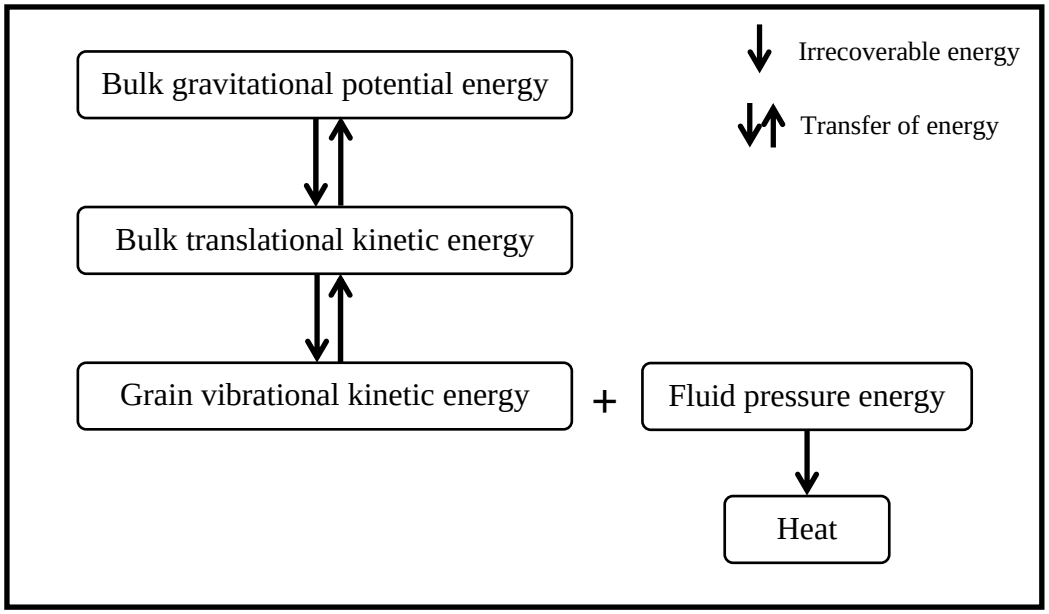

Figure 2.18: Energy conversion for debris flows (modified after Iverson, 1997)

Iverson (1997) recognised that the net efficiency of debris flow can be evaluated by equating the total potential energy lost during motion, *MgH* to the total energy degraded to irrecoverable forms by resisting forces, *MgR*, that work through the distance *L*:

$$MgH = MgRL \qquad (2.49)$$

where,

M	= flow mass
g	= magnitude of gravitational acceleration
R	= dimensionless net resistance coefficient
H	= vertical elevation of flow above the deposit
L	= horizontal distance from source to deposit

Figure 2.19 shows the schematic cross-section defining H and L. The dimensionless net resistance coefficient, R, incorporates the effects of internal

forces (or dissipation), but depends also on external forces that act at the bed to the soil flows.

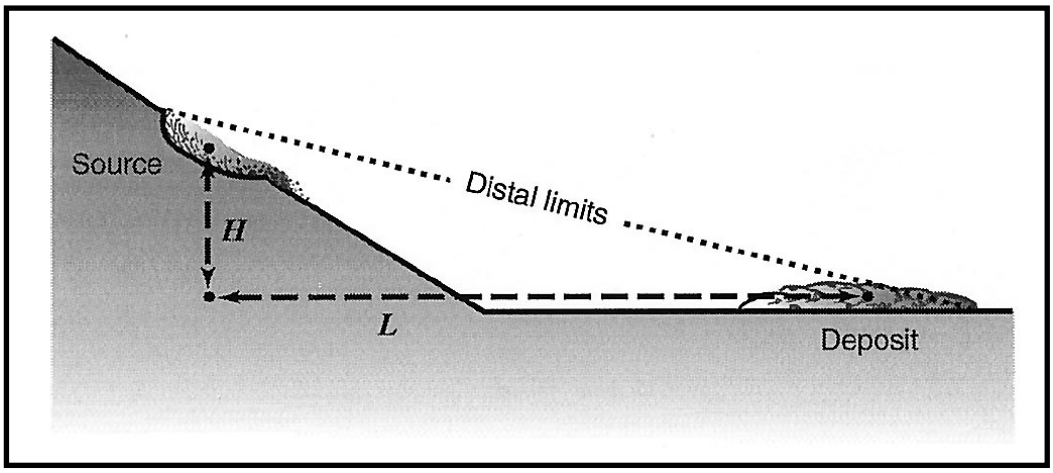

Figure 2.19: Schematic cross-section defining *H* and *L*, after Iverson (1997)

It is important to quantify the mechanical phenomena that govern R, in order to understand and predict flow motion of debris flows. Iverson (1997) proposed a simpler form from Equation (2.49) for evaluating net efficiency:

$$1/R = L/H \qquad (2.50)$$

This is obtained by dividing each side of the original net efficiency for debris flow by *MgHR*. It can be seen that the net efficiency *1/R* corresponds directly to *L* and *H*, where *1/R* increases as the runout distance *L* increases for a fixed height, *H*. It is therefore important to evaluate *L/H* from a debris flow to find typical values of (1/R) for different conditions. Based on observations and experiments, Iverson (1997) pointed out three important points upon evaluation of *L/H*:

1. (1/R) of water saturated debris flows exceeds that of drier sediment flow with comparable masses.
2. Large debris flows appear to have greater (1/R) than small flows. However based on the available database (Figure 2.5), there is no clear trend on this.

3. (1/R) depends on runout path geometry and boundary conditions such as the extent of erosion, sedimentation and flow channelisation.

2.7 Major Research Efforts

The increasing interest in offshore developments and mitigation of potential hazard requires a better understanding of submarine landslides.

According to Locat and Lee (2000), there have been some major international research projects related to submarine landslides, such as: GLORIA (1984-1991), ADFEX (Artic Delta Failure Experiment, 1989-1992), STEAM (Sediment Transport on European Atlantic Margins, 1993-1996), ENAM II (1996-1999), STRATAFORM (1995-2001) and COSTA (Continental Slope Stability, 2000-2004).

The main objective of ADFEX was to obtain real-time data on submarine debris flow, turbidity current and dynamics for the first time. STEAM and ENAM II had a strong component dedicated to submarine mass movements with particular reference to those in the North West African and North Sea continental margin respectively. STRATAFORM was aimed at developing a better understanding of the formation of sedimentary strata, including submarine mass movements. This involved a series of surveys, in-situ monitoring, observations, laboratory testing and numerical modelling.

The COSTA project, dealt with coastal slope stability with the following objectives (Locat and Lee, 2000):

- Assessment of historical records of slope instability, slope parameters, seismicity, and tectonic setting.
- Understanding of seafloor failure dynamics through 3-D imaging of sediment architecture and geometry of slope failures.

- Understanding of sediment physical, mechanical and elastic properties of slip planes and areas prone to slope failures.
- Determination of the presence of gas hydrate and its significance for slope stability.
- Modelling of forces and mechanical processes that control the initiation of slope instabilities (release mechanisms), flow dynamics and initiation of tsunamis.
- Assessment of risk-fields related to slope stability

More recently, the Research institution-based strategic project for offshore geohazards (SIP) and the Ormen Lange gas field development (2003-2007) led to a number of researches on submarine landslides which are largely carried out by the International Centre for Geohazards (ICG) and the Norwegian Geotechnical Institute (NGI).

Furthermore, the IGCP project 511 (IUGS-UNESCO's International Geoscience Programme 511) (2005-2009) carried out research on submarine mass movements and their consequences. This project has attracted numerous contributions from active researchers, groups and institutions for research in the scientific and engineering aspects of offshore geohazards.

Since the significance and importance of submarine landslides have been recognised, research in this area has gained more attention from the public as well as the professional sectors. Figure 2.20 shows the logical sequence from the recognition of submarine landslides leading to research studies, implementing designs from research output, and best practice, which leads to the ultimate objective in mitigating the occurrences of offshore geohazards.

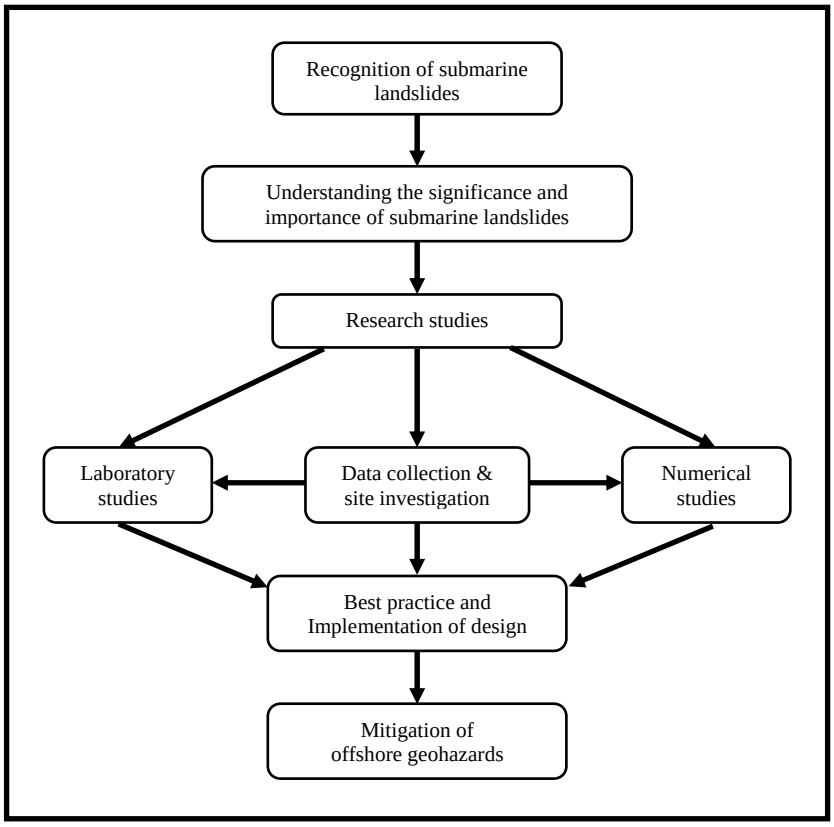

Figure 2.20: Sequence of research leading to the mitigation of offshore geohazards

Above all, these projects have inspired a number of experimental works and numerical studies on submarine landslides. The next section in this chapter covers the experimental works in 1 g environment and centrifuge tests that have been carried out by other researchers, particularly in submarine landslides. It should be noted that, to date, there are only very limited laboratory studies on submarine landslides through centrifuge modelling. Therefore, this study will particularly focus on laboratory studies of submarine landslides through centrifuge modelling.

2.8 Experimental Works by Other Researchers

Experimental works are generally performed in the context of solving a particular problem or query to support research concerning phenomena or to verify a hypothesis. Laboratory experiments are therefore important in order to

study and acquire deeper knowledge on the nature of submarine landslides as well as to give an insight into the mechanism of failures. Valuable data are not only the results from laboratory experiments; observations in experiments provide a better understanding of the physical phenomena of the research problem.

This section summarises the laboratory experimental works on submarine slopes carried out by various leading researchers in this particular field, both in 1 g environments and centrifuges. The purpose, methods, equipments, materials, geometries and limitations of the models in each experiment are discussed.

2.8.1 Past experimental works in 1 g environment

The term "1 g environment" means experiments that are carried out in the normal earth's gravity condition. There are a number of experimental works in 1 g environment on submarine slopes for various purposes and to study specific phenomenon that occur during a submarine landslide. These works include: Schwarz (1982), Mohrig et al. (1998, 1999), Marr et al. (2001), Mohrig and Marr (2003), Vendeville and Gaullier (2003), and Ilstad et al. (2004a, b and c). Table 2.2 summarises these 1 g environment experimental works in chronological order.

Although, there are a few 1 g environmental works on submarine slopes, only the most relevant experiments to the current research work are discussed in detail. These include Mohrig et al. (1998, 1999) and Ilstad et al. (2004a, b and c).

Table 2.2: Summary of submarine slope experimental works in 1 g environment

Reference	Type of Experiment	Geometry			Materials and soil properties		Methodology	Measured Parameters	Key Findings	Comments
		Slope angle	Slope Length	Slope Width	Soil Type	Soil Properties				
Schwarz (1982)	Various submarine slope experiments on sedimentation as well as sediment flow and related phenomena	10°-30°	1.6 – 3.7 m	0.48 – 0.76 m	Wet lime mud and illitic clay	Wet lime γ = 2.63g/cm^3 LL = 46.1 PL = 32.6 median size = 2.9μm illitic clay γ = 2.78g/cm^3 LL = 85.5 PL = 40.4 median size = 0.67-1μm	Three methods: 1) mud & silt grain mixed with water and pour into a water tank, 2) semi-automatic continuously stirring and pumping apparatus, 3) circuit feed system and control of sedimentation rate	Sedimentation rate and thickness of sedimentation	Organisation of slide structure and structural transformation	No pore pressure measurement
Mohrig et al. (1998)	To demonstrate hydroplaning of submarine debris flows	0° – 20°	10 m	0.2 m	Slurry (55%silt, 45%sand)	γ_{slurry} = 2.08g/cm^3 τ_y=29Pa μ_s=13Pa s K=3x10^{-12} m^2 k=3x10^{-5}m/s WC = 16.5%	Single slurry fed into a channel of hard bottom, with varying slope inclinations	Flow velocity, thickness of deposition and discharge	Hydroplaning	Influence of soil and fluid type and stresses of soil flow are not investigated
Mohrig et al. (1999)	Relative mobility of muddy submarine debris flows on different beds	1° – 6°	10 m	0.2 m	Slurry (40%clay, 35%silt, 25%sand)	γ_{slurry} = 1.60g/cm^3 τ_y=29Pa μ_s=13Pa s K=1x10^{-14} m^2 k=1x10^{-5}cm/s WC = 39.0%	Single slurry fed into a channel of hard and soft bottom, with and without water in the channel	Flow velocity, thickness of deposition and discharge	Hydroplaning is independent of rheology	Influence of soil and fluid type and stresses of soil flow are not investigated

K = hydraulic conductivity k = hydraulic permeability

Table 2.2: Summary of submarine slope experimental works in 1 g environment (cont.)

Reference	Type of Experiment	Geometry			Materials and soil properties		Methodology	Measured Parameters	Key Findings	Comments
		Slope angle	Slope Length	Slope Width	Soil Type	Soil Properties				
Marr et al. (2001)	To examine the role of clay and water content in flow dynamics and depositional structure on submarine sandy flows	$0^o – 6^o$	10 m	0.3 m	kaolinite, bentonite, white silica sand + coal slag	γ_{sand} = 2.65g/cm^3 median size = 110 μm $\gamma_{coal\ slag}$= 2.60g/cm^3 median size = 500 μm	Mixtures with varying water and clay contents, release from a head tank	Head velocity and runout distance	Strong coherent flows with plastic rheology in laminar regime, weak coherent flows increase breakup and suspension of the head flow	No pore pressure and soil stresses measurement
Mohrig and Marr (2003)	Efficiency of turbidity current generation from submarine debris flows with acoustical imaging	$1^o – 6^o$	10 m	0.2 m	kaolinite, bentonite, silica	N/A	Motion of mixtures released from a head tank were recorded; acoustical imaging methods were also used to generate images of ambient water turbulently mixed into the heads of submarine debris flow	Head velocity and acoustical reflectance	Turbulence concentrated at flow heads, developed a framework for quantifying the erosion rate of sediment from the head of the submarine debris flows	No pore pressure and soil stresses measurement
Vendeville and Gaullier (2003)	Role of pore pressure and slope angle in triggering submarine mass movements	$3^o – 6^o$	N/A	N/A	High porosity sand and clay or viscous silicone polymer	N/A	Tilting the slope and progressively increase fluid pressure (air and water)	N/A	Fluid pressure effectively triggers failure, sediment deformed as a coherent slab	No detailed information on materials used

Table 2.2: Summary of submarine slope experimental works in 1 g environment (cont.)

Reference	Type of Experiment	Geometry			Materials and soil properties		Methodology	Measured Parameters	Key Findings	Comments
		Slope angle	Slope Length	Slope Width	Soil Type	Soil Properties				
Ilstad et al. (2004)a	Measurement of pore fluid pressure and total stress on submarine debris flows	6°	9.0 m	0.2 m	Kaolin clay (Snowbrite) and fine brown silica sand (330 μm)	γ_{kaolin} = 2.75g/cm^3 γ_{sand} = 2.65g/cm^3	Various mixtures of clay/sand ratio, released from a submerged compartment into a channel	Pore pressure and total stress	Hydroplaning front for high clay/sand ratio, turbulent front for low clay/sand ratio	Influence of small soil stresses due to gravity not investigated
Ilstad et al. (2004)b	Submarine debris flows through particle tracking by high speed video	6°	9.0 m	0.2 m	Kaolin clay (Snowbrite) and fine brown silica sand (330 μm)	γ_{kaolin} = 2.75g/cm^3 γ_{sand} = 2.65g/cm^3	Various mixtures of clay/sand ratio, released from a submerged compartment into a channel, high speed video to capture the flows	Flow velocity, thickness of deposition	Strong coherent flows lower velocity, velocity decreases behind the front, weak coherent flows uniform velocity	Influence of small soil stresses due to gravity not investigated
Ilstad et al. (2004)c	Frontal dynamics and morphology of submarine debris flows	8°	9.0 m	2.25 m	Kaolin clay (Snowbrite) and fine brown silica sand (330 μm)	γ_{kaolin} = 2.75g/cm^3 γ_{sand} = 2.65g/cm^3	Mixture fully submerged at the beginning, released from a gate and captured the flow with high speed video	Front velocity and runout distance	Laboratory results are comparable with field, tensile stresses lead to formation of outrunner blocks	Influence of soil type is not investigated

2.8.1.1 Mohrig et al. (1998, 1999) experimental works

The experiments carried out by Mohrig et al. (1998, 1999) were primarily to investigate the hydroplaning phenomena of submarine debris flows and their relative mobility, which mobilise antecedent deposits.

2.8.1.1.1 Experimental setup

The experimental setup in Mohrig (1998, 1999) consisted of a glass-walled tank 10 m long, 3 m high, and 0.6 m wide. A 0.2 m wide channel with smooth transparent walls was suspended within the tank as shown in Figure 2.21.

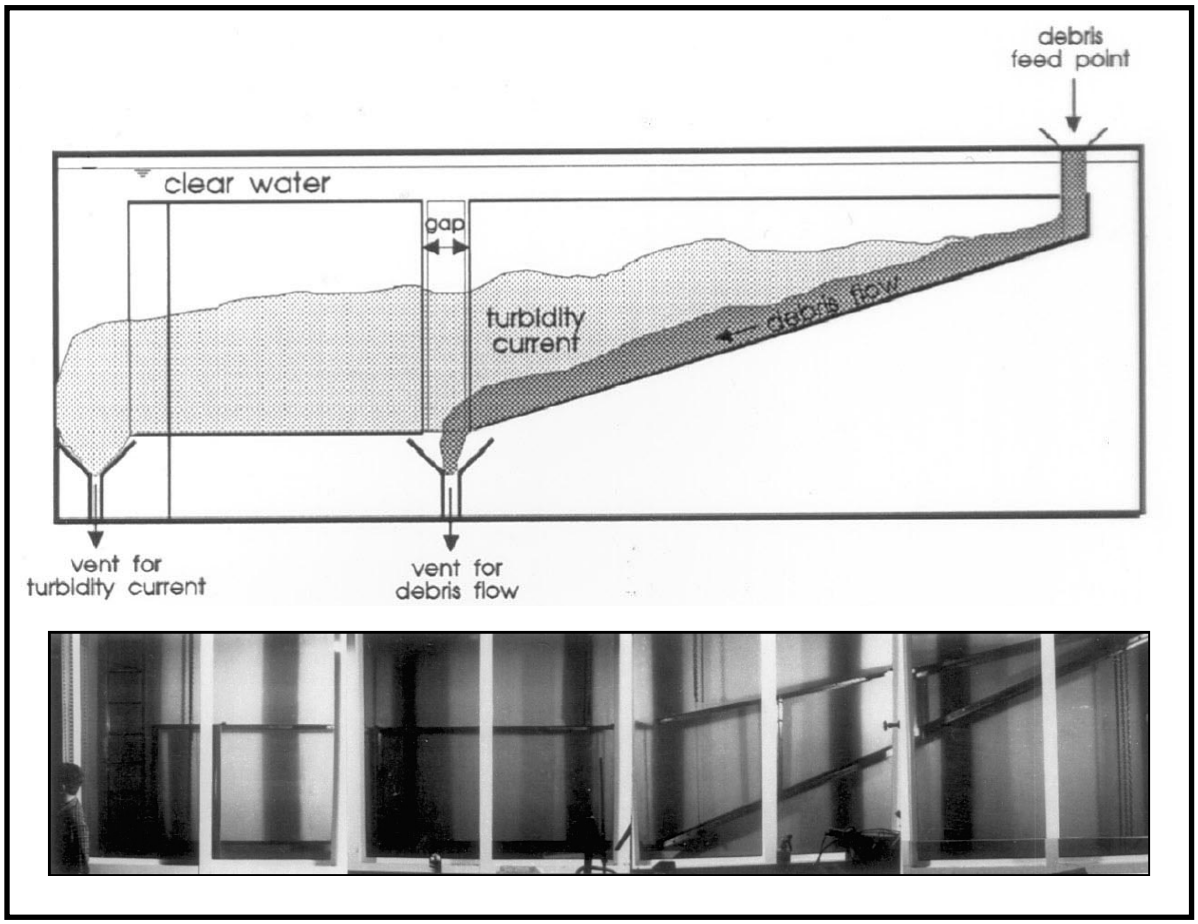

Figure 2.21: Illustration of the experimental facility (after Mohrig et al., 1998, 1999)

The suspended channel was articulated so that a slope break and/or gap in its bed may be introduced about 6 m down-dip from the channel head. It should be noted that each channel segment can be adjusted to tilt between 0^0 and 20^0.

The flow material (slurry) was continuously mixed in a head tank and fed into the channel through a debris feed point as shown in Figure 2.21. It is important to note that the slurry was not compacted or densified, and no time was allowed for consolidation. It was prepared by incrementally adding approximately 5 kg batches of sediment to a tumbling mixture in a portable concrete mixer. A complete mixing was reported to last approximately 30 min, starting with finest grain size and adding coarser material progressively.

The volume discharge of slurry into the channel was measured by either a load cell or a sonic profiler recording depending on either weight or volume change through time respectively. Multiple video cameras were used to capture the motion of the debris flow. These cameras were arranged accordingly to capture the velocity of the debris flow as well as the flow depths.

The first series of tests carried out by Mohrig et al. (1998) reported that the debris flows were released into the channel, where the bottom of the channel consisted of a rough, non-erodible rubber matting, named “hard” bottom. The second series of tests which was reported in Mohrig et al. (1999), were performed with two different conditions for the bottom of the channel, namely a hard bottom and a soft bottom.

The soft bottom, which consisted of an antecedent debris flow material, formed at the bottom of the channel in the tank by feeding the material down the channel through the debris feed point when the tank was dry. The tank was then filled with fresh water slowly so as to prevent disturbance of the base at the bottom of the channel. A water-soluble dye was added to the soil representing the slide debris to distinguish the slide material from the existing antecedent debris flow material at the bottom of the channel.

2.8.1.1.2 Materials used

A single mixture of slurry was used throughout the series of tests. It was reported that the mixture had a bulk density of 2.08 (±0.03) x 10^3 kg/m^3 and 1.60 (±0.03) x 10^3 kg/m^3 for the experiments in 1998 and 1999, respectively. The mixture in 1998 consisted of 55% silt and 45% sand, in which no clay was used. For the experiments in 1999, a mixture of 40% clay, 35% silt and 25% sand was used. It should be noted that the percentage of materials was based on weight. The water content of the mixtures was 16.5% and 39% for experiments in 1998 and 1999, respectively. The detail mineralogy of materials used was not reported in either experiments; however, the clay used in the 1999 experiment was reported as Kaolin clay with a median size of 1-3 μm.

Hydraulic permeability (k) for the soils tested were estimated by Mohrig et al. (1998, 1999) using an empirical method in which k was a function of both median grain size and particle sorting. k was estimated to be 3 x 10^{-5} m/s for the slurry in the 1998 experiments, whereas k was estimated to be 1 x 10^{-4} m/s for the slurry in the 1999 experiments.

As mentioned in the previous section, the rheological properties are important as they describe flow behaviour and hence the two main parameters used to describe the rheology are yield strength τ_y and viscosity μ_s. Mohrig et al. (1998, 1999) estimated τ_y and μ_s by means of experiments on slurry flow in half-pipe channels, of which details are given in Mohrig et al. (1999). The values for τ_y and μ_s were 29 Pa and 13 Pa.s respectively for the experiments in 1998. It should be noted that the dye used in the 1999 experiments affected the consistency of the slurry, hence resulting in three consistencies of slurry. Mohrig et al. (1999) described them as “sticky” for dye-free slurry, “runny” for the least amount of dye and “more runny” for the larger amount of dye used. The values of τ_y were 49 Pa, 36 Pa and 33 Pa for slurry of “sticky” “runny” and “more runny”, respectively. Consecutively the values of μ_s were

0.035 Pa.s, 0.023 Pa.s and 0.019 Pa.s for slurry of “sticky” “runny” and “more runny”, respectively.

All experiments were conducted using fresh water rather than sea water. It was reported that the difference between the two could have a possible effect on clay rheology, particularly for the case of active clays. However, the clay used in the 1999 experiments was Kaolin, which is known as a relatively inactive clay.

2.8.1.1.3 Observations and findings

The key observation in a number of tests performed by Mohrig et al. (1998, 1999) was that a thin layer of fluid was observed as being entrapped between the sliding soil mass and underlying surface. This served as evidence of hydroplaning, which increases the mobility of the flow. The majority of the experiments showed hydroplaning; however, there were a few exceptions.

Figure 2.22 shows the flows from the experiments in 1998. Figure 2.22A shows the subaerial debris flow, B shows the subaqueous debris flow overlying suspended sediment cloud and demonstrates the behaviour prior to hydroplaning, while C shows the hydroplaning of the subaqueous debris flow. The horizontal distances in A, B and C were reported as 61, 50, and 68 cm, respectively.

Mohrig et al. (1998, 1999) observed several characteristics of hydroplaning. The hydroplaning of a debris flow is caused by hydrodynamic pressures deforming its wetted perimeter from the stagnation point, which “s” is marked on each front down to the bed, as shown in Figure 2.23. A layer of water penetrates underneath the debris as a result of the deformation. Mohrig et al. (1998) found that the fluid with lower viscosity is easily sheared and is associated with a dramatic reduction in the bed-resistance force acting on that section of the debris flow, which is detached by a layer of fluid thick enough to submerse roughness elements on the bed. As mentioned in Mohrig et al.

(1998), the shape in Figure 2.23 (a) is shared by all non-hydroplaning flows, (b) shows the front at the very onset of hydroplaning and (c) shows the hydroplaning front with a necking in the flow behind the head.

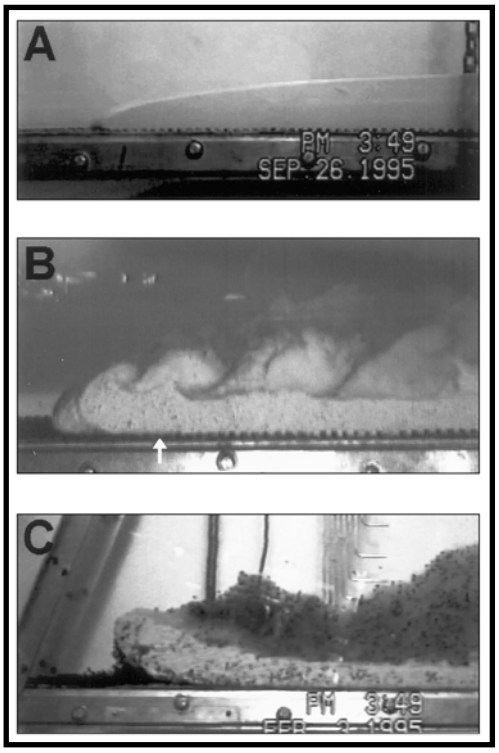

Figure 2.22: Fronts of laboratory debris flows (after Mohrig et al., 1998)

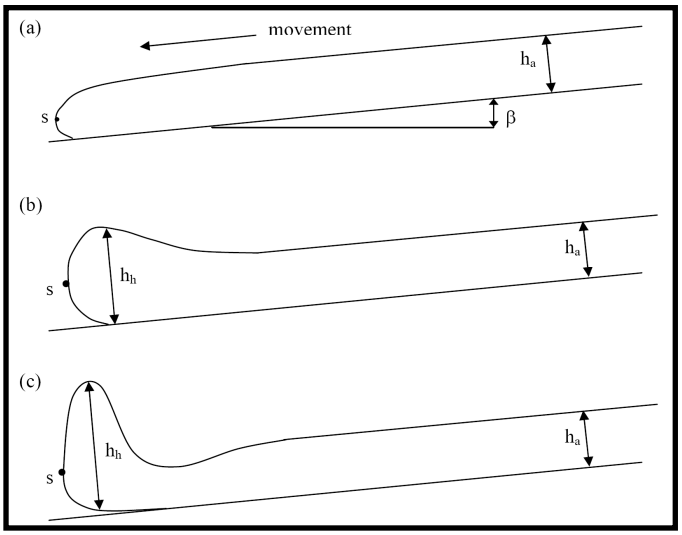

Figure 2.23: Schematic profiles of the fronts of observed debris flows (after Mohrig et al., 1998)

It was observed that the thickness of the debris flow head, h_h could be as much as three times as great as the average flow height h_a. The maximum distance underneath the hydroplaning debris flow is about 10 times h_a. It is interesting to note that the consequence of hydroplaning is the increase front velocities relative to those non-hydroplaning debris flows. It was also found that the velocity of the hydroplaning front was greater than the velocity that was supplied to the channel. This resulted in the head of the flow detaching from the body, which suggested the idea of forerunning blocks.

In the 1999 experiments, the front velocity of the flow against the distance downslope for the "soft" and "hard" bottom and different consistencies is shown in Figure 2.24. It can be seen that the front velocity of "hard" bottom flows are generally greater than the "soft" bottom in the early stage of flows; however, they become similar at the later stage of the flow regardless of their slurry consistency. It was hypothesised that a thin layer of water was entrapped due to hydroplaning, which resulted in similar velocity profiles on different conditions of the channel bottom. Therefore hydroplaning was regarded as a mechanism independent of rheology.

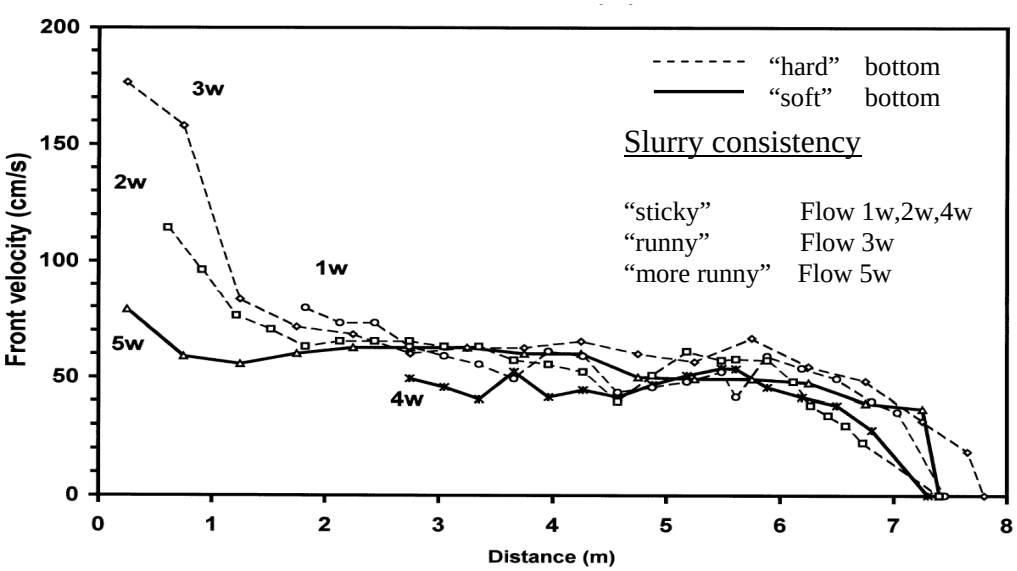

Figure 2.24: Front velocity 'vs' distance downslope (modified after Mohrig et al., 1999)

2.8.1.2 Ilstad et al. (2004a, b) experimental works

The experiments carried out by Ilstad et al. (2004a,b) were primarily to investigate the behaviour within the subaqueous flow and the effects of varying the clay-sand mass ratio of the slurry at a fixed water content, as well as to investigate the changes in pressure during subaqueous debris flows. The work was carried out as part of the PhD study of Ilstad (2005).

2.8.1.2.1 Experimental setup

The experiments were carried out in a channel 0.2 m wide and 9.5 m long suspended inside a larger glass-walled tank. The glass-walled tank was 10 m long, 3 m high and 0.6 m wide. The slope for the channel was set to be 6^0; a granular bed was placed along the channel with the roughness of 1mm to prevent undesired slip.

Measurements of both pore water pressure and total bed normal stress were performed simultaneously at the base of the channel to quantify the conditions during flow. Pore pressure transducers (PPT) and stress cells were placed in two cross-sections along the flow channel, 3.5 and 7.6 m from the head gate.

It should be noted that the experiments were recorded with two video cameras at the locations with PPTs and stress cells, while a high speed video camera was mounted on a rail. It was reported that the high speed video camera was able to film at a speed of 250 frames per second at a resolution of 480 x 512 pixels.

The experimental setup and instrumentation is shown in Figure 2.25.

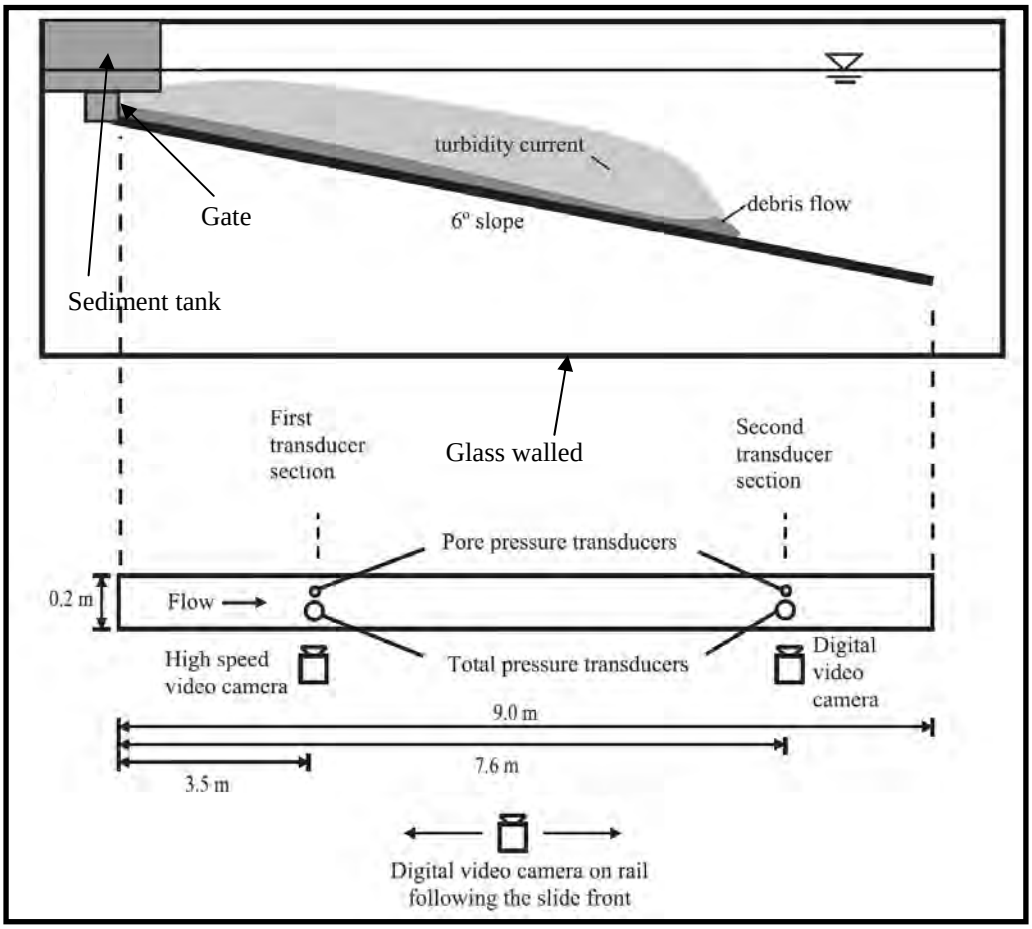

Figure 2.25: Illustration of the experimental setup (modified after Ilstad et al. 2004a, b)

The glass-walled water tank was filled with water to about 0.5 m above the gate, at the beginning of the experiment. Then 0.16 m^3 of slurry was added into the sediment tank. The slurry was released into the channel through a gate 5.3 cm high and 15 cm wide. Data acquisition started at the moment the gate opened. It was reported that all pressure signals were measured simultaneously at a rate of 500 Hz during the flow event. The high speed videos were used for particle tracking of soil grains, thus describing the flow behaviour. During the flow, measurements of pore water pressure and total stress were made using the pre-located PPTs and stress cells. The experiments were performed with slurries of various clay/sand compositions.

2.8.1.2.2 Materials used

The materials used to form the slurries were kaolin clay (snowbrite) and fine brown silica sand. The kaolin clay used had a specific density of 2.75 g/cm^3, while the fine brown silica sand had a specific density of 2.65 g/cm^3 and a median grain size of 330 μm. As stated in Ilstad et al. (2004a), a siliceous material produced as a residue from burning coal named "coal slag" was used in a small amount for the purpose of flow visualisation. The material was reported to be black in colour, which had a median grain size of 500 mm, and a specific density of 2.6 g/cm^3.

Eight slurries were prepared, all of which had the same solid content of 65% corresponding to 35% of water. It should be noted that the slurries used in the experiments were characterised by the weight of total mass. The coal slag used was less than 1% of the total weight of the slurry in each test. Table 2.3 shows the material compositions for each experiment.

The slurries were mixed using a tumbling concrete mixer, where water was loaded at the beginning followed by clay and sand. The mixing took about 1 hour to produce a homogeneous mixture. After mixing was completed, the slurry was then loaded to the sediment tank. Slurry with low clay content tended to settle; therefore, continuous stirring in the sediment tank was carried out until seconds before releasing the slurry into the channel.

Table 2.3: Slurry compositions in percentage of weight of total mass (after Ilstad et al., 2004a, b)

Exp. No.	Water (%)	Clay (kaolin) (%)	Sand (330mm) (%)	Density (kg/m^3)	Measure water content (%)
1	35	5	60	1680	37.3
2	35	10	55	1690	39.1
3	35	15	50	1690	35.3
4	35	20	45	1690	36.0
5	35	20	45	1690	35.8
6	35	25	40	1690	35.6
7	35	28.7	36.7	1690	35.1
8	35	32.5	32.5	1690	35.2

2.8.1.2.3 Observations and findings

Through the series of tests carried out by Ilstad et al. (2004a, b), a number of key observations and findings were found. One of the main findings was the hydroplaning front occurring in clay rich flows (high clay/sand ratio), as shown in Figure 2.26 A, while a turbulent front was observed for sand rich flows (low clay/sand ratio) as shown in Figure 2.26 B. They stated that hydroplaning started with the front lifting off the bed and a thin water layer penetrating underneath (Figure 2.26 A). Hydroplaning effectively reduced bed friction and significantly increased debris flow mobility. At the rear part of the hydroplaning layer, they discovered that a small amount of sediment was incorporated into the water layer in which the basal layer transformed into a mud layer, as shown in Figure 2.27. It was observed that the subaqueous debris flow sediments at the basal layer were eroded from below and mixed into the basal layer, which increased the viscosity and yield stress due to the incorporation of clay in the basal layer.

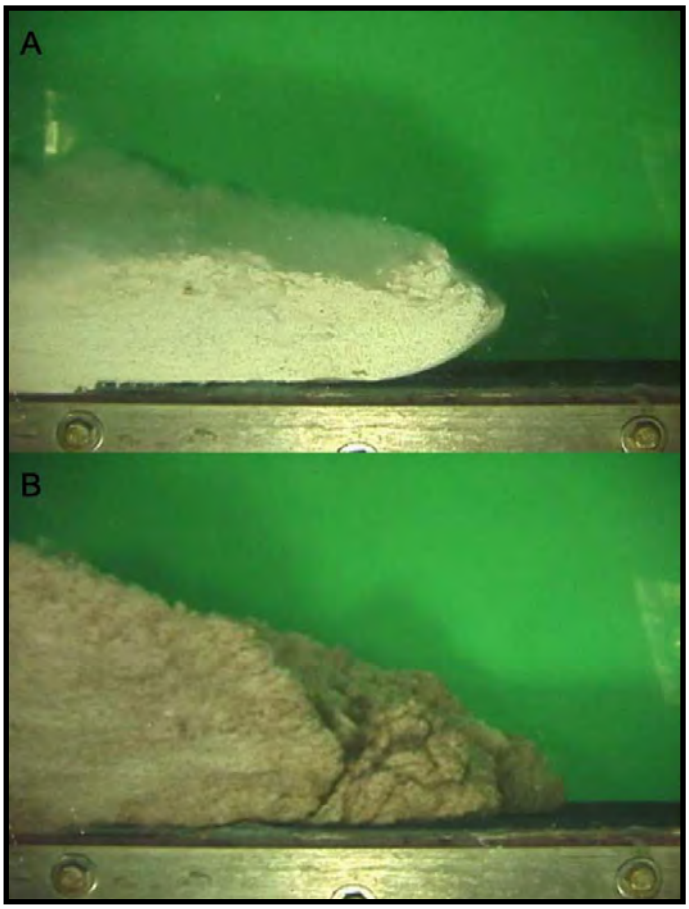

Figure 2.26: Fronts of laboratory subaqueous debris flows (after Ilstad et al. 2004a, b)

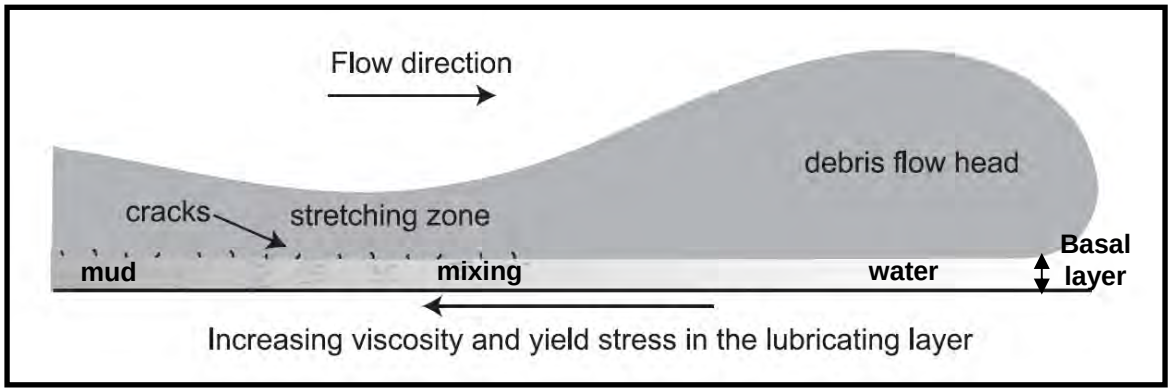

Figure 2.27: Materials from the base of the debris flow are eroded and incorporated into basal layer (after Ilstad et al. 2004b)

Figure 2.28 shows the pressure measurements at the base of a clay-rich subaqueous debris flow (28.7% clay). It can be seen that both the pore pressure and the total stress underneath the subaqueous debris flow show similar readings at the hydroplaning front; this indicates that a thin water layer

penetrates the bottom of the front flow. Towards the end of the flow, the total stress rises with a slight increase in pore pressure. This indicates an increase in the basal friction since the flow matrix is carrying parts of the debris flow weight.

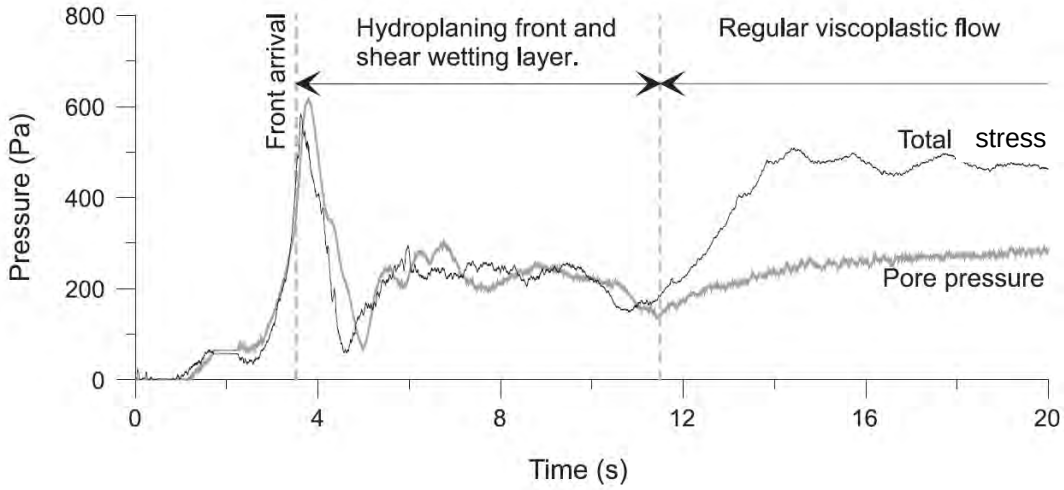

Figure 2.28: Pressure measurements at the base of a clay rich flow (modified after Ilstad et al. 2004b)

Ilstad et al. (2004a, b) proposed three main pressure patterns found in the experiments. Figure 2.29 shows the schematic overview of the three main pressure patterns. The upper panel indicates a flow with constant frictional contact with the bed, where the grains are in constant contact with the bed as they move. The middle panel represents a flow where the layer is liquefied or fluidised, in which grains may collide with the bed but will remain in suspension; therefore a fluctuating pressure can be seen. The third pattern shows a rigid block riding upon a layer of water where the total stress and pore pressure are approximately equal. This pattern particularly refers to hydroplaning.

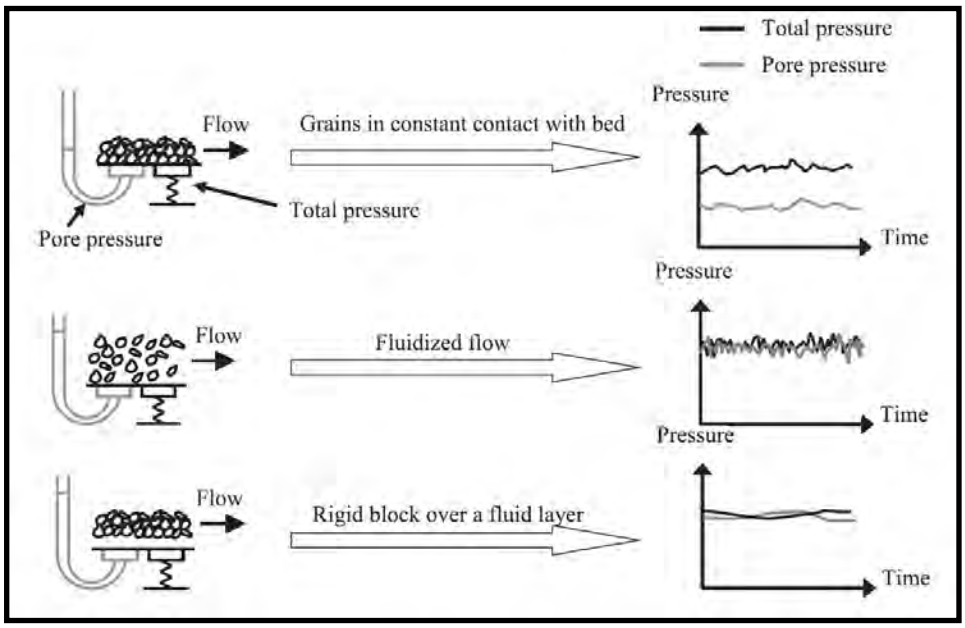

Figure 2.29: Schematic overview of the three main pressure patterns (after Ilstad et al. 2004a)

According to Ilstad et al. (2004b), the front speeds of the subaqueous debris flows were measured based on video recordings. Figure 2.30 shows the trendlines of the front speed along the channel for various slurry compositions. The highest clay-rich flow (32.5 % clay) moved with the lowest velocities of 77 cm/s in the upper part of the slope, decreasing to 68 cm/s towards the end. It can be seen that a decreasing front speed for clay-rich flows, while an almost uniform front speed, was observed for sand rich flows. It was surprising that the flow with high clay content show low flow velocity and hydroplaned.

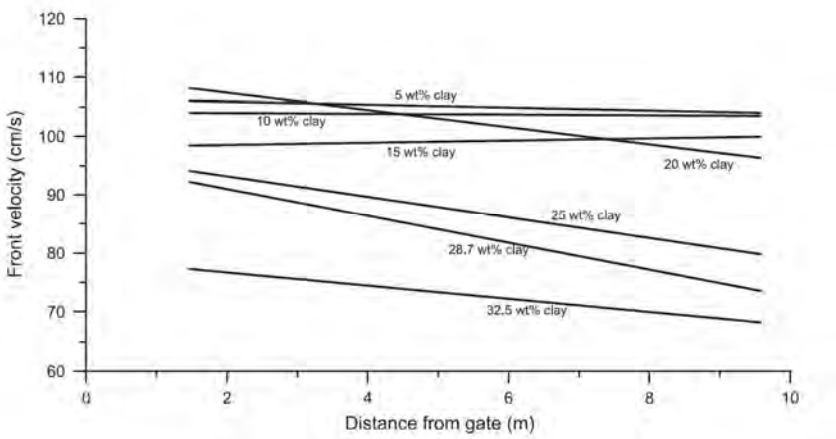

Figure 2.30: Trendlines of the front velocity along the channel for various slurry compositions (after Ilstad et al. 2004b)

2.8.2 Overview of other submarine slope experimental works in 1 g

Schwarz (1982) carried out a series of tests on sedimentation and dealt with the slide processes. Three sedimentation methods have been used as stated in Table 2.2. Tilt experiments were conducted after the end of primary consolidation by tilting of one tank section up to the critical inclination where the slope fails; the second method with sedimentation on the inclined bottom with various sedimentation rates without initiating a failure; and the third method with sedimentation on the flat bottom with an escarpment block forming a steep angle.

Observations were made on the internal organisation of slide structures and time sequences as well as the transformation of various deformational structures. Five deformation stages were proposed based on the observations from the experiments, while a structural transformation model of gravitational subaqueous slope failure was also proposed. The model gave the relationship between deformational energy and degree of deformation. Table 2.2 shows the general information of the tests; further detailed information is given in Schwarz (1982).

Marr et al. (2001) investigated the role of clay and water content in subaqueous flow dynamics. Mixtures with varying water and clay contents were prepared and released from a head tank in which the head velocity and runout distance were recorded. The main findings from the series of experiments showed that features of subaqueous gravity flow deposits were directly related to flow coherence. They found that strongly coherent flows commonly hydroplaned and flowed in a laminar regime, while moderately and weakly coherent flows showed an increasing amount of breakup and suspension of the head flow, which produced turbidity currents. It should be noted that no pore pressure and stress measurements were made throughout the series of tests. The general information of the tests is shown in Table 2.2

Another series of tests performed by Mohrig and Marr (2003) investigated the turbidity current generation from submarine debris flow, with the aid of acoustical imaging. Measurements of acoustic reflectance collected with a reversible ultrasonic transducer were used to generate images constraining the extent to which ambient water was turbulently mixed into the heads of some submarine debris flows. According to Mohrig and Marr (2003), such an imaging technique was necessary because sediment concentration in the diluted portions of these flows was so high that it could not be distinguished from unmodified parent material by visual inspection alone. This acoustical imaging showed that any production of turbulence within the parent material was focused at their flow heads. They have also proposed a framework for quantifying the erosion rate of sediment from the head of the submarine debris flows. Table 2.2 shows the general information of the tests.

Vendeville and Gaullier (2003) investigated the role of pore fluid pressure and slope angle on triggering submarine mass movements using a basic experimental setup. Experiments were done by tilting the slope and progressively increasing the fluid pressure. Compressed air was used as fluid in a scenario and water in the other scenario. The results in their experiments indicated that an increase in fluid pressure could effectively trigger instantaneous gliding of sediment strata downslope. It was also observed that, during a failure, gliding of the slope deformed as a coherent slab. The general information of the tests is shown in Table 2.2

Part of the PhD work of Ilstad (2005) investigated the frontal dynamics and morphology of submarine debris flows, as published in Ilstad et al. (2004c). The procedures of the experiments were similar to those in Ilstad et al. (2004a, b); however, particular focus was placed at the front of the flows where videos were captured in plan view. Interestingly, they found that the hydroplaning front of the flow progressively detached from the main flow forming an outrunner block. Upward flipping of the front of outrunner blocks were observed during flow. Ilstad et al. (2004c) recognised that the frontal part of a submarine debris flow can affect the dynamics of the whole body. They also concluded that, due to hydroplaning, tensile stresses led to the formation

of outrunner blocks, and the dimensions of the outrunner blocks were related to the material strength. Table 2.2 shows the general information of the tests.

2.8.3 Past experimental works in centrifuge

Soil stresses are related to self-weight, therefore centrifuges are often used for studying various geotechnical engineering problems. Information on centrifuges is further discussed in Chapter III. It should be noted that there are only very limited experiments on submarine slopes using centrifuge testing. One of the earliest experiments on submarine slopes using a centrifuge was discussed in Phillips and Byrne (1994).

Phillips and Byrne (1994) carried out centrifuge tests to model slope liquefaction due to static loading. The main intentions of the tests were to aid in the design of field events as well as to serve as a numerical model's calibration. A saturated sand model slope was formed at 16^0, with PPTs (Pore Pressure Transducers) placed within the model. A surcharge was dropped on the crest of the submerged slope causing the slope to liquefy and flow with deep-seated lateral movements. In the tests, the slope was subjected to two loading sequences. One started with a static bearing pressure and the centrifuge was accelerated up to 50 g in stages, while in another loading sequence the surcharge was dropped at a fixed drop height after the centrifuge achieved 50g in stages. They found that a static liquefaction event could be induced in a centrifuge test, where the results indicated that liquefaction occurred as confirmed in both video recordings as well as pore pressure measurements. Table 2.4 shows the general information of the tests.

Zhou et al. (2002) investigated the stability of underwater slopes through a series of centrifuge tests. The main objective of the tests was to obtain the critical slope angle for an underwater slope of silty sand and fine sand. The tests were carried out in such a way that the slope angle was increased or decreased gradually after each test in order to obtain the critical slope angle. Although the tests were carried out at different g-levels, the study

was not made on the influence of g-levels. Some of the general information of the tests is listed in table 2.4.

One of the recent experiments on submarine slopes using a centrifuge was carried by Coulter (2005), where seismic initiation of submarine slope failures was modelled. The objective of the study was to examine the dynamic response of submarine slopes exposed to earthquake loadings. The slope was instrumented with PPTs, LVDTs, miniature accelerometers, a laser sensor and a triaxial accelerometer.

Three different slope profiles were tested at the targeted g-levels. The targeted g-level for this experiment was 70 g at a depth of two-thirds the model slope height. The submerged slope was then exposed to three different earthquake, based on acceleration time histories. A substitute pore fluid (Hydroxypropyl methycellulose – HPMC) was used to saturate the model in order to satisfy the scaling differences between static and dynamic events in the centrifuge. According to Coulter (2005), this particular fluid was selected because of its similarity to water in unit weight, surface tension, Newtonian behaviour and the ability to mix into a wide range of viscosities.

Through the series of tests, Coulter (2005) found that excess pore pressure and subsequent liquefaction occurred first in downslope areas and progressed upslope. The generation of excess pore pressure increased with the increase in earthquake magnitude. Both horizontal and vertical movements of the slope were detected after the earthquakes. It was observed that a small amount of short-term surface heave was found on the slopes that failed. Liquefaction was found to occur more readily in larger earthquake motions both at deeper locations in the model as well as at drainage boundaries. It was interesting to note that the slope experienced densification and seismic strengthening with exposure to a series of smaller seismic motions; this conclusion was supported with surface settlement data as well as the decrease in excess pore pressure generation that was caused in each successive smaller earthquakes. The general information of the test is summarised in Table 2.4

More recently, Boylan et al. (2010) developed a centrifuge model capable of modelling submarine slides using a drum centrifuge. They focused on the initiation of submarine slides, in which they developed a slide triggering device for use in the drum centrifuge. The submarine slide was modelled on a flat seabed (Kaolin clay) which was consolidated in the channel of the drum centrifuge prior to the consolidation of the slide material in the slide triggering device. The slide material (presumably Kaolin clay) was partially consolidated at 100 g from slurry with a water content of 120%. The slide could then be triggered remotely in the drum centrifuge control room. The post-slide characterisation could be characterised using a miniature T-bar penetrometer and samples of the slide runout were taken for moisture content testing. There was no predetermined slope for the slide to runout but the slope was then back calculated based on the runout thickness at the toe of the runout and the thickness close to the triggering device. They found that examination of the properties of the runout material could provide an insight into the previous history of mass movement of the seabed (i.e. the moisture content of the post-slide material was lower than the original slide material). The general information of the test is summarised in Table 2.4

Table 2.4: Summary of submarine slope experimental works in centrifuges

Reference	Type of Experiment	Geometry			Materials and soil properties		Methodology	'g' Levels	Key Findings	Comments
		Slope angle	Slope Length	Slope Width	Soil Type	Soil Properties				
Phillips and Byrne (1994)	Modelling of slope liquefaction due to static loading	16°	0.94 m	0.4 m	Oil sand tailings	G_s = 2.64 e_{max} = 0.96 e_{min} = 0.53 d_{50} = 0.17mm d_{10}=0.092mm WC = 7-9% k = 1.6e-05m/s	Surcharge dropped on the crest of the slope, measurement of pore pressure with PPTs	50	Static liquefaction could be induced in a centrifuge test	Tests were carried out only in a certain g level which did not investigate the influence of g levels
Zhou et al. (2002)	To estimate the stability of underwater slope	26° – 57°	0.41m	0.3 m	Fine sand and silty sand	$\gamma_{fine\ sand}$ = 15.8-18.2kN/m^3 e = 0.8 - 0.9 c = 3.5 - 4.9 ϕ = 25.5 - 30.6 WC = 23-26.4% $\gamma_{silty\ sand}$ = 19.7kN/m^3 e = 0.54 - 0.67 ϕ = 22.5 - 29.4 WC = 16.8-22.3%	Test at different slope angles to obtain the critical slope angle	5, 60, 140, 150, 190	The critical slope angle of silty sand is steeper than fine sand, height of underwater slope has no influence on critical slope angle	Did not compare the same slope angle at different g levels
Coulter and Phillips (2003) / Coulter (2005)	Modelling of seismic initiation of submarine slope failures	26°	0.74 m	0.3 m	Fraser River sand and US fine ground silica Sil-Co-Sil 52	γ_{sand} = 1.4-1.67 g/cm^3 G_s = 2.71 e = 0.62 - 0.94 d_{50} = 0.26 mm	Three different slope profiles submerged with fluid and subjected to three different earthquakes	70	Liquefaction occurred first in downslope areas and progressed upslope, densification and seismic strengthening on smaller seismic motion	Tests were carried out only in a certain g level which did not investigate the influence of g levels
Boylan et al. (2010)	Modelling of initiation of submarine slides	N/A	N/A	N/A	Kaolin clay	γ' = 5kN/m^3 WC = 120%	Consolidate slide material from slurry and initiate the slide with a triggering device into a consolidated flat seabed	100	Examination of the properties of the runout material can provide insight into previous history of mass movement of the seabed	Tests were not carried out in a slope but on a flat seabed. Only tested in a certain g level and did not investigate the influence of g levels

2.9 Constraints of Past Experimental Works in Submarine Slopes

Through the available literature, it can be seen that there are more submarine slope experiments in 1 g test environments than centrifuge experiments. From this, it can be interpreted that 1 g laboratory tests are generally easier and cheaper to conduct. However, as mentioned previously, actual submarine slides are very large; as a small-scale model in a 1g test environment is relatively small, hence the soil stresses in such conditions are also very small. Soil stresses are gravity-dependent in which small-scale 1 g laboratory tests do not necessarily show the true soil behaviour and may not represent the real situation. It is therefore questionable as to whether the findings from 1 g test environments are representative of actual submarine landslides.

Table 2.5 summarises various aspects of submarine slope experiments in both a 1 g test environment and centrifuge tests. It should be noted that flows, sliding mechanism and sedimentation are the important aspects in submarine landslides.

Table 2.5: Summary of various submarine slope experimental works

Type of test	1 g test	Centrifuge test
Flow	✓	✗
Sliding	✓	✓
Sedimentation	✓	✗
Initiation of failure	✓	✓

Clearly, it can be seen that there are only very limited experiments on submarine slopes through centrifuge modelling, in particular the influence of different g levels towards the flow and the scaling laws for submarine

landslide flows. Also, the slope angles from the centrifuge experimental works available in the literature are generally larger than the 1 g experimental works. No doubt, that there is an urgent need to study submarine landslides through centrifuge modelling. Through centrifuge modelling, self-weight stresses and gravity-dependent processes are able to be correctly reproduced, and observations from small-scale models can be related to full-scale prototype situations using appropriate scaling laws. This will be further discussed in Chapter III.

2.10 Summary

An understanding of submarine landslide features and characteristics, mechanics, and their importance and significance, as well as the lack of knowledge in the particular area, have inspired the current study on submarine landslides, particularly focusing on submarine landslide flows through centrifuge modelling and developing the centrifuge scaling laws for submarine landslide flows.

As can be seen from the submarine landslides work by centrifuge modelling, the effects of different g levels and whether the results would scale at different g levels were not considered. It should be noted that this PhD study is considered as the pilot study for centrifuge modelling of submarine landslide flows and to develop the appropriate centrifuge scaling laws for submarine landslide flows.

Prior to this date, there have been no well-established centrifuge scaling laws for submarine landslide flows. It is therefore the main objective of this study to develop the centrifuge scaling laws for submarine landslide flows. Since this is a pilot study, this study also explores the reliability of using centrifuge modelling to study such phenomena. Chapter III discusses the concept of centrifuge modelling and proposes the scaling laws for submarine landslide flows.

CHAPTER III

3.0 CENTRIFUGE MODELLING

3.1 Introduction

The principle of centrifuge modelling is to reproduce the behaviour of a prototype in a small-scale model subjected to centrifugal acceleration of magnitude many times the earth's gravity. With this technique, self-weight stresses and gravity-dependent processes can be correctly reproduced, while observations from small-scale models can be related to the full-scale prototype situation using well-established scaling laws (Taylor, 1995).

This chapter summarises the use of centrifuges in geotechnical engineering, centrifuge scaling laws, restrictions and limitations, and introduces the mini-drum centrifuge at the Schofield Centre (The Centre for Geotechnical Process and Construction Modelling), University of Cambridge. This chapter also proposes and discusses the centrifuge scaling laws for submarine landslide flows derived through analytical solutions.

3.2 Principles of Centrifuge Modelling

Almost every scenario in geotechnical engineering is concerned with soil self-weight and stresses in which gravity effects are the significant contributing factors to soil self-weight and stresses. In order to study the soil properties related to geotechnical engineering, scaled-down models are frequently used in the laboratory to study the actual prototype's behaviour.

It is important to note that the stress-strain behaviour of soils is well known to be non-linear. Therefore, the behaviour of a small-scale model may not represent the behaviour to its prototype if the stress-strain behaviour is not

properly modelled, as shown in Figure 3.1. The scaled-down model exerts only a small fraction of stress compared to the stresses exerted by the 'N' times larger prototype.

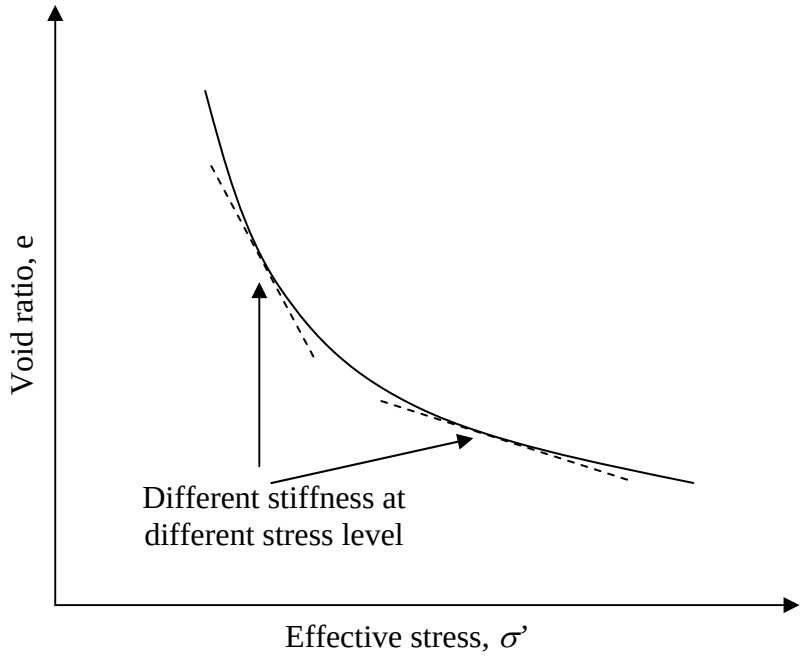

Figure 3.1: Different soil behaviour at different stress level

A centrifuge is able to provide the N times gravity environment. When a centrifuge is rotating with an angular velocity of 'ω', the centrifugal acceleration at any radius 'r' is given by:

$$\text{Centrifugal acceleration} = r \times \omega^2 \qquad (3.1)$$

In order to match this centrifugal acceleration to be the same as the prototype, therefore:

$$N \times g = r \times \omega^2 \qquad (3.2)$$

With this method, self-weight stresses and gravity-dependent processes can be reproduced. Currently, the two widely accepted basic principles for centrifuge modelling as mentioned in Schofield (1988), are:

1) The increase of self-weight by increase of acceleration is equal to the reduction of model scale.
2) The reduction of time for model tests as the scale is reduced.

The observations from small-scale models can therefore be related to the full-scale prototype using the appropriate scaling laws.

3.3 Centrifuge Scaling Laws

As mentioned above, stress similarity between model and prototype is needed, which leads to the derivation of scaling laws. Taking into consideration the different types of scaling laws in centrifuge modelling, it is essential to recognise the following three fundamentals as proposed by Fulgsang and Ovesen (1988):

- All significant influences should be modelled in similarity
- All effects not modelled in similarity should be proven secondary by experimental evidence, and
- Any unknown effect should be revealed or proven insignificant by means of the test results.

3.3.1 General scaling laws

As summarised in Barker (1998), the scaling laws for centrifuge modelling can be briefly described as follows:

a) If a soil with identical material properties is formed into geometrically similar bodies, one a full-size prototype and the other a model at scale 1/N (in dimension), and if the model has its self-weight increased by a factor of N times by being subjected to the centrifugal acceleration in a centrifuge, then the initial stress at corresponding points in the model and the prototype will be the same, provided the boundary conditions for each are also similar.

b) If the stress increment is uniquely determined by the strain increment [$\delta\sigma = f(\Delta\varepsilon)$], the strain field of the model will be the same as that of the prototype. This leads to the scaling law for displacement being: displacement (model) = (1/N) displacement (prototype). Hence, the scaling law for length remains the same.

c) If the excess pore pressure distributions within the model and the prototype are similar, then all subsequent primary pore water flows and consolidation will be modelled at times N^2 faster than in the prototype if the same pore fluid is used.

A summary of basic centrifuge modelling scaling laws is shown in Table 3.1, while Figure 3.2 shows the basic principle of scaling laws in a centrifuge.

Table 3.1: Summary of basic centrifuge modelling scaling laws (after Barker, 1998)

PARAMETER	**PROTOTYPE**	**MODEL SCALING (basic)**	**MODEL SCALING (this study)**
Acceleration of Gravity	1	N	N
Length	L	L / N	L / N
Legth (Flow distance)	L	L / N	L / N^3
Area	A	A / N^2	A / N^2
Volume	Vol	Vol / N^3	Vol / N^3
Stress	σ	σ	σ
Strain	ε	ε	ε
Displacement	δL	δL / N	δL / N
Pore Pressure	u	u	u
Hydraulic Gradient	i	Ni	Ni
Time (Seepage/Consolidation)	t	t / N^2	t / N^2
Flow velocity	v	N	v / N

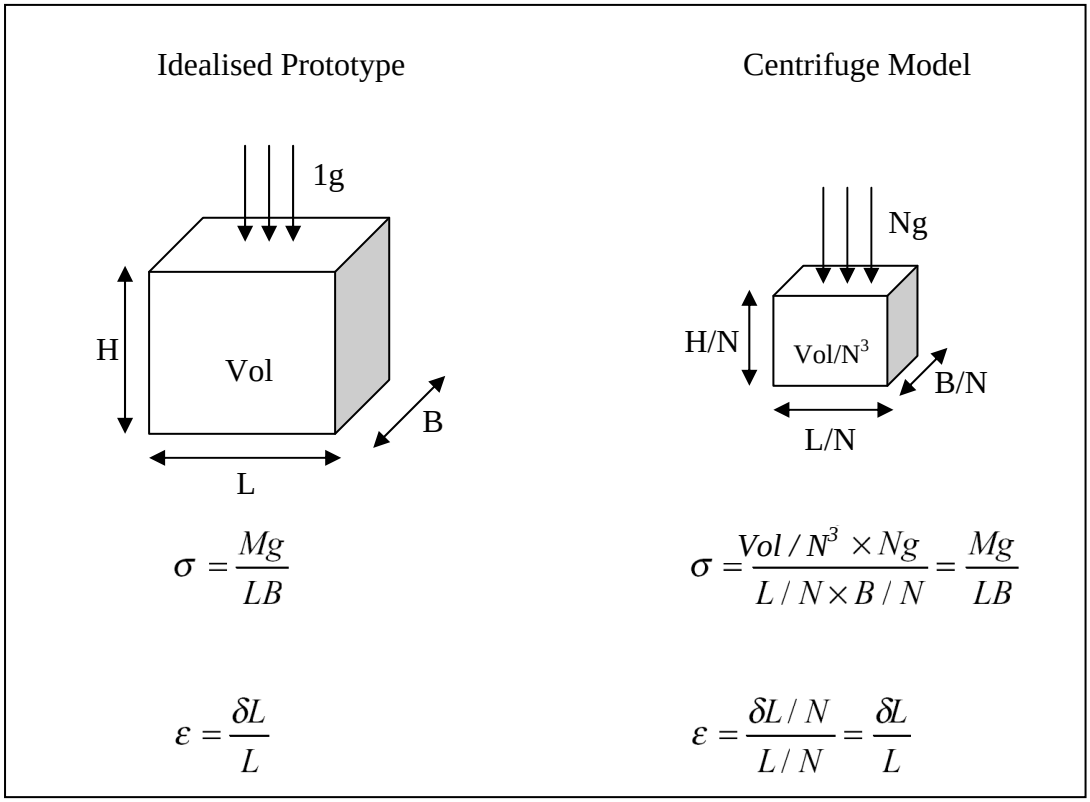

Figure 3.2: Basic principle of scaling laws

3.3.2 Development of Scaling laws for soil flow through analytical solutions

The conventional scaling law for displacement δL (and hence Length, L) comes from the fact that stress increment (i.e. satisfying the stress equilibrium condition) of a body is related to strain increment through a given stress-strain relationship of the tested soil (see Point b in Section 3.3.1). If strains in both the prototype and model are the same, then the flow distance is scaled at a given location in both the prototype and model are the same, then the ground movement is scaled at N times ($L_{prototype} = NL_{model}$) as the conventional scaling law for length. That is, the scaling law for length originates from the fact that stresses depend on strains.

In this study, the movement of the soil-fluid mixture is large, and the soil, particularly in contact at the base boundary, is extensively sheared. If the soil is at failure (critical state) and the effective stress state of the soil becomes independent of strain, the scaling law for length (or flow distance) is

indeterminate. However, by assuming that the shear resistance of a moving soil-fluid mixture has some viscous effect (strain rate dependent), a new scaling law can be derived as shown below. The derivation simplifies the problem by assuming that the movement of the soil perpendicular to the slope is negligible compared to that parallel to the slope (i.e. the depth average assumption). Hence, the scaling law of length in the direction parallel to the slope will be considered here.

As mentioned in Chapter II, Iverson and Denlinger (2001) developed a model which generalises depth-averaged mass and momentum balance equations that described finite masses of variably fluidised grain-fluid mixtures that move unsteadily across three-dimensional terrains, from initiation to deposition. It is assumed that the effective stress state of soil is governed by the failure criteria (i.e. strain independent), while the viscosity of the pore fluid contributes to the shear resistance. For specific cases, analytical solutions can be obtained to predict phenomena in the field as well as aiding comparison with numerical simulations.

Based on the equation (2.44) which enables the prediction of flow velocities with given material parameters and gravitational levels, the dimensionless groups for deducing variation in importance of mechanisms for submarine landslide flows can be deduced as:

$$\left[\bar{v}_x \frac{3\upsilon_f \mu}{(\rho-\rho_w) g_z \bar{h}^2}\right]_{model} = \left[\bar{v}_x \frac{3\upsilon_f \mu}{(\rho-\rho_w) g_z \bar{h}^2}\right]_{prototype} \tag{3.3}$$

$$\left[t \frac{3\upsilon_f \mu}{(\rho-\rho_w) \bar{h}^2}\right]_{model} = \left[t \frac{3\upsilon_f \mu}{(\rho-\rho_w) \bar{h}^2}\right]_{prototype} \tag{3.4}$$

Combining equations (3.3) and (3.4) gives,

$$\left(\frac{t_{model}\, g_{model}}{\bar{v}_{model}}\right) = \left(\frac{t_{prototype}\, g_{prototype}}{\bar{v}_{prototype}}\right) \tag{3.5}$$

where $\bar{v}_x$ is the average flow velocity at the x direction (i.e. parallel to the slope); ρ is the mixture density; ρ_w is the density of the surrounding fluid (i.e. water); g_z is the gravitational acceleration; $\bar{h}$ is the average flow height (thickness of flow); υ_f is the fluid volume fraction; and μ is the mixture viscosity. These dimensionless groups facilitate the developments of the centrifuge scaling laws for submarine landslide flows.

The main aim is to have the same stress field (effective stress and pore pressure) in both the model and the prototype. Therefore, the scaling law for the flow height is

$$\bar{h}_{prototype} = N\bar{h}_{model} \qquad (3.6)$$

This ensures that the stress field inside the moving soil body of the model is the same as the prototype, while the friction at the base will also be the same.

In this study, it is assumed that the soil is sheared extensively and that the effective stress state of the soil is independent of strain (i.e. critical state). It is noted that, if the stresses are a function of strains, the conventional centrifuge scaling laws would apply. However, based on the equation (2.44) and the abovementioned dimensionless groups (3.3), the scaling laws for submarine landslide flow velocity of the modelled soil-fluid mixture can be deduced as follows:

$$\bar{v}_{prototype} = N\,\bar{v}_{model} \qquad (3.7)$$

where $\bar{v}$ is the average flow velocity. In order to verify this scaling law, the scaled flow rate (Q= $\bar{v}$ x h x w, where w is the width of the channel and h x w gives the cross-sectional area of the flow) can be applied at different g levels, and this will be tested in this study.

The scaling law for time to model the transient behaviour can be obtained from the dimensionless groups (3.4) or (3.5):

$$t_{prototype} = N^2 t_{model} \qquad (3.8)$$

If the flow velocity is scaled at $\bar{v}_{\text{prototype}} = N\ \bar{v}_{\text{model}}$, the flow distance increment, dL, is flow velocity multiplied by flow time increment, dt.

$$dL_{model} = \bar{v}_{model} \text{ x } dt_{model} \qquad (3.9)$$

Using the scaling laws from (3.7) and (3.8), the scaling of equation (3.9) is:

$$N^3 dL_{model} = N\ \bar{v}_{model} \text{ x } N^2\ dt_{model} \qquad (3.10)$$

Therefore, it can be argued that the flow distance of the prototype is scaled at:

$$dL_{prototype} = N^3 dL_{model} \qquad (3.11)$$

It is intriguing to find that the flow distance of a prototype is scaled at N^3 times of the model. Based on the conventional centrifuge scaling law of soil body, the movement in the flow direction would have scaled at N times of the model.

3.3.3 Discussion of the proposed scaling laws for soil flow

The scaling law for height as in equation (3.6) (i.e. perpendicular to the slope) comes from the fact that the stress state is governed by the weight of the soil, which gives the basal and side frictions. This means that the variation in the change in height is considered to be small compared to the movement in the direction parallel to the slope and hence the depth average technique can be adopted. It is assumed that, in most submarine landslide problems, the soil

body is moving in one direction, while the movement in the direction perpendicular to the moving direction is very small or negligible compared to the movement in the parallel direction.

The scaling laws for velocity (equation 3.7) and movement for soil flow (equation 3.11) parallel to the slope come from (i) the equation of motion, (ii) the effective stress state being independent of strain (e.g. critical or residual state) and (iii) the viscous resistance of pore fluid. An important assumption to derive the proposed scaling laws is that the velocity profile within the moving soil body is the same between the model and the prototype, as shown in Figure 3.3. Based on the scaling law for flow height (3.6) and the scaling law for the averaged flow velocity (3.7), the velocity gradient (or strain rate) profiles will be the same between the prototype and the model. If the viscous effect is governing the movement of the moving mass, it will therefore give the same viscous resistance at the sliding boundary as shown in Figure 3.3.

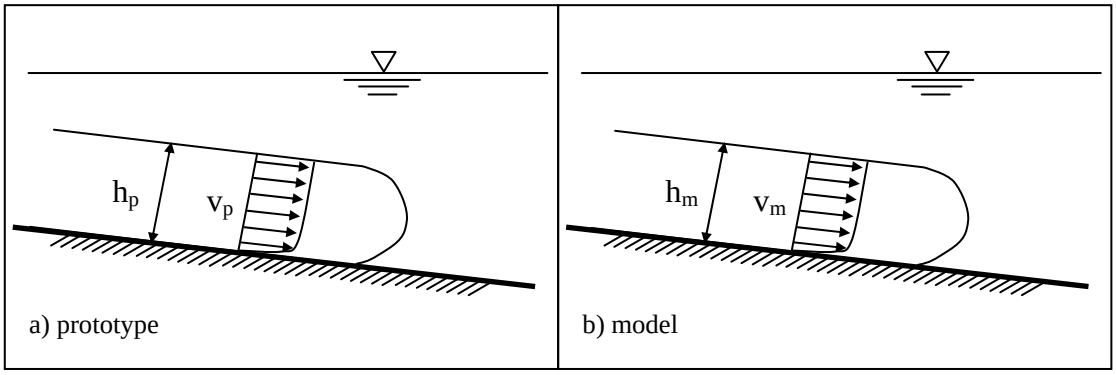

Figure 3.3: Conceptual flow profile in prototype and model

Since the proposed scaling laws for soil flow differ from the conventional scaling laws of the soil mechanics problem, this has further motivated the call for centrifuge experiments to validate the deduced scaling laws. It should be noted that, while carrying out experiments at different g levels, the various flow heights at the corresponding g levels must be scaled as in equation (3.6). Ideally, this will give the same magnitude of basal friction to resist the flow movement as well as the effective stress field in the soil skeleton to drive the soil body to move along the slope.

3.4 Restrictions and Limitations of Centrifuge Modelling

Despite the fact that the centrifuge is a very powerful tool for analysing complex problems in geotechnical engineering, there are certain restrictions and limitations. It is essential to identify and quantify these limitations in order to minimise the errors in centrifuge modelling.

3.4.1 Variations of stress and gravity field with depth

Centrifuge testing of a small-scale model in a gravity field has a strong function of distance from the centre of rotation. From, $Ng = r\omega^2$; it can be undestood that the gravity field varies with radius r. It can also be seen that the gravity field increases as the distance from the centre of rotation increases.

It should be noted that the top region of a model is typically the closest to the centre of rotation while the bottom region of the model is furthest away from the centre of rotation. This results in a greater gravity field at the bottom region of the model and lower gravity field at the top region of the model. It is important to note that a prototype would experience a linear increase in stress as depth into the soil increases due to the constant gravity put upon it by the Earth's rotation. However, the model experiences a nonlinear stress profile that increases with depth proportional to the variation of the induced acceleration field (Coulter, 2005).

Therefore, the error brought about by the change in radius in a centrifuge model is indeed an important factor. The error might be in the region of under-stress in the upper depths, or over-stress in the lower depths, as shown in Figure 3.4. These errors can be minimised by knowing the relative magnitudes of the over-stress and the under-stress in the centrifuge model.

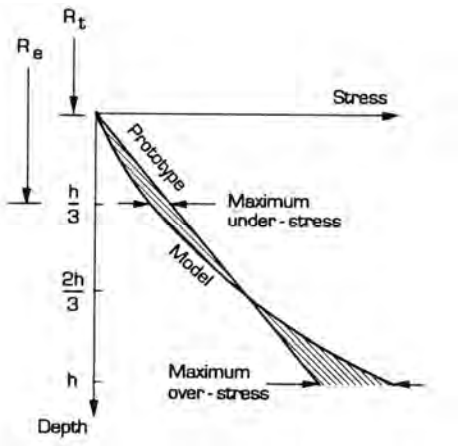

Figure 3.4: Stress variation with depth in a centrifuge model and its corresponding prototype (after Taylor, 1995)

According to Taylor (1995), the exact corresponding stress between model and prototype is at two-thirds model depth, while the effective centrifuge radius should be measured from the central axis to one-third the depth of the model. It should be noted that generally, this error is less than 3% of the prototype stress, which is considered as not overly significant. Furthermore, Schofield (1980) suggests that the acceleration level may be assumed constant with model depth without excessive error if the overall soil model depth is less than 10% of the effective centrifuge radius. In this study, the centrifuge experiments of submarine landslide flows experience the variation with depth therefore; the flows may be subjected to errors due to the stress variation with depth in the mini-drum centrifuge. Baker (1998) mentioned that the typical errors of variation with depth of the mini-drum centrifuge were 6.4 % and 7.4 %, for over-stress and under-stress respectively.

3.4.2 Radial gravity field

In a centrifuge, the centrifugal acceleration field which provides the g is in radial, while the earth's gravity field is assumed to be vertically downwards or parallel in the context of geotechnical structures. Figure 3.5 shows the error of radial gravity field. It can be seen that, at the centre of the model, the direction of the acceleration is in the vertical direction, while towards the side of the model the acceleration becomes more inclined. It can

also be seen that the error due to the radial gravity field gets worse in a smaller diameter centrifuge compared to a larger diameter centrifuge.

This effect may cause a significant error if testing activity is in the region close to the sides of the model. It is, therefore, advisable to ensure all major events of testing occur at the centre of the model where the direction of acceleration is closer to vertical. It is important to note that this problem becomes insignificant in drum centrifuge as the model is along the circular channel where the direction of the acceleration is always vertical relative to the model.

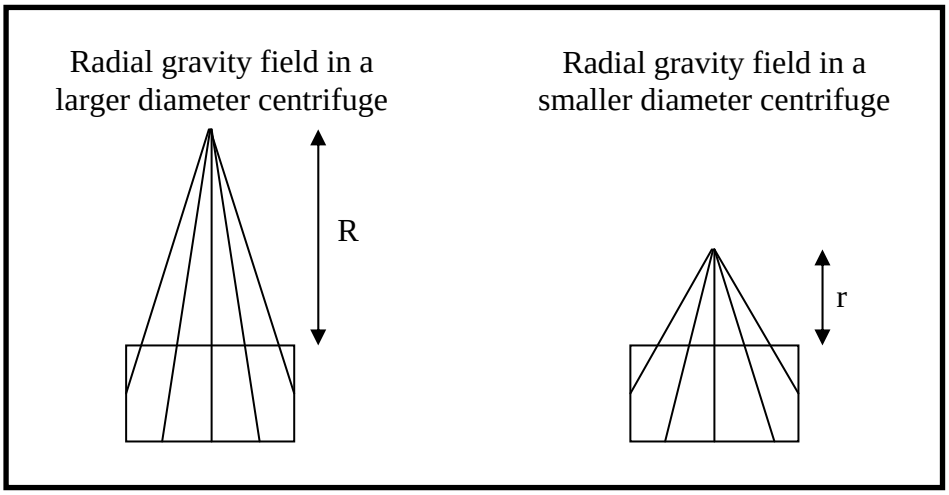

Figure 3.5: Error due to radial gravity field (after Madabhushi, 2006)

3.4.3 Coriolis effects

According to Schofield (1980), Coriolis effects occur whenever there is a radial velocity inside the model in the plane of rotation. In addition, in a centrifuge test there may be vertical velocities in the plane of rotation in which the Coriolis effects need to be assessed. Taylor (1995) stated that the Coriolis acceleration, a_c, is related to the angular velocity, ω, of the centrifuge, while the velocity, v_{mass}, of a mass within the model can be written as $a_c = 2\omega v_{mass}$.

It should be noted that the inertia acceleration, a, of the model is $a = \omega^2 R_e = \omega v_{model}$, where R_e is the effective radius of the centrifuge and v_{model} is

the velocity of the model in a centrifuge. The error due to Coriolis acceleration can be determined as the ratio between the Coriolis acceleration and the inertial acceleration (a_c/a). Taylor (1995) concluded that the Coriolis effects would be negligible if the ratio of a_c/a, is less than 10%, while the range of velocities within a model would not lead to a significant Coriolis effect, is given by $0.05v_{model} > v_{mass} > 2v_{model}$. Based on this recommendation, it is found that the centrifuge experiments in this study are within the limits.

3.4.4 Particle size effects

A well-known argument made on centrifuge modelling is that, if a model test is scaled down to 1:N, the grain size of soils in the model should also be scaled down N times in order to model the prototype. This implies that if a prototype with fine sand is to be modelled, then clay particles have to be used in the model. However, it is important to note that in soil mechanics, the stress strain behaviour of sand and clay is different. It should also be noted that soils are considered as continuum, in which the approach of modelling fine sand using clay does not portrait the true behaviour of the modelled soils.

It is therefore sensible to develop simple guidelines on the critical ratio between a major dimension in the model to the average grain diameter to avoid problems of particle size effects (Taylor, 1995). For example, Goodings and Gillette (1996) studied 61 centrifuge models of slopes brought to failure to assess side boundary and particle size effects on model behaviour. They found that the particle size effects are negligible if the model failure surface is at least 30 grain diameters below the soil surface.

3.4.5 Natural earth acceleration field (1 g effects)

It should be noted that besides experiencing the centrifugal acceleration in a centrifuge, models in a centrifuge also experience the earth's natural acceleration field. This results in centrifuge models not experiencing the acceleration field that acts truly parallel to the vertical axis of the model, where the prototype does so in its vertical axis as caused by the Earth's

gravity. Hence, this implies that centrifuge models experience a resultant acceleration field which may induce errors to the results.

This effect of the Earth's constant natural acceleration field is impossible to eliminate. However, if a centrifuge is brought up to an acceleration field many times larger than the natural earth acceleration field, this effect will be insignificant. As cited in Coulter (2005), considering a test at 100 g, the resultant acceleration will act less than 0.6 degrees from vertical. Therefore, the 1 g effect will be insignificant if a test is conducted at higher g levels.

3.5 Mini-Drum Centrifuge

The mini-drum centrifuge is specifically chosen for the submarine landslide experiments because of its flexibility for materials to move freely within the circular ring channel. Unlike beam centrifuges, the soil test package is mounted on one end of the rotating arm. The mini-drum centrifuge at the Schofield Centre is known as the Mk II mini-drum which was manufactured by Andrew N. Schofield & Associates (ANS&A) and has been in operation since 1995.

Figures 3.6 and 3.7 show the elevation of the mini-drum centrifuge with its axis horizontal and the cross-section through the main rotating components with its axis vertical, respectively. It should be noted that the mini-drum centrifuge is capable of rotating the drum through 90^0 about the pivot until the drive shaft is vertical, without stopping the spinning drum. Testing of the models is carried out with the axis vertical to minimise the ±1g variations in accelerations, which are experienced by the model when the axis is horizontal (Barker, 1998).

The mini-drum centrifuge has a radius of 370 mm with a width of 180 mm and depth of 120 mm. Figure 3.8 shows the internal dimensions of the

mini-drum centrifuge. According to Barker (1998), the maximum speed of the motor in the mini-drum is 1067 rpm which corresponds to 471 g at radius 370 mm.

It should be noted that the face plate and turntable can be rotated independently. This feature is designed for any actuator to rotate relative to the face plate. Instruments used in the mini-drum can be attached to the instrumentation housing ring as shown in Figure 3.7.

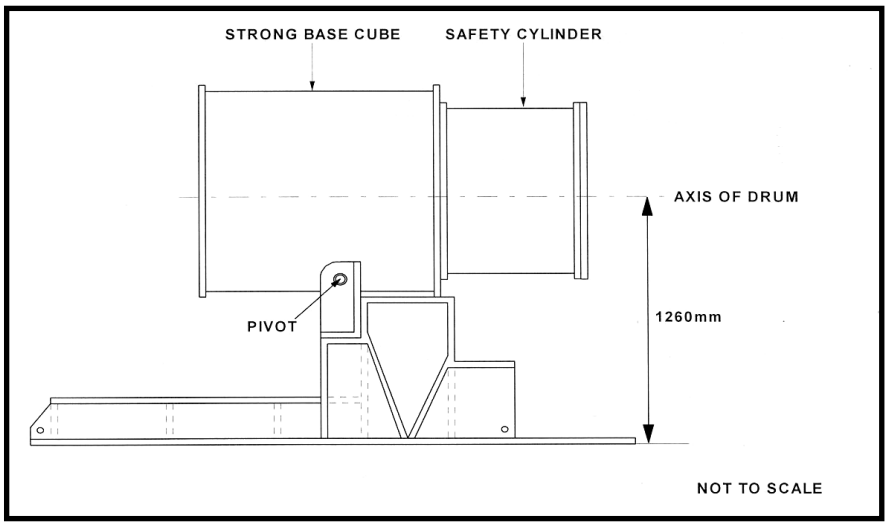

Figure 3.6: Elevation of the mini-drum centrifuge with axis horizontal (after Barker, 1998)

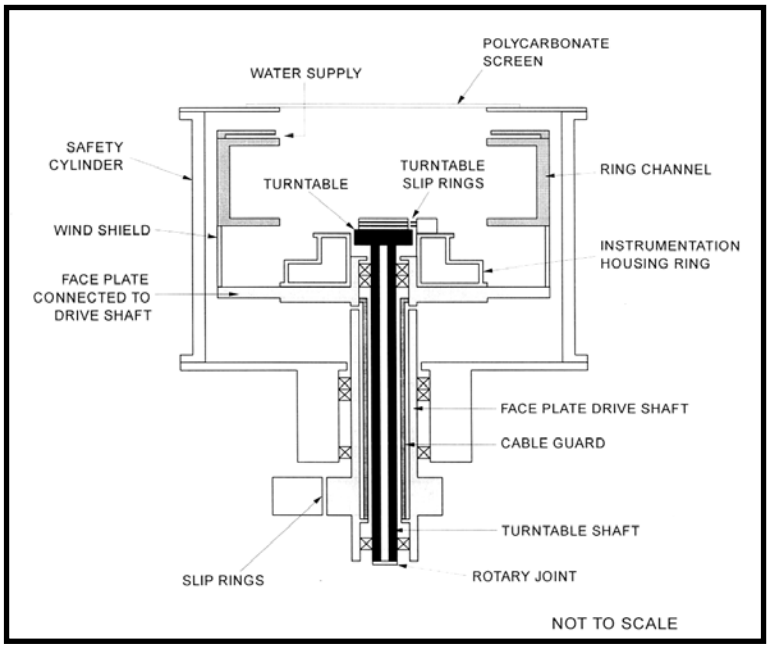

Figure 3.7: Cross-section of the mini-drum centrifuge with axis vertical (after Barker, 1998)

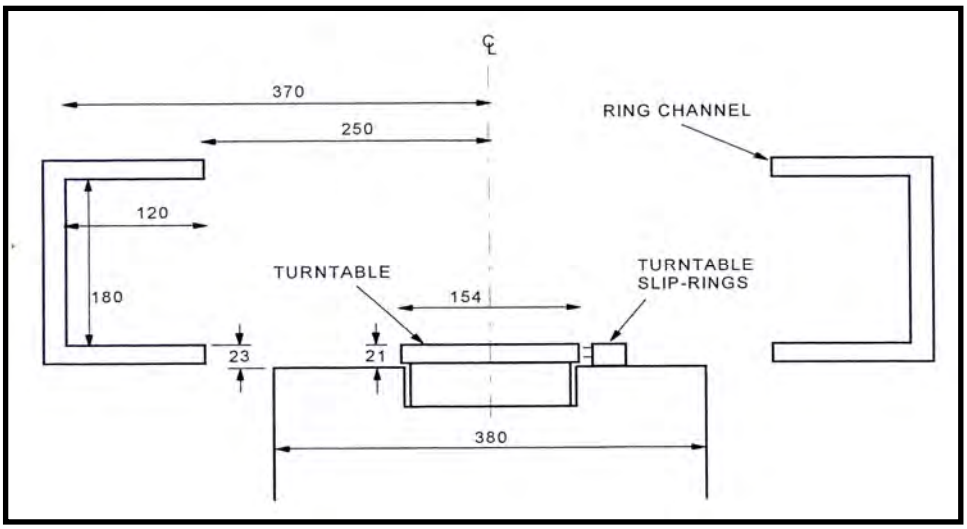

Figure 3.8: Internal dimensions of the mini-drum centrifuge (after Barker, 1998)

It is essential to note that water is supplied to the bottom of the ring channel through the water supply hole in the ring channel as shown in Figure 3.9. The water can then be drained through the drainage holes in the channel wall. The drainage of water from these holes is connected to a standpipe. This allows drainage and water levels to be controlled in the ring channel. The inclination of the standpipe is controlled by an air motor.

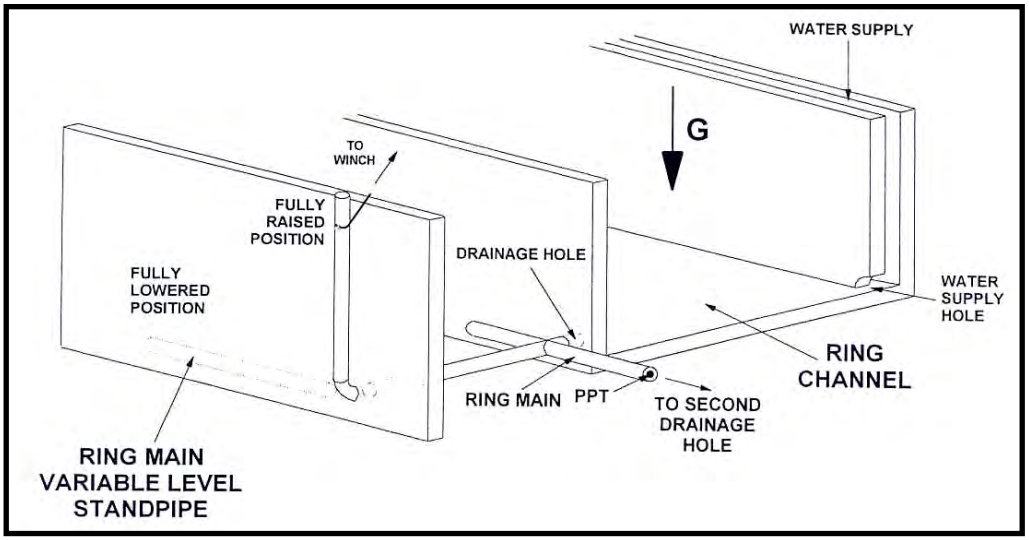

Figure 3.9: Water supply and channel drainage of the mini-drum centrifuge (after Barker, 1998)

3.6 Summary

Understanding the principles of centrifuge modelling enables the development of a centrifuge experiment to simulate submarine landslide flows. Since the mini-drum centrifuge has the flexibility to enable materials to move freely within the circular ring channel, as well as the capability of containing water, a centrifuge model specifically designed for simulations of submarine landslide flows in this mini-drum centrifuge is developed and is discussed in Chapter IV.

Scaling laws for submarine landslide flows are proposed and centrifuge experiments at various gravity fields with scaled flow heights are performed to further verify and investigate the proposed scaling laws. Chapter IV discusses the development of the model and the experimental results.

CHAPTER IV

4.0 CENTRIFUGE MODELLING OF SUBMARINE LANDSLIDE FLOWS

4.1 Introduction

As mentioned in previous chapters, this research study has been inspired by the importance and the lack of submarine landslide experiments through centrifuge modelling. The submarine landslide experimental works were carried out using the Mk II mini-drum centrifuge at the Schofield Centre, University of Cambridge. This chapter discusses the design of the centrifuge model, experimental procedures, results and interpretations of the experiments as well as the challenges faced during the development of the centrifuge model while carrying out the experiments.

4.2 Design of the Centrifuge Model

4.2.1 Geometry of the model

The geometry of the slope for the experiments is shown in Figure 4.1. In order to produce a slope inclination of 6°, the length of the slope needed to be 1 m with a height of 0.105 m. The 6° slope inclination was initially chosen for comparison with Ilstad's (2005) PhD work; however, at the later stage of the experiments, it was found that the comparison with this work was not feasible due to the material used in the experiments. This is discussed in more detail in this chapter. The width of the slope was approximately 0.1 m to leave an area for the cameras to capture the flow events. Knowing that submarine landslides have a long runout distance, the 1 m length of the slope was chosen due to the limitation of the Mk II mini-drum centrifuge. It should be noted that, while maintaining the constant slope inclination of 6°, increasing the slope length resulted in an increase of the slope height, in which the slope

height would exceed the depth of the ring channel in the mini-drum centrifuge. Also, it is noted that the depth of the ring channel in the mini-drum was 0.12 m; therefore, the slope height of 0.105 m was considered to be an optimum choice.

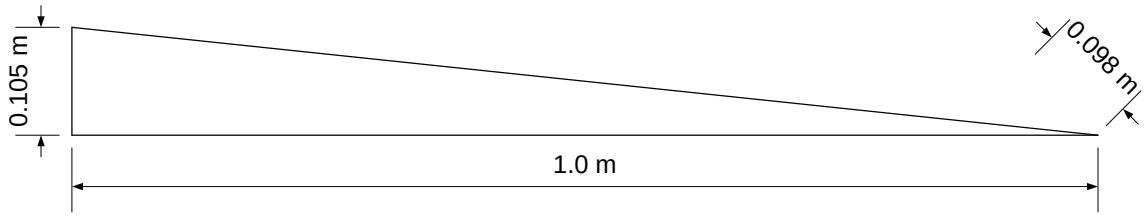

Figure 4.1: Geometry of the slope

The challenging part in designing the model was to fit the 1 m slope into the ring channel which was circular in shape. The 1 m slope therefore needed to be in a circular shape as shown in Figure 4.2. The circular slope was divided into two sections. The reason for having two separate sections was to enable the sections to be easily placed into the mini-drum's ring channel with considerations of the clearance (opening) of the mini-drum centrifuge being only 0.5 m. The material of the circular slope was made of stiff foam. The overview of the centrifuge model for the experiment is shown in Figure 4.3. The units in all drawings are in metres, unless otherwise stated.

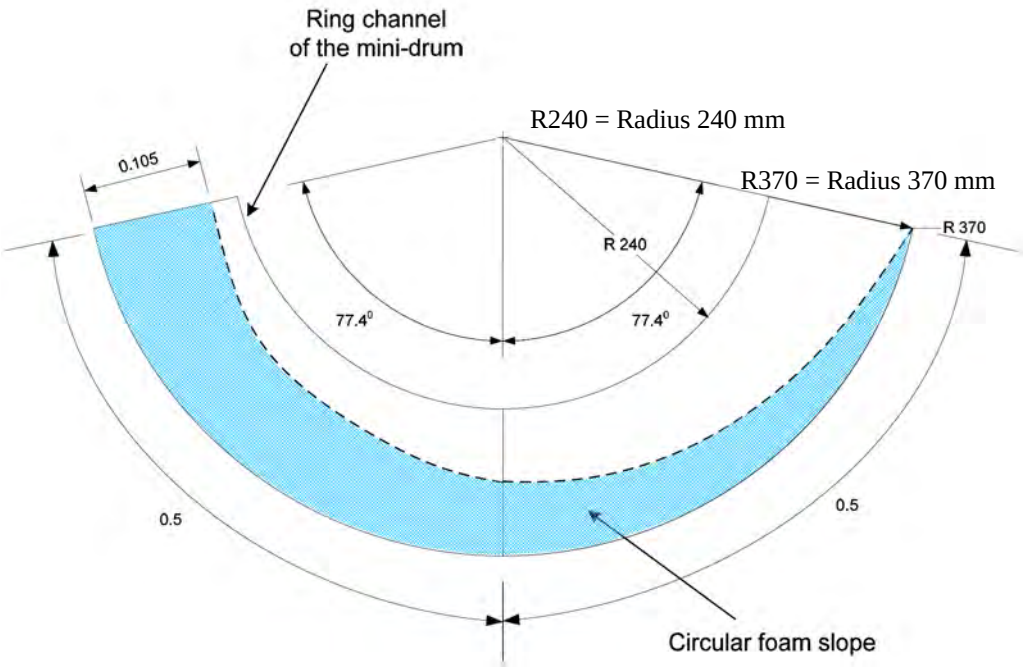

Figure 4.2: Geometry of the circular slope in the ring channel

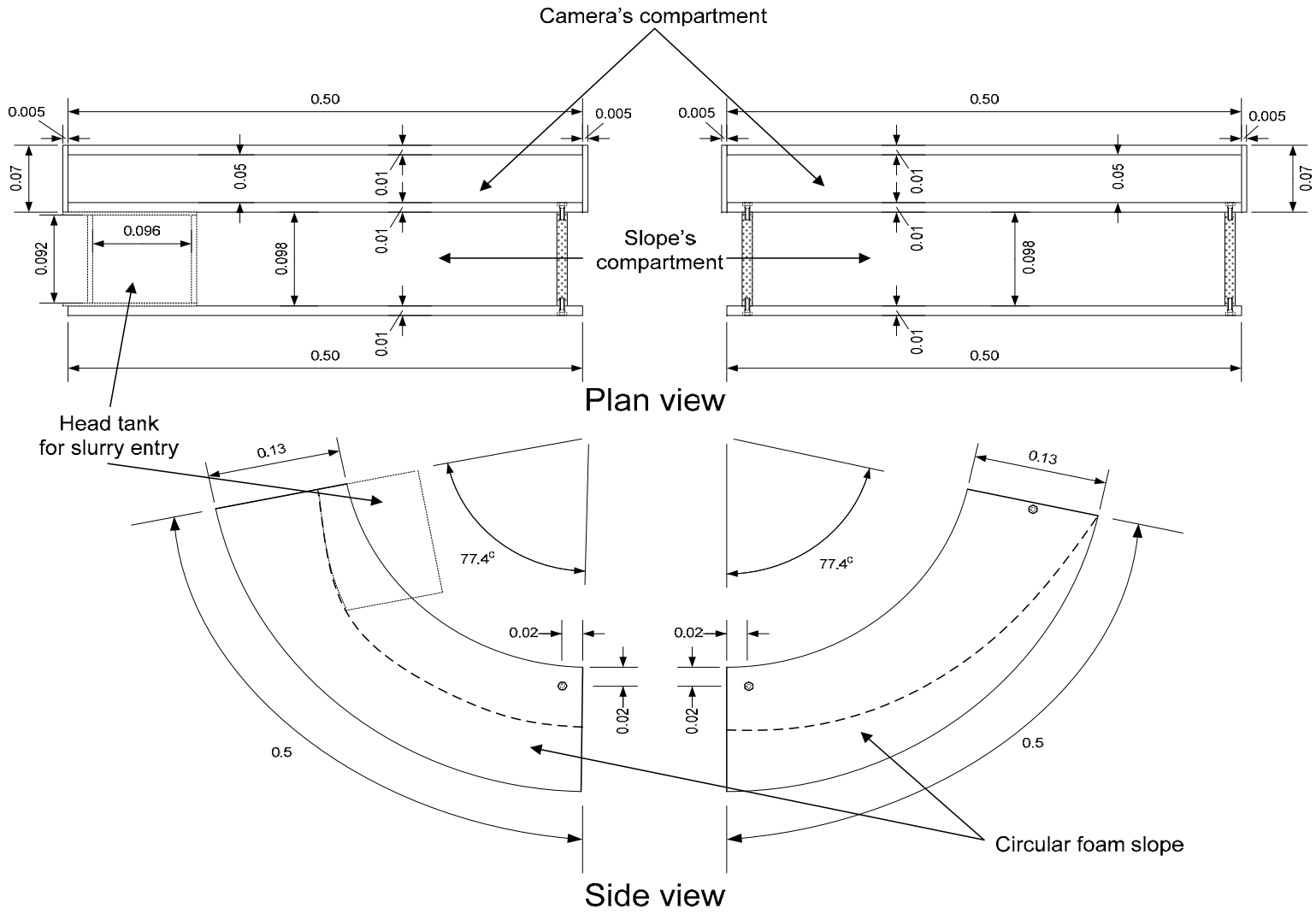

Figure 4.3: Overview of the centrifuge model

4.2.2 Compartments for slope and cameras

The model was divided into two compartments, one for the slope and the other for the cameras. The size of the slope's compartment was restricted by the width of the ring channel, as well as the need to give a clearance for the camera's compartment. The optimum slope width was approximately 0.1 m (the actual model's width measurement is 0.098 m); this left a clearance for the camera's compartment to be 0.05 m as shown in Figure 4.3. This imposed a challenge in obtaining small compact digital cameras with a very good macro mode for video recording in the experiments.

The camera's compartment was sealed at the bottom, which prevented water from entering into the compartment. This resulted in loss of weight since the entire ring channel of the mini-drum centrifuge was flooded with water during the experiment, which would affect the balance of the mini-drum centrifuge. Similarly, the weight loss due to the foam slope also contributed to the balancing of the mini-drum centrifuge. Therefore, counterweights had to be installed in the centrifuge to compensate for the weight loss. Appendix 2 shows the estimation of weight balancing in the mini-drum centrifuge.

As shown in Figure 4.3, there is a head tank in the slope's compartment. The initial idea of having a head tank was to temporarily store the slurry. There was also supposed to be an opening gate at the front of the head tank to initiate the flow, as well as to control the flow height. However, it was found that the slurry would segregate and consolidate if placed at the head tank. It was also discovered that it was not possible to control the flow height using an opening gate due to the workability of the slurry used in the experiments. The flow height of the actual experiments was controlled through the flow rates rather than an opening of a gate. This is described in more detail in the latter part of this chapter. The opening at the head tank served only as the reference for the starting point of the flows.

The events in the slope's compartment during the tests were recorded by five digital cameras, which were placed into the camera's compartment, each with a bracket holding the cameras. Perspex window openings were placed in front of each camera enabling the events in the slope's compartment to be captured. Figure 4.4 shows the details and positions of the Perspex windows within the model. Calculations were made for the bending moments imposed on the Perspex windows for safety operation under g-levels of up to 100 g. The calculations are shown in Appendix 3.

Four of the digital cameras were placed at the side of the slope corresponding to the locations of the pore pressure transducers (PPT). The fifth camera was positioned at the top end of the slope with the intention of capturing the aerial view of the flow events. Figures 4.5 and 4.6 show the actual model with the Perspex windows and the compartments for both the slope and cameras respectively. The detailed information on the digital cameras is given in sub-section of 4.2.3.2.

Both the slope and camera compartments were sealed at the bottom as shown in Figure 4.7. The overall view of the experimental setup in the mini-drum centrifuge with the labelled parts is shown in Figure 4.8.

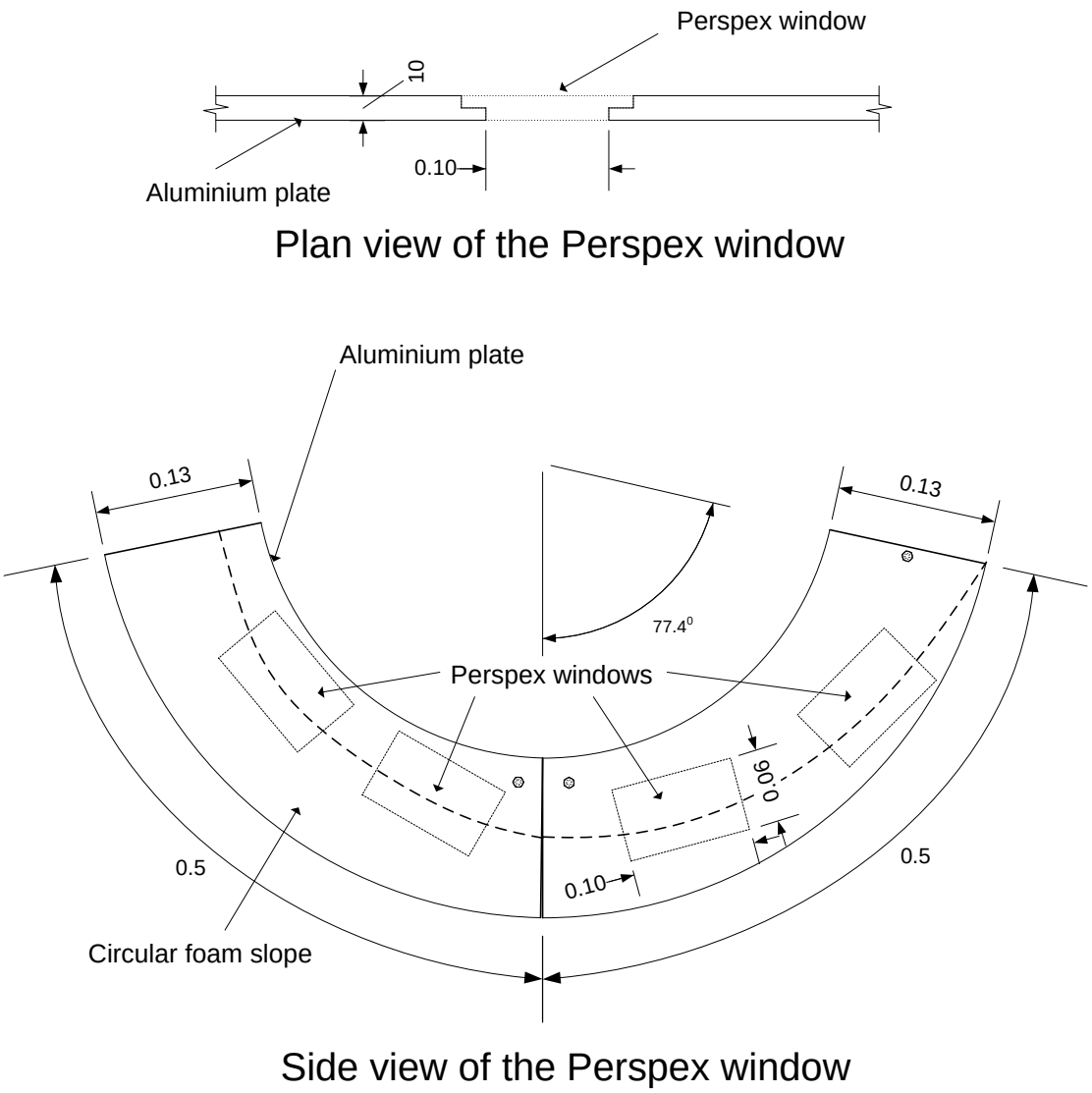

Figure 4.4: Details of Perspex windows

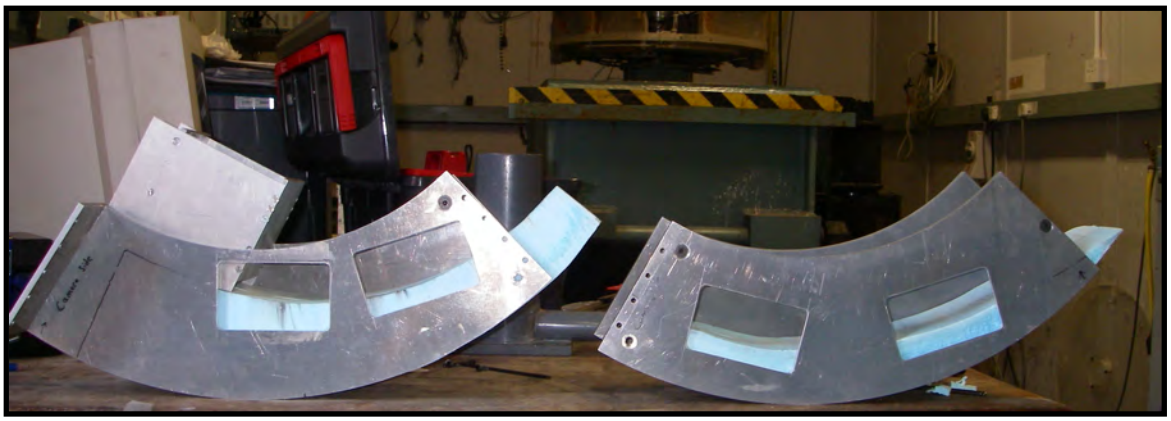

Figure 4.5: Perspex windows

Figure 4.6: Slope and camera compartments

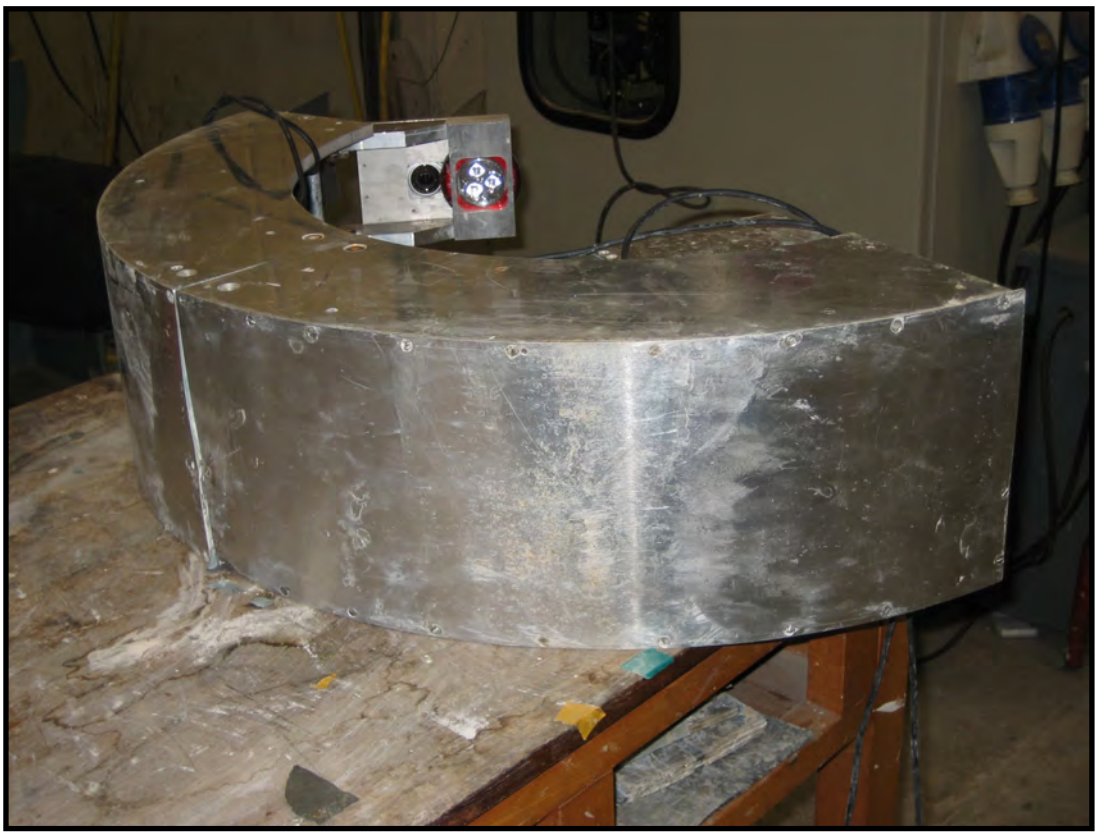

Figure 4.7: Slope and camera compartments sealed at the bottom

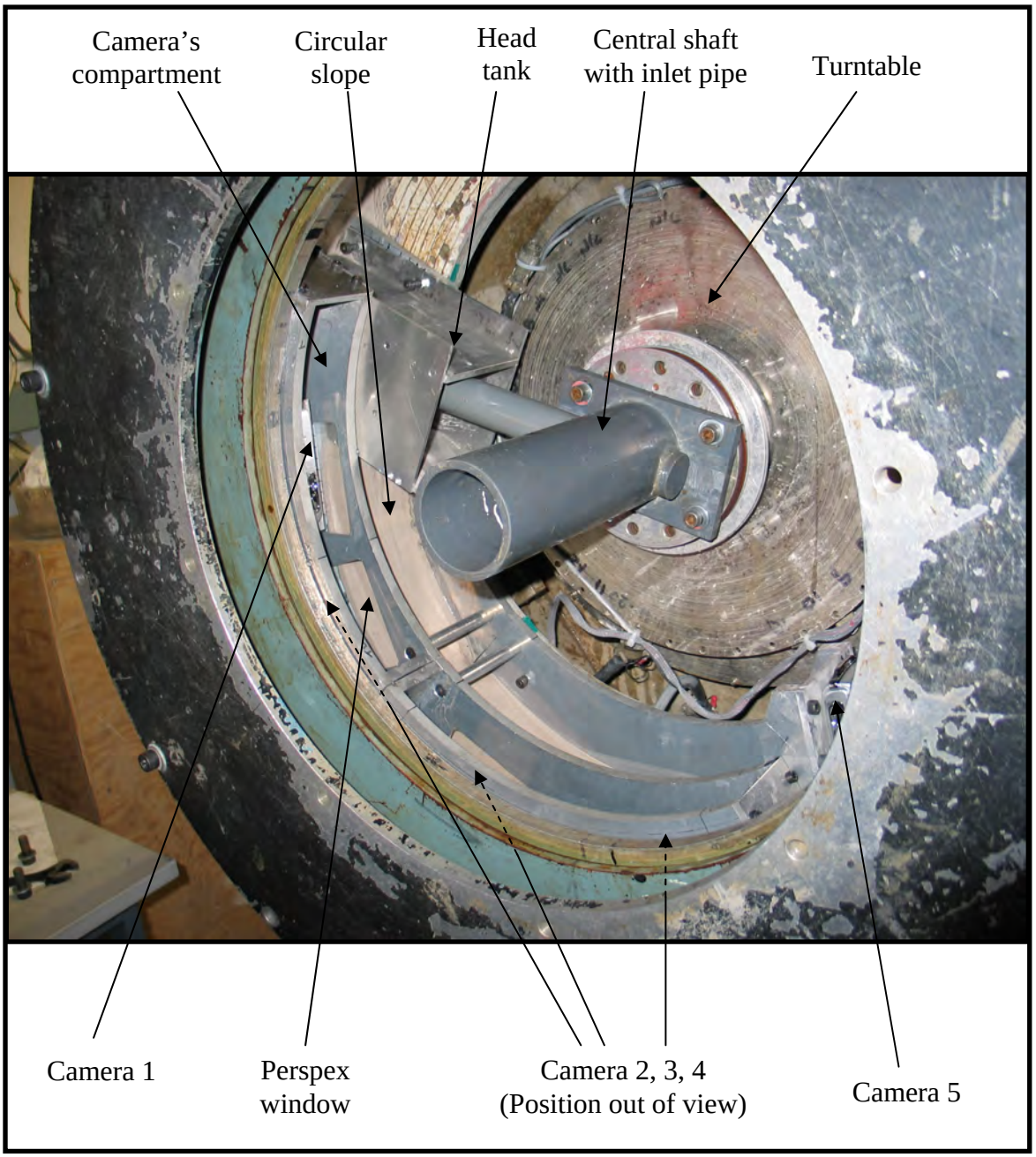

Figure 4.8: Experimental setup in the mini-drum centrifuge

4.2.3 Instrumentation

4.2.3.1 Pore Pressure Transducer (PPT) and Stress Cell

Four 1 bar Pore Pressure Transducers (PPTs) manufactured by GE Druck and four 35 bar load cells manufactured by Entran, were used to measure pore pressures and total stresses during the experiments, respectively.

It was decided to use the 1 bar PPTs for the experiments because the expected highest total pressure (slurry + water) was less than 100 kPa while running the centrifuge at 60g. Porous stones were used in the PPTs as filters. The instrumentation's layout is shown in Figure 4.9 (a). It can be seen that the spacing of PPTs and stress cells was not constant. This was to accommodate the Perspex windows where the cameras were located, so that the measurements of pore pressure and total stress corresponded to the location where the videos were recorded. Figure 4.9 (b) shows that the instrument was embedded in the foam slope. A groove was made on the foam slope and the instruments and its wiring were embedded in the foam slope. This gave the instruments and the slope the same surface level so that the measurements would represent more accurately at the bottom of the flow.

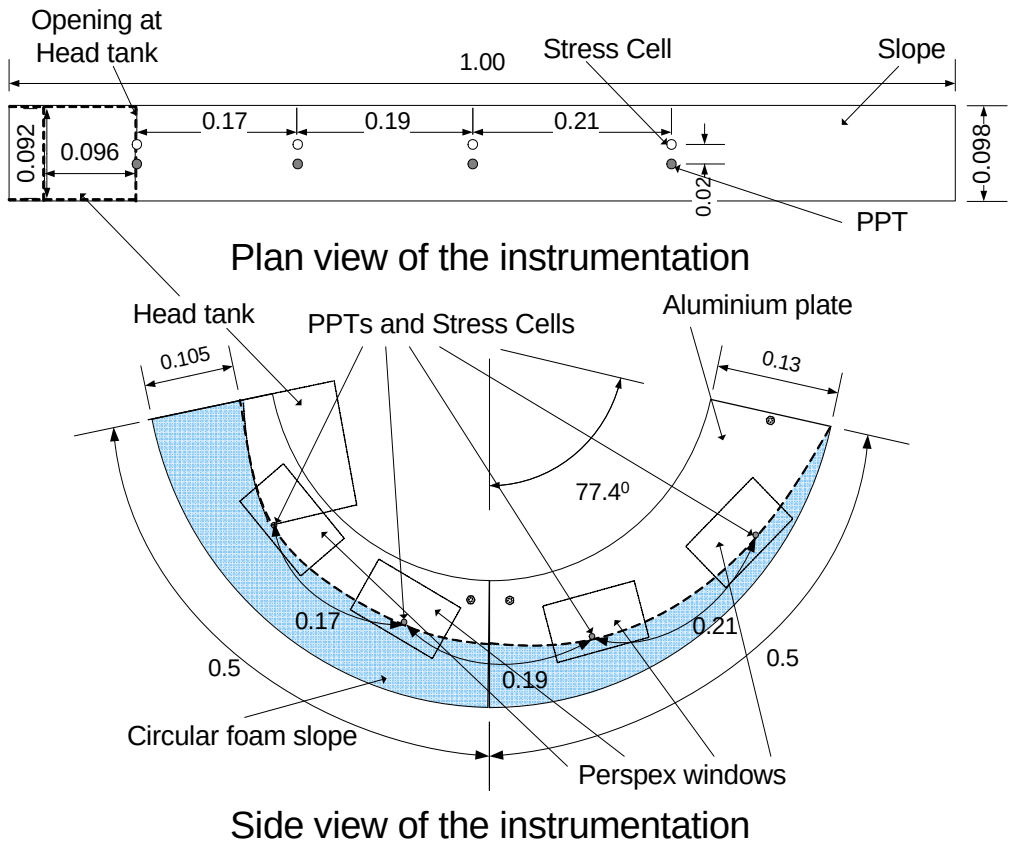

Figure 4.9 (a): Instrumentation layout in the model

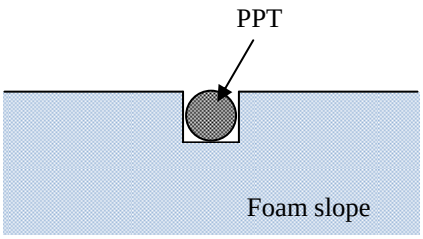

Figure 4.9 (b): Instrumentations embedded in the foam slope

4.2.3.2 Digital Camera

Five Pentax Optio W10 digital cameras were used in the experiments, all of which were dustproof and waterproof up to 1.5 metres of water. Figure 4.10 shows the actual digital camera used in the experiments together with the dimensions. A high speed 2GB Secure Digital (SD) memory card in each camera was used, enabling a continuous video of the highest possible quality of approximately 30 minutes to be recorded. This had imposed another challenge while carrying out the experiments, where all the events (starting from spinning up the centrifuge, flooding channel and the flow of the submarine landslides) for each experiment had to be finished within 30 minutes. It should be noted that the cameras were not SDHC (Secure Digital High Capacity) compatible, otherwise a larger memory card could have been used to record a longer video running time, which would allow a longer experimental running time.

The digital camera was capable of capturing videos at 640 x 480 pixels with a frame rate of 30 frames per second (fps) at the best video quality mode. The macro mode of this camera was approximately 0.01 m, where the nearest focusable distance was 0.01 m away from the lens. This was ideal for the experiments in the mini-drum centrifuge. The video format used in this camera was QuickTime Motion JPEG (MOV).

Figure 4.10: The digital camera used in the experiments

4.2.3.3 LED lights

LED lights were used in the model in order to get a better video quality and pictures. An array of LED lights was mounted around the centre shaft as shown in Figure 4.11. This provided a brighter view of the entire flow event. However, this was found to be not sufficient as the videos recorded by the cameras by the side of the flows were still dark. As a further improvement to the lighting conditions, five LED “push lights” were mounted on top of each camera, as shown in Figure 4.12, providing direct lighting to each camera. These LED “push lights” were powered by two AAA batteries each which had to be switched on manually prior to spinning up the centrifuge. Further details on the challenges encountered for getting good quality videos involving LED lights are discussed in sub-section 4.5.1.

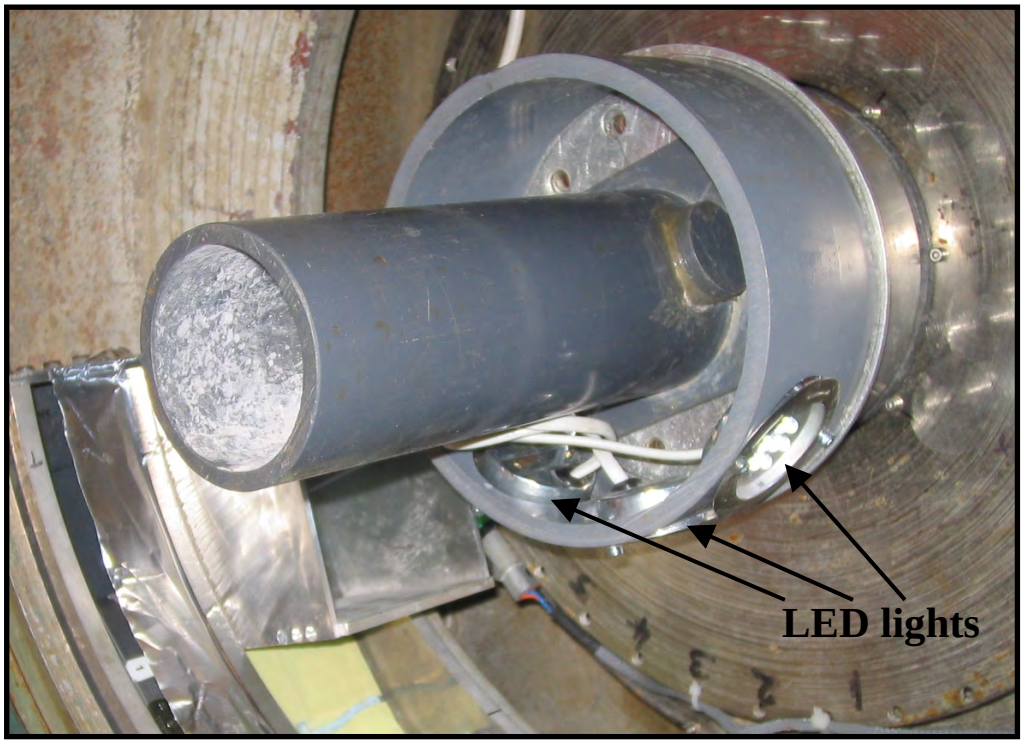

Figure 4.11: Array of LED lights mounted around the centre shaft

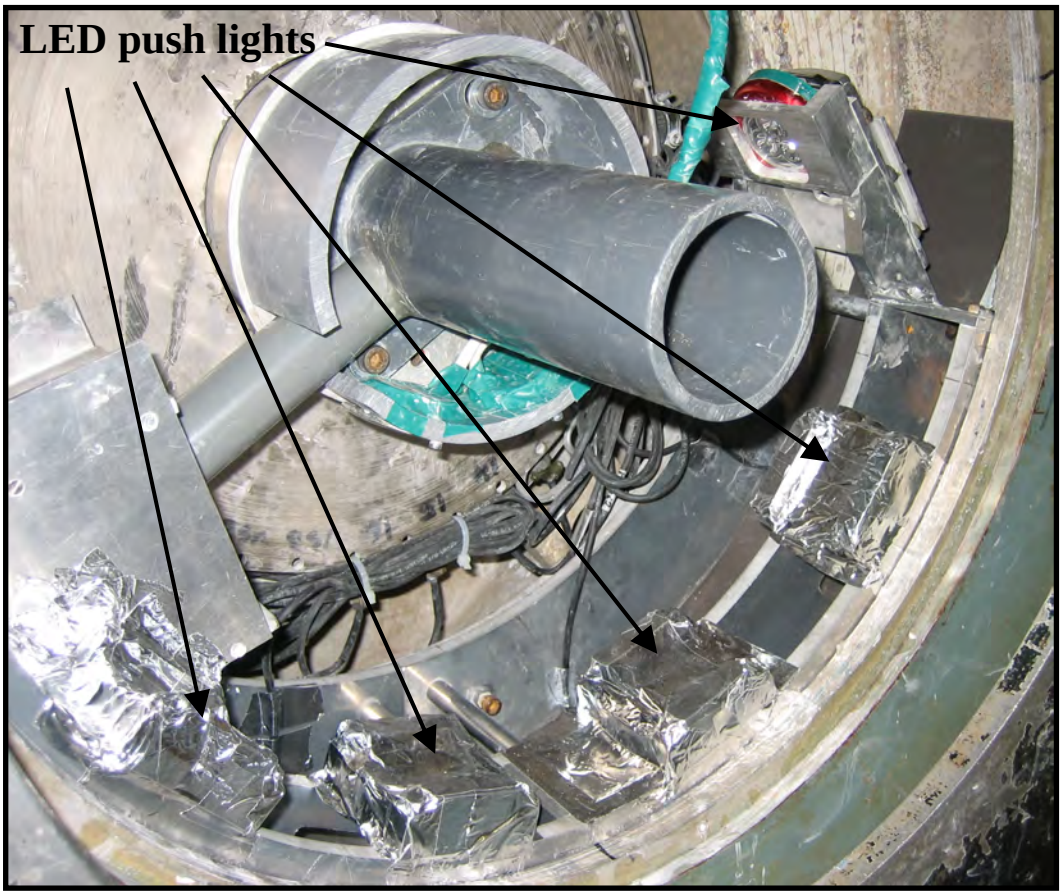

Figure 4.12: LED push lights mounted on the centrifuge model

4.3 Choice of Slurry for the Experiments

The clay slurry mixture for the experiments was made out of a mixture of E-grade Kaolin clay and water. The slurry was composed of 45% of the clay and 55% water, giving the water content of the slurry to be 122%. The plastic limit of E-grade Kaolin was 30%, the liquid limit was 58% and the density was 2600 kg/m^3. The bulk unit weight of the slurry was 13.5 kN/m^3. The viscosity of the slurry was 0.4 Pa.s and found to be relatively similar at various strain rates.

The initial plan for the choice of slurries was to replicate the slurries used in Ilstad's (2005) experiments. According to Ilstad (2005), the slurries used in the experiments were characterised by material compositions in percentage of the total mass. The compositions in his slurries were Kaolin clay (Snow-brite) with a specific density of 2750 kg/m^3 and brown silica sand with a specific density of 2650 kg/m^3 and a median size of 330 μm. The bulk density of the slurry was 16.9 kN/m^3.

However, the Kaolin clay used in Ilstad's (2005) experiments was not commonly found in the industry. Therefore, it was unavailable for the purpose of this research study. Furthermore, no other information was available on the Snow-brite Kaolin clay, such as the liquid limit and plastic limit. Such information would have been useful in order to recreate a slurry with a more similar flow behaviour.

Efforts were also made to use a slurry mixture with sand. Fraction E fine Silica sand was used in the initial phase of the experiments. Trial mixtures of slurries have been carried out, using the E-grade Kaolin and Fraction E fine Silica sand with 35% water. However, it was found that the slurry made of 35% water induced a significant segregation of clay, sand and water even after thorough mixing of the materials. The trial test for the material compositions was made in a small scale 1 g environment laboratory test as well as in the mini-drum centrifuge. The results from both tests were similar, in which the

slurry segregated into clay, sand and water. Significant segregation occurred even for the highest clay content used in Ilstad (2005), which was composed of 32.5% clay, 32.5% sand and 35% water. Figures 4.13a and b show the segregation of materials in the highest sand content (5% clay, 60% sand and 35% water).

Figure 4.13: Segregation of materials

4.4 Experimental Procedures

Due to the complexity of the experimental procedure, it is best to separate the experimental procedures into three parts: before, during and after the experiments. A detailed checklist for operating the mini-drum centrifuge to ensure a safe working environment during each test was produced as shown in Appendix 4.

4.4.1 Before the experiment

The centrifuge model package, which consisted of the slope and cameras, was assembled prior to installation into the mini-drum centrifuge. Once the centrifuge model package was installed in the mini-drum centrifuge, a layer of fine sandpaper (SIANOR B 1600) was attached on the surface of the foam slope to prevent undesired slip during the experiments. The sandpaper is replaced after each experiment.

The slurry was prepared separately outside of the mini-drum centrifuge. The slurry was mixed according to the predetermined clay and water ratio and continuous stirring was carried out until seconds before

pouring it into the mini-drum centrifuge. This was to ensure a homogenous mixture, as well as minimising the segregation of clay and water.

The PPTs and stress cells were installed into the model after the model was properly installed in the mini-drum centrifuge. It should be mentioned that small trenches were made on the foam slope in order to have the PPTs in place and have the same surface level as the slope. The wirings of the PPTs were also placed in the trenches. Sandpaper was cut to expose the PPTs and stress cells.

The porous filter stones of the PPTs were well-saturated before attaching to the model. It was important to ensure that the filter stones were saturated before the experiments, as partly saturated filter stones would affect the measurements of the pore pressure. It should be noted that attaching the PPTs was considered one of the very last things to do before the actual experiments; however, other necessary procedures had to be performed after installing the PPTs and before the actual experiments could take place. For example, the cameras had to be switched on to start recording videos, and the camera compartments had to be secured with aluminium tape to prevent water splashing onto the cameras. All these steps took a certain amount of time after the PPTs were installed into the model. However, this could have resulted in the porous stones in the PPTs not being fully saturated; therefore, some soaked tissue papers were placed on top of the PPTs to ensure that the porous stones were well saturated. The soaked tissue papers were checked to ensure they were always fully saturated to prevent the adverse effects of water escaping from the porous stones. The tissues were removed immediately before covering the mini-drum centrifuge with the safety cover.

Once everything was in place, the safety cover was then installed. The data acquisition system was switched on before spinning the mini-drum centrifuge. This was to ensure that all data before and after the experiments were recorded. Checks were performed to ensure that the changes in the measurements were due to the actual experiment and not system artefacts. The experiments were then ready to be carried out.

4.4.2 During the experiment

At the beginning of the experiment, the mini-drum centrifuge was spun up to 10 g, at which point water was then carefully introduced into the mini-drum centrifuge through a water pipe. Water steadily rose to the top of the model and then the model was spun up progressively to the desired g level for the experiments. Water was fed continuously to maintain a constant water level in the channel. The overflow water was drained off from the ring channel.

As mentioned earlier, the slurry was mixed and continuous stirring was carried out seconds before pouring it into the funnel to ensure a homogeneous mixture and to minimise the segregation of clay and water. A stopper was placed at the tip of the funnel's opening. When the slurry was full and reached the top of the funnel, the stopper was released and the slurry flowed onto the slope through the central shaft with the inlet pipe. Continuous feeding of slurry was carried out, where the slurry was always full at the top of the funnel. The stopper was placed back onto the tip of the funnel at the end of the flow while the funnel was still full. This was to ensure a constant flow rate of the slurry. For each experiment the total volume of the slurry was approximately 5.7 litres. The illustration of the experiment is shown in Figure 4.14.

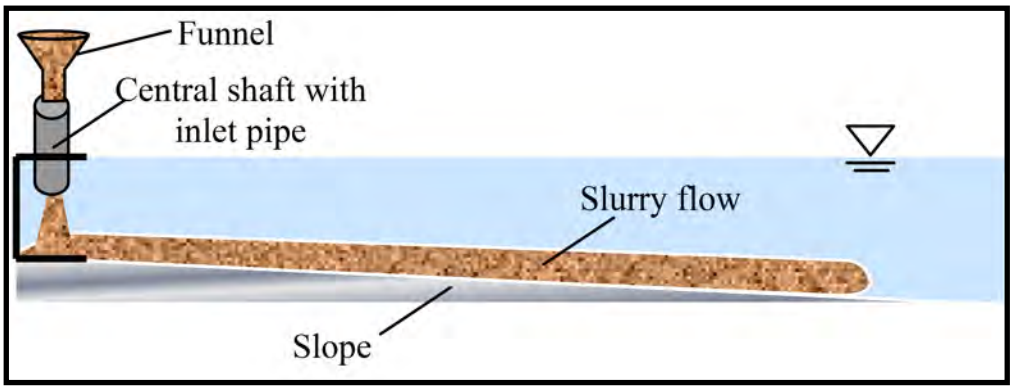

Figure 4.14: Illustration of the experiment

The experiments were carried out at different gravity levels with scaled flow rates. The different flow rates were controlled by using different funnel opening sizes of the tip. Figure 4.15 shows the various funnel opening sizes used to achieve the desired flow rates. These various opening sizes were calibrated to give the scaled flow rates. It was found that a smaller funnel opening (smaller flow rate), was better at keeping a constant flow rate. In general, the control of the flow rate through the funnel opening was relatively good, with an accuracy range from 4 to 10% as shown in Figure 4.16.

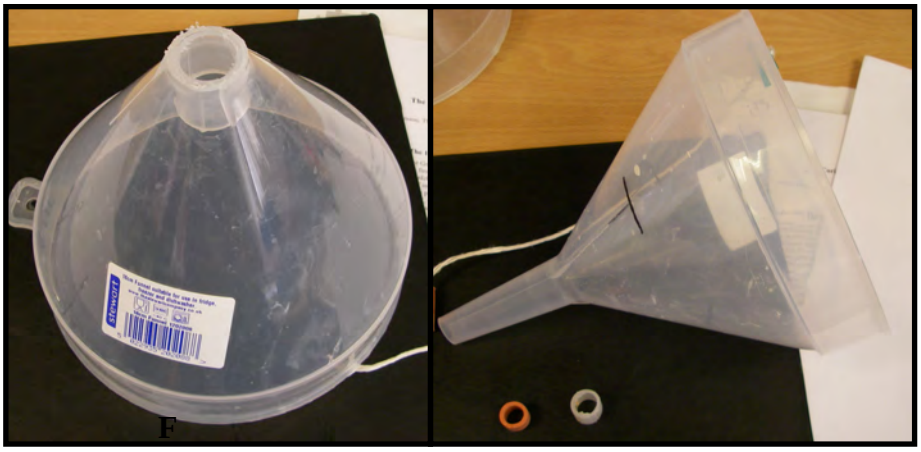

Figure 4.15: Various funnel opening sizes

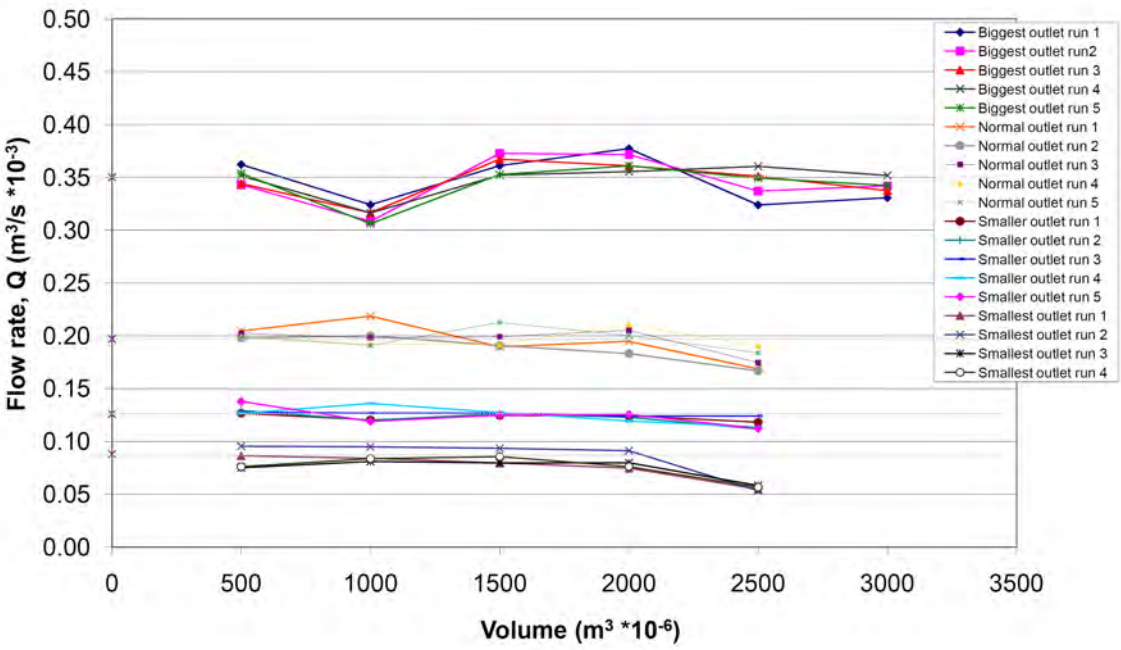

Figure 4.16: Flow rate accuracy from various funnel opening sizes

4.4.3 After the experiment

Once the slurry flow had run down the slope, the mini-drum centrifuge was allowed to continue spinning so that the clay could gain in strength to ease the cleaning and clearing of the clay after the experiments. Water in the ring channel was then slowly drained off while the mini-drum centrifuge was still spinning. The speed of the mini-drum centrifuge was lowered down progressively. The model package was removed so that the videos from the cameras could be extracted.

Once the model package had been taken out of the mini-drum centrifuge, the ring channel had to be cleaned thoroughly to avoid the drainage holes from becoming clogged up due to the fine clay particles. It should be mentioned that filter papers were attached to the drainage holes before the model package was installed and replaced after each experiment. A further flushing procedure was needed to completely flush out all the fine clay particles in the drainage system of the mini-drum centrifuge. This was done by spinning up the mini-drum centrifuge again while introducing water into the ring channel; the water was then drained off at higher g levels in order flush away any fine clay particles.

4.5 Initial Encountered Challenges

Several challenges were encountered while developing the centrifuge model package before arriving at the actual model used in the experiments. A number of trial tests were carried out without any data logging in the mini-drum centrifuge. Observations through video recordings were made during these trial tests, and problems encountered during these tests were noted. Improvements were made throughout the process to improve the quality of the experiments. Proof testing of the model package was also carried out at 70 g to ensure it was safe and working properly. The subsections below summarise the initial challenges encountered while developing the model package and how they were overcome.

4.5.1 Challenges encountered and comments

As mentioned above, several issues arose during the period of the model development as well as in the trial tests. Table 4.1 tabulates some of the challenges encountered and their comments.

Table 4.1: Initial encountered challenges while developing the model

Challenges encountered	Comments
Developing a model slope of 1 m in length for the mini-drum centrifuge.	The circular model slope was developed and separated into two sections.
Intentions of getting multiple video recordings during the flow events; however, the mini-drum centrifuge could only accommodate 1 or 2 web cameras.	Small compact digital cameras were used with very good macro mode (0.01m) and video quality. Able to capture continuous video for approx. 30 minutes with a high speed 2 GB memory card.
Uplift of foam slope while submerged in water.	Struts were installed to hold the foam with the aluminium plates.
Camera out of focus in the mini-drum centrifuge resulting in bad quality video recordings.	Managed to manually focus the camera with memory set in order to start capturing with the predetermined focal distance.
Insufficient lighting in the mini-drum centrifuge resulting in flickering images in the video recordings.	LED “push lights” were installed on top of each camera to provide constant light source. An array of LED lights was mounted around the central shaft to improve general lighting conditions around the channel.
Slurry outflow from the prefix gate height did not achieve the required thickness.	Different funnel opening sizes were used to achieve the required flow rates.
Water entering to the camera’s compartment, as well as water splashing at the cameras.	The camera’s compartment was completely sealed at the bottom and the top was sealed with aluminium tape to prevent splashing while water was injected into the ring channel.
Clogging of drainage holes from the fine sediments.	Filter papers were used to cover the drainage holes. Flushing procedure after each test.

4.5.2 Brief description of some trial tests

A few trial tests were conducted in the mini-drum centrifuge without any pore pressure and total stress measurements. One of the very first trial tests was conducted without water or slurry. The purpose of this was to examine the position of cameras and proof test for the cameras up to 70 g. Generally, all cameras were functional under the range of interested g levels.

Another trial test was carried out at 10 g with slurry while the slope was submerged with water. Unfortunately, there was a leakage within the ring channel of the mini-drum centrifuge during the test. The water level was, therefore, not enough to submerge the slope. Regardless of the dry run, it was interesting to note that the flow during the test tended to flow one-sided due to the 1 g effect. Figure 4.17 shows the sequence of flow from the view of camera 5. The 1 g effect was found to be minimal for experiments in 30 g and above; therefore, the actual experiments were carried out from 30 g to 60 g.

After the leakage of the mini-drum centrifuge was resolved, another trial test was carried out with the intention of verifying the drainage system and the water tightness of the camera's compartment as it was sealed with a rubber membrane and aqueous sealant. Minor leakage was still found in the camera's compartment. However, videos were successfully recorded but with severe flickering due to insufficient lighting sources. The video recordings were occasionally out of focus. This was because the camera's default setting was in the auto focus mode. This issue was then resolved by resetting the cameras to manual focus mode. The camera was capable of storing its previous focal settings, thus enabling preset focus and other settings to be stored. This feature was extremely useful since the cameras were positioned inside the mini-drum centrifuge prior to the test, which would be started moments before spinning. The camera compartments were completely sealed with a steel plate and aqueous sealant. This prevented any further leakage.

Figure 4.17: View of debris flow sequence from camera 5 at 10 g (slope not submerged - picture interval at 0.033s)

4.6 Results and Interpretations

This section presents the data and interpretations of the four series of centrifuge experiments that have been carried out in this study. Three of the series were carried out in the submerged condition while the other series was carried out in a non-submerged condition (dry condition). The four series of centrifuge experiments are as follows:

- Series 1: Experiments at various g levels and various flow rates
- Series 2: Experiments at only 30g with various flow rates
- Series 3: Experiments at various g levels with a large flow rate
- Series 4: Experiments at various g levels with a large flow rate in the dry condition.

4.6.1 Series 1: Experiments at various g levels and flow rates

This series of experiments was performed at various g levels (30 g, 40 g, 50 g and 60 g) with scaled flow rates in which the flow velocities and height were scaled according to the proposed scaling laws (see equations 3.6 and 3.7). The reason for going up to 60g was that the equipment such as the cameras was known to have problems focusing at higher g levels. The purpose of this series was to check on the validity of the proposed scaling laws. Table 4.2 shows the details of the experiments at various g levels with their corresponding flow rates and flow heights.

Table 4.2: Experimental details of flow rates and flow heights

g levels	Funnel opening, diameter (mm)	Average flow rate, Q (m^3/s) $*10^{-4}$	Average flow rate per unit length, Q_{ul} ($m^3/s/m$) $*10^{-4}$	Average prototype flow rate per unit length, Q_{Pul} ($m^3/s/m$) ($Q_{Pul} = N^2 Q_{ul}$)	Expected average flow height, $\bar{h}$ (mm)	Average prototype flow height, $\bar{h}_p$ (mm)
30	19.4	3.50	35.0	3.2	7.0	210
40	13.9	1.97	19.7	3.2	5.3	210
50	12.0	1.26	12.6	3.2	4.2	210
60	9.7	0.88	8.8	3.2	3.5	210

Note: The unit length is the width of the channel, which is 0.1 m. The flow velocity, v times the average flow height, h equals to the average flow rate per unit length, Q_{ul}. $\bar{v} \times \bar{h} = Q_{ul}$

Based on the proposed scaling laws, the tested cases with different flow rates at different g levels will give the prototype flow height of approximately 210 mm. Ideally, this will give the same magnitude of basal friction to resist the flow movement, as well as the soil stress field to drive the soil body to move along the slope, resulting in the motion of the soil body to be modelled by the governing equations proposed in the previous chapter. The results from the experiments of various g levels and the measured flow heights and velocities can then verify the validity of the proposed scaling laws.

Figure 4.18 shows the change in pore pressure measured at various locations and g levels beneath the submarine landslide flows along the slope. The change in pore pressure generally increases when the front of the flow arrives at the location of the PPTs. The change in pore pressure at various locations along the slope is relatively similar indicating that the flow height along the slope is relatively constant (i.e. steady state flow). It can also be seen that the change in basal pore pressure at different g levels is relatively comparable. This means that the stresses at various g levels are possibly correctly modelled.

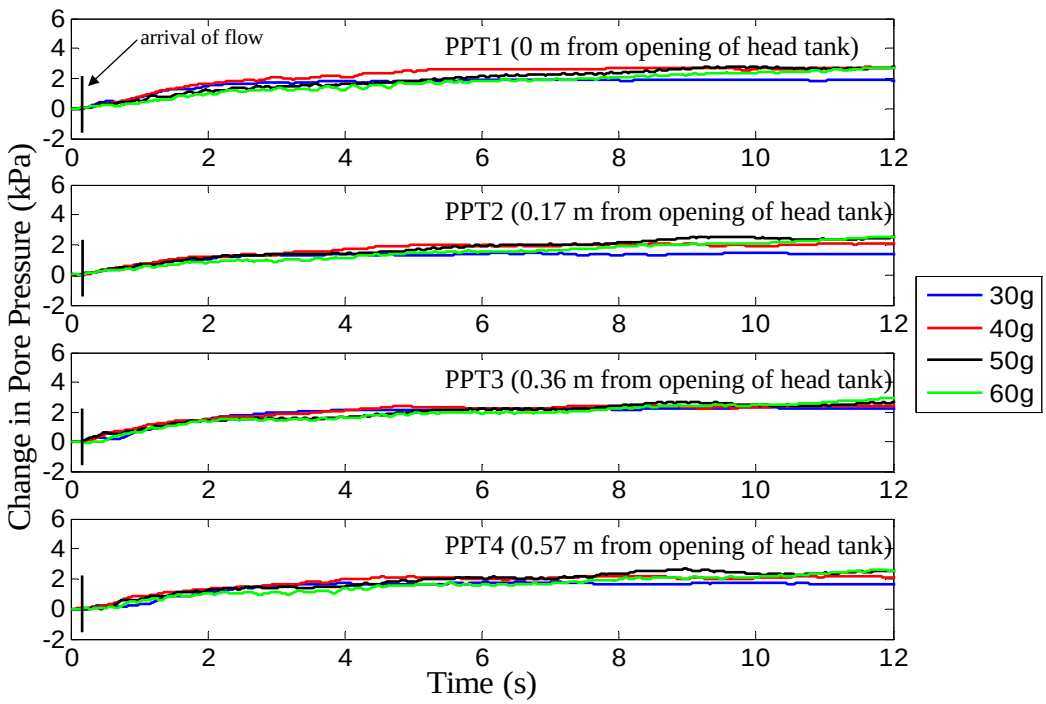

Figure 4.18: The change in pore pressure for various g levels at various locations along the slope

Figures 4.19 (a) to 4.19 (d) show the side view of the submarine landslide flows from Camera 1 for 30 g, 40 g, 50 g, and 60 g respectively at the opening of the head tank where PPT1 was located. It can be seen that the flow height decreases with increasing g level, as observed by the pore pressure data. Similarly, Figures 4.20 to 4.22, show the side view of the submarine landslide flows from Camera 2 (0.17 m from opening of head tank), Camera 3 (0.36 m from opening of head tank) and Camera 4 (0.57 m from opening of head tank) respectively for the various g levels. Note that Figures 4.19 to 4.22 were not in synced to each other, as Cameras 1 to 4 were not started together.

It can be seen that, in Camera 3 (Figure 4.21), the flow heights are higher than the other locations. This is because there is a small drop between the joint of the two slope compartments. Based on Figures 4.19 to 4.22, it can be seen that there is a turbidity current above the submarine landslide flows, and this turbidity current increases as the flow distance increases. The turbidity current was suspended in the water and it did not affect the measurement of the change in basal pore pressure, which was measured by the PPTs beneath the flows. Hence, the thickness of the turbidity current was not taken into account for the measured flow heights. Further details on the measured flow heights are discussed in the later part of this section.

The side Cameras 1 to 4 only gave a limited view of the flow distance (range between 2-3 cm long). This resulted in difficulty in checking the scaling laws on flow velocity and flow distance. In order to check the scaling laws for the flow velocity and flow distance, a larger flow distance was extracted from Camera 5 (plan view), where a flow distance of approximately 30 cm could be seen. Figure 4.23 shows the sequence of the submarine landslide flow from the plan view. The interval of these pictures is at 0.033s. In order to extract the flow distance and time from each picture frame, Photoshop was used to combine these picture frames as shown in Figures 4.24 to 4.27 for 30 g, 40 g, 50 g and 60 g respectively. Note that the measured flow distance were may be subjected to potential error as the pictures from Camera 5 were subjected to distortions since the actual model is a curvature while the pictures were capture in plan view.

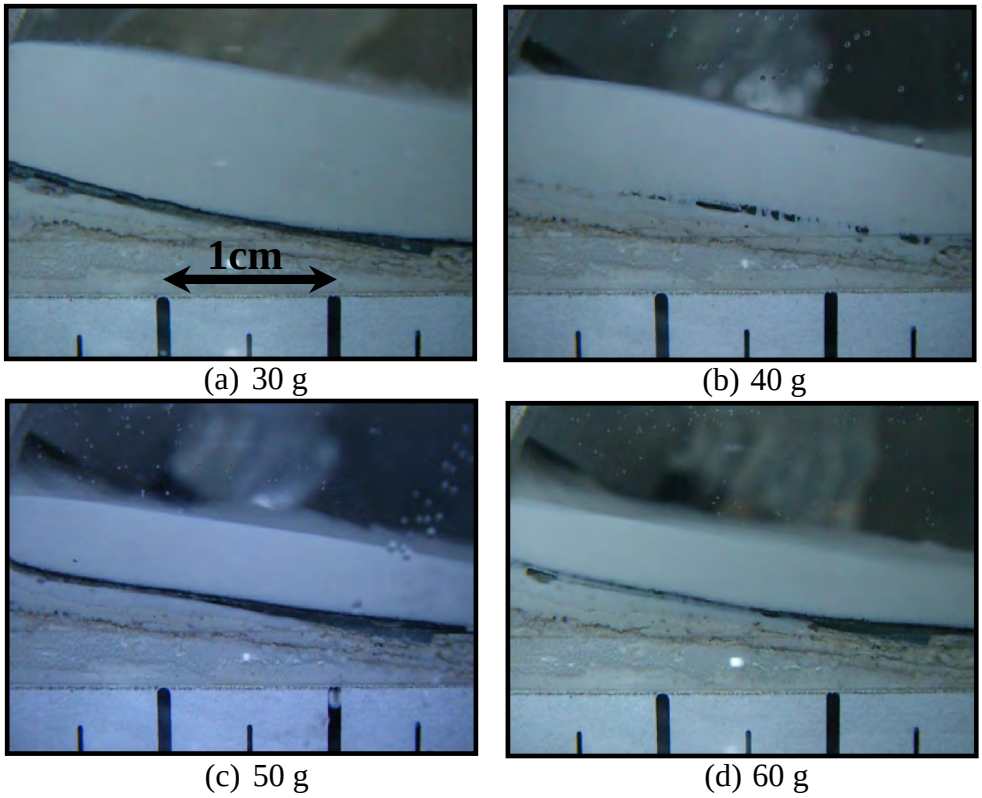

(a) 30 g (b) 40 g

(c) 50 g (d) 60 g

Figure 4.19: Side view of submarine landslide flows for various g levels from Camera 1 (0 m from opening of head tank)

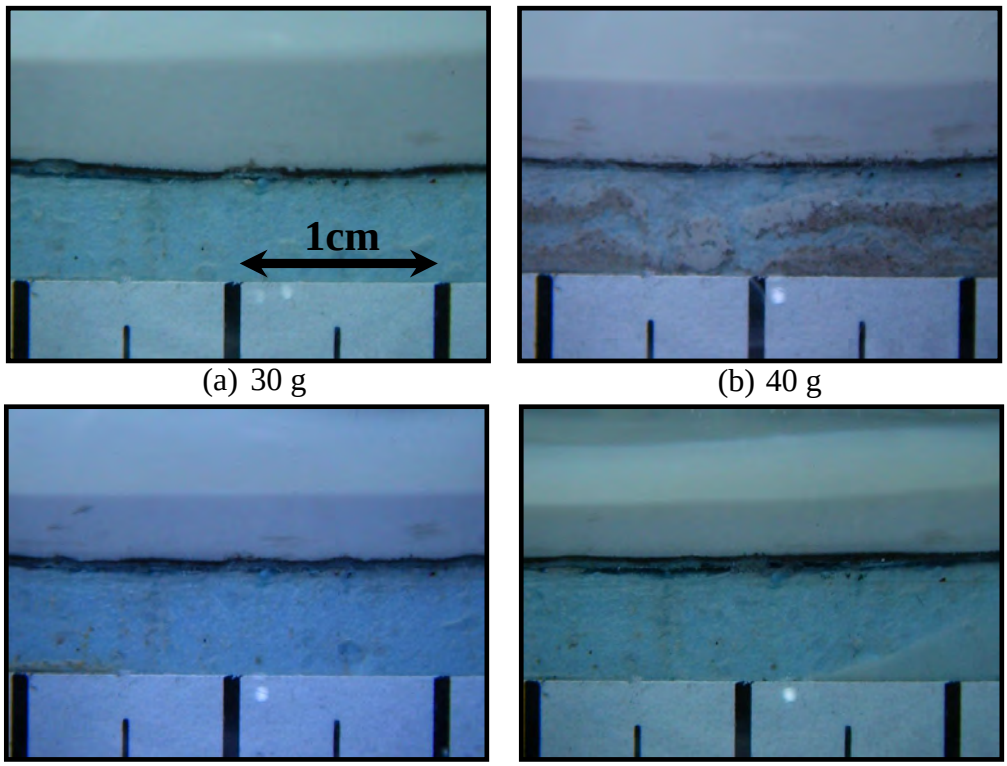

(a) 30 g (b) 40 g

(c) 50 g (d) 60 g

Figure 4.20: Side view of submarine landslide flows for various g levels from Camera 2 (0.17 m from opening of head tank)

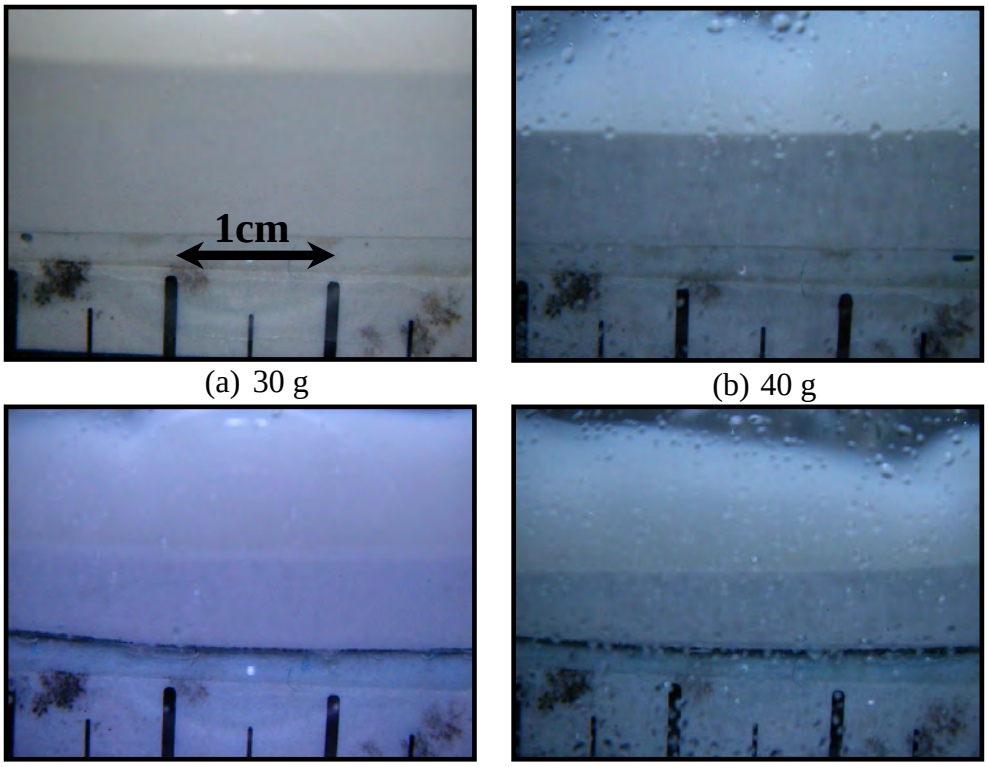

(a) 30 g (b) 40 g

(c) 50 g (d) 60 g

Figure 4.21: Side view of submarine landslide flows for various g levels from Camera 3 (0.36 m from opening of head tank)

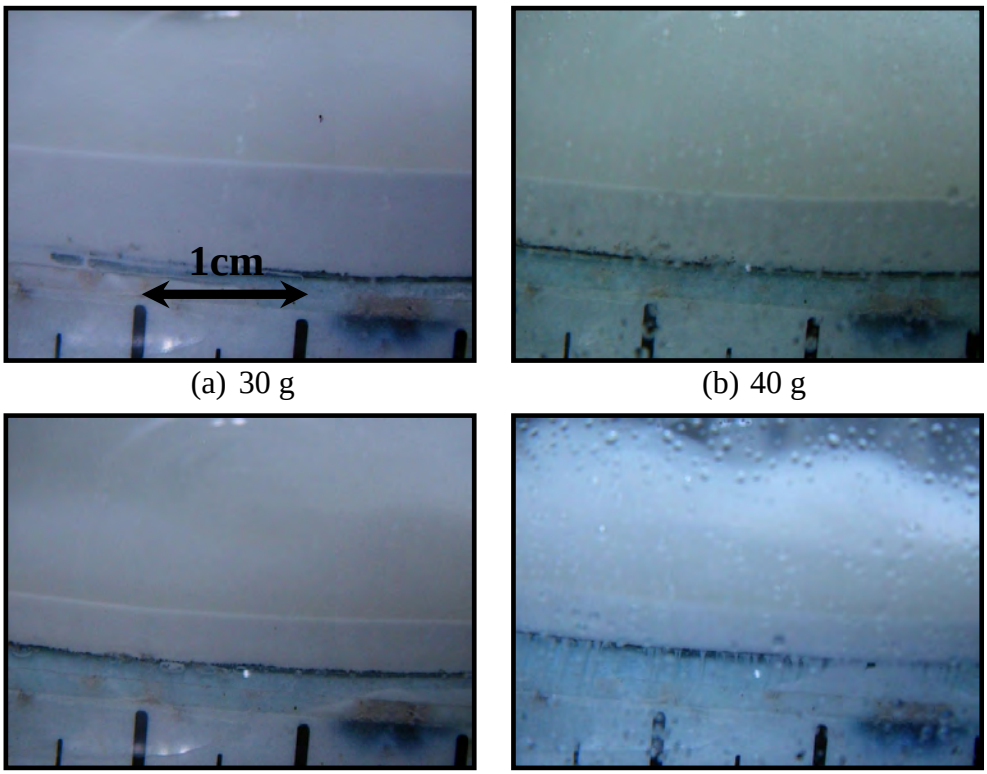

(a) 30 g (b) 40 g

(c) 50 g (d) 60 g

Figure 4.22: Side view of submarine landslide flows for various g levels from Camera 4 (0.57 m from opening of head tank)

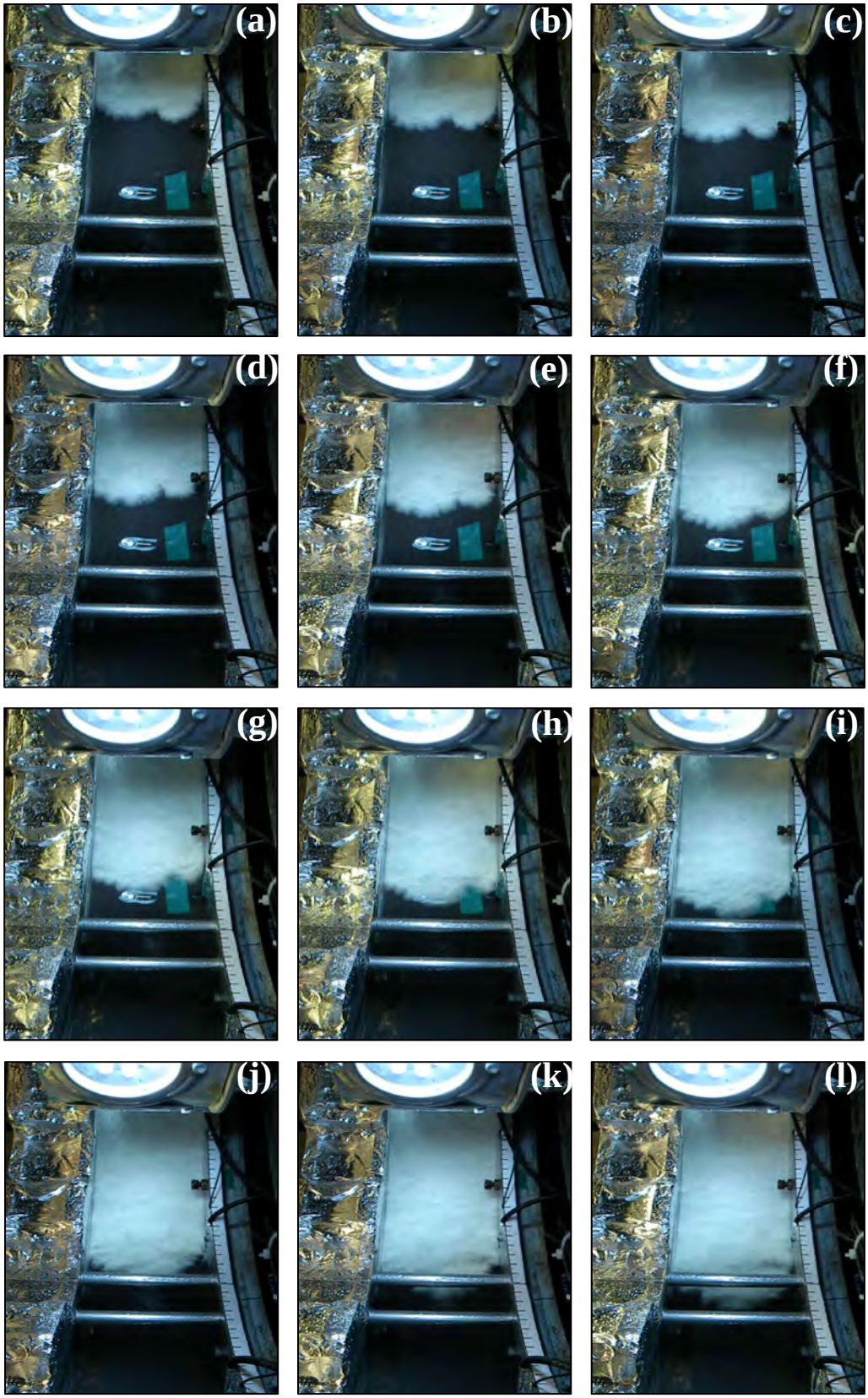

Figure 4.23: Plan view of submarine landslide flows from Camera 5 (picture interval at 0.033s)

Figure 4.24: Combined picture frames from plan view for flow at 30 g

Figure 4.25: Combined picture frames from plan view for flow at 40 g

Figure 4.26: Combined picture frames from plan view for flow at 50 g

Figure 4.27: Combined picture frames from plan view for flow at 60 g

Figure 4.28 shows the flow distance against time for various g levels. The slope of the flow distance against time gives the frontal velocity of the flow. The velocities are relatively constant after 0.3 s, while the flow at the beginning is not so representative to the overall flow due to the pouring impact of the slurry from the funnel onto the slope and the transition time required to reach the steady state condition. In addition, as mentioned before the measured flow distance were may be subjected to potential error as the pictures from Camera 5 were subjected to distortions since the actual model is a curvature while the pictures were capture in plan view, in which the earlier part of the flow is subjected to more image distortion. Therefore, an average flow velocity for each flow is established after 0.3 s, as shown in Table 4.3.

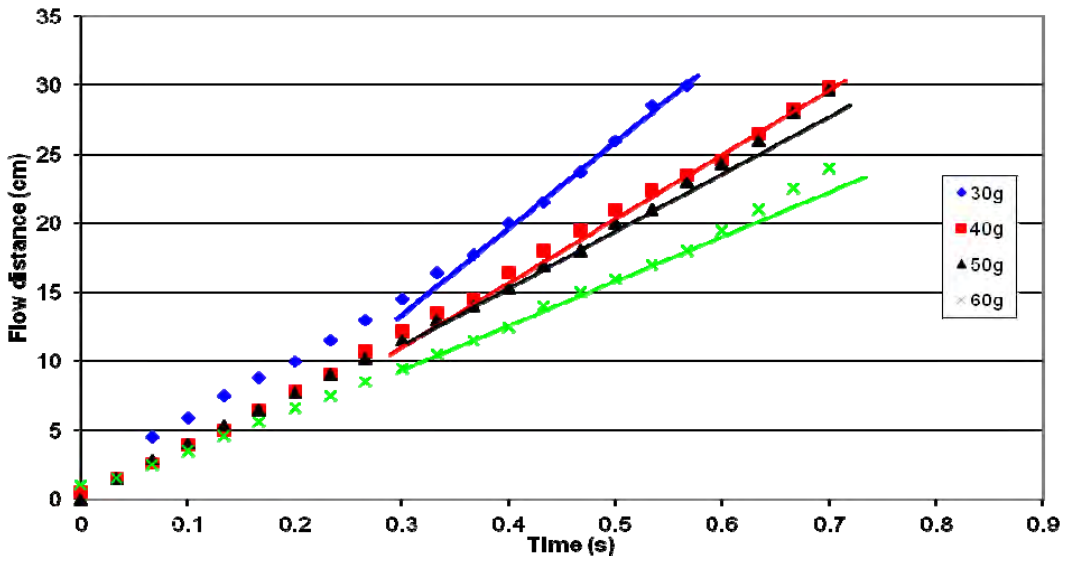

Figure 4.28: Flow distance against time for flows at various g levels

Table 4.4 shows the summary of the measured and back-calculated flow heights from the experiments at various g levels. A range of upper and lower bounds of the measured flow heights from the four side cameras are also given here. The measured flow heights are taken from the visual inspection of the videos from the side cameras. These flow heights fluctuate along the slope due to the pouring impact of the slurry from the funnel onto the slope, as well as the small drop between the joint of the two slope compartments. Since the flow height fluctuates along the slope, the back-calculated flow height for each

experiment is given in Table 4.4. The back-calculated flow heights are computed by dividing the known flow rate per unit length, Q_{ul} by the measured frontal velocity.

It can be seen that the back-calculated flow heights are slightly lower than the measured flow heights. This may be due to the suspension of the flow slurry in the submerged condition, in which the visual inspection of the flow height through the cameras may over-estimate the flow heights. In the submerged condition, water may entrap in the flow thus increasing the flow height. The back-calculated flow height is assumed to have no water entrapment.

The prototype flow velocities and flow heights in Tables 4.3 and 4.4 respectively indicate that, by specifically scaling the flow rate, the scaled flow velocity and height are achieved. It should be noted that, based on the centrifuge tests data, the scaling law for time ($t_{prototype} = N^2 t_{model}$) cannot be demonstrated due to the fact that the flow velocity reached the steady state very quickly, and therefore it was not possible to check the scaling law for time. However, the scaling law for flow velocity seems to be based on the proposed scaling laws.

Table 4.3: Summary of the measured flow velocities for various g levels

g levels	**Average flow velocity, $\bar{v}$ (m/s)**	**Average prototype flow velocity, $\bar{v}_p = N^* \bar{v}$ (m/s)**
30	0.60	18.0
40	0.45	18.0
50	0.37	18.5
60	0.32	19.2

Table 4.4: Summary of the measured and back-calculated flow heights for various g levels

g levels	Flow height, h (m)			Back calculated averaged flow height, $\bar{h}_{BC}$ (m)	Prototype flow height, $\bar{h}_P = N * \bar{h}$ (m)	Prototype back calculated flow height, $\bar{h}_{PBC} = N * \bar{h}_{BC}$ (m)
	Lower bound	Upper bound	Averaged flow height			
30	0.0066	0.0082	0.0074	0.0058	0.22	0.18
40	0.0048	0.0057	0.0052	0.0044	0.21	0.18
50	0.0032	0.0052	0.0042	0.0034	0.21	0.17
60	0.0031	0.0039	0.0035	0.0028	0.21	0.17

Figure 4.29 shows the prototype flow distance against the prototype time at various g levels. The prototype scale is based on the proposed scaling laws, where the flow distance is scaled at N^3 times of the model and the time is scaled at N^2 times of the model. It can be seen that the centrifuge experimental data from various g levels scaled reasonably well to the proposed scaling laws.

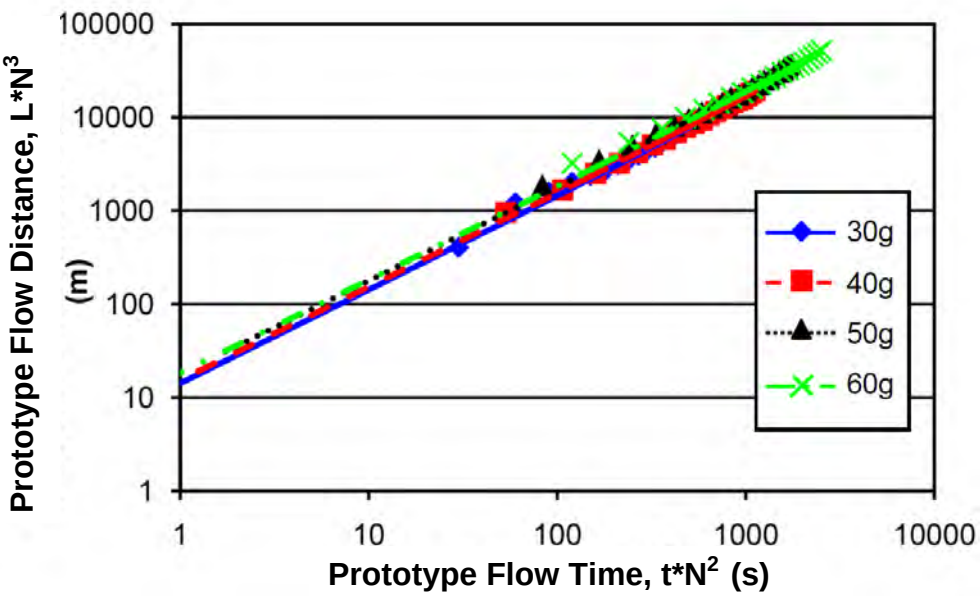

Figure 4.29: Prototype flow distance against prototype flow time based on the proposed scaling laws

Figure 4.30 shows the relationship of flow velocities and g levels. If this figure gives the correct relationship, then it will be useful in predicting the

actual flow velocity in the field when the submarine landslide thickness is approximately 0.21 m for a given boundary and soil slurry condition. It should be noted that the flow velocity in the field differs from those obtained from the experiments, as the flow velocity depends on the type of viscous fluid mixture, the thickness of flow and the basal friction. However, the proposed scaling law for flow velocity appears to be valid.

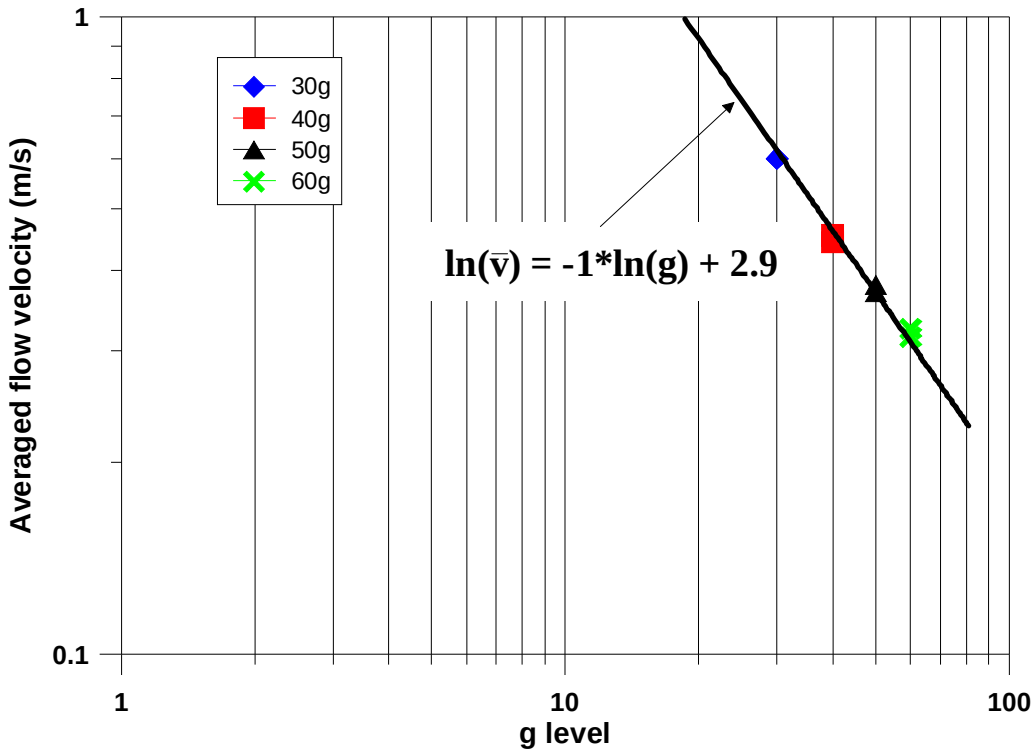

Figure 4.30: Relationship of flow velocity and g level

4.6.2 Series 2: Experiments at 30 g only with various flow rates

This series of experiments was performed only at 30 g with various flow rates. It should be noted that these experiments were carried out before the series of experiments at various g levels and flow rates in section 4.6.1. The purpose of this series of experiment was to investigate the possibility of producing results to distinguish the flows from the various flow rates under the same g level (30 g). Therefore, the flow rates used in this series of experiments were the same as in 4.6.1.

Table 4.5 shows the details of the experiments at 30 g with their corresponding flow rates. Theoretically, this will not give a similar prototype height from this series of tests as the flow heights and velocities are scaled to the appropriate g levels.

Table 4.5: Experimental details of flow rates for experiments at 30 g

g levels	Funnel opening, diameter (mm)	Average flow rate, Q (m^3/s)*10^{-4}	Average flow rate per unit length, Q_{ul} ($m^3/s/m$) *10^{-3}	Average prototype flow rate per unit length, Q_{Pul} ($m^3/s/m$)
30	19.4	3.50	3.50	3.2
30	13.9	1.97	1.97	1.8
30	12.0	1.26	1.26	1.1
30	9.7	0.88	0.88	0.8

Figure 4.31 shows the change in pore pressure measured beneath the submarine landslide flows along the slope at various locations for the four experiments at 30 g. Similar to Figure 4.18, the change in pore pressure increases when the front of the flow arrives at the location of the PPTs. The change in pore pressure at various locations along the slope for each experiment of the specific flow rate is relatively similar, thus indicating that the flow height along the slope is relatively constant (i.e. steady state). It can also be seen that the change in pore pressure increases with higher flow rates, indicating increasing modelled flow height.

Similarly, Figure 4.32 shows the averaged measured pore pressure with the input flow rate per unit width, Q_{ul}. This figure clearly indicates that, at the same g level, the high flow rates induce higher changes in pore pressure.

Figures 4.33 (a) to (d) show the side view of the submarine landslide flows from Camera 1 for flow rates of 3.50*10^{-3} $m^3/s/m$ width, 1.97*10^{-3} $m^3/s/m$ width, 1.26*10^{-3} $m^3/s/m$ width, and 0.88*10^{-3} $m^3/s/m$ width

respectively at the opening of the head tank where PPT1 was located. It can be seen that the flow heights are smaller at lower flow rates.

Similarly, Figures 4.34 to 4.36 show the side view of the submarine landslide flows from Camera 2 (0.17 m from the opening of the head tank), Camera 3 (0.36 m from the opening of the head tank) and Camera 4 (0.57 m from the opening of the head tank) respectively for the various flow rates.

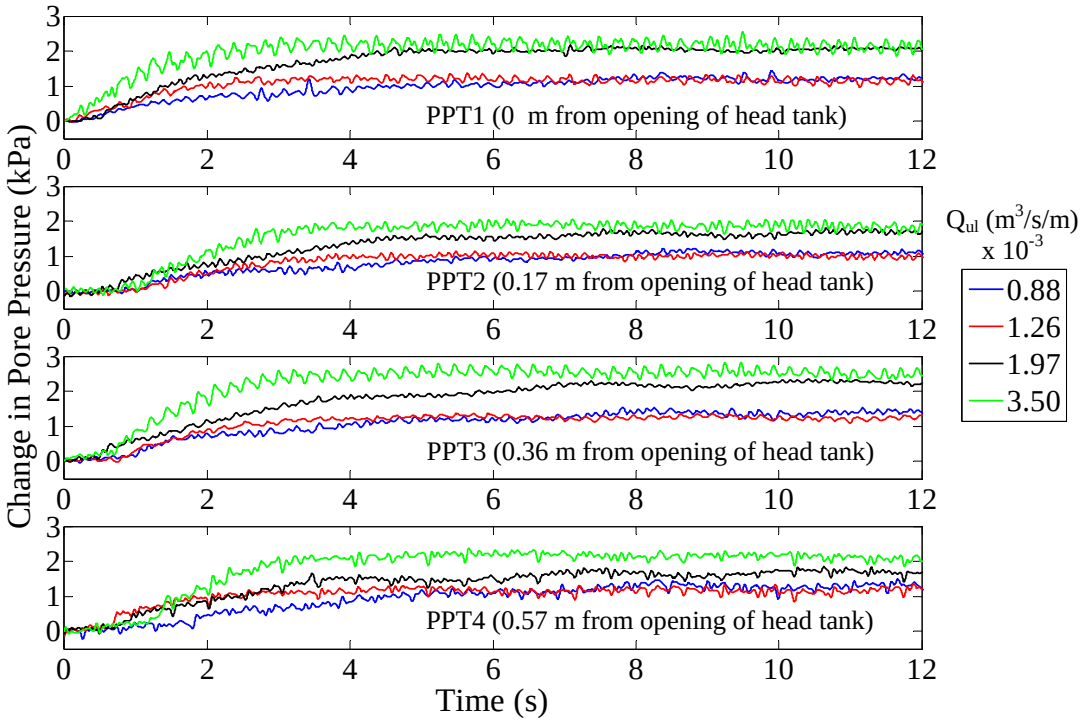

Figure 4.31: The change in pore pressure for experiments at 30 g at various locations along the slope

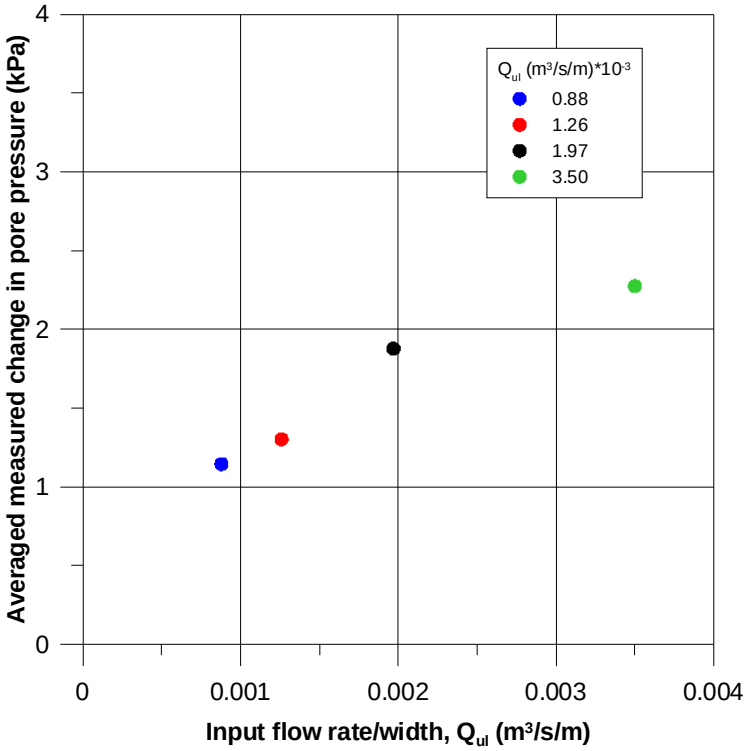

Figure 4.32: Relationship of pore pressure and input flow rate for Series 2

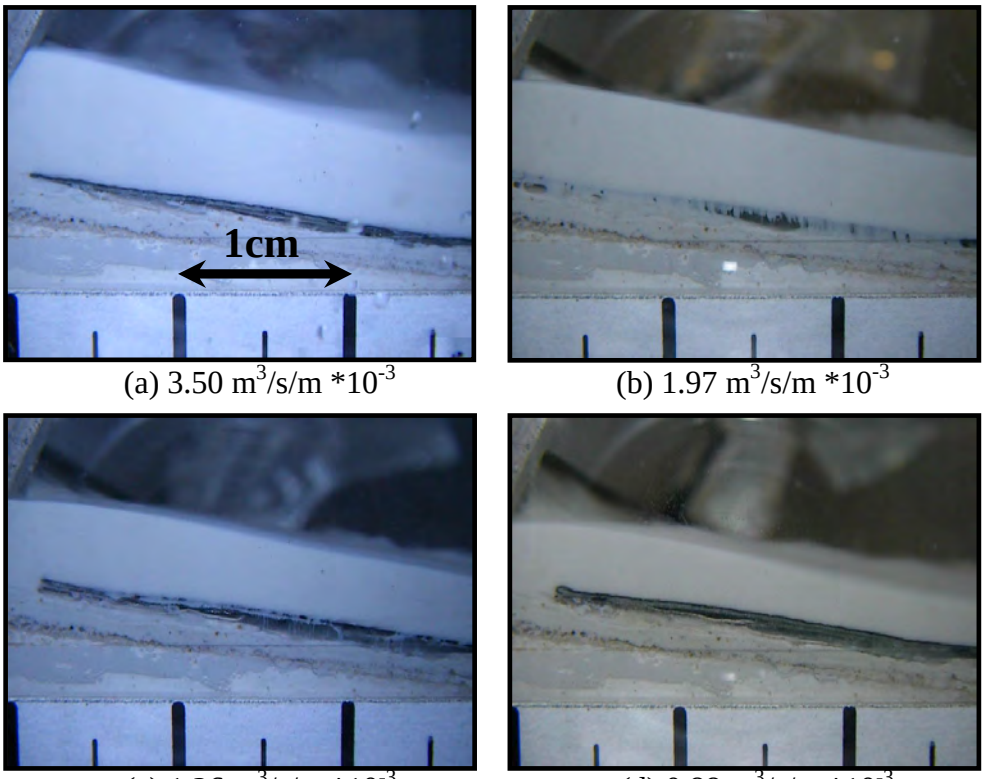

(a) 3.50 $m^3/s/m$ *10^{-3} (b) 1.97 $m^3/s/m$ *10^{-3}

(c) 1.26 $m^3/s/m$ *10^{-3} (d) 0.88 $m^3/s/m$ *10^{-3}

Figure 4.33: Side view of submarine landslide flows for various flow rates at 30 g from Camera 1 (0 m from opening of head tank)

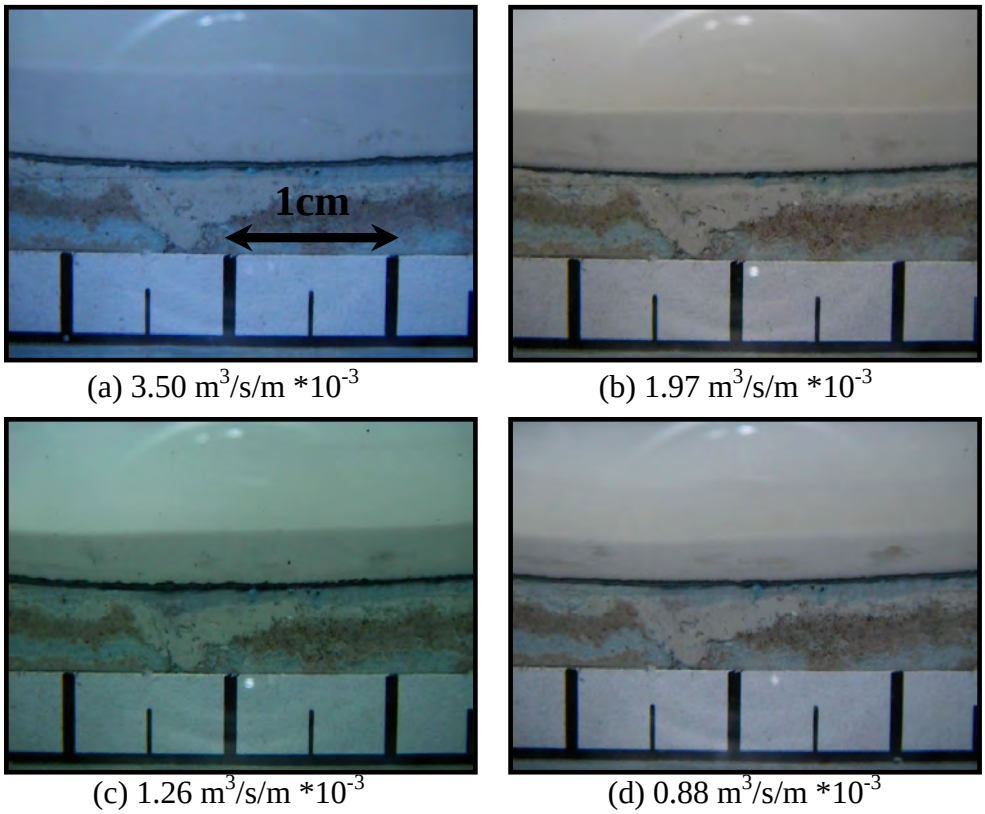

(a) 3.50 $m^3/s/m *10^{-3}$ (b) 1.97 $m^3/s/m *10^{-3}$

(c) 1.26 $m^3/s/m *10^{-3}$ (d) 0.88 $m^3/s/m *10^{-3}$

Figure 4.34: Side view of submarine landslide flows for various flow rates at 30 g from Camera 2 (0.17 m from opening of head tank)

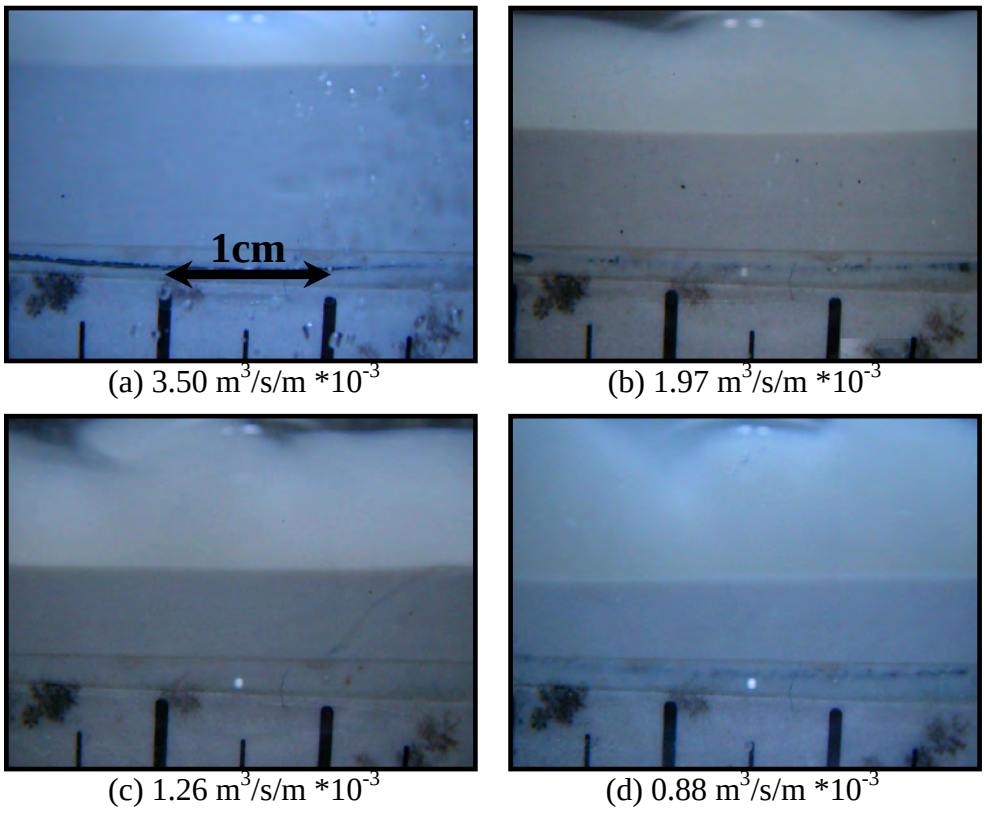

(a) 3.50 $m^3/s/m *10^{-3}$ (b) 1.97 $m^3/s/m *10^{-3}$

(c) 1.26 $m^3/s/m *10^{-3}$ (d) 0.88 $m^3/s/m *10^{-3}$

Figure 4.35: Side view of submarine landslide flows for various flow rates at 30 g from Camera 3 (0.36 m from opening of head tank)

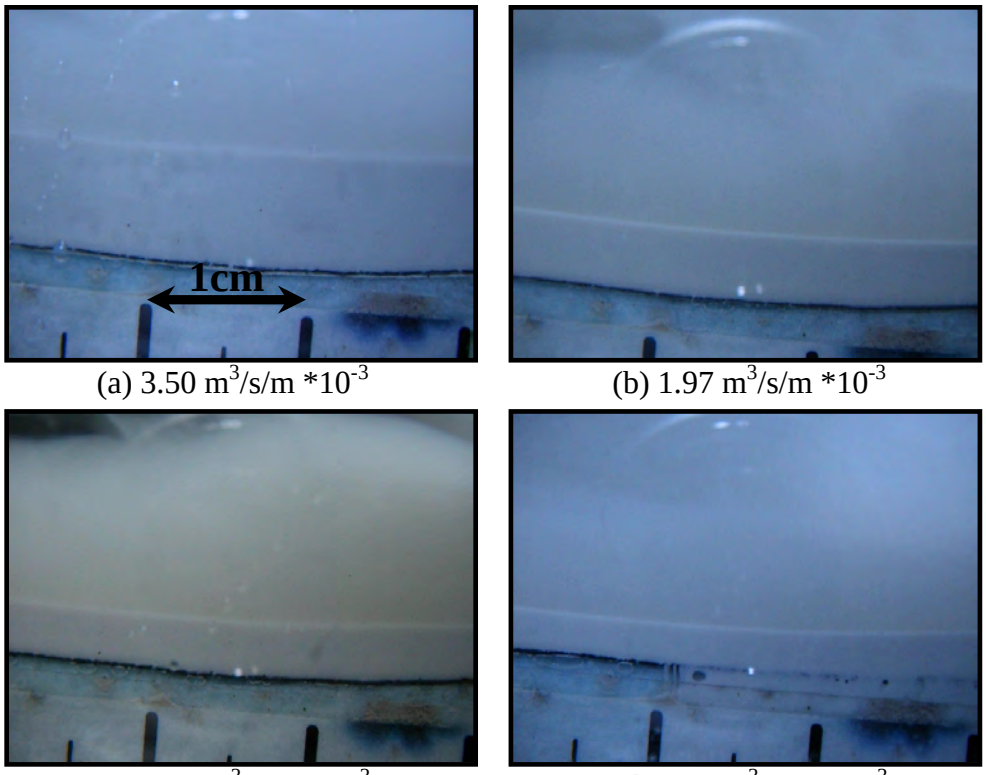

(a) 3.50 $m^3/s/m *10^{-3}$ (b) 1.97 $m^3/s/m *10^{-3}$

(c) 1.26 $m^3/s/m *10^{-3}$ (d) 0.88 $m^3/s/m *10^{-3}$

Figure 4.36: Side view of submarine landslide flows for various flow rates at 30 g from Camera 4 (0.57 m from opening of head tank)

Figure 4.37 shows the flow distance against time for various flow rates. Similar to the previous section, the range of frontal flow velocities (upper and lower bounds) for each experiment is established after 0.3 s, when the steady state condition seems to have been achieved. In addition, as mentioned before the measured flow distance were may be subjected to potential error as the pictures from Camera 5 were subjected to distortions since the actual model is a curvature while the pictures were capture in plan view, in which the earlier part of the flow is subjected to more image distortion. Therefore, an average flow velocity for each flow is established after 0.3 s, as shown in Table 4.6.

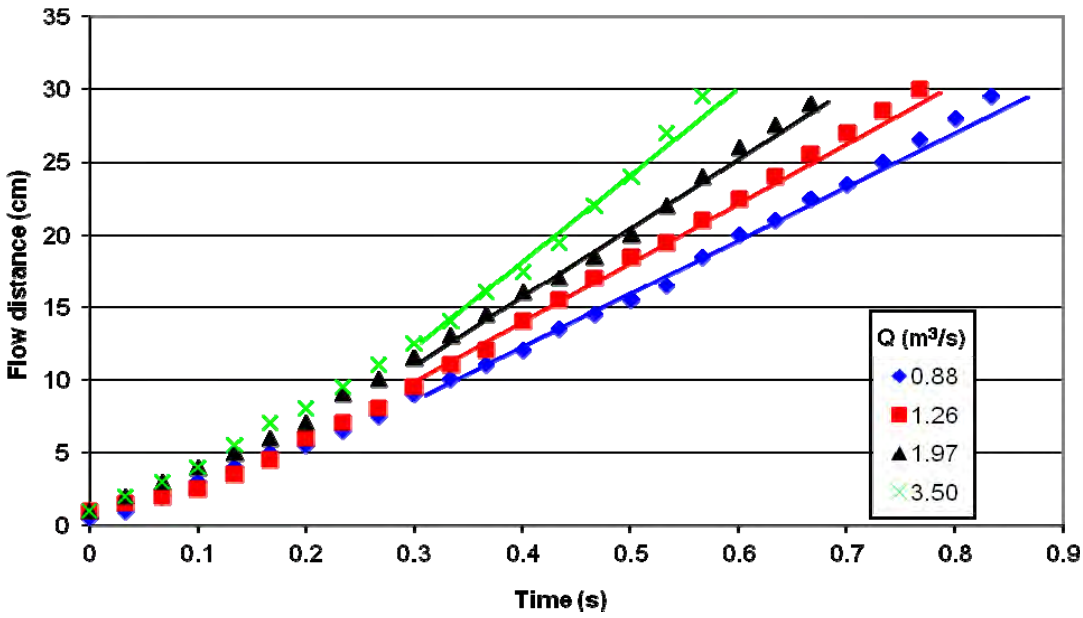

Figure 4.37: Flow distance against time for flows at various flow rates

From Table 4.6, it can be seen that the flow velocity reduces with flow rate, which also corresponds with the smaller flow heights at lower flow velocity as shown in Table 4.7. The relationship of flow rate per unit width and the range of flow velocities is shown in Figure 4.38. This clearly indicates that at a constant g level (30 g) the higher flow rates produce higher flow velocity.

Figure 4.39 shows the relationship of prototype flow velocity and prototype flow rate. Also included in this figure are the data from Series 1 (with scaled flow rates and flow velocities). This again confirms that at a constant g level (30g), the prototype flow velocity increases with the prototype flow rate. While the data from Series 1 are scaled, the prototype flow velocities and prototype flow rates are seen to be relatively similar at various g levels, as shown in this figure.

Table 4.6: Summary of the measured flow velocities for various flow rates at 30 g

Average prototype flow rate per unit length, Q_{Pul} ($m^3/s/m$)	Average flow velocity, $\bar{v}$ (m/s)	Average prototype flow velocity, $\bar{v}_p = N^* \bar{v}$ (m/s)
3.2	0.60	18.0
1.8	0.46	13.8
1.1	0.39	11.7
0.8	0.35	10.5

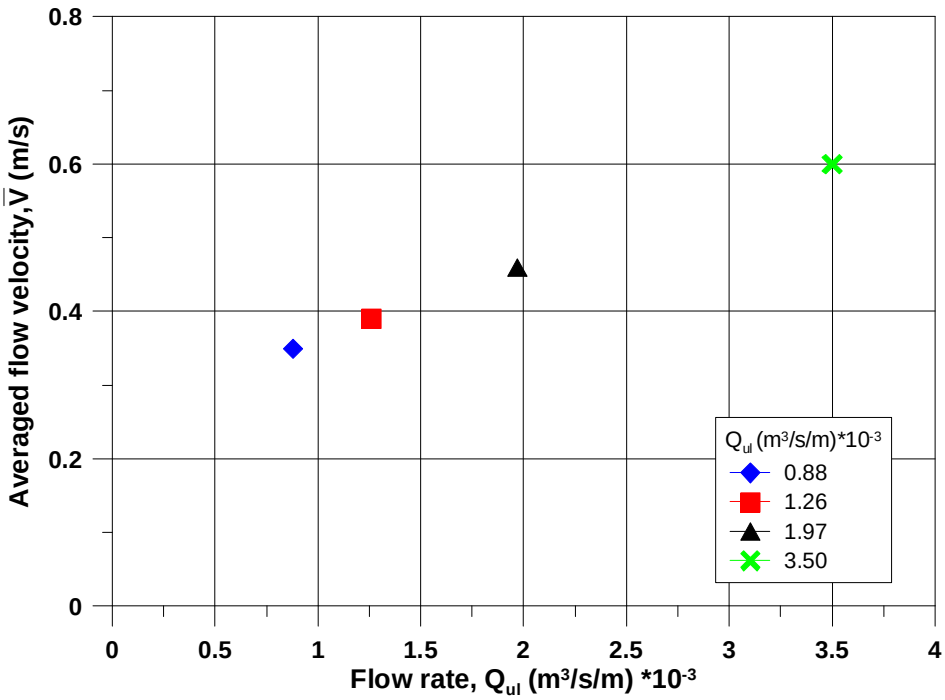

Figure 4.38: Relationship of flow velocity and flow rate at 30 g

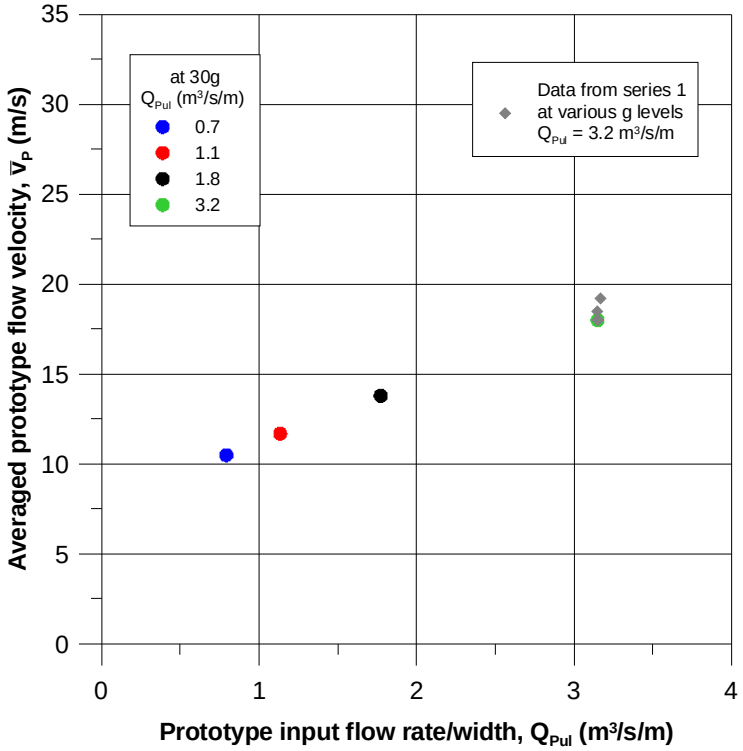

Figure 4.39: Relationship of prototype flow velocity and prototype flow rate for Series 1 and 2

Table 4.7 shows the summary of the measured and back-calculated flow heights from the experiments at various flow rates. Since the flow height fluctuates along the slope during the flow, a range of upper and lower bounds of the flow heights measured from the four side cameras are given in Table 4.7. The average flow heights are the average of the upper and lower bounds. The back-calculated flow heights are also given in Table 4.7.

Figure 4.40 shows the averaged measured flow height with the input flow rate per unit metre width, Q_{ul}. Both the measured and back-calculated flow heights are included in this figure. Similar to the previous section, the back-calculated flow heights are slightly lower than the measured flow heights. This again indicates that visual inspection of the flow height may have over-estimated the flow heights. It can be seen that the measured flow heights are consistently higher by approximately 19 to 29% than the back-calculated flow heights. Even though the back calculated flow heights are

smaller than the measured flow heights; the measured flow heights based on the visual inspection from the side cameras are shown to be consistent.

Figure 4.41 shows the relationship of prototype back-calculated flow height and prototype flow rate. Also included in this figure are the data from Series 1 (with scaled flow rates and flow heights). This also demonstrates that at a constant g level (30g), the prototype flow height increases with the prototype flow rate. Hence, the data from the tests at various g levels in Series 1 show that the prototype flow heights and prototype flow rates are relatively similar.

Table 4.7: Summary of the measured and back-calculated flow heights for various flow rates at 30 g

Average prototype flow rate per unit length, Q_{Pul} ($m^3/s/m$)	Flow height, h (m)			Back calculated averaged flow height, $\bar{h}_{BC}$ (m)	Prototype flow height, $\bar{h}_P = N^* \bar{h}$ (m)	Prototype back calculated flow height, $\bar{h}_{PBC} = N^* \bar{h}_{BC}$ (m)
	Lower bound	Upper bound	Averaged flow height			
3.2	0.0068	0.0080	0.0074	0.0058	0.22	0.18
1.8	0.0049	0.0055	0.0052	0.0043	0.16	0.13
1.1	0.0033	0.0050	0.0042	0.0032	0.13	0.10
0.8	0.0030	0.0040	0.0035	0.0025	0.11	0.08

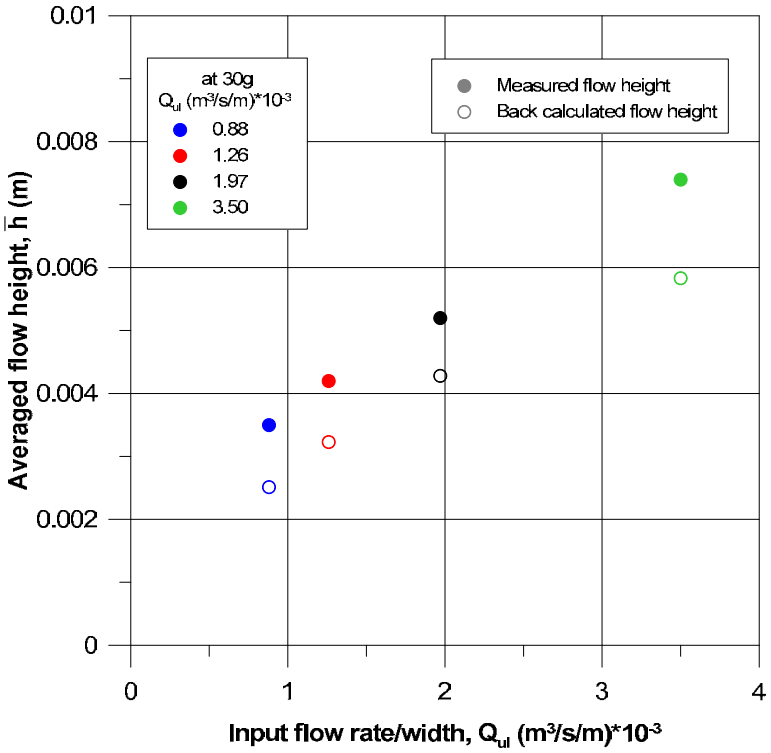

Figure 4.40: Relationship of measured and back-calculated flow height and input flow rate for Series 2

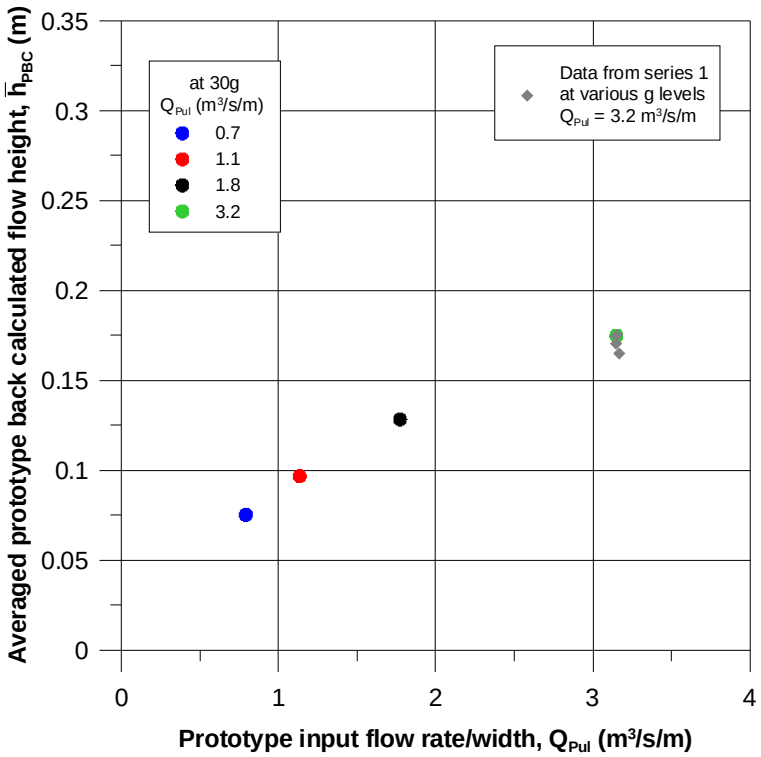

Figure 4.41: Relationship of prototype flow height and prototype flow rate for Series 1 and 2

4.6.3 Series 3: Experiments at various g levels with a large flow rate

This series of experiments was performed at various g levels with a larger flow rate. The purpose of these experiments was to simulate a higher prototype flow height. Table 4.8 shows the details of the experiments at various g levels with their corresponding flow rates and funnel opening diameters. The large flow rate from this section onwards refers to the flow rate of $1.09*10^{-3}$ m^3/s or $10.9*10^{-3}$ $m^3/s/m$ for the flow rate per unit length.

Table 4.8: Experimental details of flow rates and funnel opening diameter for the series of experiments at the large flow rate

g levels	Funnel opening, diameter (mm)	Average flow rate, Q $(m^3/s)*10^{-3}$	Average flow rate per unit length, Q_{ul} $(m^3/s/m)*10^{-3}$	Average prototype flow rate per unit length, Q_{Pul} $(m^3/s/m)$
30	46	1.09	10.9	9.8
40	46	1.09	10.9	17.4
50	46	1.09	10.9	27.3
60	46	1.09	10.9	39.2

Figure 4.42 shows the change in pore pressure measured beneath the submarine landslide flows along the slope at various locations for the experiments at various g levels with the large flow rate. Similar to the two series of experiments in sections 4.6.1 and 4.6.2, the change in pore pressure increases when the front of the flow arrives at the location of the PPTs.

The change in pore pressure at various locations along the slope for experiments at their specific g level is relatively similar, thus indicating that the flow height along the slope is relatively constant. The only exception is for the experiment at 50 g where there is a dip in the middle of the flow. This dip is consistent throughout the various locations of the slope for the experiment at

50 g. This dip is due to a sudden jerk from a slight distraction while pouring the slurry into the funnel.

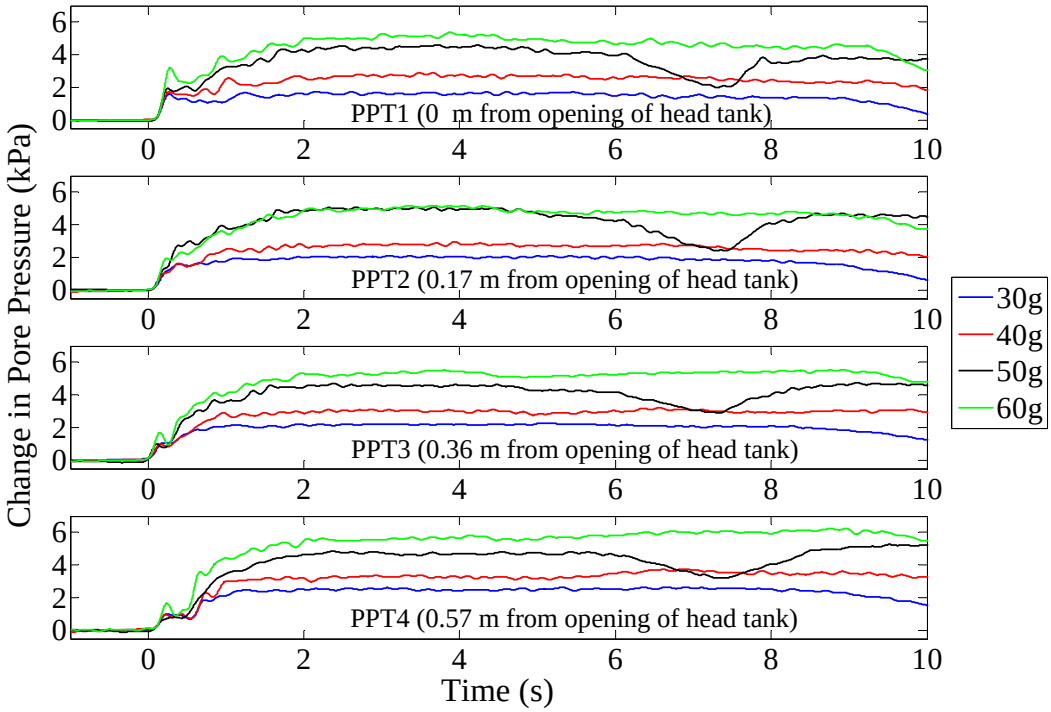

Figure 4.42: The change in pore pressure for various g levels with the large flow rate at various locations along the slope

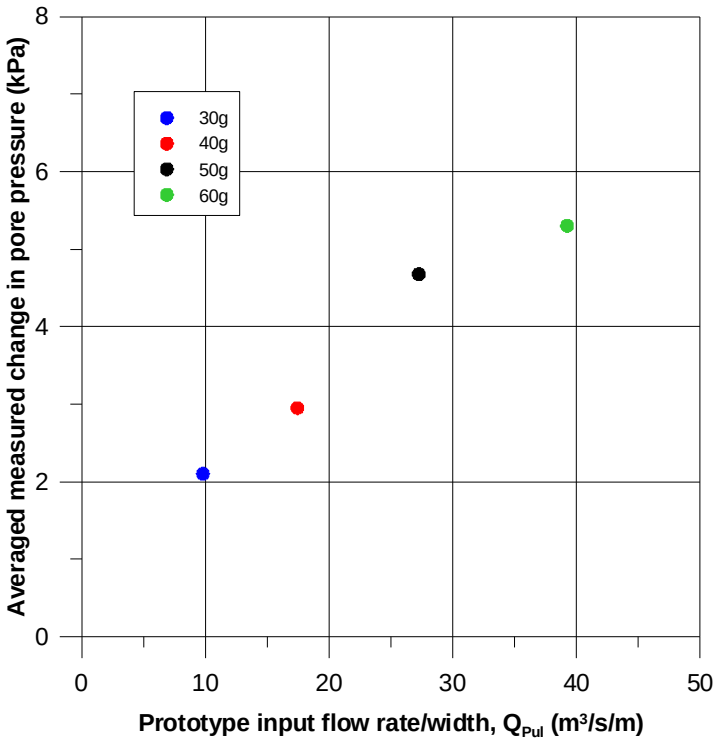

Figure 4.43: Relationship of pore pressure and the prototype input flow rate for Series 3

Figure 4.43 shows the relationship of the measured change in pore pressure and the prototype input flow rate per unit width for Series 3. It can be seen that the measured change in pore pressure increases with the prototype flow rate. This indicates that, at a similar large input flow rate, a large g test models a higher prototype flow rate hence models a submarine landslide with a larger flow height.

Figure 4.44 shows the flow distance against time for the experiments at various g levels with the large flow rate. The flow rate in the experiments of this series is relatively large, which tends to give a larger flow velocity compared to the previous series of experiments. The flow at the beginning is not so representative of the overall flow due to the pouring impact of the slurry from the funnel onto the slope. In addition, as mentioned before the measured flow distance were may be subjected to potential error as the pictures from Camera 5 were subjected to distortions since the actual model is a curvature while the pictures were capture in plan view, in which the earlier part of the flow is subjected to more image distortion. Therefore, an average flow velocity for each flow is established after 0.1 s, as shown in Table 4.9.

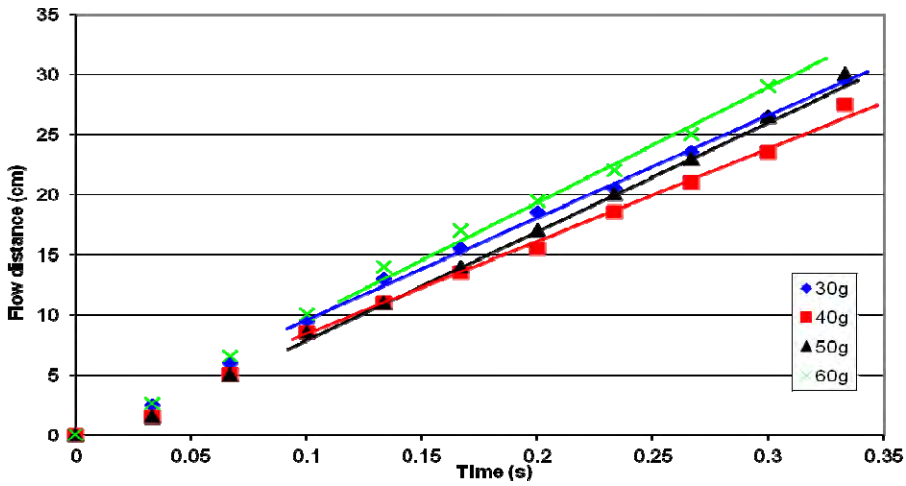

Figure 4.44: Flow distance against time for Series 3

From Table 4.9, it can be seen that the flow velocity increases with g level at a given flow rate. Table 4.10 shows the summary of the measured and back-calculated flow heights from the experiments at various g levels with a large flow rate. Since the flow height fluctuates along the slope during the

flow, a range of upper and lower bounds of the flow heights measured from the four side cameras are given in Table 4.10. The average flow heights are the average of the upper and lower bounds. The back-calculated flow heights are also given in Table 4.10.

Table 4.9: Summary of the measured flow velocities for various g levels with the large flow rate

g levels	Average prototype flow rate per unit length, Q_{Pul} ($m^3/s/m$)	Average flow velocity, $\bar{v}$ (m/s)	Average prototype flow velocity, $\bar{v}_p = N^* \bar{v}$ (m/s)
30	9.8	0.70	21.0
40	17.4	0.78	31.2
50	27.3	0.89	44.5
60	39.2	0.98	58.8

Table 4.10: Summary of the measured and back-calculated flow heights for various g levels with the large flow rate

g levels	Average prototype flow rate per unit length, Q_{Pul} ($m^3/s/m$)	Flow height, h (m)			Back calculated averaged flow height, $\bar{h}_{BC}$ (m)	Prototype flow height, $\bar{h}_P = N^* \bar{h}$ (m)	Prototype back calculated flow height, $\bar{h}_{PBC} = N^* \bar{h}_{BC}$ (m)
		Lower bound	Upper bound	Averaged flow height			
30	9.8	0.0134	0.0192	0.0163	0.0156	0.49	0.47
40	17.4	0.0138	0.0217	0.0177	0.0140	0.71	0.56
50	27.3	0.0158	0.0228	0.0193	0.0123	0.97	0.62
60	39.2	0.0183	0.0215	0.0199	0.0111	1.19	0.67

Similar to the previous section, the back-calculated flow heights are slightly lower then the measured flow heights. This again indicates that visual inspection of the flow height may have over-estimated the flow heights and may not reflect the actual flow height since the slurry is in suspension under the submerged condition. Based on the visual inspection of flow heights, the

flow heights fluctuated greatly as shown in Table 4.10, where the difference in the upper and lower bounds of the flow heights are relatively large. This may have been due to the large flow rate used in this series.

It should be noted that the flow rate used in this series of experiment is relatively large compared with the previous series. The large flow rate was more difficult to control due to the large funnel opening diameter. Also the funnel opening diameter in this series of tests was larger by approximately 137% compared to the largest opening in sections 4.6.1 and 4.6.2.

The relationship of flow velocity and g level is shown in Figure 4.45. It can be seen that the flow velocity increases with g level at a given flow rate. This tends to indicate that additional forces from the higher g level drive the slurry to a faster flow.

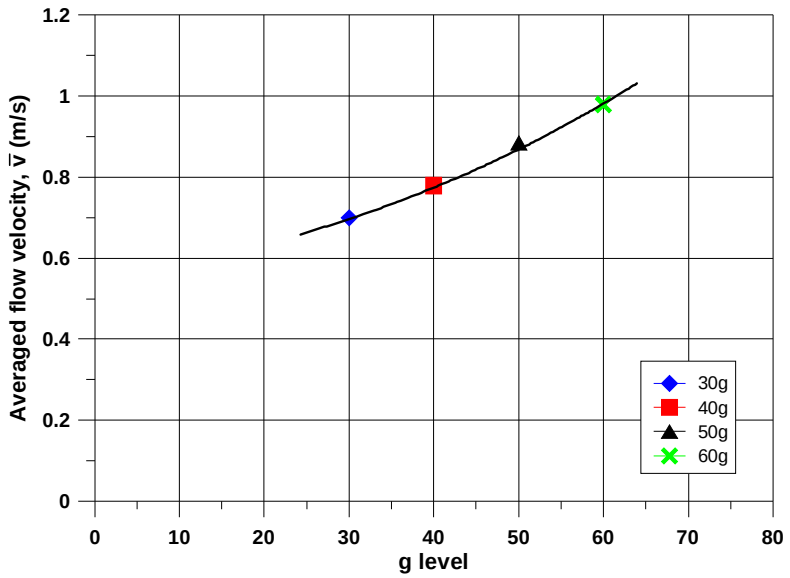

Figure 4.45: Relationship of flow velocity and g level for Series 3

Figure 4.46 shows the relationship of prototype flow velocity and prototype flow rate. This again confirms that, at a given flow rate, a higher g level increases the prototype flow velocity and the prototype flow rate. Similarly, this also reflects the relationship between prototype flow height and prototype flow rate where, at a given flow rate, a higher g level increases the prototype flow height as shown in Figure 4.47. The prototype flow heights in

this figure are the back-calculated flow heights as they are found to be a more reasonable estimate of flow heights, as mentioned previously.

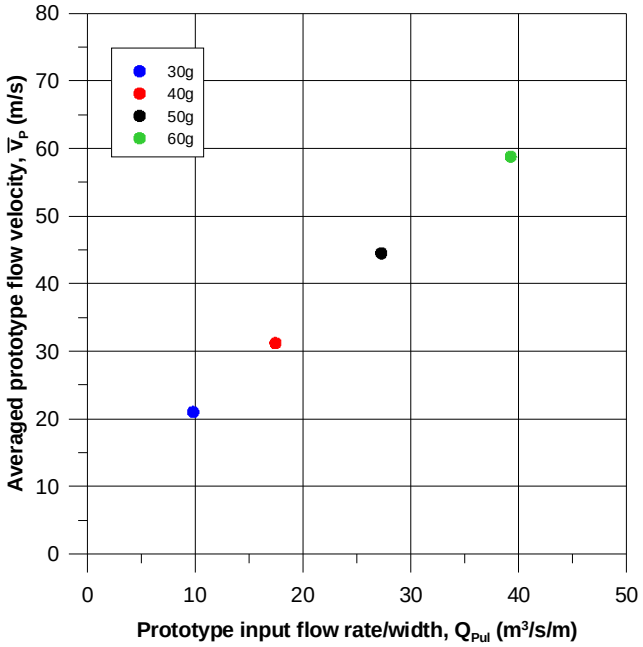

Figure 4.46: Relationship of prototype flow velocity and prototype flow rate for Series 3

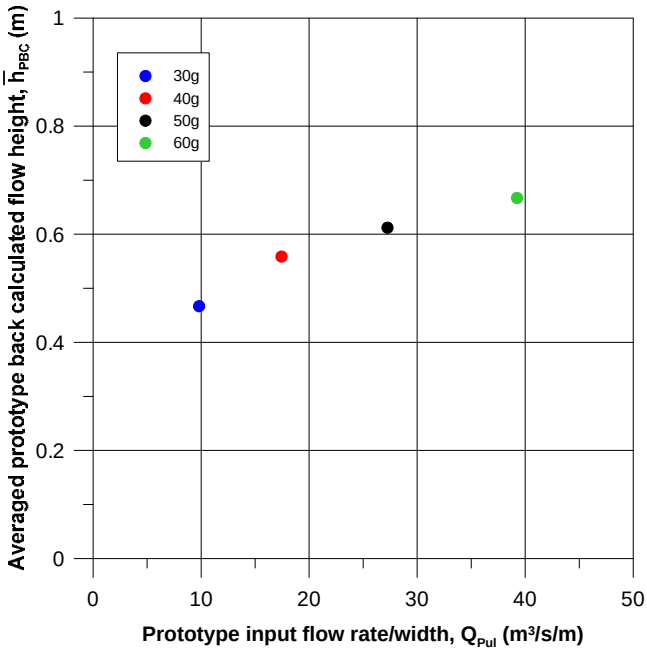

Figure 4.47: Relationship of prototype flow height and prototype flow rate for Series 3

Figures 4.48, 4.49 and 4.50 show the data from Series 1, 2 and 3 on the relationship of prototype flow rate between prototype flow velocity, prototype flow height and the measured change in pore pressure, respectively.

These three graphs consistently show that Series 1, where the flow rates are scaled at various g levels, gives a relatively similar prototype flow height, flow velocity as well as the change in pore pressure. This can be seen from the data points of Series 1 closely plotted together in these three graphs, indicating that the prototype scale is correctly modelled for the tests at various g levels.

Series 2 and Series 3 indicate that the relationship of g level, prototype flow rate, prototype flow velocity and prototype flow height are consistent with the findings between the two series of tests. Accordingly, higher g levels increase the prototype flow velocities and height at a given flow rate, while at a given constant g level (30g) the flow rate increases with the prototype flow velocity and height. It can be observed that there is a leap from Series 2 to 3. However, it is uncertain if this leap is the behaviour of the flow or subjected to other experimental subtle changes such as different clay bathes used in each series. Unfortunately, there are no data points in the transition from Series 2 to 3 to understand the leap. The measured change in pore pressure for these two series is also coherent with the increase in prototype flow height and velocity due to the increase in g levels and flow rates, as shown in Figure 4.50.

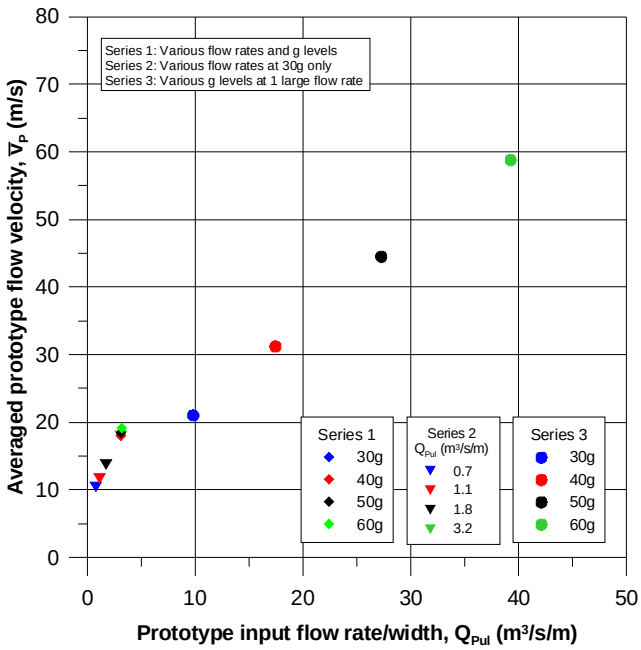

Figure 4.48: Relationship of prototype flow velocity and prototype flow rate for Series 1, 2 & 3

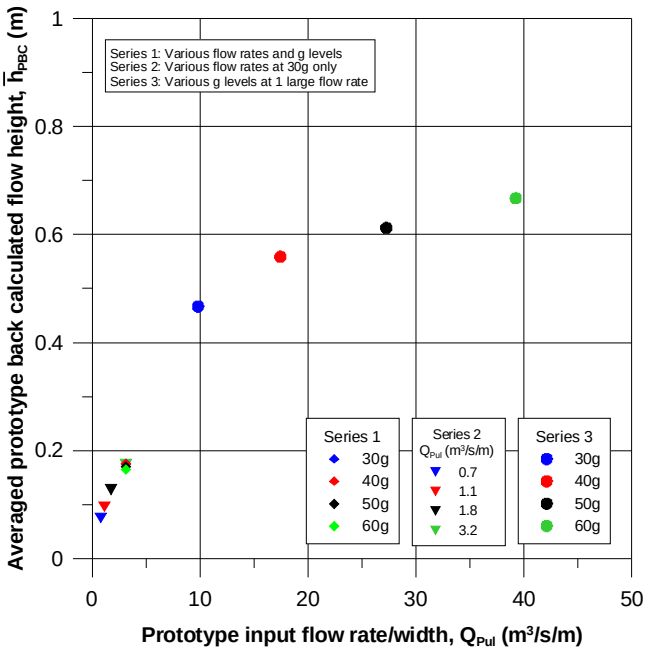

Figure 4.49: Relationship of prototype back-calculated flow height and prototype flow rate for Series 1, 2 & 3

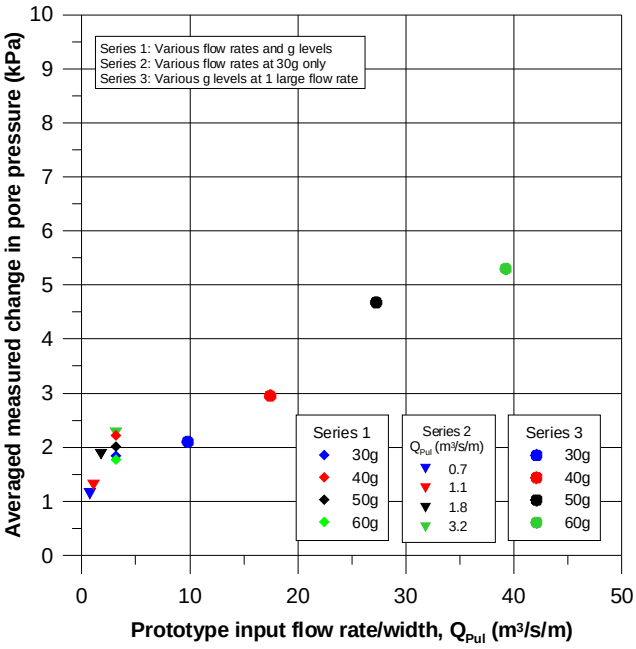

Figure 4.50: Relationship of measured change in pore pressure and prototype flow rate for Series 1, 2 & 3

4.6.4 Series 4: Experiments at various g levels with a large flow rate in the dry condition

This series of experiments was performed at various g levels with the large flow rate and in non-submerged conditions (dry condition). The purpose of these experiments was to understand the influence of drag forces towards the flow resulting from the friction of the surrounding fluid and the slurry flow. Table 4.11 shows the details of the experiments at various g levels with their corresponding flow rate and funnel opening diameter.

Table 4.11: Experimental details of flow rates and funnel opening diameter for experiments in the dry condition

g levels	Funnel opening, diameter (mm)	Average flow rate, Q (m^3/s)*10^{-3}	Average flow rate per unit length, Q_{ul} ($m^3/s/m$)*10^{-3}	Average prototype flow rate per unit length, Q_{Pul} ($m^3/s/m$)
30	46	1.09	10.9	9.8
40	46	1.09	10.9	17.4
50	46	1.09	10.9	27.3
60	46	1.09	10.9	39.2

Figure 4.51 shows the change in pore pressure measured beneath the dry landslide flows along the slope at various locations for the experiments at various g levels, with the large flow rate. It can be seen that the change in pore pressure increases steadily with higher g levels except for the experiment at 60g. This may be due to the problems encountered with the instrumentation for the particular experiment, in which the PPT may not have been fully saturated prior to the test.

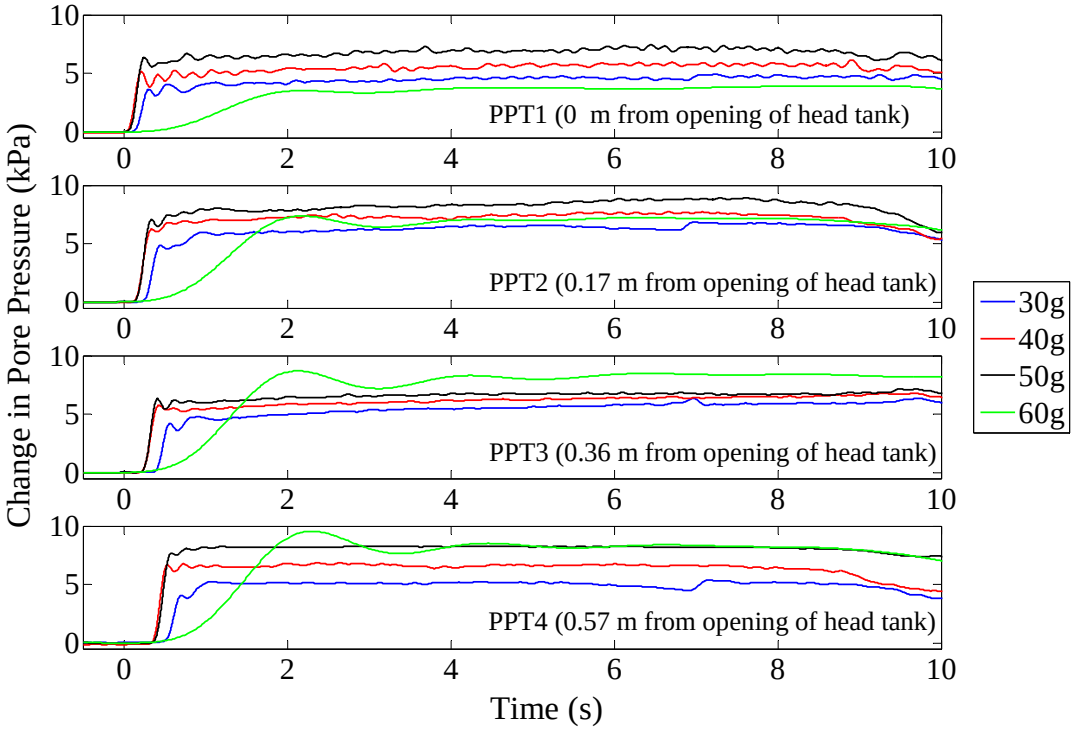

Figure 4.51: The change in pore pressure for various g levels with the large flow rate at various locations along the slope in the dry condition

Figures 4.52 (a) to 4.52 (d) show the side view of the dry landslide flows from Camera 1 for 30 g, 40 g, 50 g, and 60 g respectively at the opening of the head tank where PPT1 was located. The darker image in Figure 4.52 (a) is due to the LED push light above Camera 1 which was accidently switched off during the experiment.

Similarly, Figures 4.53 to 4.54 show the side view of the dry landslide flows from Camera 2 (0.17 m from opening of head tank) and Camera 3 (0.36 m from opening of head tank) respectively for the experiments at various g levels.

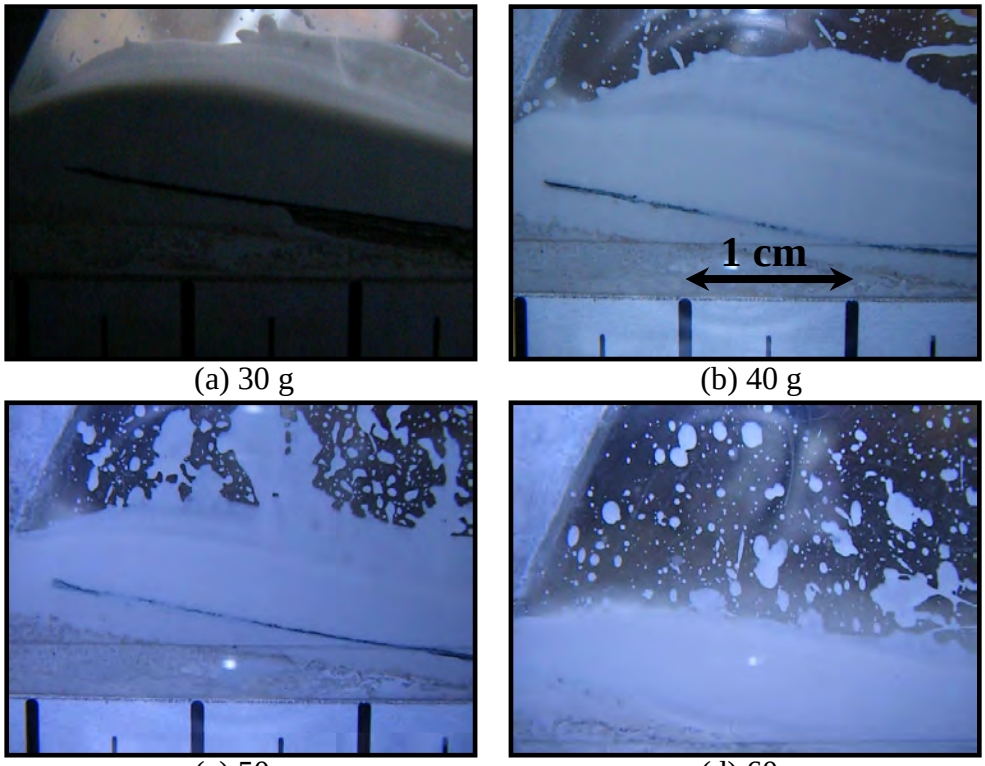

(a) 30 g (b) 40 g

(c) 50 g (d) 60 g

Figure 4.52: Side view of the dry landslide flows for various g levels from Camera 1 (0 m from opening of head tank)

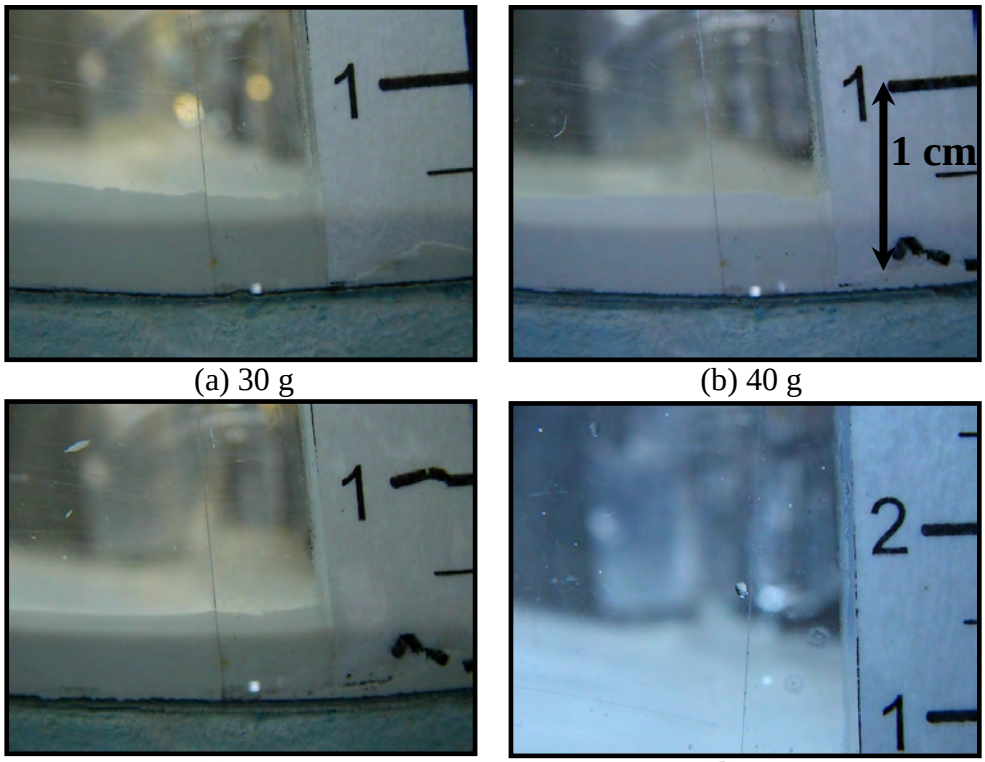

(a) 30 g (b) 40 g

(c) 50 g (d) 60 g

Figure 4.53: Side view of the dry landslide flows for various g levels from Camera 2 (0.17 m from opening of head tank)

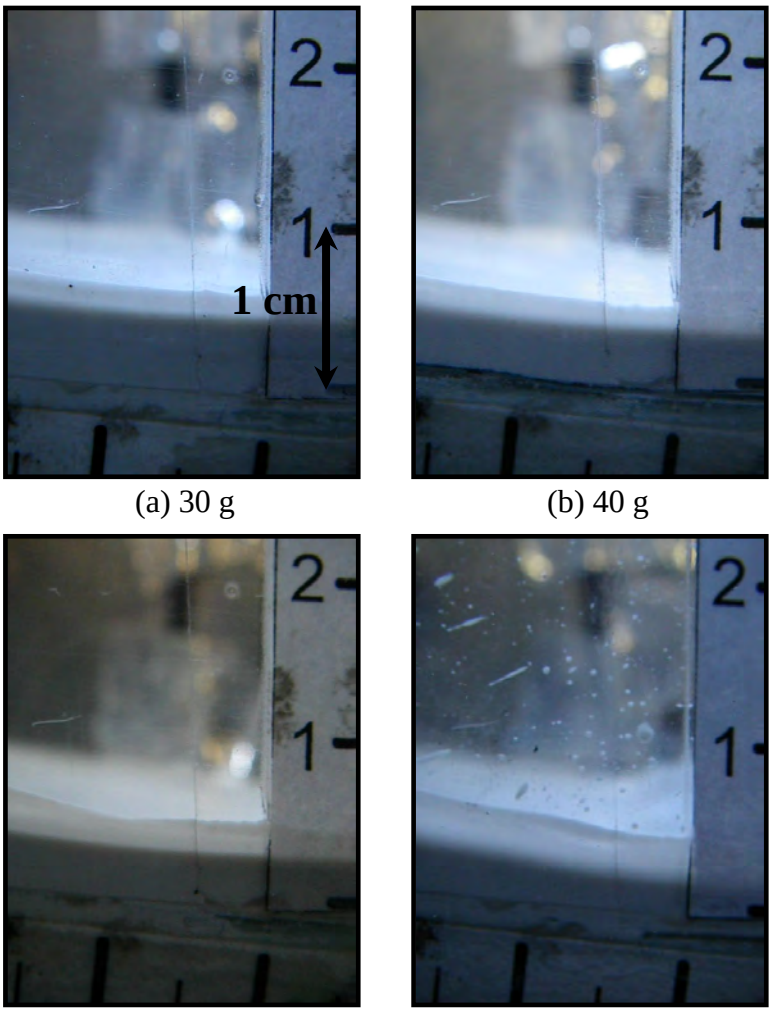

(a) 30 g (b) 40 g

(c) 50 g (d) 60 g

Figure 4.54: Side view of the dry landslide flows for various g levels from Camera 3 (0.36 m from opening of head tank)

It should be mentioned that the position of Cameras 3 and 4 were rotated from a horizontal to a vertical position. This was because a larger flow thickness was anticipated, since a large flow rate was used in this series of experiment. However, the flow thickness turned out to be very small. The large thickness in the previous series of experiments (in section 4.6.3) using the same large flow rate in the submerged conditions are most likely due to the suspension from the surrounding fluid.

Since the position of Camera 4 was rotated to the vertical position and the actual flow thickness was small, no valuable videos were recorded as the flow thickness was out of the recording range. Therefore, it was not presented here.

The plan view of the flow from Camera 5 is presented in Figures 4.55 to 4.58 for the experiments at 30 g, 40 g, 50 g and 60 g respectively. The interval of these pictures is at 0.033 s.

It can be seen that the frontal flows from the non-submerged condition in this Series (Series 4) were not as uniform as from the submerged condition in Series 1. This was possibly due to the lack of flow resistance from the surrounding fluid, since there was no surrounding fluid above the flow as Series 4 was carried out in the non-submerged condition. This is contrary to Series 1, where the surrounding fluid implied a greater flow resistance, which gave a more uniform frontal flow.

In addition, since the flow rate used in Series 4 was much larger than Series 1, the impact from the pouring process of the slurry onto the slope was much larger in Series 4 compared to Series 1. This may also have contributed to the non-uniformity of the frontal flows in this series.

Furthermore, the location of the wirings from the instruments in the non-submerged condition may have amplified the situation on the non-uniformity of the frontal flows. As can be seen from Figures 4.55 to 4.58, the flows on the right side of the slope were relatively slower compared to the left side of the slope, corresponding to the location of the wirings of the instruments, which were located on the right side of the slope at a few locations throughout the slope.

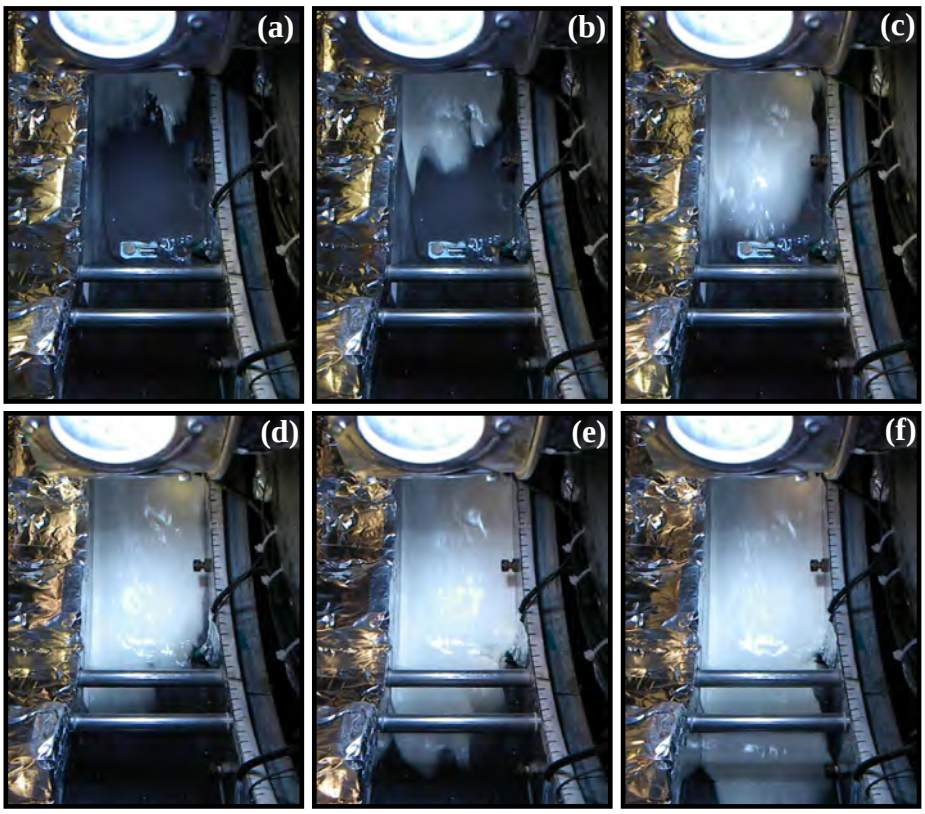

Figure 4.55: Plan view of the dry landslide flows from Camera 5 at 30 g (picture interval at 0.033 s)

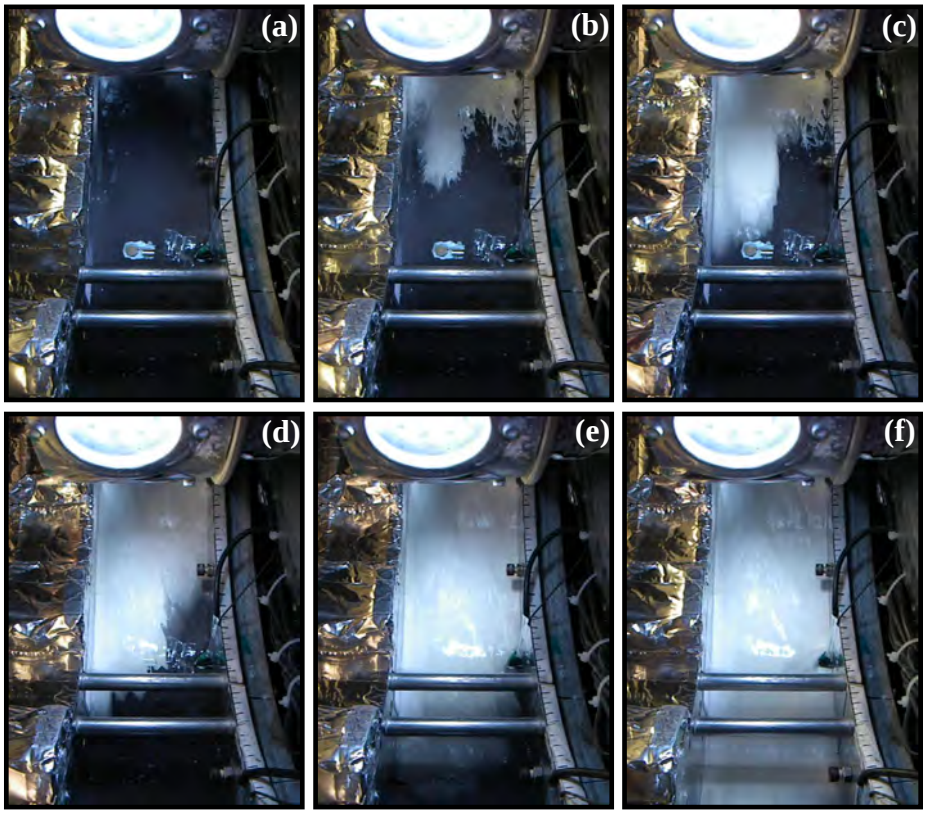

Figure 4.56: Plan view of the dry landslide flows from Camera 5 at 40 g (picture interval at 0.033 s)

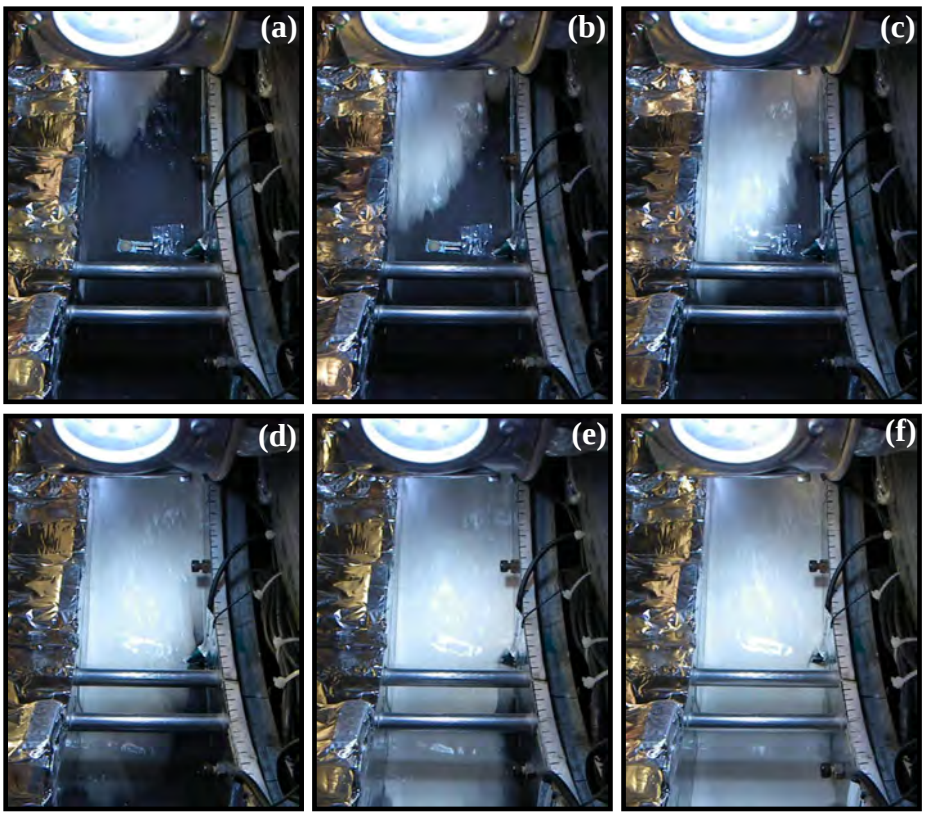

Figure 4.57: Plan view of the dry landslide flows from Camera 5 at 50 g (picture interval at 0.033 s)

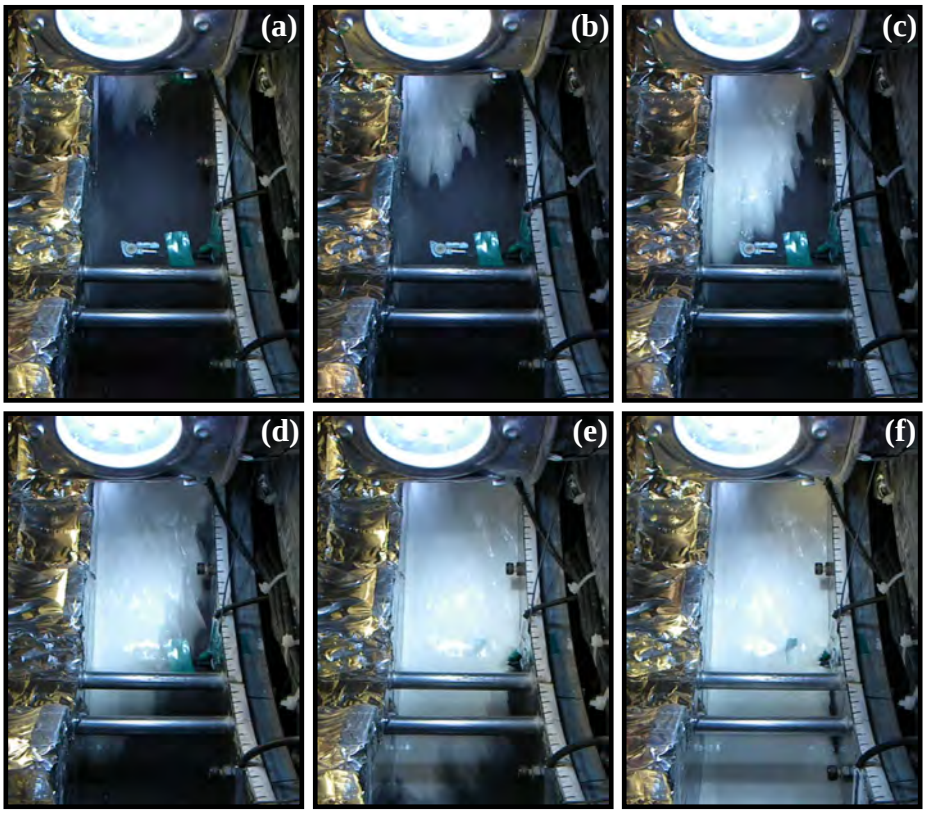

Figure 4.58: Plan view of the dry landslide flows from Camera 5 at 60 g (picture interval at 0.033 s)

Figure 4.59 shows the flow distance against time for the experiments in the dry condition at various g levels. As mentioned in the previous section, the range of flow velocities (upper and lower bounds) for each experiment is established after 0.1 s. The averaged flow velocities for each experiment, are shown in Table 4.12.

From Table 4.12, it can be seen that the flow velocity increases with g levels at a given flow rate in the dry condition. Table 4.13 shows the summary of the measured and back-calculated flow heights from the experiments at various g levels with a large flow rate in the dry condition.

The range of the upper and lower bounds of the flow heights measured from the four side cameras are given in Table 4.13. The average flow heights are the average of the upper and lower bound. The back-calculated flow heights are also given in Table 4.13.

It is interesting to note that the back-calculated flow heights are slightly higher than the measured flow heights. This differs from all the previous series, where the back-calculated flow heights are always slightly lower than the measured flow heights. In the dry condition, the flow may have flattened out (thinned) under the g levels as the slurry is not in suspension.

Although the same flow rate was used as in section 4.6.3 (in the submerged condition), the flow velocities in the dry condition are significantly higher than the flow velocities in the submerged condition. The gravitational density effect of the flow slurry plays an important role in this, where the gravitational effect for the non-submerged series (total weight of the flow slurry) is larger compared to the gravity effect for the submerged series (buoyant weight of the flow slurry), which is smaller. In addition, the lower flow velocities in the submerged condition may have been due to the drag forces from the surrounding fluid acting on the flow slurry.

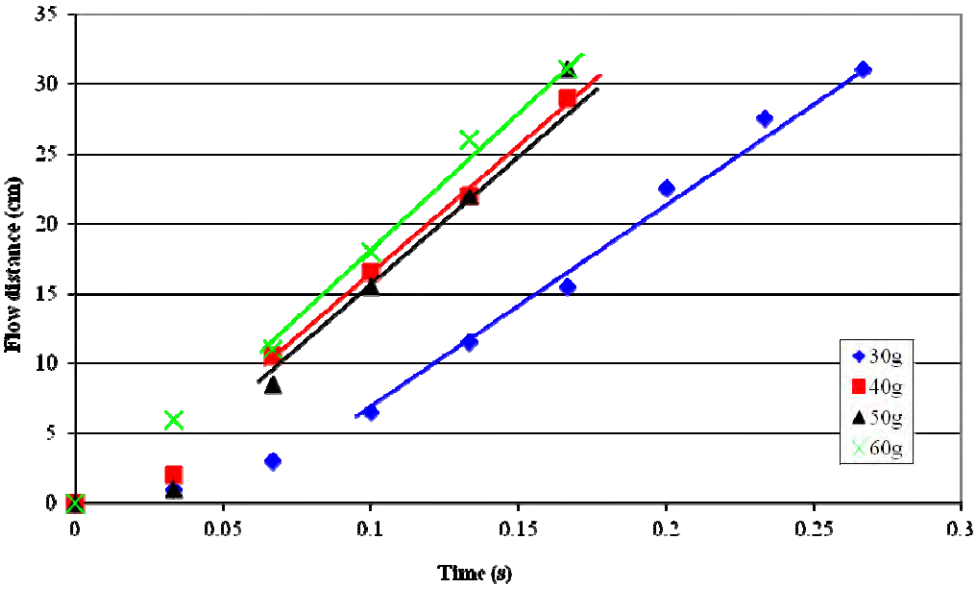

Figure 4.59: Flow distance against time at various g levels with a large flow rate in the dry condition

Table 4.12: Summary of the measured flow velocities at various g levels with the large flow rate in the dry condition

g levels	Average prototype flow rate per unit length, Q_{Pul} ($m^3/s/m$)	Average flow velocity, $\bar{v}$ (m/s)	Average prototype flow velocity, $\bar{v}_p = N^* \bar{v}$ (m/s)
30	9.8	1.45	43.5
40	17.4	1.80	72.0
50	27.3	1.83	91.5
60	39.2	1.94	116.4

Table 4.13: Summary of the measured and back-calculated flow heights for various g levels with a large flow rate in the dry condition

g levels	Average prototype flow rate per unit length, Q_{Pul} ($m^3/s/m$)	Flow height, h (m)			Back calculated averaged flow height, $\bar{h}_{BC}$ (m)	Prototype flow height, $\bar{h}_P = N * \bar{h}$ (m)	Prototype back calculated flow height, $\bar{h}_{PBC} = N * \bar{h}_{BC}$ (m)
		Lower bound	Upper bound	Averaged flow height			
30	9.8	0.0036	0.0063	0.0050	0.0075	0.15	0.23
40	17.4	0.0034	0.0064	0.0049	0.0061	0.20	0.24
50	27.3	0.0035	0.0051	0.0043	0.0060	0.22	0.30
60	39.2	0.0039	0.0051	0.0045	0.0056	0.27	0.34

The relationship of flow velocity and g level is shown in Figure 4.60. Similar to the series of experiments with the large flow rate in the submerged condition, the flow velocity in the dry condition increases with g levels at a given flow rate. This again tends to indicate that additional forces from the higher g level drive the slurry to a faster flow.

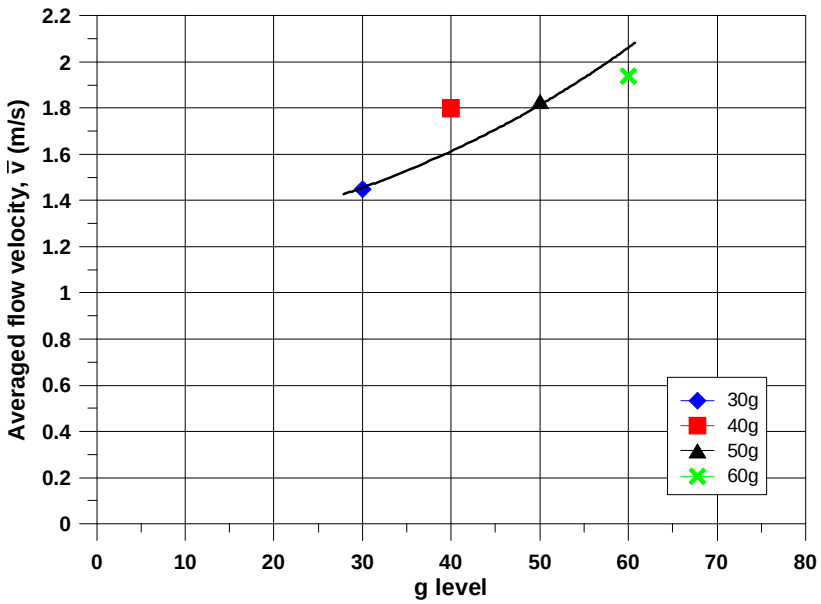

Figure 4.60: Relationship of flow velocity and g levels for various g levels with a large flow rate in the dry condition

From Figure 4.60, it can be seen that the velocity from the experiment at 40 g is relatively higher compared to the trend of flow velocities in this series of experiments. The difference between the flow velocities is most likely due to the difficulty in having a good control over the large flow rate, as mentioned in the previous section.

Figure 4.61 shows the relationship between prototype flow velocity and prototype flow rate for Series 4 (non-submerged condition). Also included in this figure are the data from Series 3 (submerged condition). This demonstrates that the prototype flow velocity for the non-submerged condition is much faster than the submerged condition, indicating that the larger the effective density the larger the flow velocity. The density of the flow slurry for Series 3 (submerged condition) is the buoyant density, while the density of the flow slurry for Series 4 (non-submerged condition) is the total density. Note that the ratio of density (submerged and non-submerged) is approximately 4; increasing the g level by a factor of 2 led to an increase in the prototype flow velocity by a factor of 3 and by extrapolating with a factor of 4 would led to increase in the prototype flow velocity by a factor of 3.

Figure 4.62 shows the relationship of prototype back-calculated flow height and prototype flow rate for Series 3 and 4. The data from Series 4 agrees with the findings from the previous series, in which the prototype flow height increases with the prototype flow rate; however, the prototype flow heights from the non-submerged condition are smaller than the submerged condition. This indicates that, for the submerged condition, the flow slurry is suspended, hence inducing a larger flow height.

Figure 4.63 shows the relationship of the measured change in pore pressure and prototype flow rate for Series 3 and 4. It can be seen that the measured change in pore pressure generally increases with the prototype flow rate, except for the test at 60 g due to the instrumentation problems encountered for this particular test, as mentioned earlier. Though the prototype flow height is smaller for the non-submerged condition, the measured change in pore pressure in the non-submerged condition is higher compared to the

submerged condition. This is due to the gravitational density effect as mentioned earlier, where the total density in Series 4 (non-submerged condition) is larger than the buoyant density in Series 3 (submerged condition).

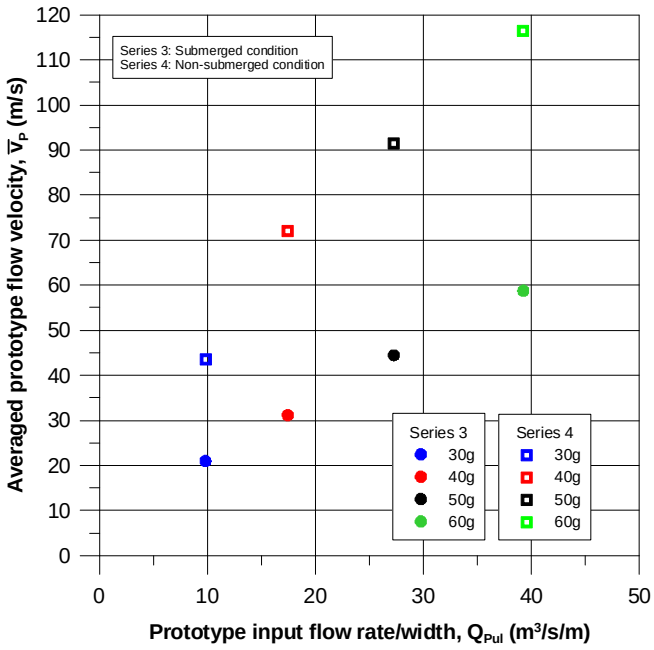

Figure 4.61: Relationship of prototype flow velocity and prototype flow rate for Series 3 & 4

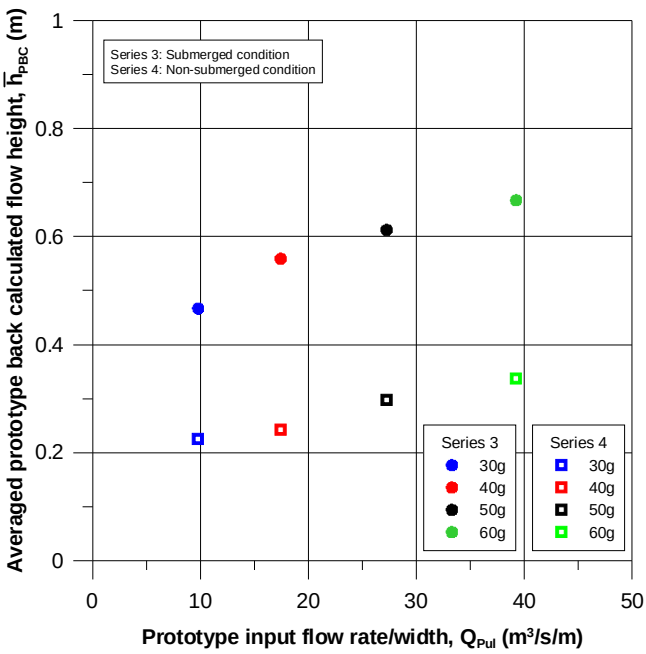

Figure 4.62: Relationship of prototype back-calculated flow height and prototype flow rate for Series 3 & 4

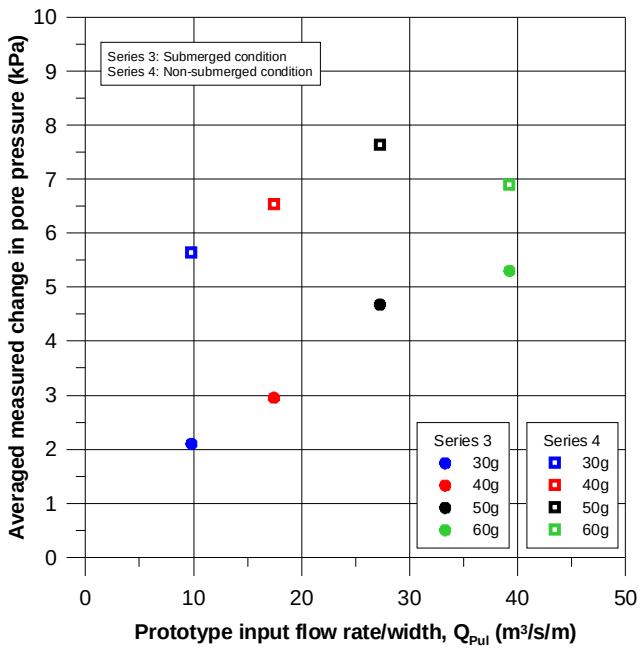

Figure 4.63: Relationship of the averaged measured change in pore pressure and prototype flow rate for Series 3 & 4

4.7 Repeatability of the Centrifuge Experiments

As mentioned earlier in section 4.6.2, there were similar experiments where the repeatability of the experiments could be evaluated. One was from the experiments at various g levels and scaled flow rates (30 g a), while one was from the experiments at only 30 g at various flow rates (30 g b). Both experiments were conducted at 30 g with the flow rate of $3.5*10^{-4}$ m^3/s. Figure 4.64 shows the measured change in pore pressure during the similar experiments.

An additional result from a trial experiment at 30 g (30 g c) with the similar flow rate of $3.5*10^{-4}$ m^3/s is also included in this figure. This trial experiment is not reported in this thesis as it was carried out during an earlier stage of this research without any video recordings of the flow. The sole purpose of this trial experiment was to find out the performance of the PPTs under the submerged slurry and g level. Since the change of pore pressures

were measured in this experiment, it is useful in describing the repeatability of the experiments. It can be seen that all three experiments with the same g level and flow rate show similar responses in the measured change in pore pressure. This indicates that the measurements of the change in pore pressure are correct and repeatable.

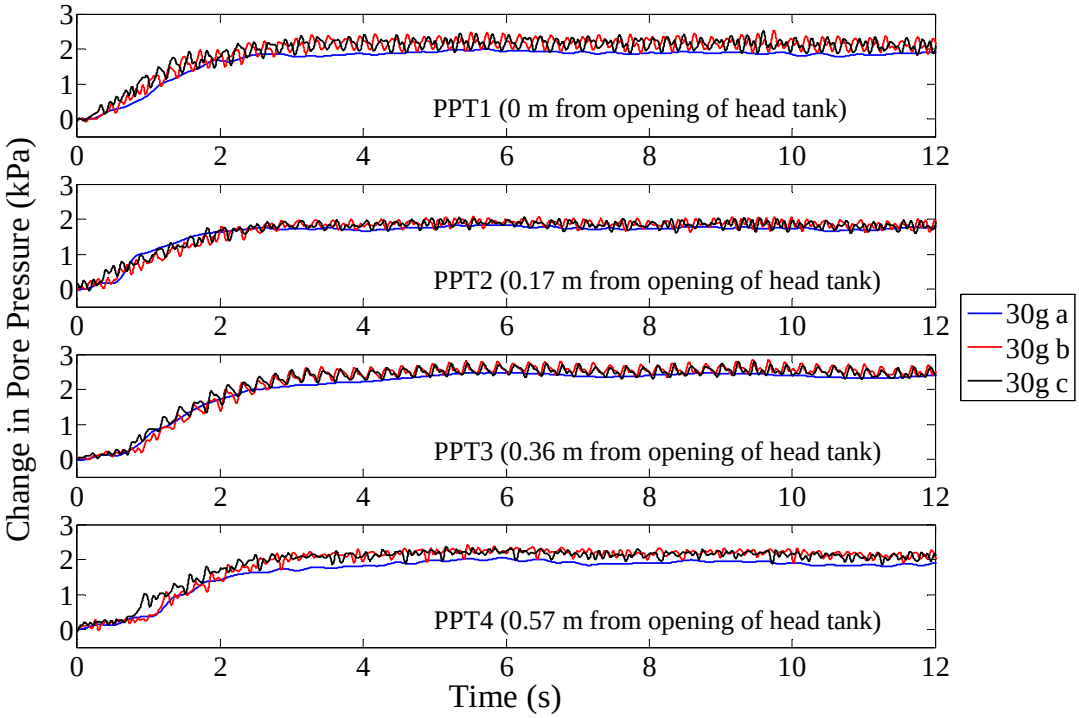

Figure 4.64: The change in pore pressure for three experiments at 30 g with flow rate of 3.5*10^{-4} m^3/s at various locations along the slope

Figure 4.65 shows the flow distance from the two experiments at 30 g (30 g a and 30 g b) with the same flow rate of 3.5*10^{-4} m^3/s. The trial experiment at 30 g c was carried out without any video recording; therefore, the flow distance cannot be obtained and it is not included in this figure.

It should be noted that the flow distance from the two experiments at 30 g were only relative to its own time measured at each experiment. Therefore, the flow distance against time does not overlay each other in Figure 4.65. However, the slope of the flow distance against time, which gives the average velocity of the flow, was shown to be similar. As mentioned earlier, the average flow velocity for each flow was established after 0.3 s. It can be

seen that the two lines in Figure 4.65 give a similar average flow velocity, where the average velocity from 30 g a and b is approximately 60 cm/s.

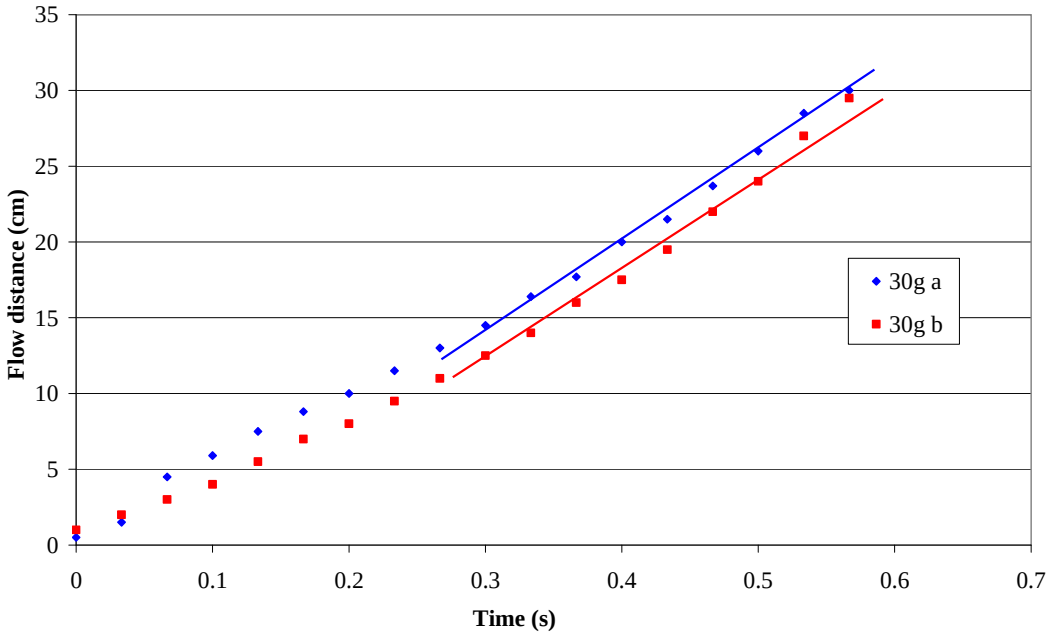

Figure 4.65: Flow distance against time for the two experiments at 30 g with flow rate of $3.5*10^{-4}$ m^3/s

The results from Figures 4.64 to 4.65 indicate that the centrifuge experiments are repeatable. This gives a higher confidence towards the results obtained from the centrifuge experiments.

4.8 Summary

A new centrifuge apparatus was developed for use in a mini-drum centrifuge, which allowed the modelling of submarine landslide flows as well as the ability to investigate the proposed centrifuge scaling laws. It is appealing to note that the centrifuge experimental results appear to follow the proposed scaling laws.

From one of the trial experiments at 10 g, it was found that there was a 1 g effect from the natural earth's gravity towards the flow where the flow

tends to be one sided due to the 1 g effect. This effect was found to be minimal from 30 g onwards.

Based on the centrifuge experiments in the submerged conditions, the measured flow heights based on visual inspection from the videos might not reflect the actual flow height and tended to over-estimate the actual flow height. This might be due to the suspension of the flow slurry in the submerged condition. With the centrifuge experiments in the non-submerged condition, the back-calculated flow heights were found to be smaller than the measured flow heights. This might be due to the flattening or thinning of the slurry flow under the g levels in the dry condition.

The flow velocities were significantly higher in the non-submerged condition compared to the submerged condition, in which the flow rates in both series were the same. This was due to the gravitational density effect, where the larger the effective density the larger the flow velocity. The density of the flow slurry for Series 3 (submerged condition) is the buoyant density, while the density of the flow slurry for Series 4 (non-submerged condition) is the total density. In addition, the drag forces from the surrounding fluid might have been acting on the flow slurry in the submerged condition, which might have reduced the flow velocity for the submerged condition.

The data from Series 1 to 4 demonstrated well that the relationship of prototype flow velocity increases with the prototype input flow rate. Results from Series 1, in which the input flow rates were scaled, proved that the prototype flow velocity were relatively similar, indicating the tests at various g levels were modelled correctly. Series 3 and 4 showed that, at a given constant input flow rate, the prototype flow velocity increased with g level. Similarly, Series 1 to 4 consistently demonstrated that the prototype flow height increased with the prototype input flow rate. The prototype flow heights were found to be relatively similar in Series 1 where the input flow rates were scaled. At the same time, at a given constant input flow rate, the prototype flow height increased with g level as shown in Series 3 and 4.

As indicated in the comparison of Series 3 and 4, the prototype flow height was smaller in the non-submerged condition compared to the submerged condition; however, the measured change in pore pressure in the non-submerged condition was higher compared to the submerged condition. This is due to the gravitational density effect as mentioned earlier, where the total density in Series 4 (non-submerged condition) is larger than the buoyant density in Series 3 (submerged condition). This is discussed in more detail in Chapter 6.

It was shown that the results from the centrifuge experiments were reasonably repeatable, demonstrating that the flow rate could be controlled properly. From the current centrifuge experiments, large flow rates were more difficult to control compared to the smaller flow rates.

CHAPTER V

5.0 NUMERICAL SIMULATIONS AND PARAMETRIC STUDIES

5.1 Introduction

Following from the previous chapter, numerical simulations were carried out to simulate the centrifuge experiments as well as to investigate the proposed centrifuge scaling laws. The Depth Average Material Point Method (DAMPM) was used in the numerical simulations. This chapter discusses the DAMPM, results from the numerical simulations and the sensitivity of the model.

5.2 Depth Average Material Point Method (DAMPM)

The Material Point Method (MPM) is categorised as one of the mess-less methods formulated in an arbitrary Lagrangian-Eulerian description of motion. In MPM, a body is to be analysed as a cluster of material points, in which a material point has information of physical properties on a particular position and stress. The material points, which carry all Lagrangian parameters, can move freely across cell boundaries of a stationary Eulerian lattice and the information is distributed to each node of belonging cells (Numada and Konagai, 2009).

The MPM proposed by Sulsky et al. (1994) states that the material points are followed so that interpolation for history dependent variables is not required and the parameters assigned to the material points are updated at each step. One of the main advantages of MPM is its ability to deal with large deformation without mesh distortion, which is the limitation of conventional finite element methods.

The depth-averaged concept is based on Hungr (1995) and is a model for runout analysis of a debris mass where the debris mass is modelled as a group of material columns. Figure 5.1 shows the Hungr (1995) depth-averaged concept. The concept of modelling a flow slide in a homogeneous "apparent fluid" replaces the slide mass as shown in Figure 5.1 (a). The moving mass, which may in reality be heterogeneous and complex, is replaced by an equivalent fluid whose bulk properties approximate the behaviour of the prototype. Figure 5.1 (b) shows the forces on a block, which are responsible for the flow along a slope.

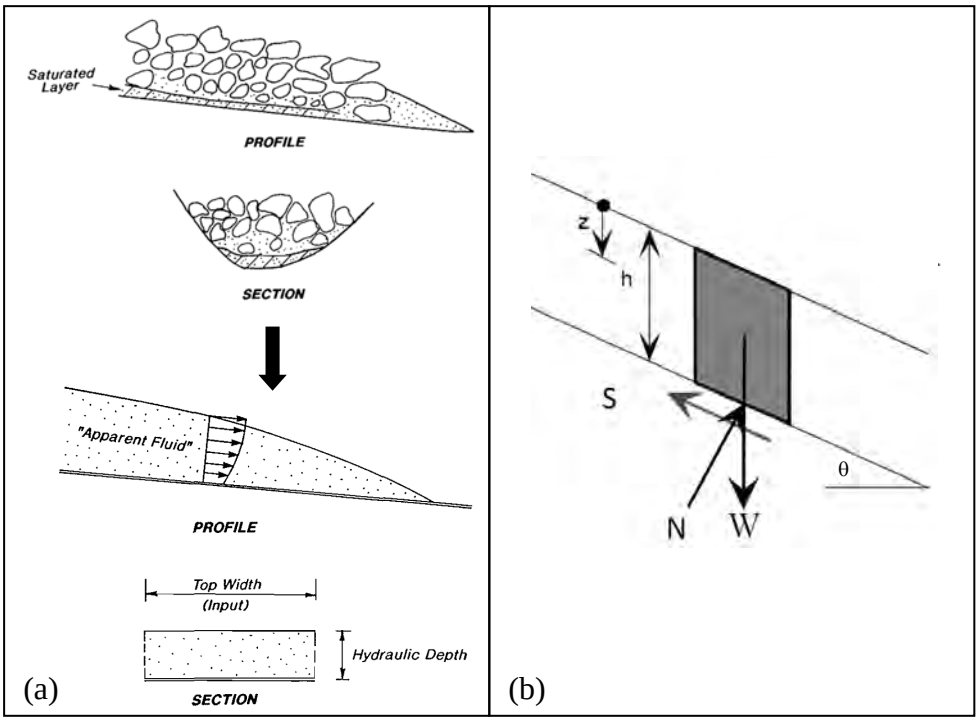

Figure 5.1: Hungr's depth-averaged concept (modified after Hungr, 1995)

The Depth Averaged Material Point Method (DAMPM) is the combination of the MPM and the depth-averaged concept. It is a numerical method for runout analysis of material with a complicated constitutive law, such as for debris flows. The algorithm for this method is based on the discretisation of St. Venant's depth averaged-equation of shallow open channel fluid flow (Abe, 2008). DAMPM has been successfully used in recent

research such as Abe et al. (2007, 2008) in predicting long run-out debris flows. This study utilises the code originally developed by Abe et al. (2007).

Figure 5.2 shows the concept of DAMPM, where the material body consists of a group of Lagrangian particles that carry the physical variables of the body on the Eulerian background meshes. At the nodes of the background meshes, the Newtonian equation of motion is solved with nodal variables, which are introduced from the physical variables carried by the particles. All the Lagrangian parameters assigned to the particles are updated at each step. The depth integration is performed normal to bed, with the z axis of Cartesian coordinate shown in Figure 5.2.

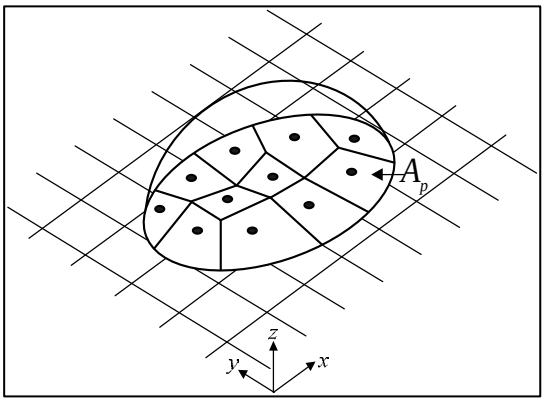

Figure 5.2: Illustration of DAMPM (after Abe, 2008)

5.2.1 Governing equations

The governing equations used in the DAMPM for soil flows are derived using classical shallow water theory and Iverson and Denlinger's depth-averaged theory on the flow of variably fluidised granular masses with the incorporation of effective stress theory.

Chow (1959) proposed the following assumptions for the classical shallow water theory:

- The flow depth varies gradually and is small compared with the area of debris mass
- Flow surface is stress-free

It should be noted that the centrifuge experiments have been carried out in two different conditions, one in a submerged condition and the other in the non-submerged condition. Therefore, two different sets of governing equations need to be used for these two conditions.

5.2.1.1 Governing equations for submerged condition

The depth-averaged equations governing mass balance of a column of moving material are as follows, (note that x is the horizontal direction parallel to the flow, y is the horizontal direction perpendicular to the flow and z is the vertical direction to the flow):

$$\frac{\partial h}{\partial t}+\frac{\partial(h\bar{v}_x)}{\partial x}+\frac{\partial(h\bar{v}_y)}{\partial y}=0 \tag{5.1}$$

where $\bar{v}, h$ and t are the depth-averaged flow velocity, flow height and time respectively. The momentum balance in the x and y directions are as follow:

$$\rho\frac{\partial(h\bar{v}_x)}{\partial t}=-\int_0^h\left[\frac{\partial\sigma'_{xx}}{\partial x}+\frac{\partial p_w}{\partial x}+\frac{\partial\sigma'_{xy}}{\partial y}+\frac{\partial\sigma'_{xz}}{\partial z}-\rho g_x\right]dz \tag{5.2a}$$

$$\rho\frac{\partial(h\bar{v}_y)}{\partial t}=-\int_0^h\left[\frac{\partial\sigma'_{yy}}{\partial y}+\frac{\partial p_w}{\partial y}+\frac{\partial\sigma'_{xy}}{\partial x}+\frac{\partial\sigma'_{yz}}{\partial z}-\rho g_y\right]dz \tag{5.2b}$$

where σ' is the effective stress, ρ is the density of the flow material, g is the gravity and p_w is the pore water pressure. The p_w is divided into an excess pore water pressure, p_{we} and a static pore water pressure, p_{ws}. Hence, the equations (5.2a and 5.2b) are turned into the following equations:

$$\rho\frac{\partial(h\bar{v}_x)}{\partial t}=-\int_0^h\left[\frac{\partial\sigma'_{xx}}{\partial x}+\frac{\partial}{\partial x}\left(p_{we}+p_{ws}\right)+\frac{\partial\sigma'_{xy}}{\partial y}+\frac{\partial\sigma'_{xz}}{\partial z}-\rho g_x\right]dz \tag{5.3a}$$

$$\rho\frac{\partial(h\bar{v}_y)}{\partial t}=-\int_0^h\left[\frac{\partial\sigma'_{yy}}{\partial y}+\frac{\partial}{\partial y}\left(p_{we}+p_{ws}\right)+\frac{\partial\sigma'_{xy}}{\partial x}+\frac{\partial\sigma'_{yz}}{\partial z}-\rho g_y\right]dz \tag{5.3b}$$

Suppose a condition as shown in Figure.5.3; the static pore water pressures at both sides of a unit of a mass are represented by the following equations:

$$p_{ws}+\frac{\partial p_{ws}}{\partial x}dx=\rho_w g\left(z_1-z\right)\cos\theta \tag{5.4a}$$

$$p_{ws}=\rho_w g\left(z_2-z\right)\cos\theta \tag{5.4b}$$

$$\therefore\quad \frac{\partial p_{ws}}{\partial x}=\rho_w g\,\frac{z_1-z_2}{dx}\cos\theta \tag{5.4c}$$

Here, $\left(z_1-z_2\right)/dx=\tan\theta$, so

$$\frac{\partial p_{ws}}{\partial x}=\rho_w g\sin\theta=\rho_w g_x \tag{5.5}$$

Hence, Equations (5.3a) and (5.3b) are turned into the following equations:

$$\rho\frac{\partial(h\bar{v}_x)}{\partial t}=-\int_0^h\left[\frac{\partial\sigma'_{xx}}{\partial x}+\frac{\partial p_{we}}{\partial x}+\frac{\partial\sigma'_{xy}}{\partial y}+\frac{\partial\sigma'_{xz}}{\partial z}-\left(\rho-\rho_w\right)g_x\right]dz \tag{5.6a}$$

$$\rho\frac{\partial(h\bar{v}_y)}{\partial t}=-\int_0^h\left[\frac{\partial\sigma'_{yy}}{\partial y}+\frac{\partial p_{we}}{\partial y}+\frac{\partial\sigma'_{xy}}{\partial x}+\frac{\partial\sigma'_{yz}}{\partial z}-\left(\rho-\rho_w\right)g_y\right]dz \tag{5.6b}$$

Then Equations (5.6a) and (5.6b) are turned into the following equations:

$$\rho\frac{\partial(h\bar{v}_x)}{\partial t}=\frac{\partial\left(h\bar{\sigma}'_{xx}\right)}{\partial x}+\frac{\partial\left(h\bar{p}_{we}\right)}{\partial x}+\frac{\partial\left(h\bar{\sigma}'_{xy}\right)}{\partial y}+\left(\rho-\rho_w\right)hg_x-\sigma'_{xz}\Big|_{z=0} \tag{5.7a}$$

$$\rho\frac{\partial(h\bar{v}_y)}{\partial t}=\frac{\partial\left(h\bar{\sigma}'_{yy}\right)}{\partial y}+\frac{\partial\left(h\bar{p}_{we}\right)}{\partial y}+\frac{\partial\left(h\bar{\sigma}'_{xy}\right)}{\partial x}+\left(\rho-\rho_w\right)hg_y-\sigma'_{yz}\Big|_{z=0} \tag{5.7b}$$

where $\sigma_{xz}\big|_{z=0}$ and $\sigma_{yz}\big|_{z=0}$ are the basal frictional stresses.

The stress components are calculated by the following equations, assuming that the distribution of stress and pore pressure are triangular. The depth-averaged normal total stress $\overline{\sigma}_{zz}$ is separated into depth-averaged effective normal stress $\overline{\sigma}'_{zz}$ and the excess pore water pressure $\overline{p}_{we}$ by a pore pressure coefficient (ratio of pore pressure to the total normal stress at the base), λ as follows:

$$\overline{\sigma}'_{zz} = \frac{1}{2}(\rho - \rho_w) g_z h (1 - \lambda) \tag{5.8}$$

$$\overline{p}_{we} = \frac{1}{2}(\rho - \rho_w) g_z h \lambda \qquad \text{or} \quad \lambda = \frac{p_{we}}{(\rho - \rho_w) g_z h} \tag{5.9}$$

The parameter λ is similar to the parameter r_u used in earthquake engineering.

The other stress components are computed from the constitutive equation of the fluidised material using the following equation.

$$\overline{\sigma}'_{ij} = \overline{T}_{ijkl} \overline{\varepsilon}_{kl} \tag{5.10}$$

where $\overline{\sigma}'_{ij}$ is the local depth-averaged stress tensor, $\overline{T}_{ijkl}$ is the local stiffness and $\overline{\varepsilon}_{kl}$ is the local depth-averaged strain tensor.

The basal frictional stresses $\sigma_{xz}\big|_{z=0}$ and $\sigma_{yz}\big|_{z=0}$ are important in driving the soil body to move along a slope. In this study, it is assumed that Newtonian flow (for the fluid phase) as well as a Coulomb frictional law (for the solid phase) are applied as the basal frictional force as follows:

$$\sigma'_{xz}\big|_{z=0} = (\rho - \rho_w) g_z h \left(1 + \frac{a_c}{g_z}\right)(1 - \lambda) \tan\phi' + 3 v_f \mu \frac{\overline{v}_x}{h} \tag{5.11a}$$

$$\sigma'_{yz}\big|_{z=0} = (\rho - \rho_w) g_z h \left(1 + \frac{a_c}{g_z}\right)(1 - \lambda) \tan\phi' + 3 v_f \mu \frac{\overline{v}_y}{h} \tag{5.12b}$$

where a_c is the centrifugal acceleration (dependent on the curvature radius of the flow path), ϕ' is the basal frictional angle, v_f is the fluid volume fraction, and μ is the fluid viscosity. The first term on the right-hand side comes from the soil's frictional resistance, whereas the second term comes from the viscosity of the pore fluid inside the moving soil-fluid mixture.

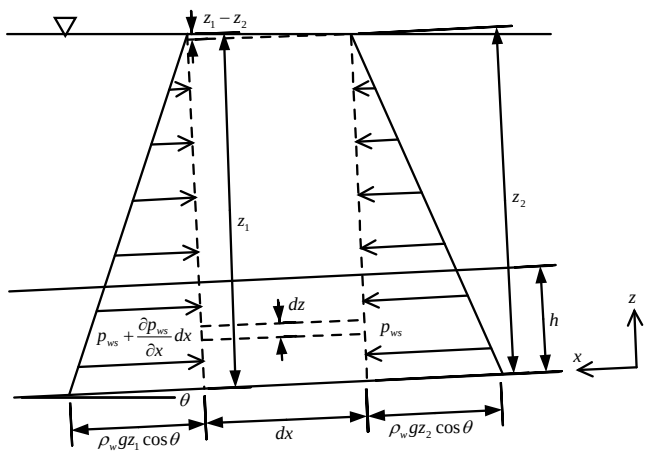

Figure 5.3: Condition of a unit of a mass in submerged case

5.2.1.2 Governing equations for non-submerged condition

The governing equations for a non-submerged condition are relatively similar to the governing equations with the submerged condition, with a few exceptions to the calculation of the stresses and pore water pressure.

The depth-averaged equations governing mass and momentum balance of a column of material moving are the same in equations 5.1 to 5.2b. Equations 5.2a and 5.2b are turned into the following equations:

$$\rho \frac{\partial (h\bar{v}_x)}{\partial t} = \frac{\partial (h\bar{\sigma}'_{xx})}{\partial x} + \frac{\partial (h\bar{p}_w)}{\partial x} + \frac{\partial (h\bar{\sigma}'_{xy})}{\partial y} + \rho h g_x - \sigma'_{xz}\big|_{z=0} \tag{5.13a}$$

$$\rho \frac{\partial (h\bar{v}_y)}{\partial t} = \frac{\partial (h\bar{\sigma}'_{yy})}{\partial y} + \frac{\partial (h\bar{p}_w)}{\partial y} + \frac{\partial (h\bar{\sigma}'_{xy})}{\partial x} + \rho h g_y - \sigma'_{yz}\big|_{z=0} \tag{5.13b}$$

The stress components are calculated by the following equations. The depth-averaged normal total stress $\bar{\sigma}_{zz}$ is separated into depth-averaged

effective normal stress $\overline{\sigma}'_{zz}$ and the pore water pressure $\overline{p}_w$ by a pore pressure coefficient λ as follows:

$$\overline{\sigma}'_{zz} = \frac{1}{2}(\rho - \rho_w) g_z h (1 - \lambda) \tag{5.14}$$

$$\overline{p}_w = \frac{1}{2}(\rho - \rho_w) g_z h \lambda + \frac{1}{2} \rho_w g_z h \tag{5.15}$$

$$\overline{\sigma}'_{ij} = \overline{T}_{ijkl} \overline{\varepsilon}_{kl} \tag{5.16}$$

The basal frictional stresses $\sigma_{xz}\big|_{z=0}$ and $\sigma_{yz}\big|_{z=0}$ are the same as in the submerged conditions, in equations 5.11a and b.

5.3 Model Details

The schematic for the numerical simulation is shown in Figure 5.4. The geometry of the simulation is mainly based on the centrifuge experiments. The boundary of the simulation consists of a confined channel of a 6° slope, with a runout slope length of 2 m. It should be noted that the slope length in the numerical simulation is longer than the actual centrifuge experiments (1 m). The reason for having a longer runout is to provide a better understanding of the submarine landslide flows and to avoid the particles hitting the end of the slope too early; the particles may build up or bounce back at the end of the slope, thus affecting the flow mechanism.

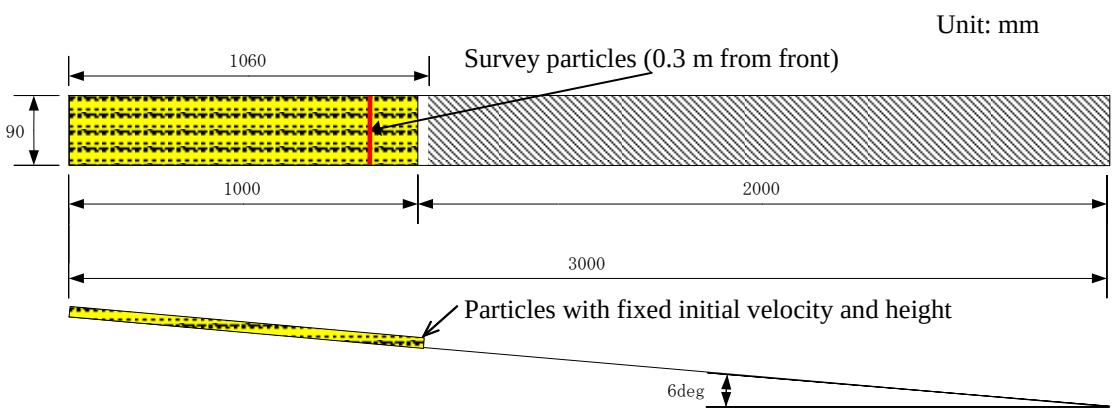

Figure 5.4: Schematic of the numerical simulation

The initial conditions are, however, slightly different from the centrifuge experiments due to the complexity of simulating the pouring process, as in the centrifuge experiments. The slurry is represented by a group of particles from the initial area at the top of the slope (the yellow section in Figure 5.4), with a prefixed initial velocity and height. The initial area is set as a frictionless base without setting any gravity. This means that the particles in the initial area do not have any forces. In other areas, a frictional base and gravity are assigned.

The simulation starts with releasing of the particles from the initial area, in which the movements of the particles in the yellow section down the slope are driven by the initial velocity. Once the particles come out from the yellow section, the movement and the changes in flow velocity and height of the particles can be tracked while moving along the slope.

For the simulations of this study, the averaged flow height and velocity are based on the average of a group of particles at 0.3 m from the movement front, represented by a red line as shown in Figure 5.4. The reason for choosing the group of particles at 0.3 m instead of the front of the flow is that the flow height is more constant, starting at 0.3 m from the movement front to the back of the flow, which is more representative of the overall flow. The immediate front of the flow is oscillated due to numerical error and is not representative to the overall flow; this is further discussed in the later part of this chapter.

The background mesh size, or the grid spacing used in the simulations of this study, is 0.01 x 0.01 m. A smaller background mesh size was also investigated, which is again discussed in the later part of this chapter.

The simulation can be repeated with different gravity levels as in the centrifuge experiments. The other basic parameters for the numerical simulations are shown in Table 5.1. The density of the slurry, fluid volume fraction and viscosity are based on the actual measurements from the slurry

used in the centrifuge experiments. The other parameters are assumed based on the typical values of a soil under a given effective stress condition.

The basal friction angle, internal friction angle and side wall friction angle are determined after rigorous parametric studies, as well as correlation with the results from the centrifuge experiments. This will be discussed in the later part of this chapter regarding the sensitivity of the model.

Table 5.1: Basic parameters for the numerical simulations

Density of flow slurry	1350 kg/m^3
Density of water	1000 kg/m^3
Basal friction angle	12.5^o
Internal friction angle	25°
Side wall friction angle	5°
Pore pressure ratio, λ	1
Fluid volume fraction (Porosity)	0.76
Viscosity of flow slurry	0.4 Pa.s
Number of particles in a simulation	3528

5.4 Simulations of Experiments at Various g Levels with Scaled Flow Velocity and Height

This series of numerical simulations are performed based on the centrifuge experiments which were carried out at various g levels (30 g, 40 g, 50 g and 60 g) with the scaled flow velocities and heights according to the proposed scaling laws. The purpose of this series of numerical simulations was to try to match the centrifuge experiments as well as to check on the validity of the proposed scaling laws (e.g. whether any initial and boundary conditions have an effect on the proposed scaling laws).

The basic parameters for the four simulations in this series are shown in Table 5.1. The input for the simulations of the initial flow velocities and heights with their corresponding g levels is shown in Table 5.2. The initial flow velocities are based on the centrifuge experiments, while the initial flow heights are back-calculated based on the input flow rates used in the centrifuge experiments, as described in Chapter IV.

Table 5.2: Initial details for the numerical simulations of experiments at various g levels with scaled flow velocity and height

g levels	Initial flow velocity, v_i (m/s)	Initial flow height, h_i (m)	Input flow rate per unit length, Q_{ul} ($m^3/s/m$)*10^{-4}	Prototype input flow rate per unit length, Q_{Pul} ($m^3/s/m$) ($Q_{Pul}=N^2Q_{ul}$)
30	0.60	0.0058	35.0	3.2
40	0.45	0.0044	19.7	3.2
50	0.37	0.0034	12.6	3.2
60	0.32	0.0028	8.8	3.2

Note: The unit length is the width of the channel, which is 0.1 m. The initial flow velocity, v_i times the initial flow height, h_i equals the input flow rate per unit length, Q_{ul}. ($v \times h = Q_{ul}$)

Figures 5.5 to 5.8 show the developments of the flow from initiation up to 1.8 s of the flow time for simulations at 30 g, 40 g, 50 g and 60 g respectively. It can be seen that the flow developments are relatively similar to those from the centrifuge experiments (Figures 4.23 – 4.27).

Numerical oscillation at the front can be seen on Figures 5.5 to 5.8. It can be seen that the oscillation increases with time. The numerical oscillation is caused by the frontal movement.

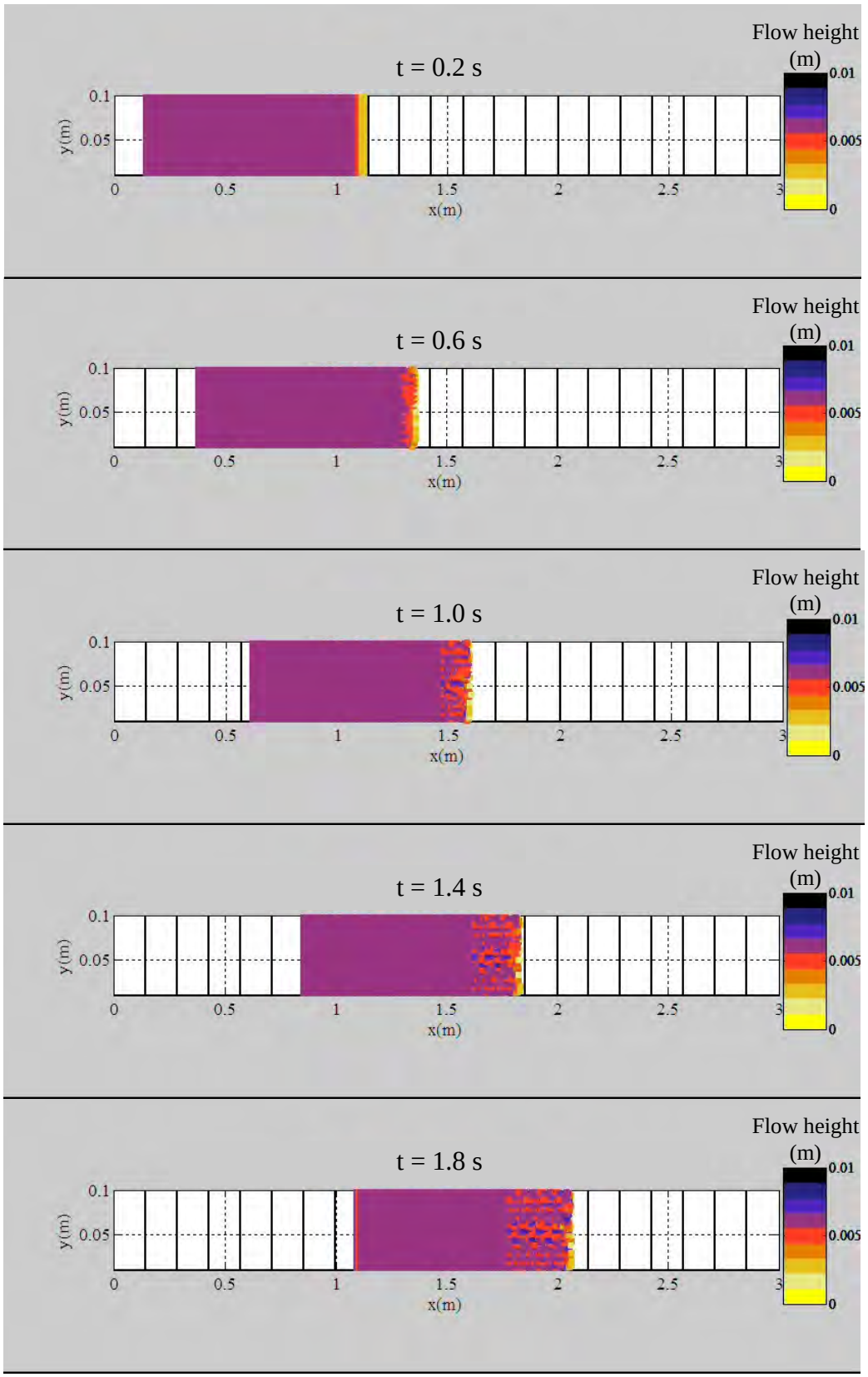

Figure 5.5: Flow developments at 30 g

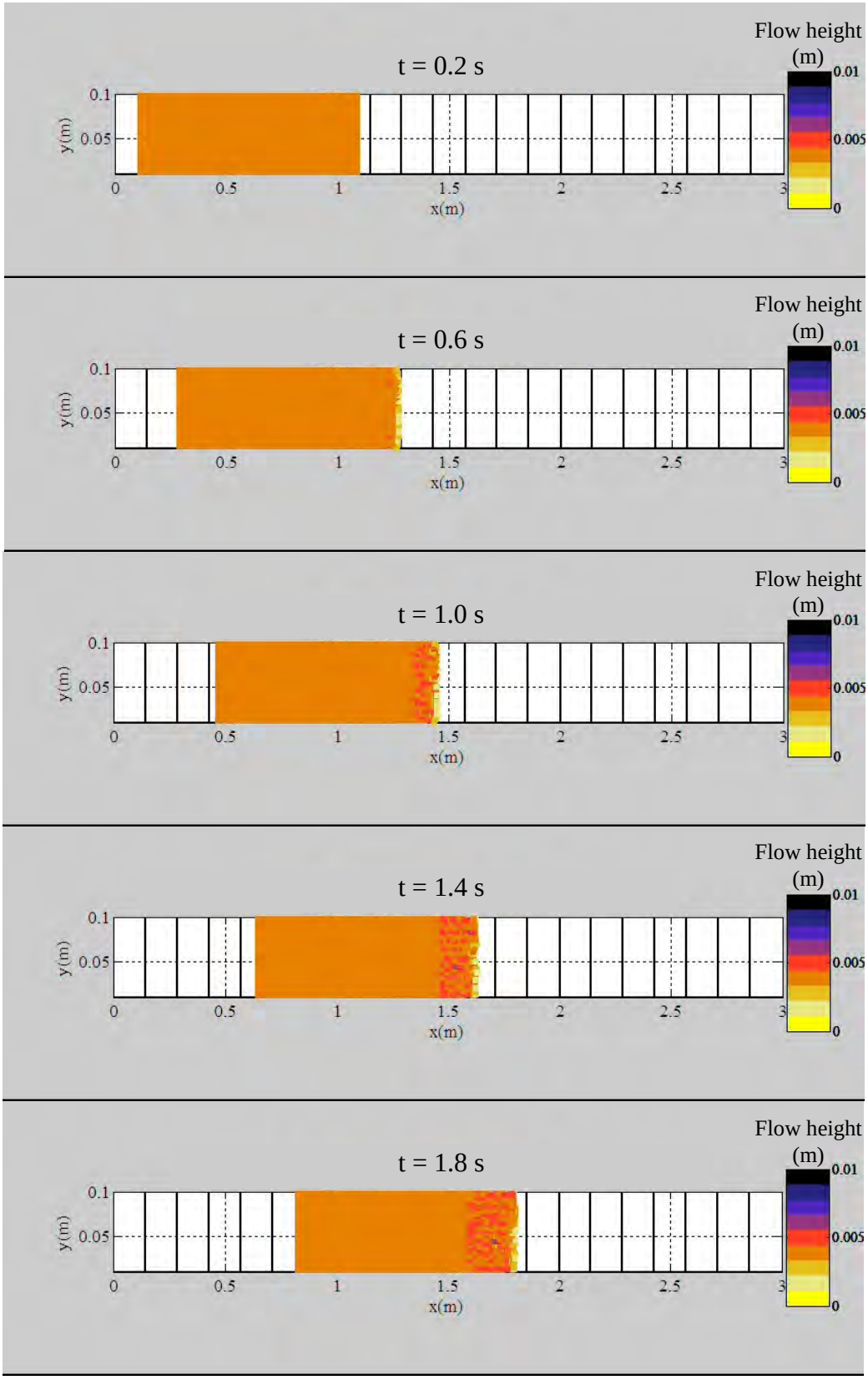

Figure 5.6: Flow developments at 40 g

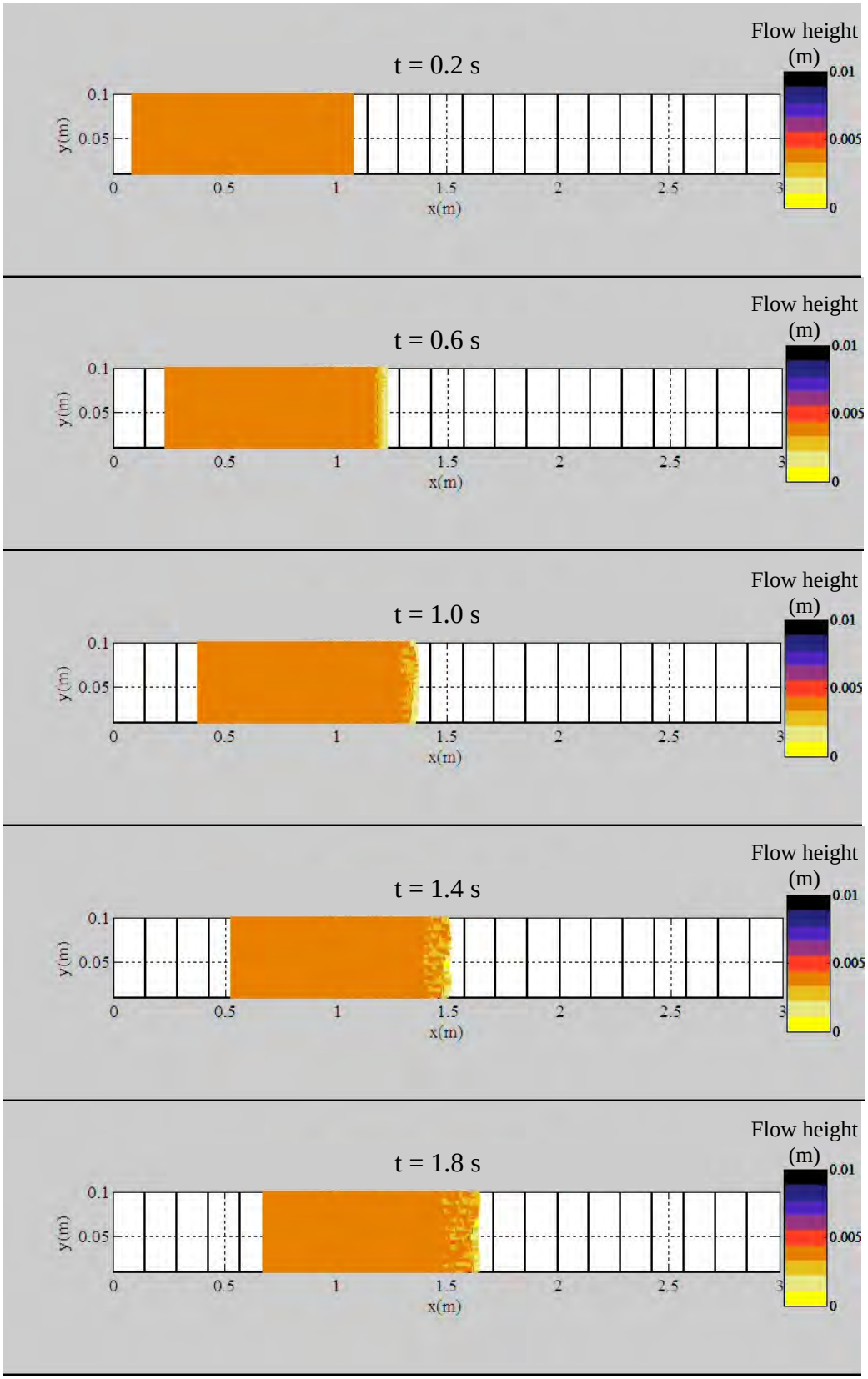

Figure 5.7: Flow developments at 50 g

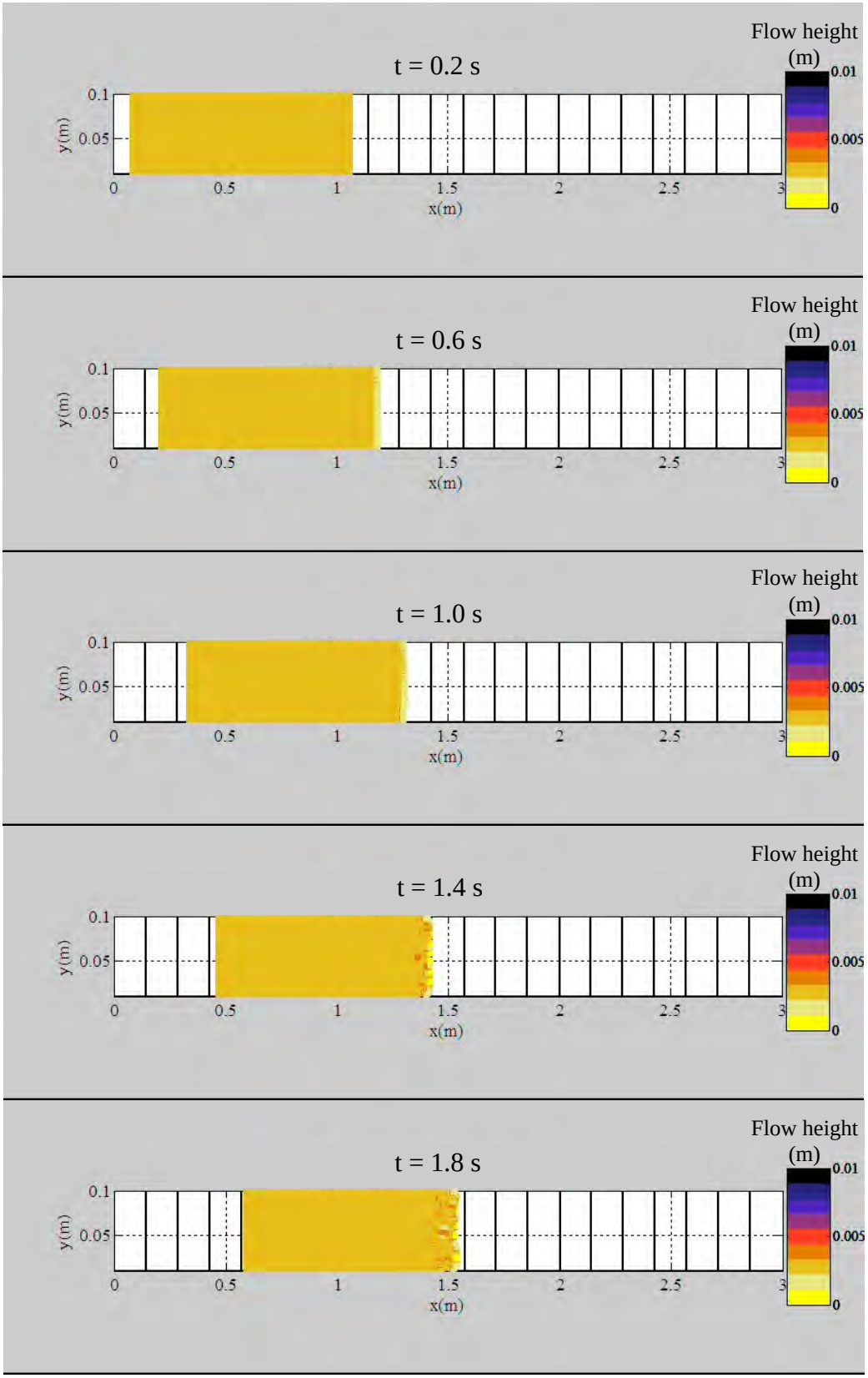

Figure 5.8: Flow developments at 60 g

Figure 5.9 shows the averaged flow velocity against time along the monitored front line (0.3 m from the movement front) for the simulations at various g levels. Slight numerical oscillations can be seen to increase with time in Figure 5.9, similar to those reflected in Figures 5.5 to 5.8. In general, the averaged flow velocities from each simulation as shown in Figures 5.9 demonstrate that the flow velocities are fairly constant throughout the flow.

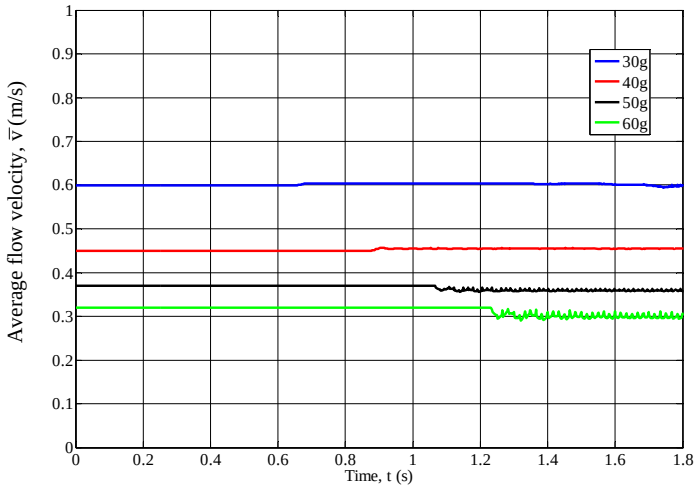

Figure 5.9: Averaged flow velocity against time for various g levels

Figure 5.10 shows the averaged flow height against time along the monitored front line (0.3 m from the movement front) for the simulations at various g levels. The slight changes in the flow heights here are due to the oscillations as seen in Figure 5.9. Similar to the averaged flow velocities in Figure 5.9, the averaged flow heights from each simulation are found to be fairly constant throughout the flow.

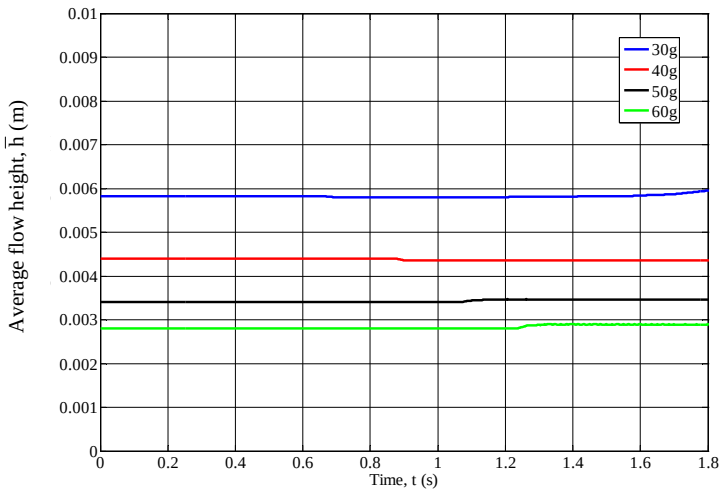

Figure 5.10: Averaged flow height against time for various g levels

Figure 5.11 (a to d) shows the development of flow height against the slope distance at various time intervals for simulations at 30 g, 40 g, 50 g and 60 g, respectively. The initial flow height represented by the grey line (t = 0 s) in Figure 5.11 (a to d) is at slope distance from 0 to 1 m. It can be seen in Figure 5.11 (a to d) that the flow height profiles are relatively constant throughout the flow except at the flow fronts, which are due to the numerical oscillations. Both Figures 5.10 and 5.11 indicate that the averaged flow height profiles throughout the flow are relatively constant.

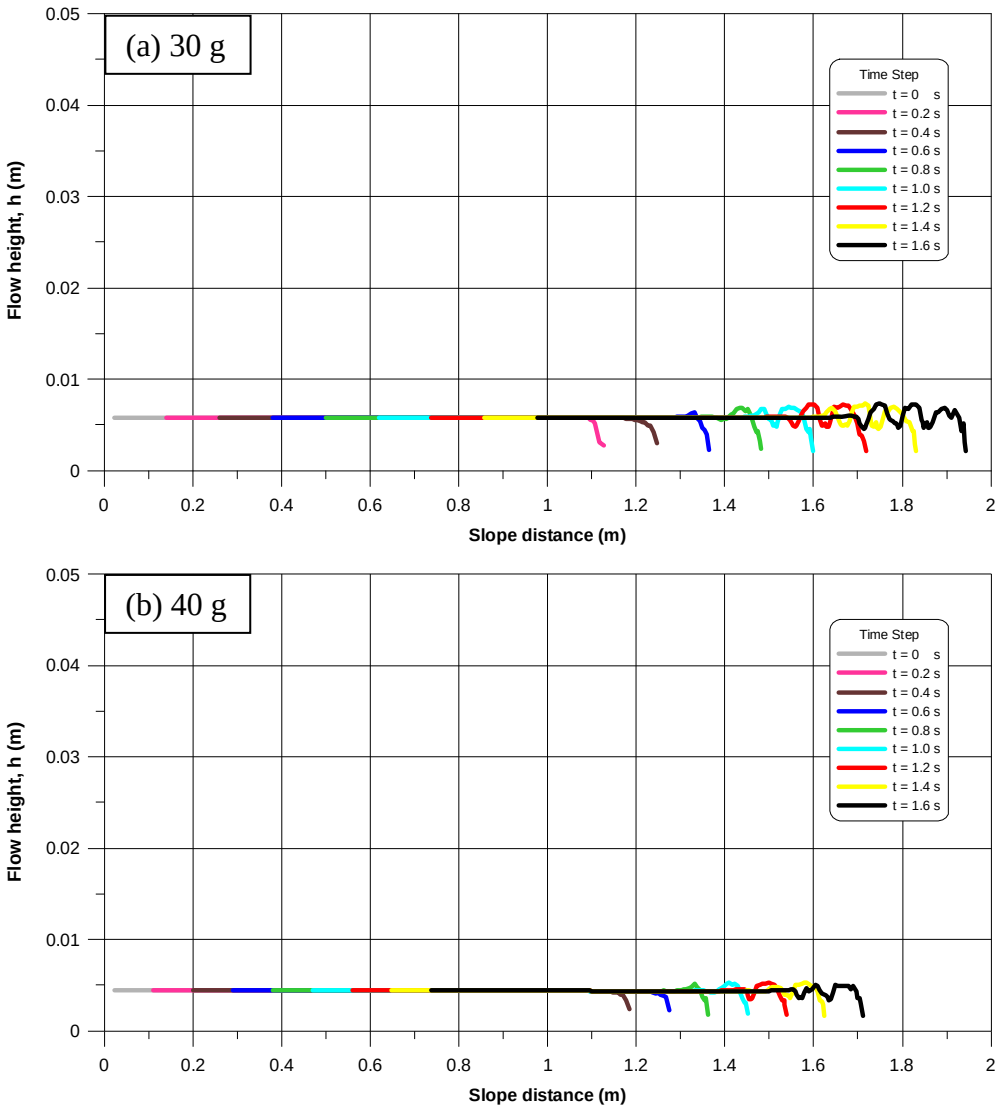

Figure 5.11: Flow height developments against slope distance at various time intervals

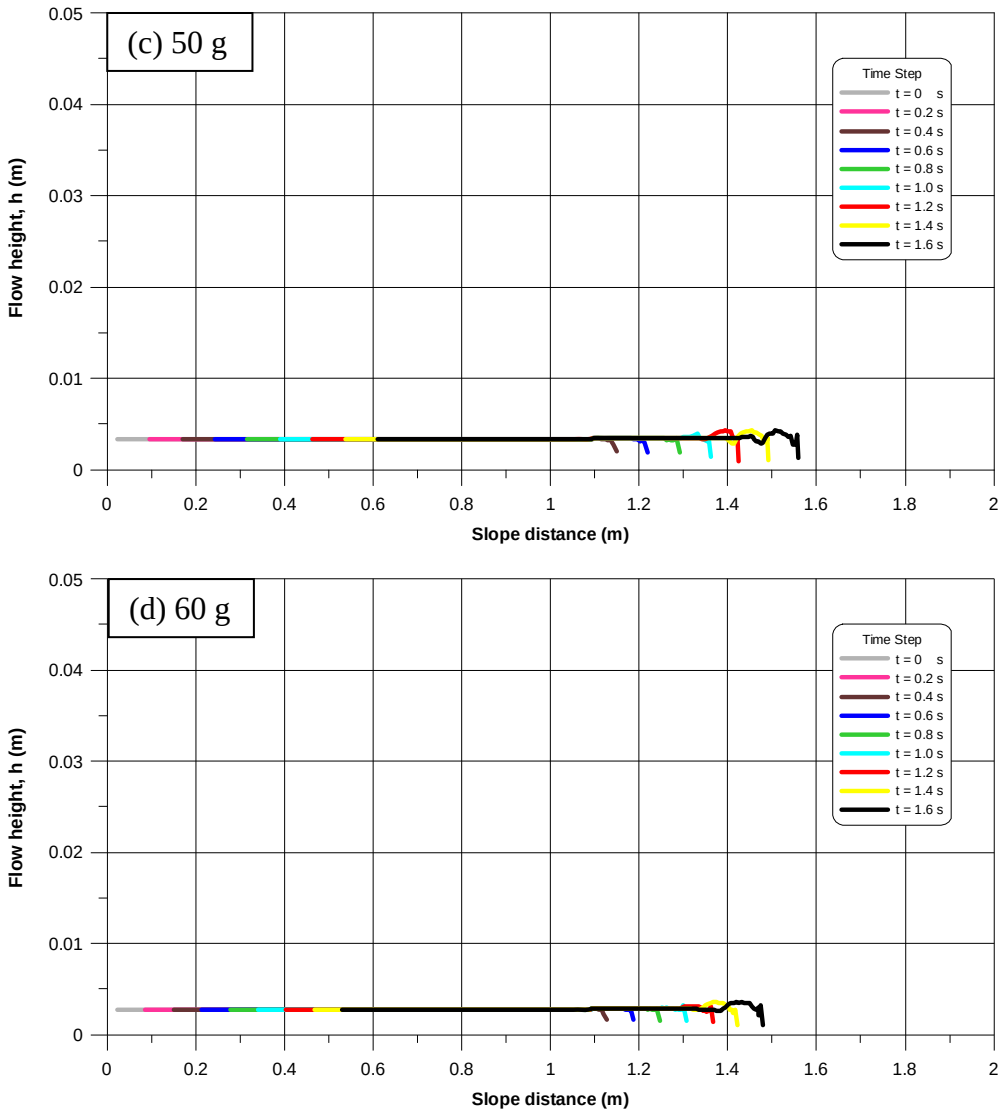

Figure 5.11 (cont.): Flow height developments against slope distance at various time intervals

Figures 5.12 and 5.13 show the flow distance and the prototype averaged flow distance against time respectively along the monitored line (0.3 m from the front line). The slopes from each simulation in Figure 5.12 represent the averaged flow velocities for each simulation. These flow velocities correspond well with the averaged flow velocities in Figure 5.9, indicating that the movements are more or less in the steady state. Figure 5.13 shows that, when the flow distances are normalised based on the proposed

scaling law for flow distance, they follow well with the proposed scaling law for flow distance, where the flow distance is scaled at N^3 times of the model.

Table 5.3 shows the summary results from the numerical simulations. It can be seen that the average prototype flow velocities and flow heights from each experiments are relatively constant and similar with the results from centrifuge experiments (Tables 4.3 & 4.4). The comparison of results from numerical simulations and centrifuge experiments will be discussed in the next chapter.

Based on the above results, it can be seen that the numerical simulations show the validity of the proposed scaling laws for the experimental conditions given and demonstrate that the soil movements in the centrifuge tests were close to the steady-state condition.

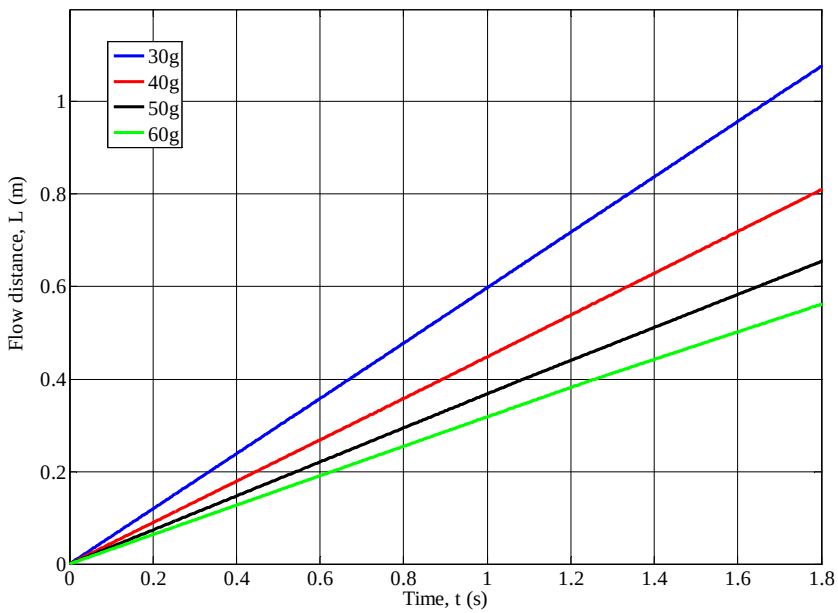

Figure 5.12: Flow distance against time for various g levels

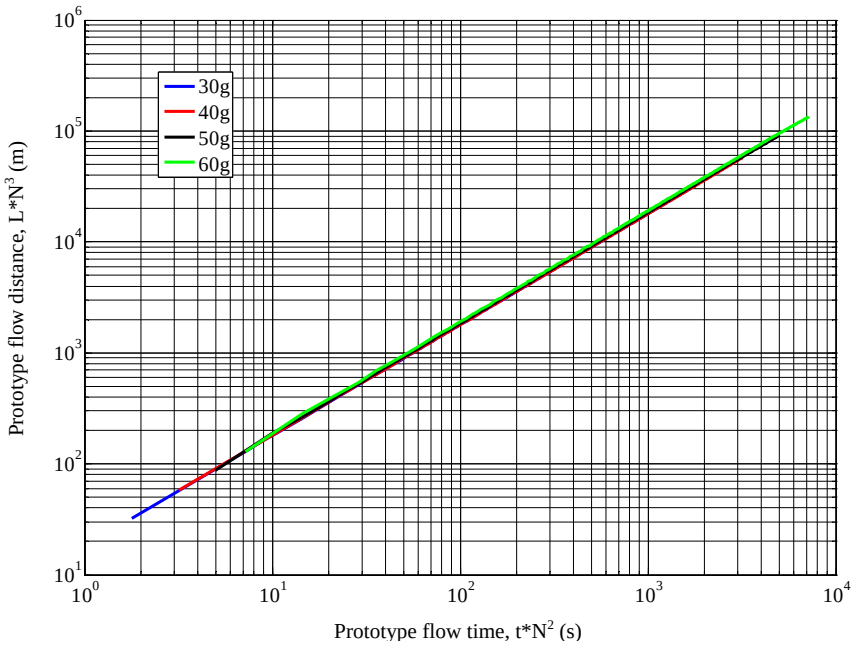

Figure 5.13: Prototype flow distance for various g levels

Table 5.3: Summary of results from numerical simulations

g levels	**Average flow velocity, $\bar{v}$ (m/s)**	**Average flow height, $\bar{h}$ (m)**	**Average prototype flow velocity, $\bar{v}_p$ =N* $\bar{v}$ (m/s)**	**Average prototype flow height, $\bar{h}_p$ =N* $\bar{h}$ (m)**
30	0.60	0.0058	18.1	0.17
40	0.45	0.0044	18.1	0.18
50	0.37	0.0034	18.4	0.17
60	0.31	0.0029	18.6	0.17

It should be noted that this chapter only presents the numerical simulation results from the scaled series (Series 1 of the centrifuge tests). The numerical simulations from the other series are presented and discussed in Chapter VI.

5.5 Sensitivity of the Model

The sensitivity of the model was investigated through a series of parametric studies. Parameters such as the background mesh, number of particles, time step, side friction, basal friction and pore pressure ratio, λ were investigated.

It should be noted that the simulations shown below were carried out at the submerged condition at 30 g, in which the initial flow velocity of 0.6 m/s and the initial flow height of 0.007 m were used. The basic parameters used herein are those as shown in Table 5.1, unless otherwise stated.

5.5.1 Background mesh

Two different background meshes were investigated. The background mesh that was used in all the presented results in the previous subsections is denoted as the "normal mesh". A finer background mesh was generated denoted as the "finer mesh" for comparison purposes. The mesh size of the "normal mesh" was 0.01 x 0.01 m, while the "finer mesh" size was 0.005 x 0.005 m. Figures 5.14 and 5.15 show the effects of background mesh on the averaged flow velocity and averaged flow height respectively, both with the same number of particles.

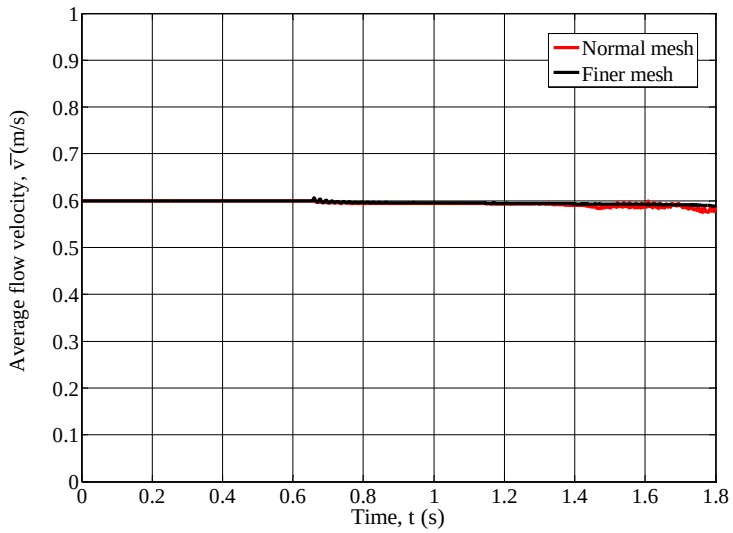

Figure 5.14: Effects of background mesh on the averaged flow velocity

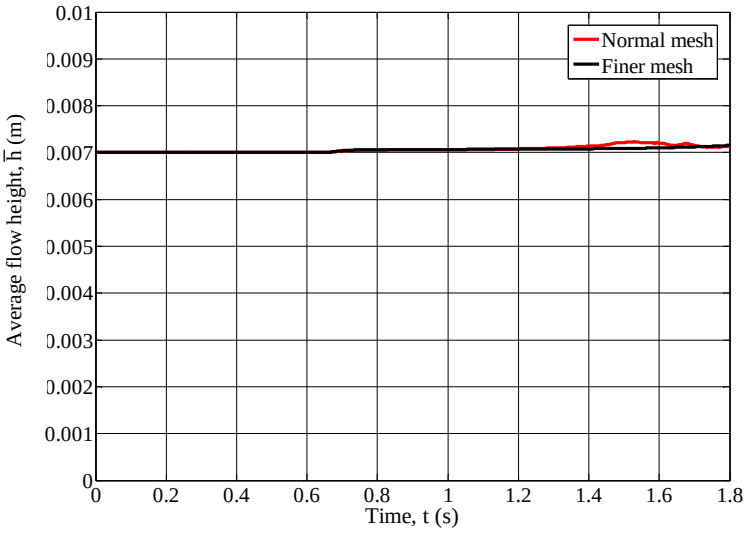

Figure 5.15: Effects of background mesh on the averaged flow height

It can be seen that the simulations with the "finer mesh" gave a slightly more consistent averaged flow velocity and flow height. This indicated that the accuracy increased with the finer mesh.

Although the simulation with the "finer mesh" was more accurate, both simulations yielded relatively similar results, where both the flow velocity and flow height were relatively similar in the "finer mesh" and in the "normal mesh". Since there was relatively no effect from using the "normal mesh" or "finer mesh", the "normal mesh" was therefore chosen in order to reduce the computation time.

5.5.2 Number of particles

The number of particles in the model can have an influence on the overall flow velocity and flow height. Comparisons was made on two analyses: (i) with 3,528 particles, denoted as the smaller number of particles and (ii) with 7,938 particles, denoted as the larger number of particles. Figures 5.16 and 5.17 show the effects of the number of particles on the averaged flow velocity and averaged flow height respectively.

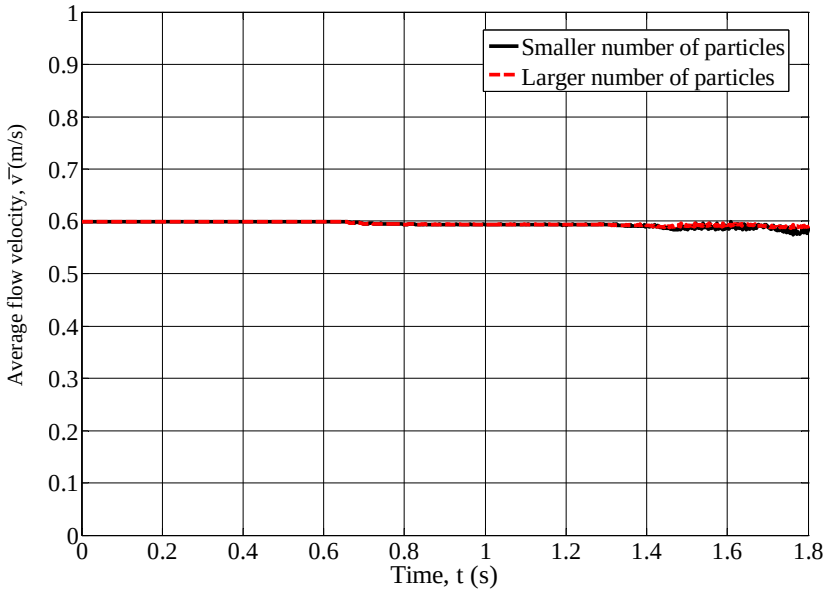

Figure 5.16: Effects of number of particles on the averaged flow velocity

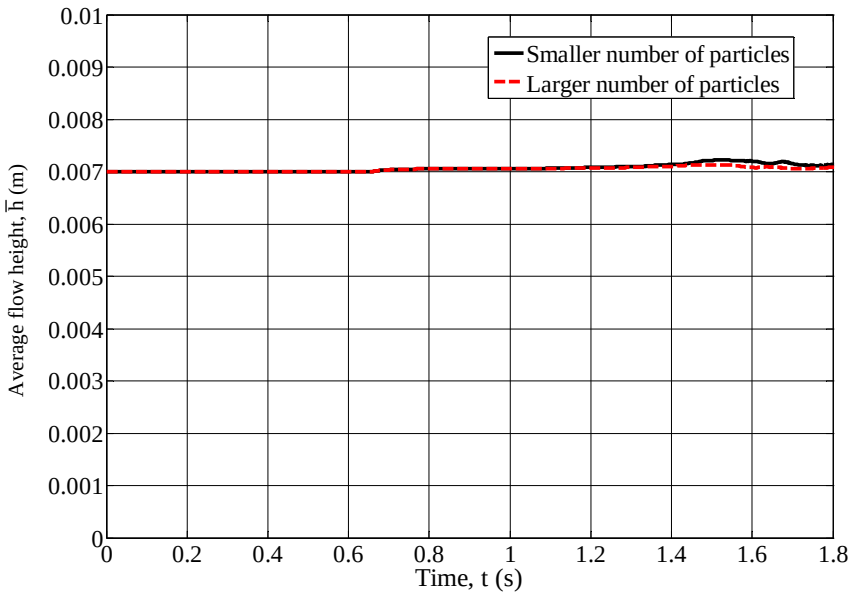

Figure 5.17: Effects of number of particles on the averaged flow height

It can be seen that the simulations with the larger number of particles gave a slightly more consistent averaged flow velocity and flow height. This indicated that the accuracy increases with number of particles.

Although the simulation with the larger number of particles was more accurate, both simulations yielded relatively similar results. Therefore, the smaller number of particles was chosen for all the simulations in this study in order to reduce the computational time.

5.5.3 Time step

The code uses the explicit time integration scheme. It is known that a larger time step in a simulation will reduce the computational time, but a larger time step may affect the accuracy of a simulation. It is therefore essential to find an optimum time step for a time-effective and accurate simulation.

Based on the experience from Abe (2009), the time step of dt = 1.0 x 10^{-5} seconds is known to be the optimum time step for simulating runout from a typical landslide. An attempt was made to reduce the computation time for the simulations in this research, where a larger time step of dt = 1.0 x 10^{-4} seconds was used and compared with.

Figures 5.18 and 5.19 show the effects of different time steps on the averaged flow velocity and averaged flow height respectively. The red line in the figures represents the larger time step of dt = 1.0 x 10^{-4} seconds, while the black line represents the time step of dt = 1.0 x 10^{-5} seconds. The smaller time step of dt = 1.0 E-6 seconds is also included in both Figures 5.18 and 5.19 for comparison.

The results show that the time steps of dt = 1.0 x 10^{-5} seconds and dt = 1.0 x 10^{-6} seconds are relatively similar. It can be seen that the time steps of dt = 1.0 x 10^{-6} seconds and dt = 1.0 x 10^{-5} seconds tend to have a more constant flow where the flow velocity and height are more constant throughout the flow; in this case the results are similar to the centrifuge tests, where the flow velocity and height are relatively constant throughout the flow.

This indicates that the larger time step (dt = 1.0 x 10^{-4} seconds) is not as accurate as the smaller time step. Therefore, the time step of dt = 1.0 x 10^{-5} seconds was chosen for all the simulations in this study.

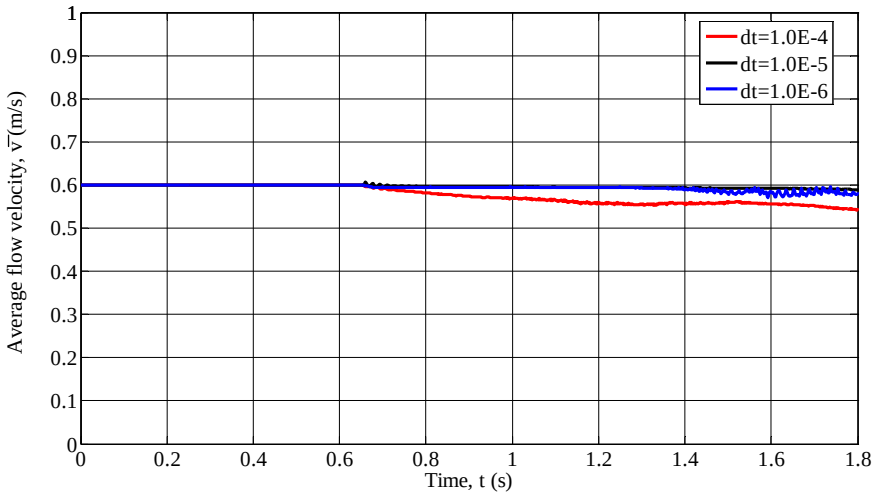

Figure 5.18: Effects of time step on the averaged flow velocity

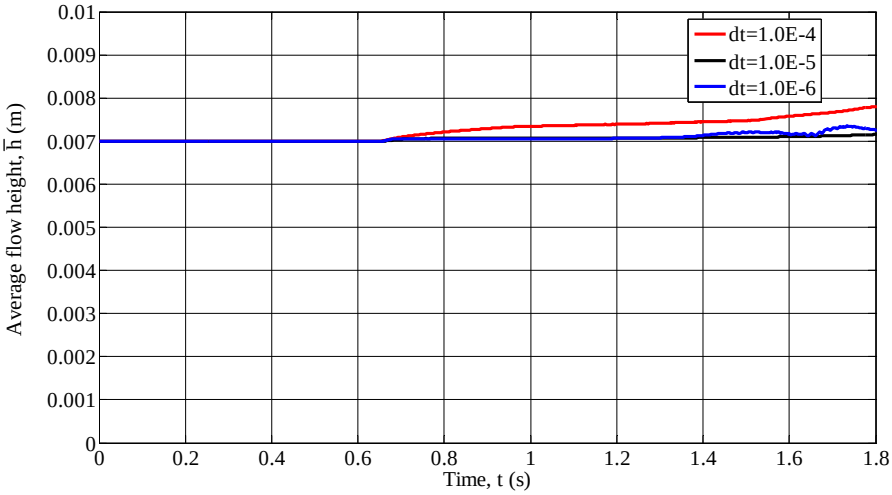

Figure 5.19: Effects of time step on the averaged flow height

5.5.4 Side wall friction

Since the submarine landslide flows in the centrifuge models are simulated in a channel, the side wall friction of the channel may play an important role in the overall flow behaviour. A number of simulations were carried out at various side wall frictions, and the flow developments from the simulations are compared with the flow developments from the centrifuge tests.

Figures 5.20 and 5.21 show the effects of various side wall frictions on the averaged flow velocity and averaged flow height respectively. A wide

range of side wall frictions is investigated in order to match the flow developments, as in the centrifuge tests which also gives the similar averaged flow velocity and flow height. It can be seen that increasing the side wall friction induces slightly more fluctuations in the averaged flow velocity and flow height. In high side wall friction (i.e. $\theta = 10^o$) case, the flow velocity is slightly slower by approximately 3% compared to the flow velocity of the case without side friction (i.e. $\theta = 0^o$). Therefore, the side wall friction can be considered to be negligible in the centrifuge experiments.

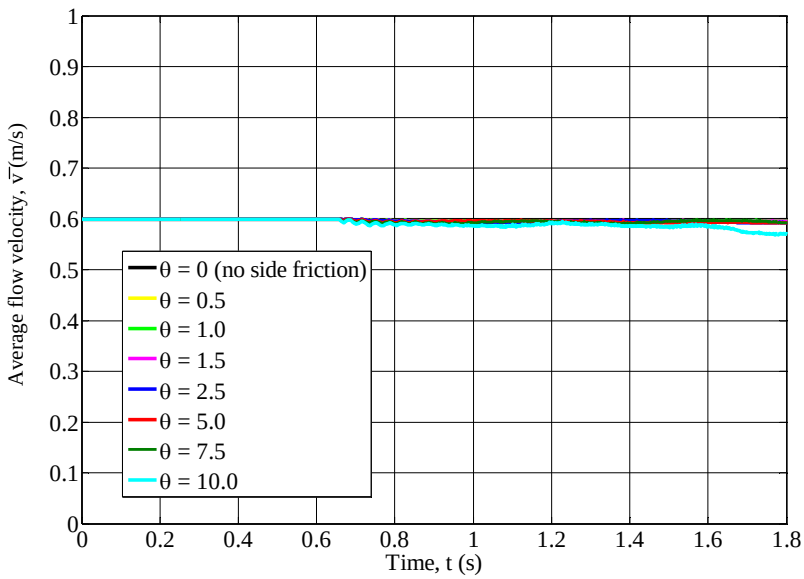

Figure 5.20: Effects of various side wall frictions on the averaged flow velocity

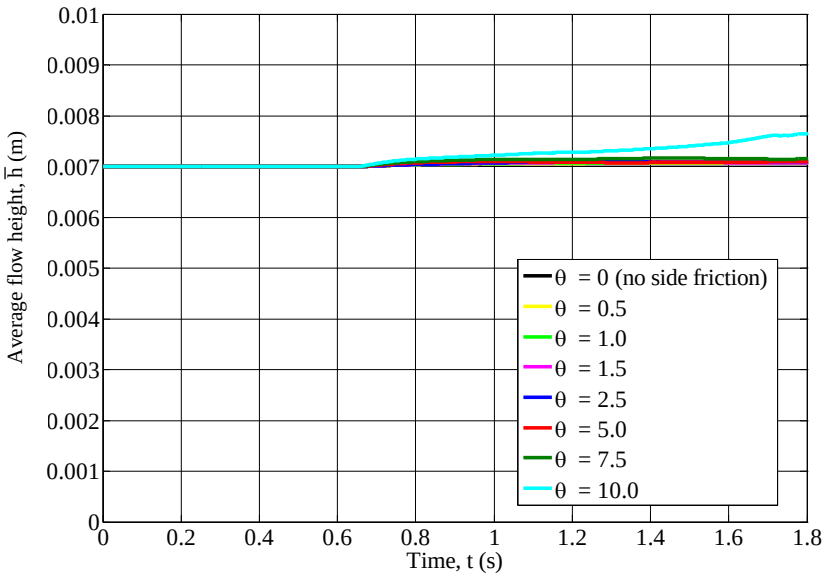

Figure 5.21: Effects of various side wall frictions on the averaged flow height

Figure 5.22 shows the velocity profile (0.3 m from the front line) of various side wall frictions (at 1.6 s into the flow process). It can be seen that the side wall friction is more pronounced at θ = 10°, as the flow velocity at both side walls are lower compared to the middle of the flow. The figure also shows that the effects on the flow velocity are minimal for side wall frictions lower than 10°.

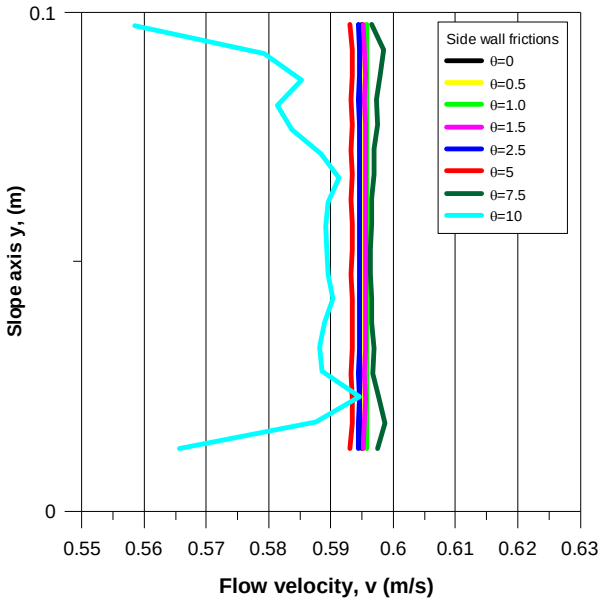

Figure 5.22: Velocity profile at various side wall frictions

Figures 5.23 (a to h) shows the flow developments from the various side wall frictions. The flow developments can be compared with the actual flow developments in the centrifuge experiments as shown in Figure 4.23. It can be seen that, for the simulation without side wall friction (θ = 0°), the front of the flow is relatively smooth, while increasing the side wall frictions gives a rougher and irregular flow front. The rougher and irregular flow front is due to the numerical oscillation.

The flow heights in the flow developments are relatively constant and similar at various side wall frictions, as shown in Figure 5.23. Therefore, the effect of side wall friction is minimal if the side wall friction is less than 10°. The side wall friction of θ = 5° was used throughout all the simulations in this study.

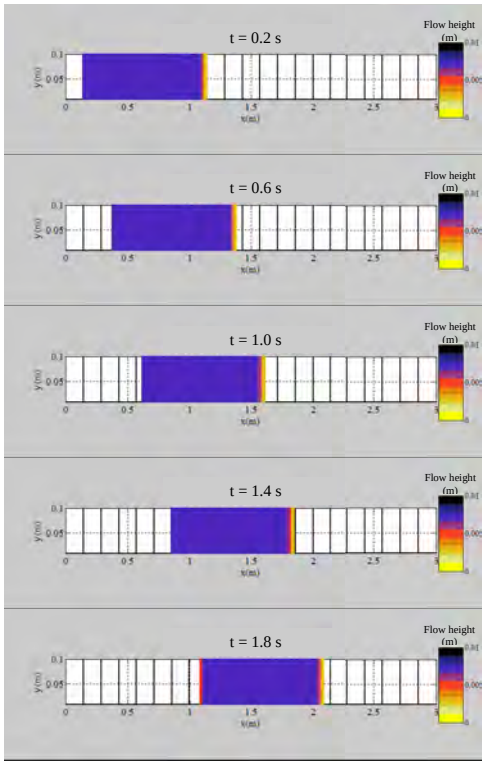

(a) θ = 0°

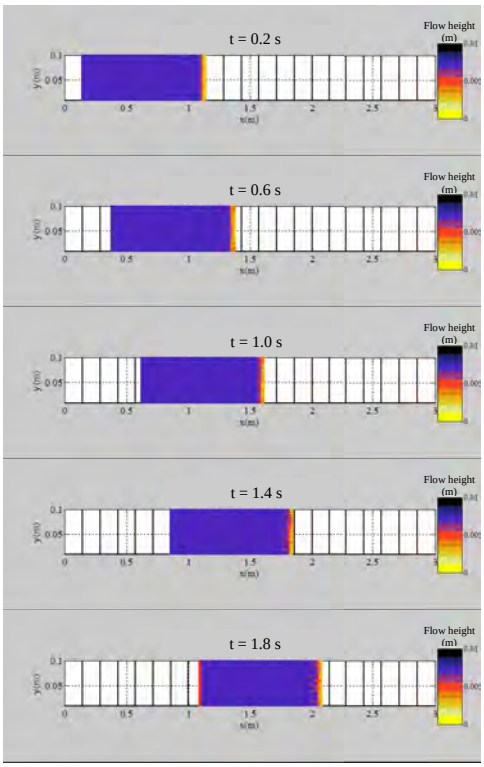

(b) θ = 0.5°

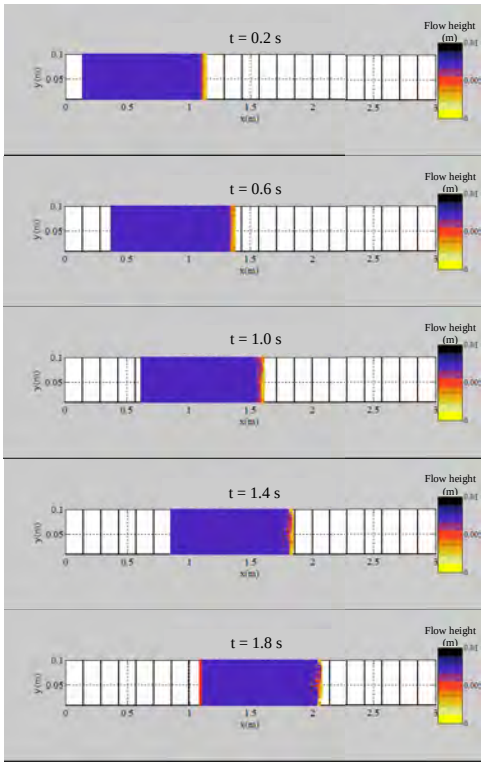

(c) θ = 1.0°

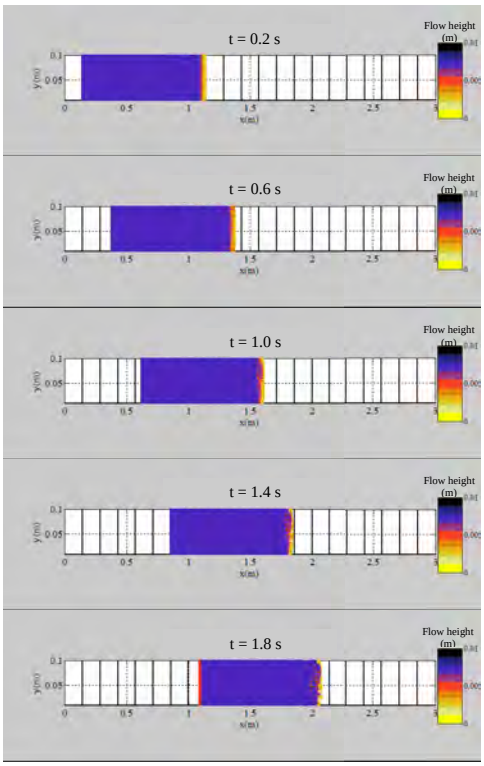

(d) θ = 1.5°

Figure 5.23: Effects of various side wall frictions on the flow developments

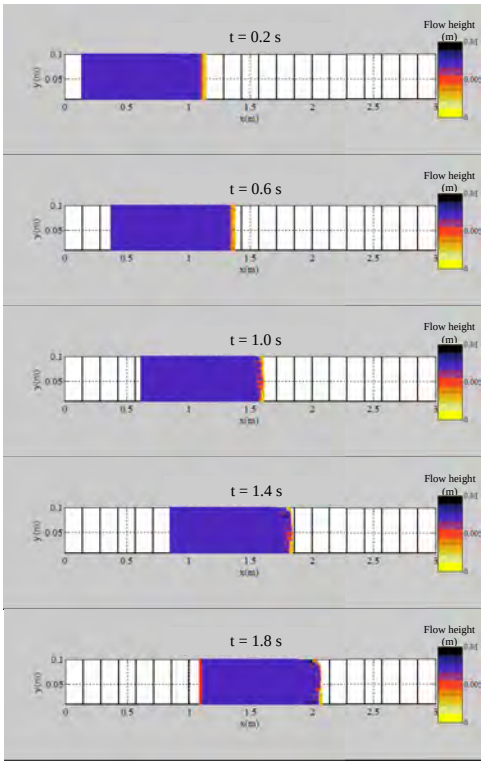

(e) θ = 2.5°

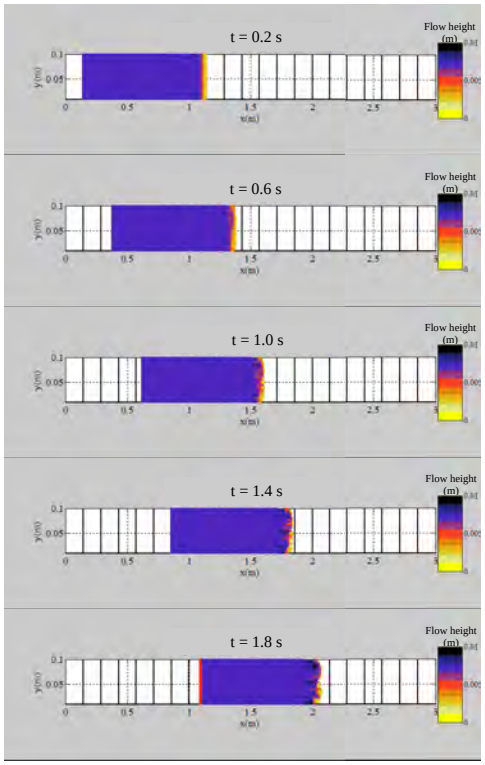

(f) θ = 5.0°

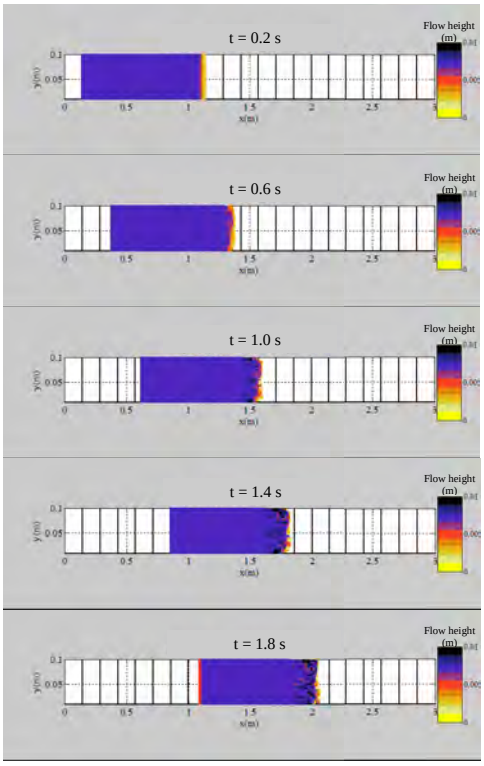

(g) θ = 7.5°

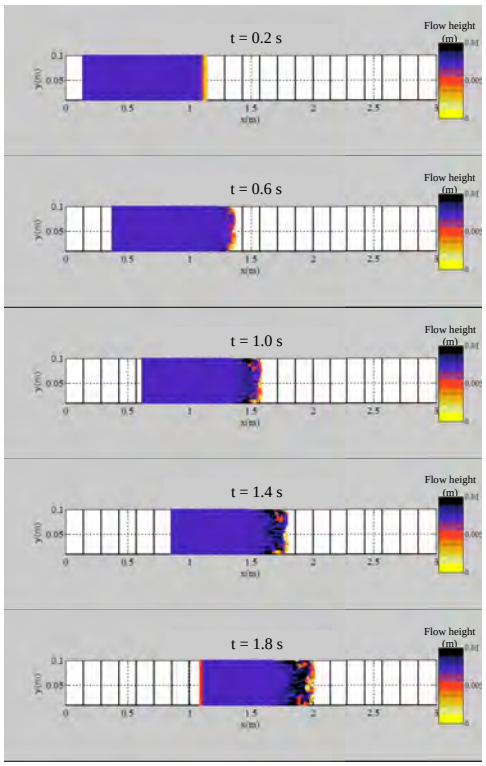

(h) θ = 10.0°

Figure 5.23 (cont.): Effects of various side wall frictions on the flow developments

5.5.5 Basal friction and pore pressure ratio (λ)

The basal friction angle and pore pressure ratio, λ, directly influences the basal stresses that are important in driving the soil body to move along a slope, as shown in equations 5.11 a and b. Therefore, the basal friction angle and λ, are considered as significant parameters. Various λ values and two different basal friction angles have been investigated, one without basal friction angle = 0° and one at basal friction angle = 12.5^o.

Figures 5.24 and 5.25 show the effects of various λ on the averaged flow velocity at basal friction angles, 0° and 12.5^o respectively. Figures 5.26 and 5.27 show the effects of various λ on the averaged flow height at basal friction angles, 0° and 12.5^o respectively.

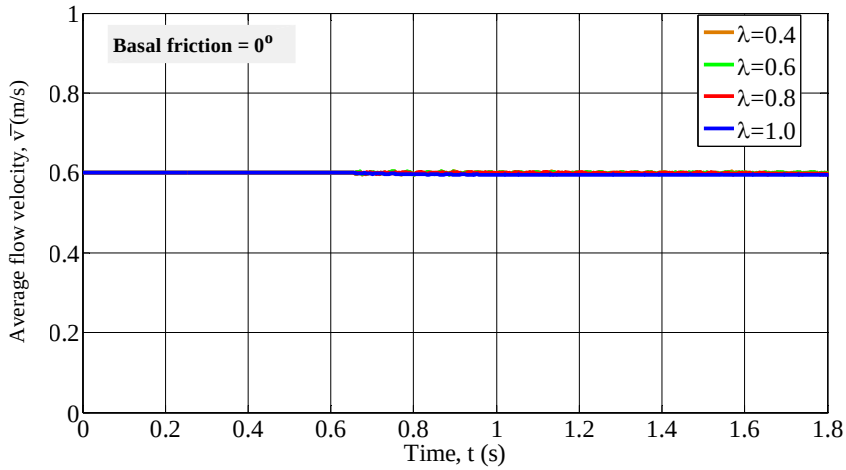

Figure 5.24: Effects of various λ on flow velocity at basal friction = 0°

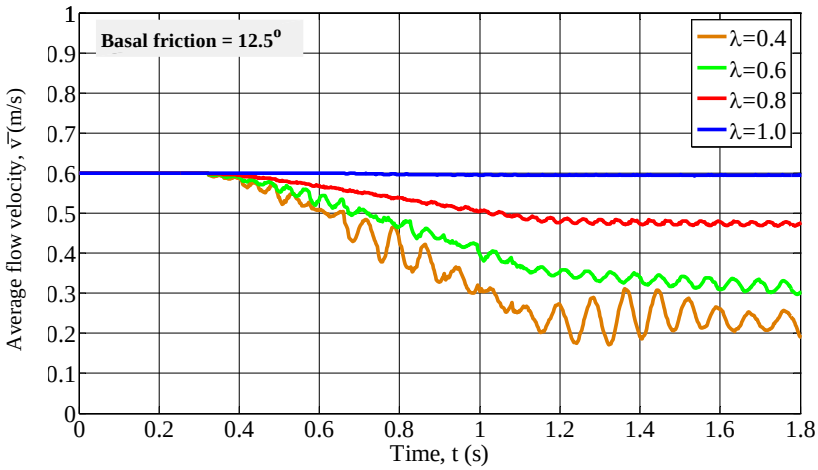

Figure 5.25: Effects of various λ on flow velocity at basal friction = 12.5^o

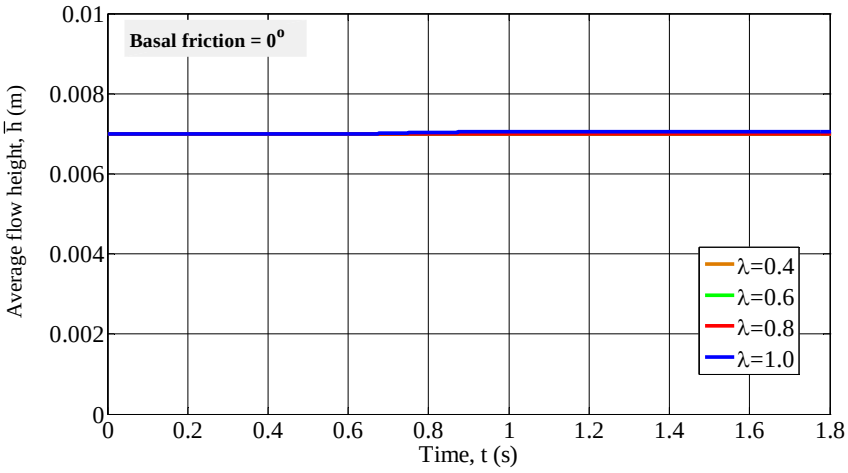

Figure 5.26: Effects of various λ on flow height at basal friction = 0°

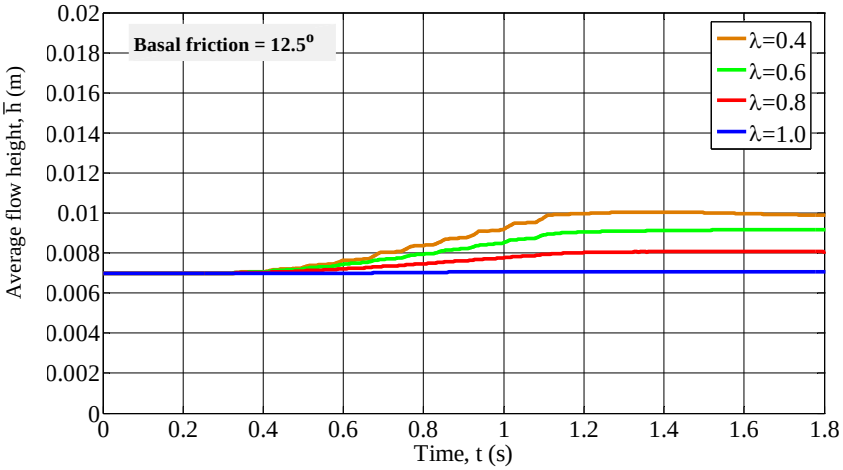

Figure 5.27: Effects of various λ on flow height at basal friction = 12.5°

It can be seen that, at basal friction angle = 0°, the averaged flow velocities and flow heights at various λ are the same, as shown in Figures 5.24 and 5.26.

For the scenario of basal friction angle = 0°, this can be understood as the flow being fully liquefied with no apparent effective stress. Based on equations 5.11 a and b for the basal frictional stress, in that if λ is equal to 1, the basal stress is only dependent on the fluid fraction and the viscosity term, which is similar to having a zero basal friction. Since the fluid fraction and the viscosity are the same in these simulations, the results should be the same. Therefore, λ has relatively no effects on the flow movements when the basal friction angle = 0°.

At basal friction angle = 12.5^o, the averaged flow velocity increases with λ while the averaged flow height reduces with λ. This indicates that the flow movements are faster at higher λ where the apparent effective stress of the soil body is less. Since the volume input rate is the same, the flow height will be smaller. It should be noted that the averaged flow velocities and flow heights in Figures 5.25 and 5.57 are the averaged of 0.2 to 0.4 m from the front. Having an average of a bigger range (0.2 to 0.4 m from the front) is to reduce numerical oscillations. It can be seen that the numerical oscillations are more obvious for the smaller λ value as shown in Figure 5.25.

Based on the results from these simulation, the flow with λ = 1 at basal friction angle = 12.5^o corresponded well with the results from the centrifuge experiments. A comparison of results from the centrifuge experiments and numerical simulations will be discussed in more detail in the next chapter.

5.6 Summary

Numerical simulations using the DAMPM have successfully simulated the submarine landslide flows and closely modelled the centrifuge experiments to examine the proposed centrifuge scaling laws. The results from the numerical simulations show that the scaling laws follow the findings from the centrifuge experiments.

The sensitivity of the model was investigated and it was found that the model was relatively stable even at the “finer mesh” and “larger number of particles”. Comparisons have been made between the “normal mesh” and the “finer mesh” as well as “smaller number of particles” and “larger number of particles”. The results from all these variants show similar results, indicating that the model is acceptable for the purpose of this study, even though some numerical oscillations were noticed.

Parametric studies on various soil properties have been made to fine tune the numerical model. It is found that the pore pressure ratio, λ, is a very important parameter in determining the submarine landslide flow progress, in particular for determining the apparent effective stress of a soil body. Further comparison and discussions of the results from the centrifuge experiments and numerical simulations are presented in the next chapter.

CHAPTER VI

6.0 DISCUSSION AND COMPARISONS OF RESULTS

6.1 Introduction

Both chapters IV and V have demonstrated the results from the centrifuge experiments and the numerical simulations following the proposed scaling laws. This chapter aims to compare the two methods and the details of both methods will be investigated more thoroughly. This chapter also presents and discusses the additional results from the numerical simulations that simulate the series of centrifuge tests other than the scaled cases.

6.2 Comparisons of Results with the Developed Scaling Laws

As described in Chapter III, the proposed scaling laws for soil flow differ from the conventional scaling laws for soil mechanics problems. The conventional scaling law for length is related to strain increment; however, if straining is so large that the stress state is not a function of strain anymore, then the scaling for length (flow distance) may not be a conventional one, which originates from the fact that stress increment (i.e. satisfying the stress equilibrium condition) is related to strain increment (giving the length scaling law of $L_{prototype} = NL_{model}$).

Phenomena such as submarine landslide flows in this study involve very large movements of a soil-fluid mixture, where the soil in contact at the base boundary is extensively sheared. The soil at this stage can be understood to be at failure (critical state) where the effective stress state of the soil becomes independent of strain, which results in the length scaling law being indeterminate. Assuming that the soil flowing along the slope is at critical

state and the fluid component of the soil is giving a viscous resistance to the flowing soil, the following scaling laws can be deduced; $\bar{h}_{prototype} = N\bar{h}_{model}$, $\bar{v}_{prototype} = N\bar{v}_{model}$ and $L_{prototype} = N^3 L_{model}$ (as in equations 3.6, 3.7 and 3.11). The scaling law in height (i.e. perpendicular to the slope) comes from the fact that the stress state is governed by the weight of the soil (which gives the basal and side frictions). This means that the variation in the change in height is considered to be small compared to the movement in the direction parallel to the slope, hence the depth average technique can be adopted. Therefore, the scaling laws for velocity and length in parallel to the slope come from (i) the equation of motion, (ii) the effective stress state to be independent from strain (i.e. critical or residual state) and (iii) the viscous resistance of pore fluid.

According to the proposed scaling laws, the scaled series in which the prototype input flow rates were the same for the various g levels gave a similar prototype flow velocity and height at the various g levels. Table 6.1 shows the summary results from the centrifuge experiments and the numerical simulations for the scaled series. It can be seen that the averaged flow velocity and height were relatively similar at various g levels for both centrifuge experiments and numerical simulations. This indicated that the centrifuge experiments and numerical simulations from various g levels scaled reasonably well to the proposed scaling laws.

Table 6.1: Summary of results from centrifuge experiments and numerical simulations

g levels	Input flow rate per unit length, Q_{ul} ($m^3/s/m$) $*10^{-4}$	Prototype input flow rate per unit length, Q_{Pul} ($m^3/s/m$) ($Q_{Pul}=N^2Q_{ul}$)	Centrifuge experiments				Numerical simulations			
			$\bar{v}$ (m/s)	$\bar{h}$ (m)	$\bar{v}_p$ $=N*\bar{v}$ (m/s)	$\bar{h}_p$ $=N*\bar{h}$ (m)	$\bar{v}$ (m/s)	$\bar{h}$ (m)	$\bar{v}_p$ $=N*\bar{v}$ (m/s)	$\bar{h}_p$ $=N*\bar{h}$ (m)
30	35.0	3.2	0.60	0.0058	18.0	0.18	0.60	0.0058	18.1	0.17
40	19.7	3.2	0.45	0.0044	18.0	0.18	0.45	0.0044	18.1	0.18
50	12.6	3.2	0.37	0.0034	18.5	0.17	0.37	0.0034	18.4	0.17
60	8.8	3.2	0.32	0.0028	19.2	0.17	0.31	0.0028	18.6	0.17

Note:
$\bar{v}$ =Average flow velocity
$\bar{h}$ = Average flow height
$\bar{v}_p$ = Average prototype flow velocity
$\bar{h}_p$ = Average prototype flow height

Figure 6.1 shows the averaged flow height against the averaged flow velocity from the centrifuge experiments and the numerical simulations, demonstrating the results from centrifuge experiments and numerical simulations are relatively similar. Figures 6.2 and 6.3 show the relationship of averaged prototype flow height and averaged prototype flow velocity against the g level respectively for the results from both the centrifuge experiments and the numerical simulations. It can be seen that both consistently show that the averaged prototype flow height and flow velocity were relatively similar at various g levels for both centrifuge experiments and numerical simulations. This again indicates that the centrifuge experiments and numerical simulations are modelled and scaled correctly according to the proposed scaling laws.

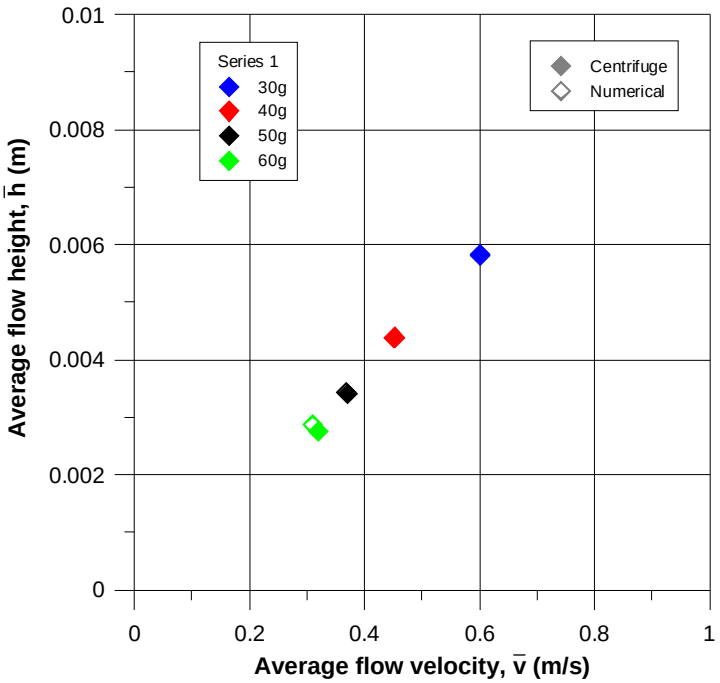

Figure 6.1: Averaged flow height against averaged flow velocity from centrifuge experiments and numerical simulations

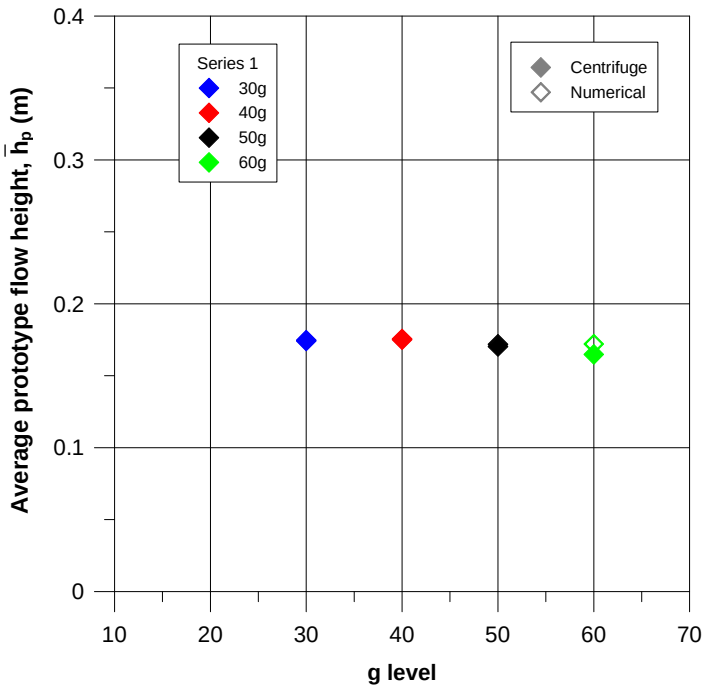

Figure 6.2: Comparisons of averaged prototype flow height between centrifuge experiments and numerical simulations

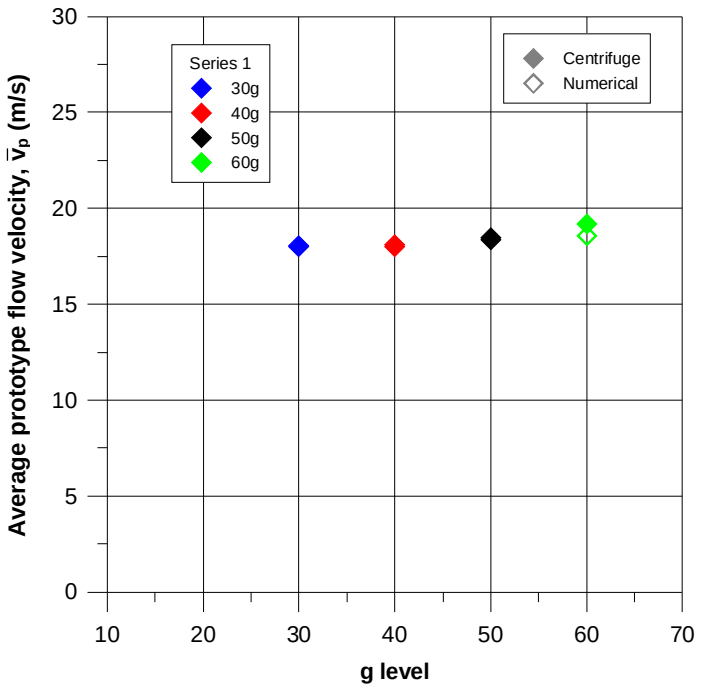

Figure 6.3: Comparisons of averaged prototype flow velocity between centrifuge experiments and numerical simulations

6.3 Comparisons of Centrifuge Experiments with Numerical Simulations (All series)

The results from the numerical simulations in Chapter V presented only the scaled series, while in Chapter VI the results of the centrifuge experiments were given for the other non-scaled series. This section compares the results of centrifuge experiments and numerical simulations from the non-scaled series, in particular the series with a large flow rate.

6.3.1 Flow velocity and flow height

Figures 6.4 and 6.5 show the relationship of averaged prototype flow height and averaged prototype flow velocity against the prototype input flow rate, respectively. The results are from both the centrifuge experiments and numerical simulations of the series with a large flow rate (Series 3).

Unlike the results for the scaled series (Series 1), the results from the numerical simulations do not match the results from centrifuge experiments for this series (Series 3). It can be seen that the averaged prototype flow heights from the numerical simulations are lower compared to the centrifuge experiments, while the averaged prototype flow velocities are higher from the numerical simulations compared to the centrifuge experiments.

This leads to a number of investigations on why the numerical simulations for this series do not match the centrifuge results. The parameters used in the numerical simulation for this series were the same for the scaled series (Series 1). All the basic soil parameters should remain the same, as the flow materials used were the same, except the input flow rates in this series (Series 3) were larger.

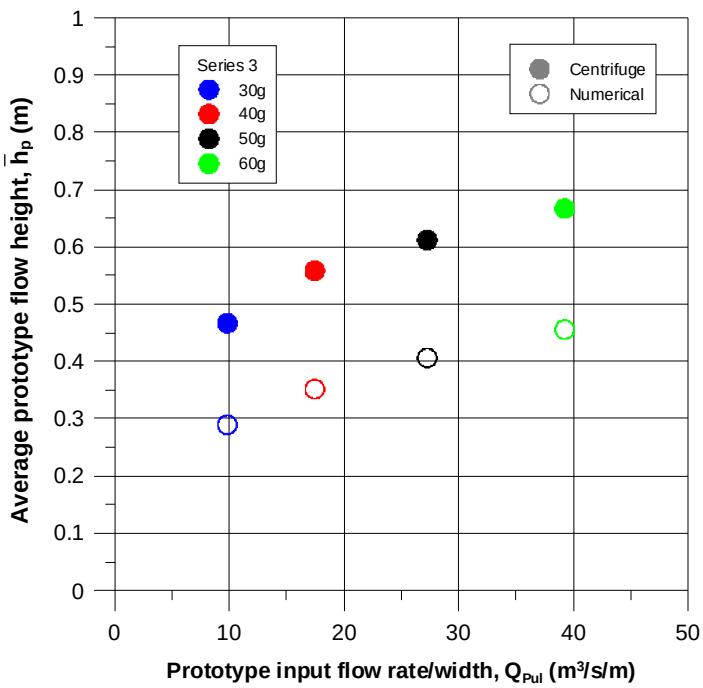

Figure 6.4: Comparisons of averaged prototype flow height between centrifuge experiments and numerical simulations (Series 3)

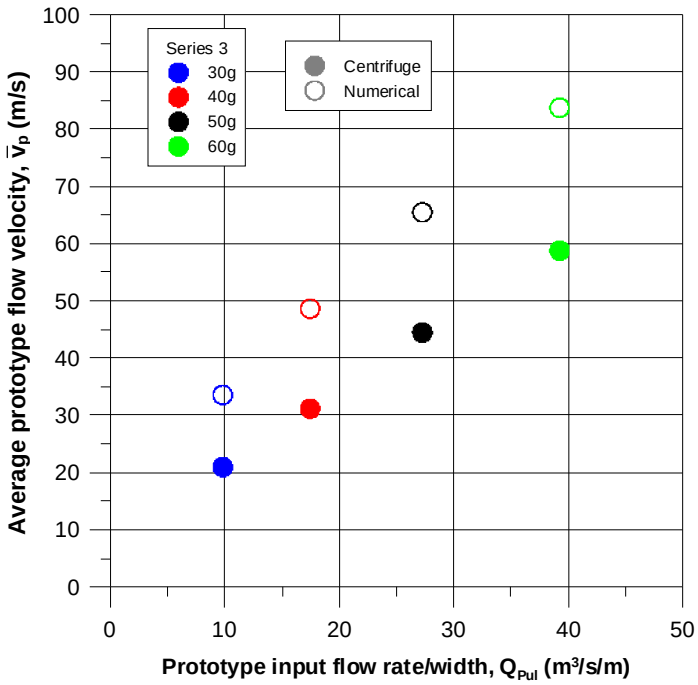

Figure 6.5: Comparisons of averaged prototype flow velocity between centrifuge experiments and numerical simulations (Series 3)

Based on all the input parameters for the numerical simulations (refer to Table 5.1 in Chapter V), the only parameter that could be different between each series is the pore pressure ratio, λ, which could be affected by the large input flow rate. Therefore, various λ values have been used to match the results from the centrifuge experiments.

Figures 6.6 and 6.7 show the contours of λ values on the averaged prototype flow height and flow velocity, respectively, for Series 3. It can be seen that the λ value that best represents the results in the centrifuge experiment for this series (Series 3) is 0.7. It should be noted that, for the scaled series (Series 1), the λ value is 1, in which the flow slurry is considered to be completely liquefied and there is no effective stress at the base boundary. This is because the prototype input flow rate in Series 1 is small, which results in shallow flows. When the prototype input flow rate increases, the thickness of the prototype flow increases and hence there is more resistance at the base. Here, with a thicker flow in Series 3, the λ value is 0.7 indicating that the flow slurry is not completely liquefied.

Figure 6.6 shows that the averaged prototype flow height increases by decreasing the λ value, while Figure 6.7 shows that the averaged prototype flow velocity decreases by decreasing the λ value. By decreasing the λ value, larger shear resistance is created by the increasing effective stress of the soil and hence the soil flows slower. A smaller flow height produces a smaller effective stress at the base boundary, resulting in a larger pore pressure ratio, λ.

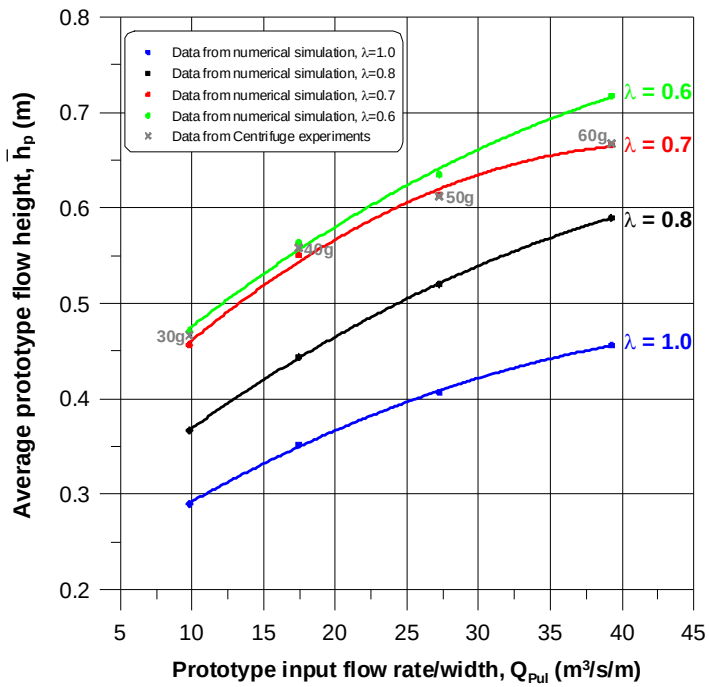

Figure 6.6: Contours of λ values on the averaged prototype flow height (Series 3)

The relationship of λ values and their corresponding flow height and velocity in Figures 6.6 and 6.7 is unique for the materials used in the centrifuge experiments. However, such a relationship is only useful in predicting the averaged flow height and velocity of an actual submarine landslide flow in the field when the numerical model is calibrated to the site-specific soil parameters.

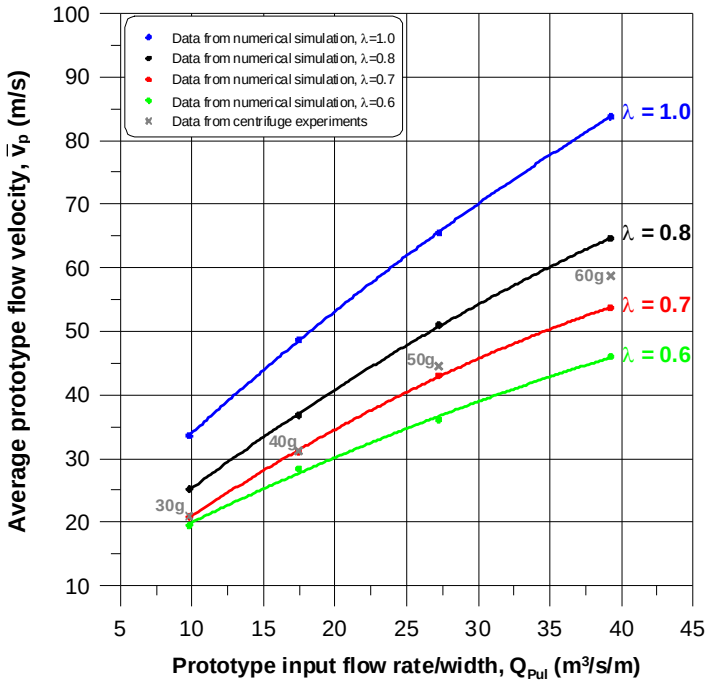

Figure 6.7: Contours of λ values on the averaged prototype flow velocity (Series 3)

Figures 6.8 and 6.9 show the contours of λ values on the averaged prototype flow height and flow velocity respectively for the non-submerged series (Series 4). Similar to the results from Series 3, Figure 6.8 shows that the averaged prototype flow height increases by decreasing the λ value, while Figure 6.9 shows that the averaged prototype flow velocity decreases by decreasing the λ value. It can be seen that the λ value that best represents the results in the centrifuge experiments for this series (Series 4) is 0.5. For the range of prototype input flow rate considered here, the results indicate that the effective stress state of soil is much greater in the non-submerged series compared to the submerged series. Hence, less excess pore pressure is generated at the base for the non-submerged series due to the fact that the effective stress level is much greater than the submerged series.

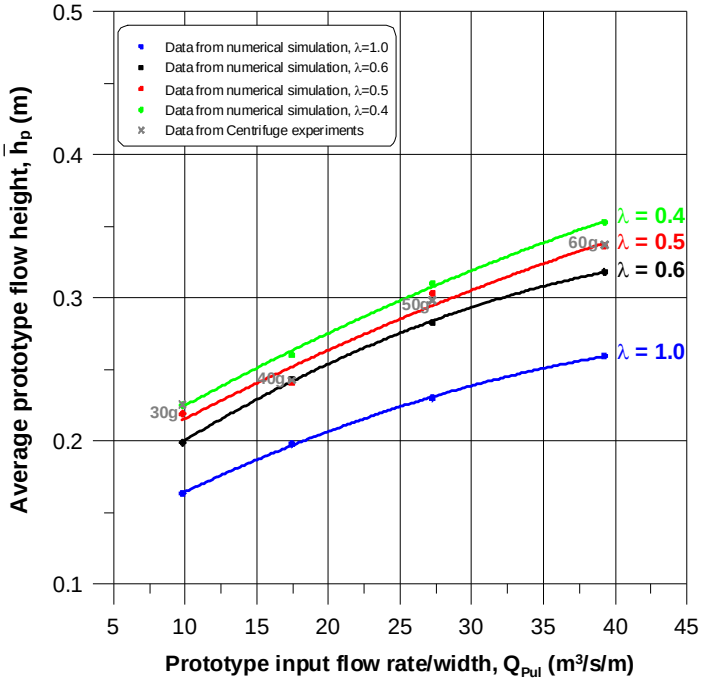

Figure 6.8: Contours of λ values on the averaged prototype flow height (Series 4)

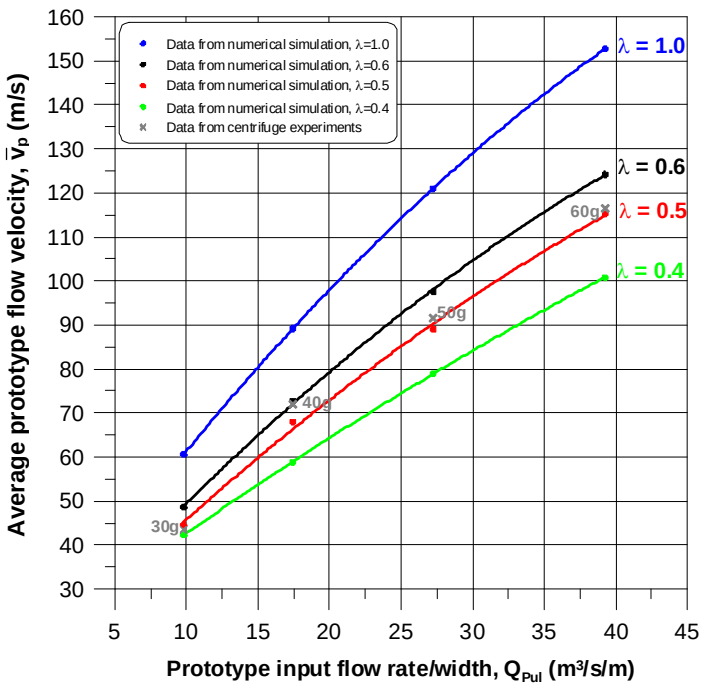

Figure 6.9: Contours of λ values on the averaged prototype flow velocity (Series 4)

The relationship of prototype flow height and prototype flow velocity with the prototype input flow rate for all four series are summarised in Figures 6.10 and 6.11 respectively. It can be seen that the results from numerical simulations match the results from centrifuge experiments reasonably well for all four series. The λ values for Series 1 and 2 is 1.0, while for Series 3 and 4, the λ values are 0.7 and 0.5 respectively.

With the same input flow rates for Series 3 and 4, the dry or non-submerged series (Series 4) has a smaller prototype flow height and a larger prototype flow velocity compared to Series 3, as shown in Figures 6.10 and 6.11. This is because the gravity effect for the non-submerged series (total weight of the flow slurry) is larger compared to the gravity effect for the submerged series (buoyant weight of the flow slurry) which is smaller. This is also reflected on the numerical simulations, where a smaller λ value (λ = 0.5) for the non-submerged series is used to match the centrifuge experiments compared to the submerged series (λ = 0.7). This again indicates that the effective stress level is much greater for the non-submerged series.

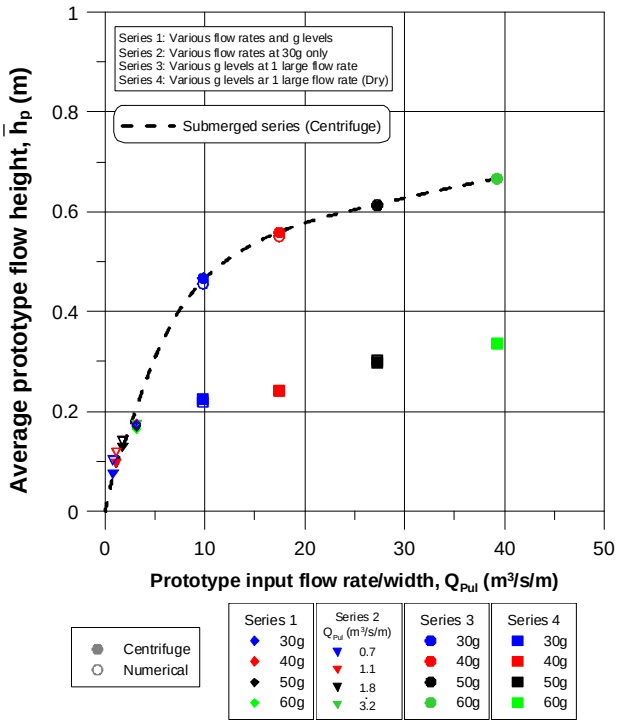

Figure 6.10: Comparisons of averaged prototype flow height between centrifuge experiments and numerical simulations (All series)

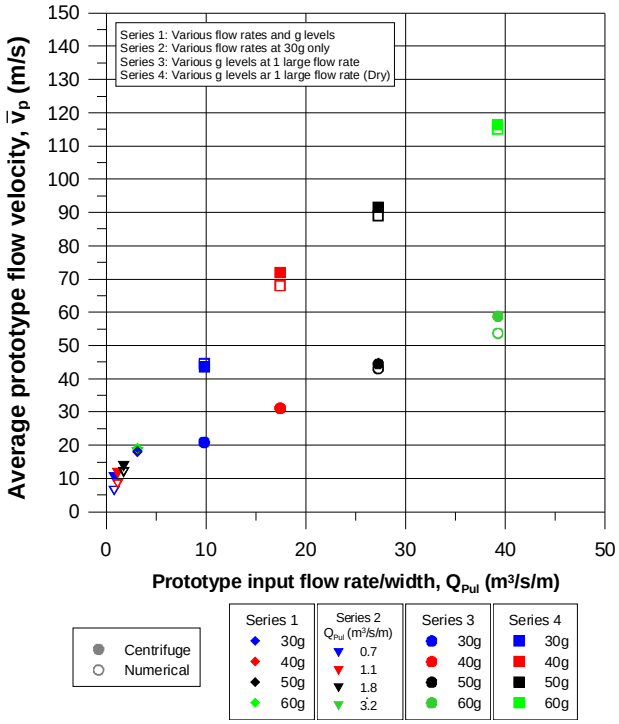

Figure 6.11: Comparisons of averaged prototype flow velocity between centrifuge experiments and numerical simulations (All series)

Furthermore, it can be seen that the λ values are smaller for the larger prototype input flow rates (Series 3 & 4) as compared to Series 1 and 2. This indicates that the effective stresses are larger at larger prototype input flow rates, in which the prototype flow heights are larger in Series 3 compared to Series 1 & 2.

The dotted lines in Figure 6.10 show the relationship between flow height versus input flow rate for the slurry tested in this study (E-grade Kaolin clay with water content of 122 %). This demonstrates that charts such as Figures 6.10 and 6.11 can be developed experimentally by conducting various input flow rates for different types of soils (or actual field materials) in a centrifuge. These charts can then be used to assess the flow velocity and flow height for a given input flow rate scenario.

As mentioned in Chapter IV, there is a leap from Series 2 to 3. However, it is uncertain if this leap is the behaviour of the flow or subjected to

other experimental subtle changes such as different clay bathes used in each series. Unfortunately, there are no data points in the transition from Series 2 to 3 in order to understand the leap.

6.3.2 Relationship of flow height, flow velocity and change in pore pressure

The results from the numerical simulations, in particular the flow heights and λ values, can be used to back-calculate the change in pore pressure and compare with the measured change in pore pressure (measured at the base of the flow slurry) obtained from the centrifuge experiments. It should be noted that the numerical simulations are unable to provide direct results of the change in pore pressure due to the flow slurry. However, back calculation can be made based on the information such as flow heights and λ values. The pore pressure ratio, λ, is the ratio of change in pore pressure, ΔU and the total incremental stress, Δσ.

$$\lambda = \frac{\Delta U}{\Delta \sigma} \tag{6.1}$$

Based on the results from the numerical simulations, Δσ can be calculated as the prototype flow height multiplied by the slurry density. It should be noted that, in order to compute Δσ, the effective slurry density was used for the submerged series to compensate the buoyancy effect as the slope was submerged with water before the flow slurry. For the non-submerged series (dry), the total incremental stress was solely due to the flow slurry; therefore, the total slurry density was used instead of the effective density.

Figure 6.12 shows the change in pore pressure versus prototype input flow rate for all the series. The solid symbols are the actual measured change in pore pressure at the base of the flow slurry from the centrifuge experiments, while the open symbols are the back-calculated changes in pore pressure based on the results of flow heights and λ values from the numerical simulations. It

can be seen that the back-calculated change in pore pressure is much lower than the measured change in pore pressure. This indicates that the measured change in pore pressure from the centrifuge experiments may not be correct.

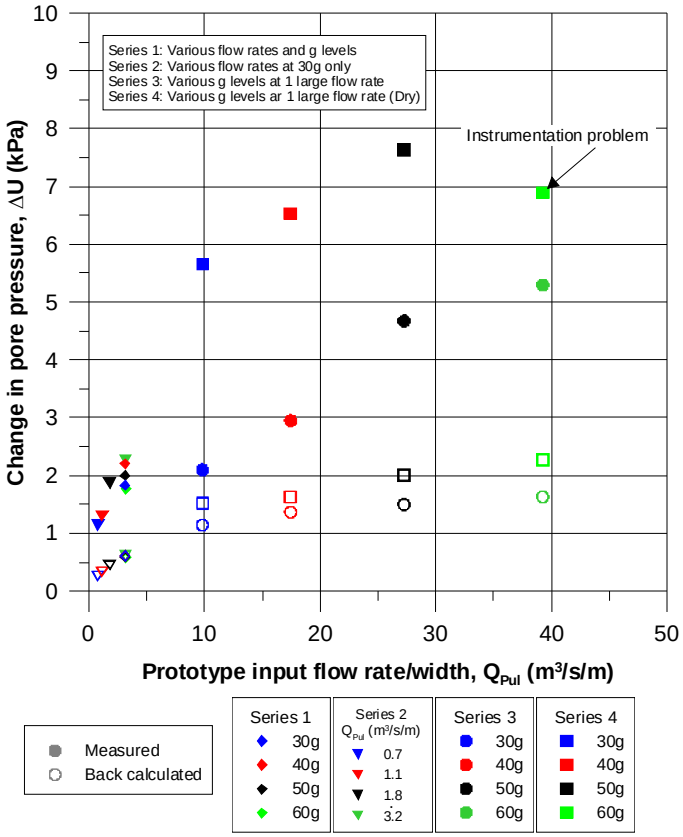

Figure 6.12: Comparison of the measured change in pore pressure and the back-calculated change in pore pressure

It can be seen in Figure 6.12 that the back calculated change in pore pressures for Series 4 (non-submerged) are still slightly larger than Series 3 (submerged), even though the flow heights in Series 4 are smaller than Series 3. However, the total incremental stress, $\Delta\sigma$, is larger in Series 4 compared to Series 3. It should be noted that the total incremental stress, $\Delta\sigma$, is higher in Series 4 even with a smaller flow height; this is due to the fact that the $\Delta\sigma$ in Series 4 is solely due to the total density of flow slurry, while the $\Delta\sigma$ in Series 3 has to take into account of the buoyancy effect. It is, therefore, reasonable for $\Delta\sigma$ to be smaller in Series 3 even with a larger flow height, hence resulting in a larger λ value compared to Series 4.

With the understanding of the relationships of total incremental stress, flow height, λ value and change in pore pressure lead to a preliminary conclusion that the measured change in pore pressure from the centrifuge experiments are somewhat not correct, though the trend is correct. A few possibilities for the variation in the measured and the back-calculated change in pore pressure due to the flow events are examined here.

Hypothesis 1: Error in water depth

This leads to the question of the reliability of the PPTs in measuring the change in pore pressure. In order to check the reliability of the measured change in pore pressure from the PPTs, the designed water depths in the centrifuge model are compared with the back-calculated water depths from the measurements of PPTs before the flow slurry.

Figure 6.13 shows the back-calculated water depths from measurements of change in pore pressure from the PPTs along the slope moments before introducing the flow slurry, as well as the designed water depth based on the actual PPTs location (depth) along the slope. It should be noted that the water level in the model moments before the flow slurry was actually at the top of the model, while water was fed continuously to maintain a constant water level in the channel and the overflow water was drained off from the ring channel as described in Chapter IV. Therefore, the designed water depths relative to the PPTs can be calculated since the water depth in the model was constant at that moment.

It can be seen that, in Figure 6.13, the designed water depths are consistently higher than the back-calculated water depths obtained from the PPTs measurements in the centrifuge experiments at various g levels (data obtained from Series 1).

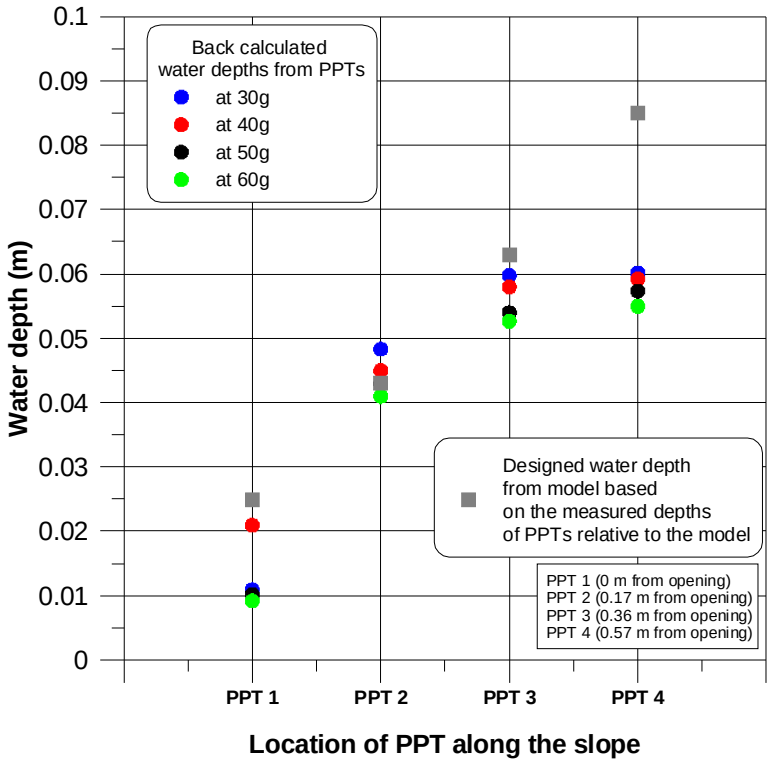

Figure 6.13: Designed and back-calculated water depths along the slope

It can be seen that the difference between the designed and measured change in pore pressure is larger at higher g level as well as at the further end of the slope (PPT4 at 0.57 m from opening). This is in fact due to the uplifting of the foam slope in which the higher the g level, the higher the uplifting force. Although struts were installed to prevent the foam slope from uplifting, as mentioned in Chapter IV, uplifting of the foam slope was not fully prevented. The uplifting of the foam slope resulted in elevation of the PPTs relative to the model and hence resulted in shallower water depths. This resulted in a smaller measured change in pore pressure compared to the designed water depths as shown in Figure 6.13. The smaller water depths and measured change in pore pressure are further exaggerated towards the end of the slope, such as in PPT 4, due to the thickness of the foam slope being thinner at the end of the slope, hence more uplifting at this location.

To further illustrate the uplift of the foam slope, Figure 6.14 a) shows the foam slope without uplifting and b) shows the foam slope with uplifting

due to the higher water pressure. Note that the uplifting of the foam slope in Figure 6.14 is exaggerated for illustration purposes.

Evidence of uplifting of foam slope at the location near to PPT 4 from the centrifuge experiments are shown in Figure 6.15. Figure 6.15 a) shows the foam slope when not submerged in water and before uplifting, while Figure 6.15 b) shows the uplifting of the foam slope when submerged in water.

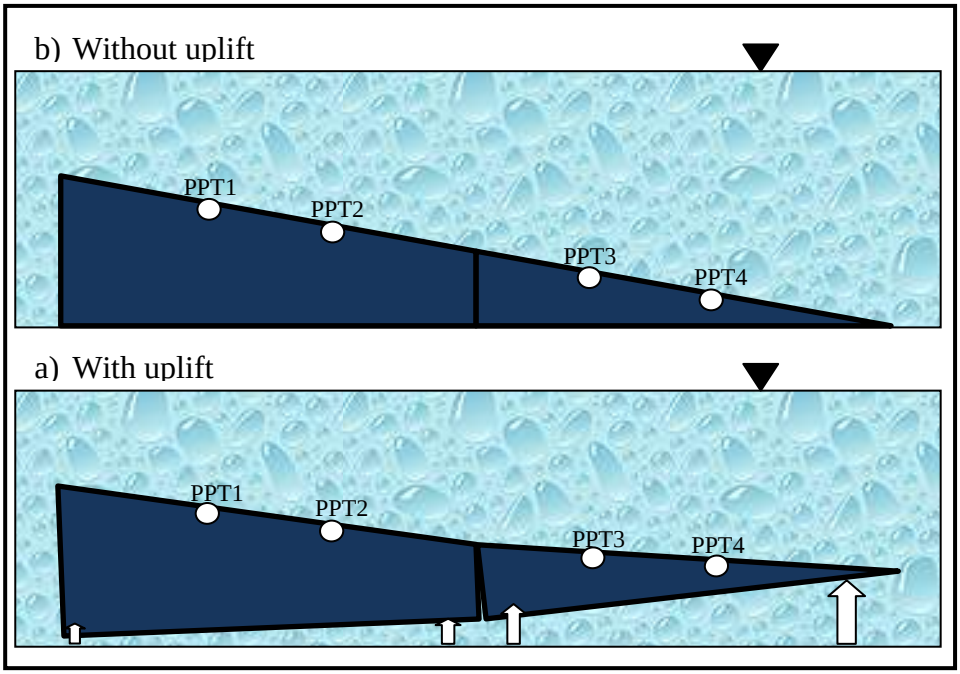

Figure 6.14: Uplifting of foam slope

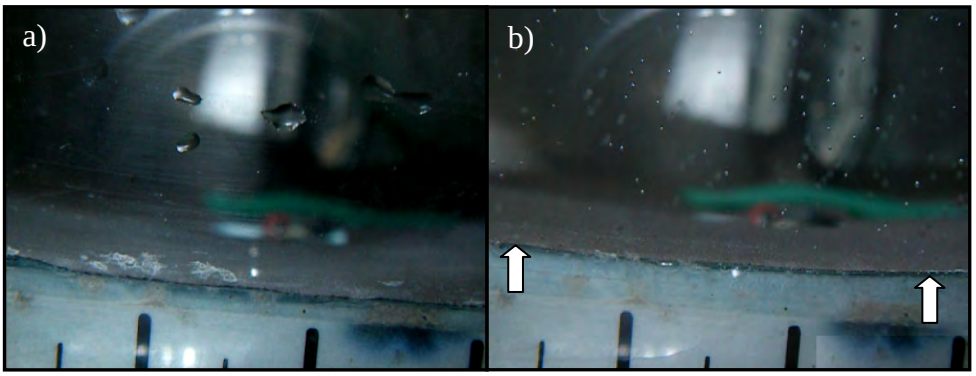

Figure 6.15: Evidence of uplifting of foam slope in the centrifuge experiment

Since the data acquisition in the experiments were logged before the centrifuge was spun, it would be useful to show the data of the measured change in pore pressure while the centrifuge progressed from stationary to the appropriate g level to check if the PPTs were giving the correct measurements. However, the water was only introduced gradually into the centrifuge after the centrifuge had achieved 10 g. While increasing the g level of the centrifuge progressively to the desired g level, the water was still being introduced gradually into the centrifuge and the water level was yet to achieve the maximum level at the top of the model. Therefore, the water levels were unknown before reaching the maximum level. Once the water level rises to the top of the model (maximum level), feeding of water continues and the additional water overflows from the top of the model thus creating a constant water level. This resulted in unknown water levels in the centrifuge during the period between stationary and up to the desired g level; the only way to correctly determine the water level was when the water level was at the top of the model.

Hypothesis 2: Impact force on the PPT

As mentioned in Chapter IV section 4.2.3.1, the PPTs were embedded in a groove within the foam slope, as shown in Figure 4.9 b. When the flow slurry approached near the PPTs, the PPTs experienced a sudden surge of acceleration. This sudden acceleration of slurry around the PPTs might have exerted an impact force (Impact force = acceleration of slurry x mass of slurry) on the PPTs, which might increase the measured change in pore pressure. The orientation of the PPTs might have also influenced the impact force as there was a gap between the groove and the PPTs, in which the flow slurry in the groove around the PPTs might have increased the impact force. The larger the slurry flow velocity was, the larger the sudden acceleration around the PPTs became; hence, a larger impact force was applied on the PPTs. This impact force might have contributed to the error in the measured change in pore pressure.

In an alternative method of understanding the “error” due to the impact force, the difference in the measured and back-calculated change in pore pressures are plotted with the flow velocity to quantify the “error”. Figure 6.16 shows the relationship of the “error” with the averaged flow velocity. The “error” here is defined as the back-calculated change in pore pressure, ΔU_{BC} minus the measured change in pore pressure from the centrifuge experiments, ΔU.

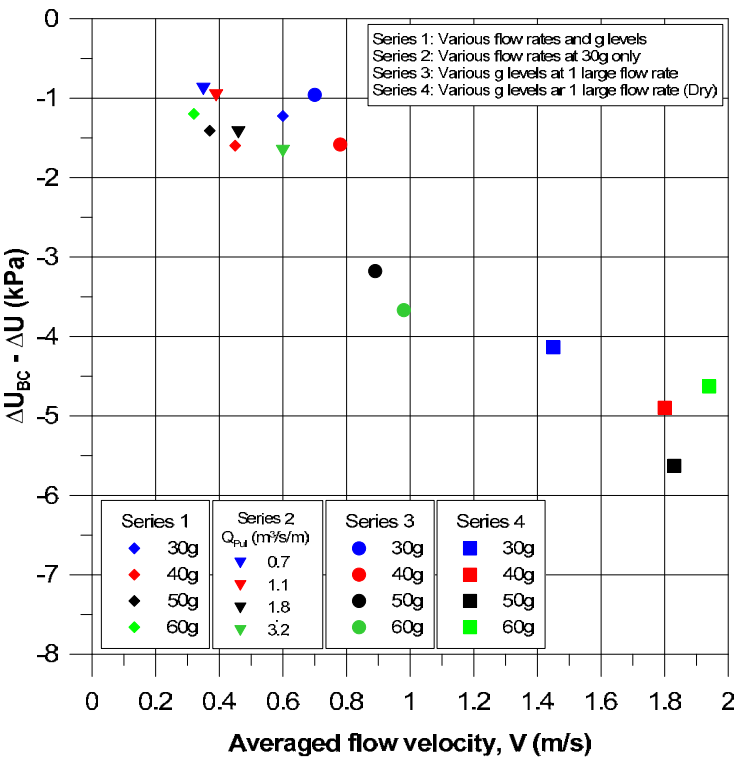

Figure 6.16: Relationship of error in measured change in pore pressure and the averaged flow velocity

Figure 6.16 clearly shows the trend of increasing difference from the measured change in pore pressure and the back-calculated change in pore pressure with larger flow velocity. This indicated that the acceleration of slurry around the PPTs was larger at larger flow velocity in which larger impact forces might have acted on the PPTs. Hence, the "error" on the measured change in pore pressure was larger at larger flow velocity. Further work is needed to understand the mechanisms of this result.

6.4 Summary

The results from centrifuge experiments and the numerical simulations for the scaled series (Series 1) show that they follow the proposed centrifuge scaling laws. In addition, the results from the numerical simulations accord with the centrifuge experiments when it is assumed that $\lambda = 1$.

Variations of results between centrifuge experiments and numerical simulations, in particular for Series 3 and 4, are found to be due to the difference in the pore pressure ratio, λ. With the proper λ values for each series, the results from the numerical simulations can match well with the centrifuge experiments. The results from numerical simulations show that by decreasing the λ value, the prototype flow height increases while the prototype flow velocity decreases. This indicates that a larger input flow rate produces a thicker flow (larger flow height), which results in increasing of soil shear resistance by the increase in effective stress and decrease in λ value. This also suggests that a small scale 1g model may produce a condition close to liquefaction and hence hydroplaning is likely to form as seen in the literature (Ilstad et al., 2004a) as mentioned in Chapter 2. The higher g condition as in the centrifuge, will give thicker deposits and the data show that effective stress increases. Hence, hydroplaning may not develop fully like the one observed in a small scale 1g model.

Based on the findings from Series 3 and 4, where the prototype input flow rates are the same for both series, show that the non submerged series has a smaller prototype flow height and a larger prototype flow velocity compared to the submerged series. This is because the gravity effect for the non submerged series (total weight of the flow slurry) is larger compared to the gravity effect for the submerged series (buoyant weight of the flow slurry) which is smaller. Considering the density of the material, the effective stress level is greater for the non submerged series compared to the submerged series. For the numerical simulations, a smaller λ value was needed for the non submerged series to match the centrifuge experiments compared to the

submerged series which needed a larger λ value. Thus, indicating smaller λ values yield larger effective stresses.

The causes for the discrepancy in the measured and back calculated change in pore pressure have been explored. It is found that the higher measured change in pore pressure from the PPTs compared to the back calculated change in pore pressure maybe due to the following; (i) error in water depths and (ii) impact force on PPTs. The uplifting of the foam slope resulting in different water depths also contributes to the difference in the measured and back calculated change in pore pressure. In addition, the "error" on the measured change in pore pressure is larger at larger flow velocity due to the sudden acceleration of flow slurry around the PPTs. This might have produced an impact force on the PPTs and thus increases the measured change in pore pressure. Further work is needed to understand the mechanisms involved in this.

CHAPTER VII

7.0 CONCLUSIONS AND RECOMMENDATIONS FOR FUTURE WORK

7.1 Introduction

This dissertation was concerned with developing centrifuge scaling laws for submarine landslide flows through the study of modelling submarine landslide flows in a mini-drum centrifuge. Numerical simulations using the DAMPM were carried out to further examine the proposed centrifuge scaling laws as well as to evaluate the results from the centrifuge experiments. From the literature it can be seen that most submarine landslide flows were investigated through 1 g experiments, while this study served as a pilot study on submarine landslide flows through centrifuge modelling. A new centrifuge apparatus was specifically developed for this research study. The findings presented in this dissertation were intended to contribute towards a more realistic and complex future research on submarine landslide flows through centrifuge modelling as well as through numerical simulations. Recommendations for possible future research work are also suggested in this chapter.

7.2 Summary and Conclusions

Through the available literatures, it was evident that the studies on submarine landslides were concentrated on 1 g experiments, while the studies through centrifuge experiments in this field were very limited.

Centrifuge scaling laws for submarine landslide flows were developed in this study. The proposed centrifuge scaling laws for submarine landslide flows differ from the conventional centrifuge scaling laws, in particular the

scaling law for flow distance, where the flow distance of a prototype is scaled at N^3 times that of the model. Based on the conventional centrifuge scaling law of a soil body, the movement in the flow direction would be scaled at N times that of the model.

It is noted that the conventional scaling law for length comes from the fact that the stress increment of a body is related to strain increment ($L_{prototype} = NL_{model}$), in which the stress equilibrium condition is satisfied. However, in this study, the movement of the submarine landslide flow (soil-fluid mixture) is considered very large and the soil, particularly that in contact at the base boundary, is extensively sheared. Therefore, if the soil is at failure (critical state) and the effective stress state of the soil becomes independent of strain, then the scaling law for length (or flow distance) is indeterminate. However, by assuming the shear resistance of a moving soil-fluid mixture has some viscous effect (strain rate dependent), a new scaling law can be derived as mentioned earlier, based on the assumption or simplification that the movement of the soil perpendicular to the slope is negligible compared to that which is parallel to the slope.

In order to investigate the proposed centrifuge scaling law, a new centrifuge apparatus has been successfully developed for use in a mini-drum centrifuge, which allows the modelling of submarine landslide flows. The development of the centrifuge apparatus included transferring the geometry of the slope into a circular mini-drum centrifuge, getting the right cameras and compartments of the model, instrumentation, providing sufficient lighting in the mini-drum centrifuge, and choosing appropriate slurry for the experiments.

Centrifuge experiments were successfully carried out at various g levels with scaled flow heights and velocities, in order to give the same magnitude of basal friction to resist the flow movement, as well as the soil stress field, to drive the soil body to move along the slope. The results showed that they achieved the same stress field in both the model and the prototype. Therefore, the results from the centrifuge experiments appeared to follow the proposed centrifuge scaling laws.

In addition, it was found that the measured flow heights from the centrifuge experiments based on visual inspection of the video recordings may not reflect the actual flow height. The flow slurry was under suspension in the submerged condition, resulting in an over-estimation of the actual flow height. The back-calculated flow height based on the flow velocity and the known input flow rate seems to be a better approach by which to estimate the flow height.

The submarine landslide flow centrifuge experiments were found to be reasonably repeatable, provided that the input flow rate could be controlled properly. It was found that the larger input flow rates were more difficult to control compared to the smaller input flow rates.

Further complementing the centrifuge results, numerical simulations through DAMPM have been successful in simulating submarine landslide flows, which closely modelled the centrifuge experiments and agreed well with the proposed centrifuge scaling laws.

The DAMPM is a relatively new method; therefore, the sensitivity of the model was investigated and it was found that the model was relatively stable even at different number of particles, as well as different background mesh sizes. Parametric studies on various soil properties were carried out using the DAMPM. It was found that the pore pressure ratio, λ, was a very important parameter in determining the progress of submarine landslide flows, in particular for determining the apparent effective stress of a soil body.

The issues on the variations of results between centrifuge experiments and numerical simulations, in particular for the series of non-scaled larger input flow rates (Series 3 and 4), were found to be due to the difference in the pore pressure ratio, λ. The results from numerical simulations show that, by decreasing the λ value, the prototype flow height increases while the prototype flow velocity decreases. This indicates that a larger input flow rate produces a

thicker flow (larger flow height), which results in an increase of soil shear resistance by the increase in effective stress and decrease in λ value.

Furthermore, the causes for the discrepancy in the measured and back-calculated change in pore pressure were explored using the results from both the numerical simulations and the centrifuge experiments.

Despite the above short-comings, the results from centrifuge experiments and the numerical simulations show that they follow the proposed centrifuge scaling laws and both methods were valuable for research studies on submarine landslide flows. The proposed centrifuge scaling laws for submarine landslide flows may be used to extrapolate centrifuge results to the field event when centrifuge experiments are carried out with various input flow rates for the specific type of soil (or actual field materials). Once the soil parameters are calibrated through the centrifuge modelling, the numerical simulation method can be used to study more complex submarine landslide problems that represent field events.

7.3 Recommendation for Future Research Work

The centrifuge experiments and the numerical simulations in this study were limited to the specific flow slurry used, which was a mixture of E-grade Kaolin clay and water (water content of 122%). This material does not resemble, and neither is it trying to replicate, an actual field material or field event; however, the results and findings from this study provide some insights into centrifuge modelling of submarine landslide flows. Therefore, further research work is required to model and to study more complex and field-related events of submarine landslide flows with the aid of the findings in this study. Below is a list of recommended future research work to further advance and supplement the knowledge in this field:

- Modelling of the submarine landslide from the initiation of failure progressing to the flow run-out; as this study only involved submarine landslide flows.
- The initiation of failure can be triggered either by a rapid sedimentation process to build up the excess pore pressure to initiate the failure or by increasing the pore pressure from the base of an existing soil layer in a centrifuge.
- Improvement on the centrifuge experimental process such as having an automated system (mechanical) of feeding the slurry material or more advanced actuators to initiate the failure.
- Further exploration on the methods and apparatus to measure the change in pore pressure is essential.
- The material used as the base of the slope shall be a denser material to avoid uplifting when subjected to high g level in the submerged condition.
- The centrifuge experiments shall be carried out at a smaller g level, preferably less than 60 g to avoid the camera being out of focus due to the shifting of camera lens in high g levels. If higher g levels are required to simulate an event, the proposed centrifuge scaling laws in this study can be used to extrapolate the results.
- It will be useful to investigate the impact forces due to the submarine landslide flows, such as the impact of the flow on offshore platforms and pipelines. This will benefit in the design process of offshore platforms and pipelines.
- Using realistic soil samples from the field is an add-on advantage as this will give site specific and yet more relevant results.
- Comparisons of results on either the centrifuge experiments or the numerical simulations to a large scaled experimental study or an actual field event would be valuable.
- The numerical simulations through DAMPM can be used to investigate more complex situations when the investigated problems are beyond the time and financial limits of a centrifuge experiment.

These suggested recommendations for future research work can be investigated using the same methodology from this study. Both centrifuge experiments and numerical simulations should supplement each other in order to carry out the abovementioned recommendations for future research work. Undoubtedly, this will further contribute towards the knowledge in the area of submarine landslide flows.

REFERENCES AND BIBLIOGRAPHY

Abe, K, Johansson, J. and Konagai, K. (2007). A new method for the run-out analysis and motion prediction of rapid and long-traveling landslides with MPM, JSCE journal of geotechnical and geoenvironmental engineering, Vol. 63(1), pp. 93-109. In Japanese.

Abe, K. (2008). Manual for Depth Averaged Material Point Method. 15/Nov/2008, Ver.1.

Abe, K., Tateyama, M., Shinoda, M., and Konagai, K. (2008). Run-out analysis of debris flow using MPM and depth averaged equation. Proc. of the Annual Conference of the Society for Multiphase Flow, University of Aizu, Japan. In Japanese.

Abe, K. (2009). Personal communication.

Andresen, A. and Bjerrum, L. (1967). Slides in subaqueous slopes in loose sand and silt. Marine Geotechnique, Adrian F.Richards Ed., University of Illinois Press, 221-239.

Barker, H.R. (1998). Physical Modelling of Construction Processes in the Mini-Drum Centrifuge. PhD Thesis, University of Cambridge.

Biscontin, G., Pestana, J.M. and Nadim, F. (2004). Seismic triggering of submarine slides in soft cohesive soil deposits. Marine Geology, 203: 341-354.

Boukpeti, N., White, D.J., and Randolph, M.F. (2011). Analytical modelling of the steady flow of a submarine slide and consequent loading on a pipeline. Geotechnique, (DOI): 10.1680/geot.10.P.001.

Boyland, N., Gaudin, C., White, D.J. and Randolph, M.F. (2010). Modelling of submarine slides in the geotechnical centrifuge. 7th Int. Conf. Physical Modelling in Geotechnics, Zurich, 1095-1100.

Bryn, P., Berg, K., Forsberg, C.F., Solheim, A., Kvalstad, T.J. (2005). Explaining the Storegga Slide. Marine and Petroluem Geology, 22: 11-19.

Chow, V.T. (1959). Open-channel hydraulics. McGraw-Hill, New York.

Coleman, J.M. and Prior, D.B. (1978). Submarine landslides in the Mississippi River Delta. Proceedings of the 10th Offshore Technology Conference, Houston, Vol. 2: 1067-1074.

Cornforth, D.H. and Lowell, J.A. (1996). The 1994 submarine slope failure at Skagway, Alaska. Proceedings of the 7th International Symposium on Landslides, Trondheim 17-21 June, Vol. 1, pp. 527-532.

Cornforth, D.H. (2004). Observations and analyses of the 1994 submarine landslide at Skagway, Alaska. Advances in Geotechnical Engineering. The Skempton Conference, Thomas Telford Ltd. Vol.2, pp. 822-833.

Coulter, S.E. and Phillips, R. (2003). Simulating submarine slope instability initiation using centrifuge model testing. Proceedings of the 1st International Symposium on Submarine Mass Movements and their Consequences, pp. 29-36.

Coulter, S.E. (2005). Seismic initiation of submarine slope failures using physical modeling in a geotechnical centrifuge. MEng Thesis, Memorial University of Newfoundland.

Coussot, P. and Piau, J.M. (1994). On the behaviour of fine mud suspensions. Rheologica Acta, 33: 175-184.

De Blasio, F.V., Engvik, L., Harbitz, C.Z., Elverhøi, A. (2004). Hydroplaning and submarine debris flows. Journal of Geophysical Research, 109, C01002, doi:10.1029/2002JC001714.

Edgers, L. and Karlsrud, K. (1982). Soil flows generated by submarine slides – Case studies and consequences. Proceedings of the Third International Conference on the Behaviour of Offshore Structures, Vol. 2: 425-437.

Fuglsang, L.D. and Ovesen, N. K. (1988). The application of the theory of modelling to centrifuge studies. Centrifuges in Soil Mechanics, Craig, James & Schofield (eds), Balkema, Rotterdam, 119-138.

Goodings, D.J. and Gillette, D.R. (1996). Model size effects in centrifuge models of granular slope instability. Geotechnical Testing Journal, Vol. 19, No. 3: 277-285.

Gue, C.S., Soga, K., Bolton, M., and Thusyanthan, N.I. (2010). Centrifuge modelling of submarine landslide flows. 7th Int. Conf. on Physical Modelling in Geotechnics, Springman, Laude & Seward (eds), Taylor & Francis Group, London, 1113-1118.

Hampton, M.A., Lee, H.J. and Locat, J. (1996). Submarine landslides. Reviews of Geophysics, 34(1): 33-59.

Hance, J.J. (2003). Development of a database and assessment of seafloor slope stability based on published literature. MSc Thesis, University of Texas at Austin.

Henkel, D.J. (1970). The role of waves in causing submarine landslides. Geotechnique, 20: 75-80.

Huang, X. and Garcia, M.H. (1997). A perturbation solution for Bingham-plastic mudflows. Journal of Hydraulic Engineering, ASCE, Vol. 123, No. 11: 986-994.

Huang, X. and Garcia, M.H. (1998). A Herschel - Bulkley model for mud flow down a slope. Journal of fluid mechanics, Cambridge University Press, Vol. (374): 305-333.

Huang, X. and Garcia, M.H. (1999). Modeling of non-hydroplaning mudflows on continental slopes. Marine Geology, (154): 131-142.

Hungr, O. (1995). A model for the runout analysis of rapid flow slides, debris flows, and avalanches. Canadian Geotechnical Journal. 32: 610-623.

Ilstad, T., Marr, J.G., Elverhøi, A., Harbitz, C.B. (2004a). Laboratory studies of subaqueous debris flows by measurements of pore-fluid pressure and total stress. Marine Geology, 213: 403-414.

Ilstad, T. Elverhøi, A., Issler, D., Marr, J.G. (2004b). Subaqueous debris flow behaviour and its dependence on the sand/clay ratio: a laboratory study using particle tracking. Marine Geology, 213: 415-438.

Ilstad, T., De Blasio, F.V., Elverhøi, A., Harbitz, C.B., Engvik, L., Longva, O., Marr, J.G.(2004c). On the frontal dynamics and morphology of submarine debris flows. Marine Geology, 213: 481-497.

Ilstad, T. (2005). On the Dynamics and Morphology of Submarine Debris Flows. PhD thesis, University of Oslo.

Imran, J., Harff, P. and Parker, G. (2001). A numerical model of submarine debris flow with graphical user interface. Computers & Geosciences, 27: 717-729.

Iverson, R.M. (1997). The physics of debris flow. Reviews of Geophysics, 35, 245-296.

Iverson, R.M. and Denlinger, R.P. (2001). Flow of variably fluidized granular masses across three-dimensional terrain – 1. Coulomb mixture theory. Journal of Geophysical Research, Vol. 106, No. B1, pp. 537-552.

Kvalstad, T.J., Andresen, L., Forsberg, C.F., Bryn, P., Wangen, M. (2005). The Storegga slide: evaluation of triggering sources and slide mechanics. Marine and Petroluem Geology, 22: 245-256.

Lewis, K. B. (1971). Slumping on a continental slope inclined at 10 - 40. Sedimentology, 16: 97-110.

Locat, J. and Lee, H.J. (2000). Submarine landslides: Advances and Challenges. Proceedings of the 8th International Symposium on Landslides, Cardiff, UK, 2000. Also published in the (2002) Canadian Geotechnical Journal, 39: 193-212.

Madabhushi, S.P.G. (2006). Lecture notes for 5R5 Advanced Experimental Methods in Geomechanics. University of Cambridge.

Marr, J.G., Harff, P.A., Shanmugam, G. and Parker, G. (2001). Experiments on subaqueous sandy gravity flows: The role of clay and water content in flow dynamics and depositional structures. Geological Society of America Bulletin: Vol. 113, No. 11, pp. 1377–1386.

Mohrig, D., Whipple, K.X., Hondzo, M., Ellis, C. and Parker, G. (1998). Hydroplaning of subaqueous debris flows. Geological Society of America Bulletin, March, Vol. 110, No.3: 387-394.

Mohrig, D., Elverhøi, A. and Parker, G. (1999). Experiments on the relative mobility of muddy subaqueous and subaerial debris flows, and their capacity to remobilise antecedent deposits. Marine Geology, (154): 117-129.

Mohrig, D. and Marr, J.G. (2003). Constraining the efficiency of turbidity current generation from submarine debris flows and slides using laboratory experiments. Marine and Petroleum Geology, (20): 883-899.

Moore, D.G. (1961). Submarine slumps. Journal of Sedimentary Petrology, 31: 343-357.

Morgenstern, N.R. (1967). Submarine slumping and the initiation of turbidity currents. Marine Geotechnique, Adrian F.Richards Ed., University of Illinois Press, 189-220.

Mulder, T. and Cochonat, P. (1996). Classification of offshore mass movements. Journal of sedimentary research, Vol.66, No.1, 43-57.

Norem, H., Locat, J., Schieldrop, B. (1990). An approach to the physics and the modelling of submarine flowslides. Marine Geotechnology, 9: 93-111.

Norwegian Geotechnical Institute (NGI) (2005). Offshore geohazards. Summary report for research institution-based strategic project 2002-2005, NGI report no. 20021023-2.

Numada, M., and Konagai, K. (2009). The research on the movement and deformation of landslide mass. Seisan Kenkyu, 61, pp. 1017-1020.

Paull, C.K., Ussler III, W. and Dillon, W.P. (2000). Potential role of gas hydrate decomposition in generating slope failures. Natural gas hydrate: In oceanic and permafrost environments, Max, M.D. (Ed), Kluwer Academic Publishers, Dordrect, Nertherlands, 149-156.

Phillips, R. and Byrne, P.M. (1994). Modelling slope liquefaction due to static loading. 47th Canadian Geotechnical Conference, Halifax, Canada, 317-326.

Prior, D.B. (1984). Subaqueous landslides. Proceedings of the IV International Symposium on Landslides, Toronto, Vol. 1: 179-196.

Savage, S.B., and Hutter, K. (1989). The motion of a finite mass of granular material down a rough incline. Journal of Fluid Mechanics, Vol. 199, 177-215.

Schofield, A.N. (1980). Cambridge geotechnical centrifuge operations. Geotechnique, 30: 227-268.

Schofield, A.N. (1988). An introduction to centrifuge modelling. Centrifuges in Soil Mechanics, Craig, James & Schofield (eds), Balkema, Rotterdam, 1-9.

Schwarz, H.-U. (1982). Subaqueous Slope Failures – Experiments and Modern Occurences. Contributions to Sedimentology, 11, Stuttgart.

Silva, A. (2003). Underwater landslides as causes of tsunamis. Presentation file at Workshop on model validation and benchmarking for tsunami generation by submarine mass failure, Hawaii.

Sulsky, D., Chen, Z., Schreyer, H.L. (1994). A particle method for history-dependent materials. Comput. Methods Apple. Mech. Engrg, 118, pp. 179-196.

Synolakis, C.E., Bardet, J-P., Borrero, J.C., Davies, H.L., Okal, E.A., Silver, E.A., Sweet, S. and Tappin, D.R. (2002). The slump origin of the 1998 Papua New Guinea Tsunami. Proceedings of the royal society A: Mathematical, physical and engineering sciences, 458: 763-789.

Taylor, R.N., ed. (1995). Geotechnical Centrifuge Technology. Blackie Academic & Professional, London, UK.

Terzhagi, K. (1956). Varieties of submarine slope failures. Harvard Soil Mechanics Series No. 52, Harvard University, also published in 8th Texas Conference on Soil Mechanics and Foundation Engineering, Austin, USA, pp. 1-41.

Vanneste, M., Forsberg, C.F., Glimsdal, S., Harbitz, C.B., Issler, D., Kvalstad, T.J., Løvholt, F. and Nadim, F. (2011). Submarine landslides and their consequences: What do we know, what can we do?. Proceedings of the second World Landslide Forum, 3 -7 Oct 2011, Rome.

Vendeville, B.C. and Gaullier, V. (2003). Role of pore fluid pressure and slope angle in triggering submarine mass movements-natural examples and pilot experimental models. Proceedings of the 1st International Symposium on Submarine Mass Movements and their Consequences, pp. 137-144.

Zhou, S.H., Liu, J.G., Wang, B.L., Yang, L.C. and Gong, Q.M. (2002). Centrifugal model test on the stability of underwater slope. In Phillips, R., Guo, P.J., and Popescu, R., editors, Physical modelling in Geotechnics: ICPMG' 02, pages 759-764, Canada, Swets & Zeitlinger Lisse, A.A. Balkema.

Appendix 1

Summary of the characteristics of selected submarine landslides

Slide	Max. Length (m)	Max. Height (m)	Volume (m^3)	L_{max}/H_{max}	Slope Angle	Triggering Mechanism	Soil Type	Reference
Bassein	215000	2200	8.00E+11	98	N/A	Sed & EQ	N/A	Edgers and Karlsrud (1982)
Storegga	160000	1700	8.00E+11	94	1	N/A	N/A	Edgers and Karlsrud (1982)
Grand Banks	750000	5000	7.60E+11	150	3.5	EQ	Sand / Silt	Edgers and Karlsrud (1982)
Spanish Sahara	700000	3100	6.00E+11	226	N/A	Sed	Gravelly clayey sand	Edgers and Karlsrud (1982)
Rockall	135000	700	2.96E+11	193	N/A	Sed	N/A	Edgers and Karlsrud (1982)
Walvis Bay S.W. Africa	250000	2100	9.00E+10	119	N/A	N/A	N/A	Edgers and Karlsrud (1982)
Messina	220000	3200	1.00E+06	69	N/A	EQ	Sand / Silt	Edgers and Karlsrud (1982)
Orleansville	100000	2600	1.00E+06	38	N/A	EQ	N/A	Edgers and Karlsrud (1982)
Icy Bay / Malaspina	12000	80	3.20E+10	150	N/A	EQ	Clayey silt	Edgers and Karlsrud (1982)
Copper River	8000	85	2.40E+10	94	N/A	Sed	Sand / Silt	Edgers and Karlsrud (1982)
Ranger	37000	800	2.00E+10	46	N/A	Sed & EQ	Clayey and sandy silt	Edgers and Karlsrud (1982)
Mid. Alb. Bank	5E+06	600	1.90E+10	8833	N/A	EQ & Sed	Silty clay	Edgers and Karlsrud (1982)

Slide	Max. Length (m)	Max. Height (m)	Volume (m^3)	L_{max}/H_{max}	Slope Angle	Triggering Mechanism	Soil Type	Reference
Wil. Canyon	60000	2800	1.10E+10	21	N/A	Sed	Silty clay and silt	Edgers and Karlsrud (1982)
Kidnappers	11000	200	8.00E+09	55	2.5	EQ ?	Sandy silt and clay	Edgers and Karlsrud (1982)
Kayak Trough	18000	150	5.90E+12	120	N/A	Sed & EQ	Clayey silt	Edgers and Karlsrud (1982)
Paoanui	7000	200	1.00E+09	35	N/A	EQ ?	Silt / Sand	Edgers and Karlsrud (1982)
Mid. Alb. Cont. Slope	4E+06	300	4.00E+08	11667	N/A	Sed	Silty clay	Edgers and Karlsrud (1982)
Magdalena R.	24000	1400	3.00E+07	17	2	Sed	N/A	Edgers and Karlsrud (1982)
California	35000	150	2.50E+11	233	N/A	EQ ?	Clayey and sandy silt	Edgers and Karlsrud (1982)
Suva, Fiji	110000	1800	1.50E+11	61	3	EQ	Sand	Edgers and Karlsrud (1982)
Valdez	1E+06	168	7.50E+10	7619	6	EQ	Gravelly silty sand	Edgers and Karlsrud (1982)
Orkdalsfjord	22500	500	2.50E+10	45	N/A	Man Made	Sand / Silt	Edgers and Karlsrud (1982)
Sokkelvik	5000	100	1.00E+06	50	N/A	N/A	Quick clay + sand?	Edgers and Karlsrud (1982)
Sandnessjoen	1E+06	180	1.00E+05	6667	N/A	Man Made	N/A	Edgers and Karlsrud (1982)

Slide	Max. Length (m)	Max. Height (m)	Volume (m^3)	L_{max}/H_{max}	Slope Angle	Triggering Mechanism	Soil Type	Reference
Helsinki Harbour	400000	11	6.00E+03	36364	N/A	Man Made	Sand / Silt	Edgers and Karlsrud (1982)
Grand Banks	110000	365	7.60E+10	301	3.5	N/A	N/A	Hampton et al. (1996)
Hawaii	160000	2000	N/A	80	6	N/A	N/A	Hampton et al. (1996)
Bay of Biscay	21000	250	N/A	84	N/A	N/A	N/A	Hampton et al. (1996)
Rockall	160000	330	3.00E+11	485	2	N/A	N/A	Hampton et al. (1996)
Bassein	37000	360	N/A	103	6	N/A	N/A	Hampton et al. (1996)
Agulhas	106000	375	N/A	283	N/A	N/A	N/A	Hampton et al. (1996)
Copper River delta	18000	115	N/A	157	1	N/A	N/A	Hampton et al. (1996)
Albatross Bank	5300	300	N/A	18	7	N/A	N/A	Hampton et al. (1996)
Portlock Bank	6500	200	N/A	33	4	N/A	N/A	Hampton et al. (1996)
Kayak Trough	15000	115	N/A	130	1	N/A	N/A	Hampton et al. (1996)
Atlantic Coast 1	3400	30	N/A	113	3.8	N/A	N/A	Hampton et al. (1996)
Atlantic Coast 2	4800	80	N/A	60	5.7	N/A	N/A	Hampton et al. (1996)
Atlantic Coast 3	2300	18	N/A	128	6.8	N/A	N/A	Hampton et al. (1996)
Mississippi River Delta	N/A	20	4.00E+07	N/A	0.5	N/A	N/A	Hampton et al. (1996)

Slide	Max. Length (m)	Max. Height (m)	Volume (m^3)	L_{max}/H_{max}	Slope Angle	Triggering Mechanism	Soil Type	Reference
Typical Atlantic Ocean	4000	1200	N/A	3	4	N/A	N/A	Hampton et al. (1996)
Cape Fear	30000	700	N/A	43	4.2	N/A	N/A	Hampton et al. (1996)
Blake Escarpment	42000	3600	6.00E+11	12	8.6	N/A	N/A	Hampton et al. (1996)
East Break East	70000	1150	1.30E+10	61	1.5	N/A	N/A	Hampton et al. (1996)
East Break West	110000	1100	1.60E+11	100	1.5	N/A	N/A	Hampton et al. (1996)
Navarin Canyon	6000	175	5.00E+09	34	3	N/A	N/A	Hampton et al. (1996)
Seward	3000	200	2.70E+06	15	25	N/A	N/A	Hampton et al. (1996)
Alsek	2000	20	N/A	100	1.3	N/A	N/A	Hampton et al. (1996)
Sur	70000	750	1.00E+10	93	0.5	N/A	N/A	Hampton et al. (1996)
Santa Barbara	2300	120	2.00E+07	19	4.8	N/A	N/A	Hampton et al. (1996)
Alika-2	95000	4800	3.00E+11	20	N/A	N/A	N/A	Hampton et al. (1996)
Nuuanu	230000	5000	5.00E+12	46	N/A	N/A	N/A	Hampton et al. (1996)
Tristan de Cunha	50000	3750	1.50E+11	13	N/A	N/A	N/A	Hampton et al. (1996)
Kitimat Slide	6000	200	2.00E+08	30	N/A	N/A	N/A	Legros (2002)
A1	370000	1700	2.50E+11	218	N/A	N/A	N/A	Legros (2002)
A2	160000	1500	2.20E+10	107	N/A	N/A	N/A	Legros (2002)
A3	140000	1400	8.50E+09	100	N/A	N/A	N/A	Legros (2002)
A4A	130000	1300	2.70E+10	100	N/A	N/A	N/A	Legros (2002)

Slide	Max. Length (m)	Max. Height (m)	Volume (m^3)	L_{max}/H_{max}	Slope Angle	Triggering Mechanism	Soil Type	Reference
A4B	400000	2000	3.20E+11	200	N/A	N/A	N/A	Legros (2002)
Kae Lae slide	60000	5000	4.00E+10	12	N/A	Volcanic	N/A	Legros (2002)
Molokai slide	130000	5200	1.10E+12	25	N/A	Volcanic	N/A	Legros (2002)
Oahu slide	180000	5500	1.80E+12	33	N/A	Volcanic	N/A	Legros (2002)
Alika slide	105000	5300	1.80E+12	20	N/A	Volcanic	N/A	Legros (2002)

*N/A : Not Available

EQ: Earthquake

Sed: Sedimentation

Appendix 2

Appendix 2

Weight balancing in the Mini-Drum Centrifuge

Weight from model				
Item	Description	Weight (kg)	Radius (m)	Weight x Radius (kgm)
1	Model	12,4	0,224	2,778
2	Water	5,06	0,232	1,174
3	Slurry	4	0,230	0,920

Counter weight				
Item	Description	Weight (kg)	Radius (m)	Weight x Radius (kgm)
1	Water	17,97	0,227	4,078
2	Counter weight	2,540	0,310	0,787

Model	Before adding water	Total =	2,778	kgm
	After adding water	Total =	3,952	kgm
	After adding water & slurry	Total =	4,872	kgm

Counter weight	Before adding water	Total =	0,787	Out of balance =	1,990	kgm	Counter weight =	8,960 kg
	After adding water	Total =	4,866	Out of balance =	-0,914	kgm	Counter weight =	-0,409 kg
	After adding water & slurry	Total =	4,866	Out of balance =	0,006	kgm	Counter weight =	2,559 kg

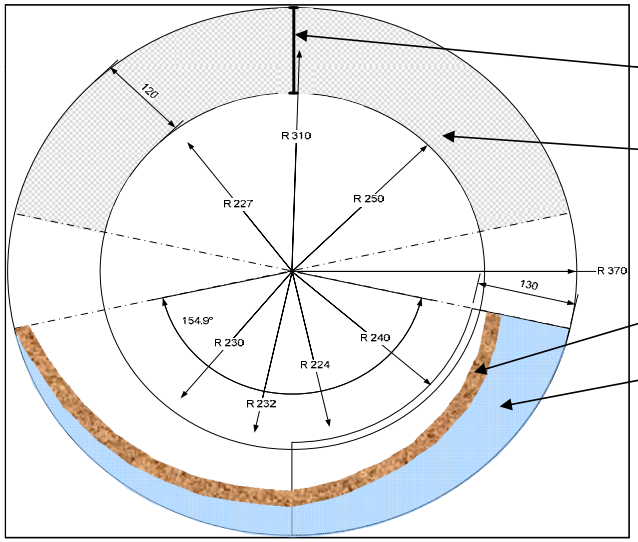

Counter weight

Assumed counter weight water

Slurry

Foam slope

Actual counter weight used = 2.54 kg

Water displaced due to counter weight = 0.114 kg

Original water weight at counter weight side = 18.08 kg

Original model weight = 12.4 kg

Drawing units in mm

*Radius is from centriod of mass to the centre of centrifuge
* ' - ' indicates counterweight is greater than the weight of model

Appendix 3

APPENDIX 3

Calculation of bending moments against Perspex window

Maximum water depth at Perspex = 0.1 m

$\therefore$ Water pressure at 0.1 m = 0.1 x 10 = 1 kN/m^2

Assume γ soil = 20 kN/m^3 and 0.02 m above the foam

$\therefore$ Soil pressure = 20 x 0.02 = 0.4 kN/m^2

$\therefore$ Total pressure against the Perspex at 0.1m = 1.4 kN/m^2

At 100 g, total pressure against the Perspex at 0.1m = 140 kN/m^2

Size of Perspex 0.1 x 0.06 m

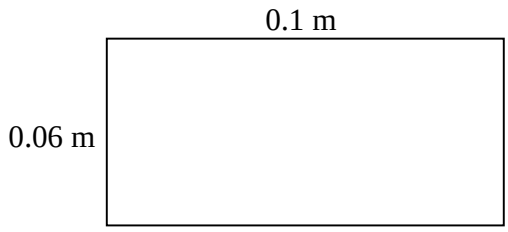

Assume uniform distributed load on the 0.1 m length of Perspex =140 x 0.06 = 8.4 kN/m

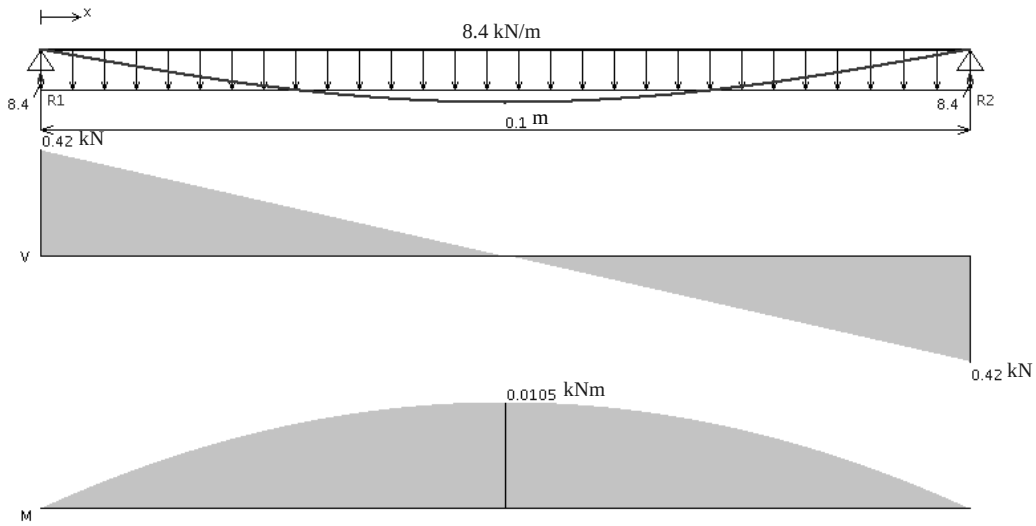

Thickness of Perspex 10mm @ 0.01 m

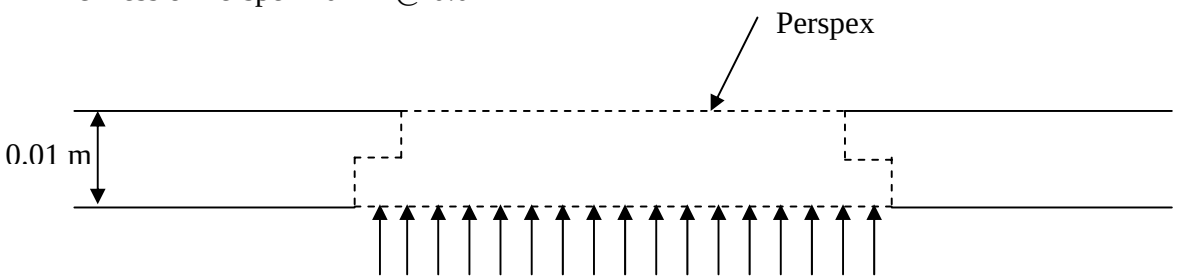

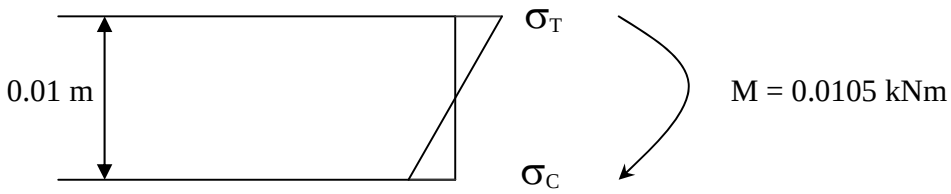

$$\sigma = \frac{M}{I} y \qquad I = \frac{bh^3}{12} = \frac{0.06 \times 0.1^3}{12} = 0.000005 \text{ m}^4$$

$$\sigma = \frac{0.0105}{0.000005} \times 0.005 = 10.5 \text{ kN/m}^2$$

The tensile strength of Perspex = 49 MPa

The compressive strength of Perspex = 73 MPa

σ_T & σ_C = 10.5 kPa <<<<< 49 @ 73 MPa

∴ The applied pressure is safe for the Perspex.

Mechanical properties of Perspex - **Polymethyl methacrylate (PMMA)**

Mechanical Properties		Conditions		
		State 1	State 2	ASTM
Elastic Modulus (MPa)	2553 - 3174	compressive		D638
	2243 - 3243	tensile		D638
Flexural Modulus (MPa)	2243 - 3174	23 ºC		D790
Tensile Strength (MPa)	49 - 73	at break		D638
	54 - 74	at yield		D638
Compressive Strength (MPa) at yield or break	73 - 125			D695
Flexural Strength (MPa) at yield or break	73 - 132			D790
Elongation at break (%)	2 - 6			D638
Hardness	68 - 105	Rockwell M		D638
Izod Impact (J/cm of notch) 1/8" thick specimen unless noted	0.1 - 0.2			D256A

Ref: www.efunda.com

Appendix 4

Checklist for operating the mini-drum centrifuge

No.	Checklist Items	Remarks
1	Prior to adjusting the mini-drum to its horizontal or vertical axis; please check the ***safety bolts*** !	
2	Ensure the ***clutch is on*** if the turntable and face plate is to spin together.	
3	While adjusting the mini-drum, ensure ***wirings and cables*** around the mini-drum are not obstructing the movement.	
4	Cover the top of the mini-drum with the ***safety cover*** .	
5	Switch on the main supply.	
6	Ensure the ***compressor*** in the laboratory is on.	
7	Adjust the standpipe up or down depending on the type of test.	
8	At the mini-drum power supply, turn on the control (***Control ON***).	
9	Turn on the turntable (***TURNTABLE ON***) and face plate (***FACE PLATE ON***).	
10	Press ***F4*** on key pad (***ON***), check if there is a ***OK*** sign a the power supply.	
11	To start spining, press ***F3*** motion key.	
12	Press ***F1*** for face plate.	
13	Set the speed by entering the ***rpm*** .	
14	Press ***Enter*** .	
15	***Double check*** on the entered rpm, press ***YES*** if it is correct.	
16	Increase or decrease speed ***gradually.***	
17	After test, ***check the safety bolts again before adjusting*** the mini-drum.	
18	***Switch off*** the TURNTABLE, FACE PLATE control, and the main supply.	

Notes: